UNIVERSITY OF CALIFORNIA

Santa Barbara

Fluvial Processes Affecting the Texture of a Gravel Bed with an Emphasis on Salmon Spawning Habitat

A dissertation submitted in partial satisfaction of the

requirements for the degree Doctor of Philosophy

in Environmental Science and Management

by

Matthew Armand Meyers

Committee in charge:

Professor Thomas Dunne, Chair

Professor Derek Booth

Professor James Frew

Professor Edward Keller

June 2017

The dissertation of Matthew Armand Meyers is approved.

_____

Derek Booth

_____

James Frew

_____

Edward Keller

_____

Thomas Dunne, Committee Chair

June 2017

Fluvial Processes Affecting the Texture of a Gravel Bed with an Emphasis on Salmon Spawning Habitat

by

Matthew Armand Meyers

DEDICATION

I dedicate this work to my mother, Mary Inez Meyers (Phelan), whose invariable example of purposeful existence, selfless guidance, and positive encouragement provided my motivation and inspires me to get more from life by contributing.

ACKNOWLEDGEMENTS

Over the past nine years, I have received support and encouragement from many individuals. Tom Dunne has been an inspiring and incredibly patient mentor from the inception of the research plan thorough final review; while devoted to product completion, he encouraged, by expression and warm hospitality, a healthy balance between professional and personal lives for which I am grateful. I would like to thank my dissertation committee of Derek Booth, James Frew, and Ed Keller for their advice and encouragement during research development. In addition, Scott McBain, Bob Mussetter, and Scott Wright graciously provided useful insights on my research.

My colleagues Dave Encinas, Kevin Faulkenberry, and Paul Romero enabled this work both logistically and financially, through the California Department of Water Resources San Joaquin River Restoration Program. I am grateful to have worked with courageous field assistants who collected dependable notes and data during the long and incredibly hot days: Anthony Cemo, Steven Garcia, Tom Holley, Alex Jones, William Lee-Decatur, Eddie Mendez, Trent Sherman, Andy Shriver, Grizelda Vigil (Soto), and Abeje Temesgen. McBain Associates generously loaned me their backpack pump and provided guidance on hydraulic conductivity monitoring. During data collection and writing, my wife, Erica Marie Meyers (Eisch), spent countless hours listening to me talk about this research, giving encouragement and proofreading, and caring and providing for our family. To all the above, I have benefitted much from our conversations and will forever appreciate the times with your company on those dry, sun-scorched summer days on the San Joaquin River.

VITA OF MATTHEW ARMAND MEYERS

JUNE 2017

EDUCATION

Bachelor of Science in Earth Science, emphasis on Surficial Processes, University of California, Santa Cruz, December 1995
Master of Environmental Science and Management in Water Resource Management, University of California, Santa Barbara, June 2008
Doctor of Philosophy in Environmental Science and Management, University of California, Santa Barbara, June 2017 (expected)

PROFESSIONAL EMPLOYMENT

1997-99: Staff Geologist, Consolidated Geoscience, Inc., Brea, California
1999-2000: English as a second language instructor: Oxford University, Vicenza, Italy
2000-01: Web Developer, Broadchoice Inc., San Mateo, California
2001-06: Project Geologist, Cambria Environmental Technology, Inc., Emeryville, California
2007-10: Graduate student researcher, Institute of Computational Earth System Science, University of California, Santa Barbara
2008-10: Graduate student assistant, California Department of Water Resources, Fresno, California
2010-present: Engineering Geologist, California Department of Water Resources, Fresno, California

PUBLICATIONS

"Steelhead Passage Restoration Options for Canada de Santa Anita, Santa Barbara County, California," Unpublished thesis submitted in partial fulfillment of the requirements for the Master of Environmental Science and Management degree in Water Resources Management, University of California, Santa Barbara, 2008. 108 pp.

"Perspectives on disconnects between scientific information and management decisions on post-fire recovery in western U.S.," *Environmental Management*, 52(6) (2013), 1415-1426.

AWARDS

Special Recognition for poster presentation at San Joaquin River Restoration Program science symposium, 2015

FIELDS OF STUDY

Major Field: Fluvial Geomorphology

A Study of Gravel-bed Entrainment Using Tracers: Measured and Explained with Professor Thomas Dunne
A Study of Frictional Resistance of In Situ Grains on a Gravel-bed with Professor Thomas Dunne
Using an Artificial Redd to Implicate Physical Process that Affect Incubation Habitat Quality with Professor Thomas Dunne

ABSTRACT

Fluvial Processes Affecting the Texture of a Gravel Bed with an Emphasis on Salmon Spawning Habitat

by

Matthew Armand Meyers

Spawning salmon depend on fluvial processes to maintain the bed texture of gravel bedded rivers as suitable spawning and incubation habitat. The coarse texture of a gravel bed is maintained by flow strengths capable of moving the gravel and removing fine sediments, thereby providing loose substrate that enhances its ability to conduct flow (i.e., its hydraulic conductivity). The flow strength that corresponds to the beginning of movement (i.e., entrainment) of a grain on a gravel bed is variable and, therefore, it needs to be measured to predict flow levels capable of bed texture maintenance. Lower flows can deliver fine sediment, which may accumulate in the gravels overlying salmon nests (i.e., redds) reducing the hydraulic conductivity and impairing salmon embryo development. I examine these processes to explain the variability in (i) the rate of change in the proportion of a gravel size fraction entrained as a function of flow strength and (ii) the rate of decrease in hydraulic conductivity as a function of the cumulative transport of fine sediment that depends on flow level.

I used tracer gravel and cobble grains and a two dimensional flow model to determine the flow strengths capable of gravel bed entrainment using binary plots of the occurrence or absence of tracer movement to approximate the fraction of the bed sediment entrained as a logistic function of increasing flow strength. The method provides an approximation of the flow strength capable of entraining the least resistant through the most resistant grains, thereby providing a new method to approximate the flow strength that is capable of fully entraining the bed. The results are confirmed by comparing the measurements of two study sites.

To measure the resistance of individual gravel and cobble grains to downstream movement, I used force gages and a theoretical force balance model that incorporates the frictional resistance of a grain and the lift and drag forces applied by stream flow. I measured the frictional resistance of grains at six sites with different morphologies to evaluate influences on grain resistance. Grain resistance varied depending on the grain size and sorting, amount of infiltrated sand, streamwise position along a gravel bar, and degree of fluctuation in the flow strength. The force balance model predicts that the dimensionless instantaneous flow strength capable of entraining a given proportion of a relative grain size varies along a bar. I tested the force balance model predictions by comparison with the tracer measurements from the tracer study. The differences between the force balance predictions and the tracer entrainment measurements are due to the definition of the flow strength as the time-averaged value from the 2D flow model and the instantaneous value from the force balance model. Adjusting the force balance model predictions by a simple factor that quantifies their difference and that corresponds with an index describing the fluctuations of the instantaneous flow strength about its time-

averaged value produces agreement with the tracer measurements. This adjustment to force gage measurements from two sites on opposite limbs of a bar indicates that the time-averaged dimensionless flow strength capable of entraining a given proportion of a relative grain size is constant along a bar.

I constructed artificial redds at five sites to monitor changes in hydraulic conductivity and sand accumulation with cumulative bed load transport. I applied two backfill treatments to examine the effects of the presence and absence of grains smaller than 6.4 mm. Hydraulic conductivity varies temporally due to sand deposition and spatially due to the initial sand content of the backfill and the local sediment supply rate. The rate of change in hydraulic conductivity as a function of increasing cumulative transport is statistically significant but does not differ between backfill treatments or with location. I predicted the effect of flow on egg survival using an empirical relationship between hydraulic conductivity and egg survival with results that indicate hydraulic conductivity is dependent on sediment transport rate as a function of flow rate.

This work provides additional understandings of the relationship between flow and bed texture maintenance processes and useful tools for managing gravel bed rivers.

TABLE OF CONTENTS

I. Explaining Gravel-bed Entrainment Trends Measured Using Tracers

A. Introduction

Fluvial transport of bed material has been studied for over a century [*Gilbert*, 1914] and yet principal mechanisms of the transport process remain to be adequately quantified. The surface of a streambed is the initial source of transported material [*Laronne et al.*, 2001] and with flow strength it controls the onset and rate at which grains move. This has important implications to the resiliency of benthic ecosystems that are dependent on the stability of the gravels and cobbles on the bed surface [*Biggs et al.*, 2002]. However, flushing fine sediment from a gravel bed is an important process for maintaining salmon incubation habitat and requires moving the gravel and cobble to expose trapped sand to erosive flow forces [*Kondolf and Wilcock*, 1996; *Wilcock et al.*, 1996]. The balance between stability and mobility is controlled by the onset and increase of bed material entrainment with increasing flow strength.

Entrainment refers to the moment an immobile grain is moved and enters the transport field. Moving a static grain is the first limitation to its transport. The final limitation to entrainment involves complete entrainment of the bed, such that every grain size fraction is fully entrained. Both of these limitations can also be used to describe the mobility of a grain size fraction and while a grain size fraction may be immobile or fully entrained other fractions may not. Within this range of limitations there are several physical factors controlling the ability of a grain to be moved (e.g., frictional resistance,

packing, roughness, projection, and hiding). Each of these factors affects the entrainment processes and their effect is expressed in different facets of the process.

The different facets of entrainment can be defined as: the threshold at which the first grains on a bed begin to move (incipient entrainment), the condition in which some grains on a bed move and others remain immobile (partial entrainment), and the threshold above which all grains on a bed will be entrained (full entrainment). Together these facets of entrainment define the domain of partial entrainment and have been studied in regards to describing entrainment of a bed area [*Konrad et al.*, 2002; *Haschenburger and Wilcock*, 2003] or of individual grain size fractions, referred to as fractional entrainment [*Wilcock and McArdell*, 1997]. Additionally, *Komar* [1987] referred to the tendency for the shear stress producing the onset of entrainment to increase as a function of increasing grain size as selective entrainment because it causes smaller grains to preferentially mobilize relative to larger grains. In order to predict the proportion of grain size fractions that will be moved for a given flow strength, each of these facets must be quantified.

While these facets of entrainment have been studied individually and in combinations, there are no documented field studies that collectively integrate them on a mixed bed. This may be in large part due to a paucity of research that investigates entrainment together with grain size and flow strength, as well as a lack of tested field methods that are able to directly detect entrainment at the local flow strength.

The flow strength responsible for entraining grains is most often quantified by the bed shear stress, τ, and that capable of inducing incipient entrainment is referred to as the critical shear stress, τ_c where subscript 'c' refers to the critical incipient entrainment threshold. *Shields* [1936] non-dimensionalized laboratory flume results, which he

suggested could be scaled to rivers, are summarized for the range of flows and particle sizes of interest in most rivers in the *Shields*' equation:

$$\tau_c^* = \frac{\tau_c}{Dg(\rho_s - \rho)} \quad (1)$$

where g is gravity, and ρ_s and ρ are the grain and fluid density, and τ_c^* is the dimensionless critical shear stress for motion of a particle of size D. Shields emphasized that this formula was to be interpreted statistically in terms of mean local velocities and particle sizes, and the onset of transport was defined by extrapolating a plot of transport rate versus τ backward to zero transport. In the case of "mixed bedload", "weak movement" of the finer fractions "corresponds most closely to the beginning of movement" [*Shields*, 1936, p. 11]. His results indicated that the value of τ_c^* for gravel in rough flow was approximately 0.06, although later values of 0.030 [*Neill*, 1968] and 0.046 [*Gessler*, 1971] were proposed and accepted as constant for many applications in sediment transport calculations [*Miller et al.*, 1977; *Yalin and Karahan*, 1979; *Wilcock*, 1993; *Parker et al.*, 2008]. However, when the *Shields'* equation began to be applied to heterogeneous channels, especially with gravel beds, a constant τ_c^* was found to be an imprecise predictor of incipient motion of both the average size of bed material and of each grain size fraction [*Buffington and Montgomery*, 1997].

Other ways of identifying τ_c^* have involved analysis of large datasets of transport measurements from the field [*Parker et al.*, 1982] and laboratory data [*Meyer-Peter and Müller*, 1948; *Wong and Parker*, 2006]. In doing so, researchers have typically relied on bed load transport observations at many flow levels to define the onset of motion from (i) interpolating or curve-fitting to plots of transport rate versus τ to determine the τ value that produces a sufficiently small, predetermined reference transport rate to suggest the

beginning of transport [*Parker and Klingeman*, 1982]; (ii) using the τ and the largest grain in transport to define a $\tau_{c,i}$ value, where '*i*' refers to the grain size fraction [*Andrews*, 1983; *Hammond et al.*, 1984]; or (iii) noting the τ value at which the beginning of grain motion is visually discerned [*Gilbert*, 1914; *Meyer-Peter and Müller*, 1948]. *Buffington and Montgomery* [1997] compiled eight decades of research that used these methods to define τ_c^* and found that they produce systematic methodological biases such that $\tau_{c,50}^*$ values, where subscripted '*50*' refers to the median grain size, determined from the reference and visual methods $\tau_{c,50}^*$ range from 0.052-0.086 and 0.030-0.073, respectively, and the largest grain results are described as "less well defined" with their tabulated results ranging from 0.025-0.059. These differences in the methods results imply that the methods definitions of τ_c are not equivalent.

Wilcock and McArdell [1997] used a flume to compare reference transport-defined approximations of τ_c values to proportions of fractional entrainment. They quantified entrainment from a mixed bed using sequential photography and color-coded grain size fractions. They found that the reference method results in a greater τ_c value than indicated by low proportions (0.1) of fractional entrainment and that the difference decreases with increasing grain size. Thus, they explicitly demonstrated differences in both the magnitude and trend of the τ_c value with grain size that depends on the definition of incipient motion. In this case, the methods definitions of τ_c differ as the reference-based approach approximates τ_c as a fitting parameter to compensate for unknown aspects of transport mechanics, while the entrainment approach provides a physical expression of the rate of change in the onset of motion.

Indeed, differences in the methods estimate of the onset of motion have been noted to be dependent on the definition of τ_c. To improve on this, researchers have proposed (i) avoidance of a deterministic definition by citing the stochastic nature of the process thereby making a determination of a τ_c^* value arbitrary [*Einstein*, 1950; *Paintal*, 1971; *Lavelle and Mofjeld*, 1987] or (ii) continued reliance on transport-based methods but with strict accounting for bed area undergoing entrainment, number of grains in motion, and the duration of the measurement [*Wilcock*, 1988]. However, such approaches have not been widely adopted.

Meanwhile, *Buffington and Montgomery* [1997] advocate for choosing defensible τ_c^* values based on the intended application, thereby implying that the variability in the value is only attributed to the definition of τ_c. To this end, *Wilcock and McArdell* [1997] results demonstrated that the proportion of a grain size fraction entrained increases with increasing shear stress, suggesting entrainment measurements can also be used to extrapolate to zero entrainment. If so, an entrainment-based method would provide an alternative to transport-based approaches that depend on entrainment from unknown source areas and that are therefore less able to detect to finer levels of movement, such as extra-patch grain displacement [see *Garcia et al.*, 2007].

The documented variability in bed mobility may not just be limited to the methodological definition of τ_c. *Lamb et al.* [2008] plotted a large compilation of field and laboratory measured $\tau_{c,50}^*$ values from the three aforementioned transport-based methods and found that they decrease with decreasing channel slope. Similar results were found when evaluating only reference transport measurements from field [*Mueller et al.*, 2005] or laboratory studies [*Prancevic and Lamb*, 2015] thereby alluding to a slope

dependent mechanism for a variable incipient entrainment threshold that is independent of method. Therefore, the variability in the $\tau^*_{c,50}$ value indicates that practical methods to measure τ^*_c values on different beds are necessary.

Much less study has been devoted to understanding the full entrainment threshold shear stress, τ_f. Current understanding is from *Wilcock and McArdell* [1997], who fit-by-eye log-normal distributions to fractional proportion entrained as a function of τ. As described, as the τ increases the proportion entrained of a grain size fraction on the bed asymptotically approaches a value of 1.0, which defines $\tau_{f,i}$. This asymptotic trend was demonstrated from fractional transport measurements that increase steadily with the proportion of the grain size fraction entrained and τ until exceeding a proportion of ~0.9. Thus, the τ value at which a grain size fraction becomes fully entrained $\tau_{f,i}$ is not as explicit as it is for $\tau_{c,i}$. It is assumed that for this reason *Wilcock and McArdell* relied on the fractional proportion entrained of 0.9 to characterize the upper limit of fractional partial entrainment. By doing so, they quantified the differences in the τ values producing the proportion entrained values of 0.1 and 0.9 for a given grain size fraction, D_i, as a factor of two. The factor difference and degree to which it varies on natural riverbeds holds potential for further explaining the entrainment process. However, studies in natural channels document that large floods with low recurrence intervals did not fully entrain a gravel-bedded channel [*Haschenburger and Wilcock*, 2003] and while smaller grain sizes become fully entrained though the larger grains are only partially entrained [*Church and Hassan*, 2002] it makes determination of the bed's τ_f value seemingly unattainable. Therefore, a method that objectively and quantifiably defines this threshold would be useful to furthering this understanding.

In this paper, I evaluate a method of measuring fractional entrainment as a function of τ and using the measurements to define the $\tau_{c,i}$, approximate the less studied $\tau_{f,i}$, and, thus, quantifiably characterize the domain of and trends in partial entrainment. The method utilizes tracer grains to approximate the fractional proportion entrained with increasing τ and uses that trend to define the thresholds τ values (similar to *Wilcock and McArdell* [1997]). In doing so, this study provides a method that will extend the sparse knowledge of entrainment and its contribution to the transport process and its effect on sediment transport formulae thereby improving their application.

B. Study Site

I selected field sites at two riffles on the San Joaquin River 10 and 11 km downstream of Friant Dam near Friant, California. Here, the river has a gravel-bed channel with riffle-pool morphology. At bankfull flow (approximately 42 m^3/s), the channel width is between 20 m and 60 m (Figure 1). The modern channel is incised into the alluvium of the pre-dam riverbed and its banks are composed of relict bed material, such that overbank flooding is confined within the pre-dam channel banks. Other channel characteristics are listed in Table 1.

Table 1. Physical characteristics of the reach and study sites on the San Joaquin River, California. Bed surface grain size statistics were determined from pebble counts: for the reach using eight samples of n=100 collected at three riffles within the reach, and for the sites (R38 and R40) average using the mean of the average distributions at each of the four upstream most cross sections. A McNeil sampler [see *McNeil and Ahnell*, 1964] was used to collect bulk bed samples for quantifying grain size distributions of the surface and subsurface layers by weight. The armor ratio was calculated from the bulk sample surface D_{50} over the subsurface D_{50}.

Characteristic	Reach	R38	R40
Bed gradient (rise/run)	0.0007	0.004*	0.005*
Bankfull discharge (m^3/s)	42	42	42
Mean channel width (m)	60	48	50
Mean bankfull depth (m)	2.2	1.2	1.5
Channel morphology	riffle-pool, sinuous	straight	straight
Bar form	NA	lateral	mid-channel
Pebble Count Statistics			
D_{16} (mm)	26	21	22
D_{50} (mm)	63	48	64
D_{84} (mm)	102	88	103
Bulk Sample Statistics	n = 8	n = 3	n = 4
Surface D_{50} (mm)	78	73	84
Subsurface D_{50} (mm)	39	42	35
Surface sand content	1%	2%	1%
Subsurface sand content	11%	9%	14%
Armor ratio	2.0	1.7	2.4

* Slope of riffle from its crest to the downstream pool.

I intentionally selected sites with sedimentological differences so as to compare the sedimentology at other sites and provide a reasoned assessment of their mobility based on relative differences with the two study sites. These sites, designated R38 and R40, are 1.5 km apart within straight channel sections. Each site extends across a riffle from the upstream pool tail through to the downstream pool. Channel traversing cross sections (XS) are staked across the upstream pool tail-out (XSA), riffle crest (XS1), middle riffle (XS2), riffle tail (XS3), pool head (XS4), and to the downstream pool tail (XS5). I use areas immediately upstream and downstream of the cross sections to deploy tracers and survey the bed surface grain size distributions (*GSD*), respectively. The differences in the sites sedimentology are fairly large considering they are only 1.5 km apart and without

intervening tributaries. R40 is coarser and with less longitudinal variation as compared to other riffles within 8 km. Also, large patches (~25 m^2) of bed surface at R40 containing thick periphyton growth on the exposed surfaces of cobbles (D_i > 64 mm) indicated that they have had relatively long exposure on the bed surface without entrainment. Periphyton growth was not observed at R38.

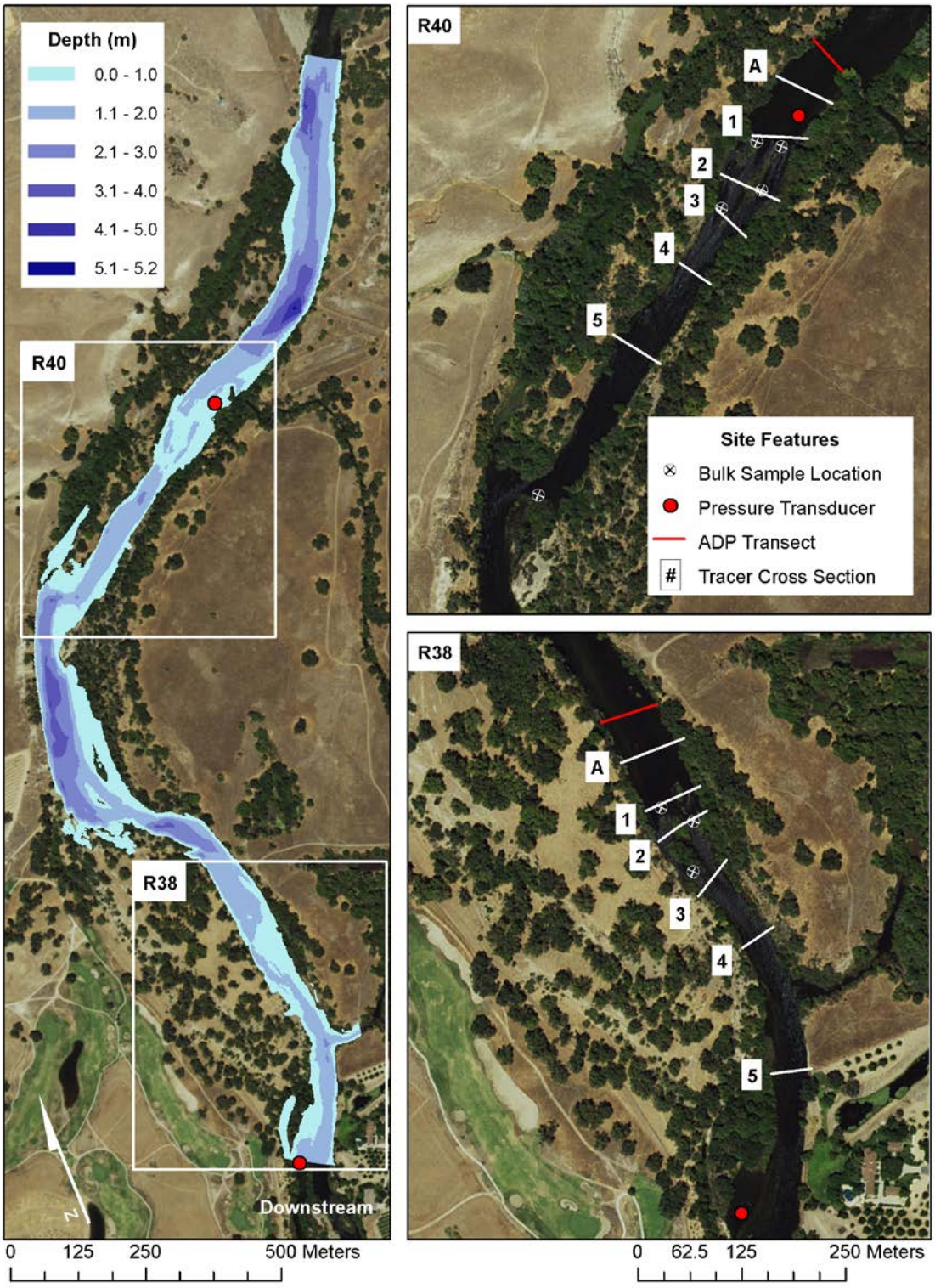

Figure 1. Hydraulic modeled reach (left) and tracer deployment sites (right). (Left) Reach map shows hydraulic model's stream-wise domain (blue-purple), site locations (white box), and pressure transducer locations (red dot). Simulated flow depths at 42 m^3/s (bankfull discharge) illustrate the channel limits and morphology (e.g., light blue areas are riffles and channel margins, purple areas are pools). (Right) Site maps with tracer deployment cross sections identified. Base map source: Esri, DigitalGlobe, USDA, and the GIS User Community.

C. Field Methods

1. Tracer Monitoring

I used gravel- to cobble-size grains from each site as tracers and separated them into five size classes (D_i) based on retaining sieve sizes of 32 mm, 45 mm, 64 mm, 90 mm, and 128 mm. I inserted each tracer with a radio frequency identification (RFId) tag by drilling a 4.8 mm diameter hole and securing with silicon caulk. Hole depth and RFId tag size depended on D_i: typically, 32 mm tracers were drilled to 15 mm and inserted with a 13 mm tag, 45 mm and 64 mm to 25 mm with a 23 mm tag, and >64 mm tracers to 35 mm with a 32 mm tag. Greater tag size allows greater antenna read range. Each tracer was painted, marked with an alternate identification (AltId) number on its surface, measured (weight, three axial diameters, and size class), and catalogued. The painted surface allowed more rapid visual location and the RFId tag enabled detection within 1 m with an antenna, thereby enabling identification and location of tracers that were buried or otherwise invisible because of algae, staining, or chipped paint.

Beginning in Summer 2010, I deployed and surveyed tracers along the cross sections shown in Figure 1 (except XS5 that was established by February 2012) such that one tracer from each D_i was placed approximately every 3 m. At R40 XSA (Figure 1), the bed topography, wide channel, and bed texture are more consistent and, therefore, 6 m spacing was deemed sufficient. With the aid of an underwater viewing scope, I positioned the tracers by replacement of an *in situ* grain of similar size and shape, and such that the tracer also replicated its position, orientation, and relationship with neighboring grains thereby avoiding unrepresentative positioning. Upon deployment I surveyed each tracer's downstream edge using a real-time kinematic (RTK) Global Positioning System (GPS)

fitted to a rigid survey rod and bull's eye level thereby resulting in <2 cm accuracy. With each tracer I recorded the AltId, survey point number, distance from the left bank cross section monument, axial orientation relative to flow direction (defined as downstream) and perpendicular to the bed surface. I also recorded its relationship with neighboring grains (classified as imbricated, sheltered, loosely exposed, clustered, embedded (%), buried (%)).

Subsequent surveys scanned the cross sections and downstream to located as many tracers as possible. Upon location, the tracer's attributes were again recorded as before using an underwater viewing scope so as to avoid disturbing the water-worked position of the grain. I noted any signs of burial or embeddedness such that ≥50% of the tracer's surface area was within tightly packed sediment. Tracers noted to be part of the subsurface layer were excluded from the analysis of surface entrainment. I left all tracers in place and undisturbed after each monitored flow. If a tracer traveled >2 m from the cross section another was deployed via replacement of an *in situ* grain near the same location on the cross section.

I plotted the surveyed tracer positions for each monitoring event in a GIS and analyzed for >15 cm difference from initial position in the downstream direction. This mobilization detection length is supported by RTK GPS equipment accuracy of <2 cm, consistent placement of the survey rod at the downstream end of each tracer, and bed pockets were generally of this length such that if a tracer tumbled into the next pocket downstream the movement would be detected. In subsequent surveys I checked previous detections of movement or immobility by examining the consistency in position and movement direction.

2. Flow Monitoring

I re-located the tracers and re-surveyed their positions after six peak flows, three of them overbank floods, between January 2010 and May 2012 (Figure 2). In this analysis, I did not use the first two peaks due to transient large woody debris that affected tracer entrainment but did not allow for adequate hydraulic modeling. I used the following four peak flows and their associated tracer entrainment measurements for the analysis: Winter 2011 (5 January 2011 peak flow of 173 m^3/s, 7.5 yr average return interval frequency and at the 70th percentile of the 60 yr daily average flow-duration curve), Spring-Summer 2011 (8 July 2011 peak flow of 221 m^3/s, 10 yr return interval and 63rd percentile), Fall 2011 (20 October 2011 peak flow of 20 m^3/s and 97th percentile), and Spring 2012 (13 May 2012 peak flow of 31 m^3/s and 95th percentile) flows.

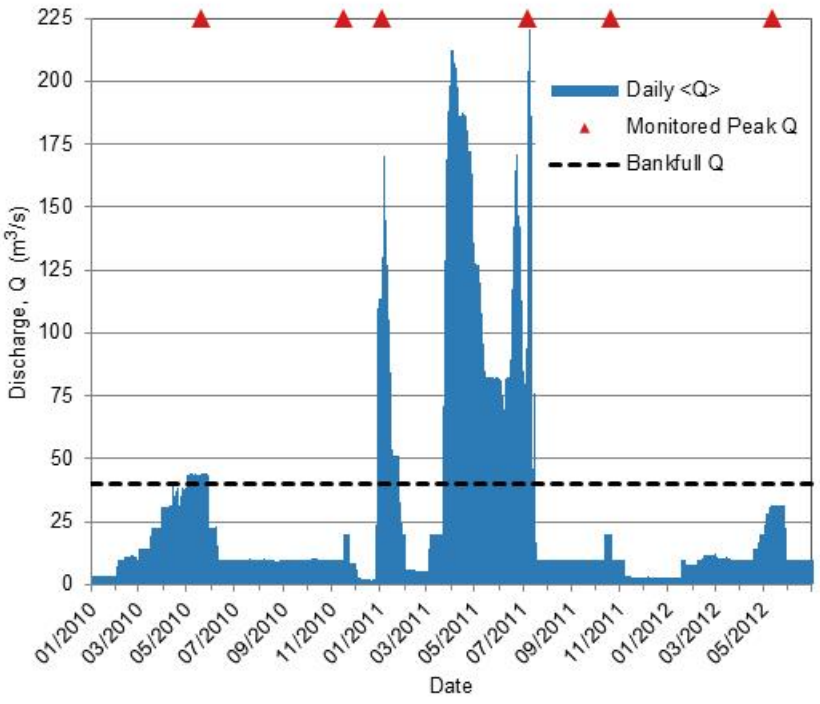

Figure 2. Monitored hydrograph of daily average flows from Friant dam and tributary contributions during the monitored period [*San Joaquin River Restoration Program*, 2015]. The bankfull flow (42 m^3/s), as identified in the field, is included for reference along with the dates of monitored peak flows (triangle symbols).

To calibrate the hydraulic model for each monitored flow peak, I surveyed water surface elevations (WSE) along water edges at both sites with the RTK GPS. In addition, two pressure transducers, that measure and record flow depth every 15 minutes, were installed in the channel within the model domain and surveyed to provide a WSE continuous record throughout the study. One is located at the downstream end of the domain and the other is located at R40 between XSA and XS1 (Figure 1).

I measured cross-sectional profiles of flow velocity and depths on each cross section at both sites to validate the calibrated hydraulic model simulations. I used SonTek's RiverSurveyor S5 acoustic Doppler profiler (ADP) (velocity resolution of 0.001 m/s and accurate to within 0.25%, depth resolution of 0.001 m and accurate to within 1%) mounted to the manufacturer's trimaran raft and tethered to either a kayak or channel traversing pulley-system line to measure flow velocity fields. A transect in the pool tail region at R40 was surveyed with a moving boat a minimum of four times per monitoring event in order to compare variability in flow velocity and depth with the mean as estimated by the flow model. The ADP system consists of five transducers with four angled at 25 degrees from vertical, operating at 3.0 MHz and a single echo-sounder that is directed vertically and samples at 1.0 MHz. The instrument's transducer sensor's submerged depth was 4 cm and an additional 20 cm of initial blanking depth is screened from the measurements. The ADP measures velocities at multiple depths simultaneously within vertical cells of 15 cm at a frequency of 30 pings/s. The position of each vertical velocity profile was simultaneously recorded with a system-integrated differential GPS (accurate to <1.0 m). The ADP internal compass was calibrated at the site prior to each monitoring event.

3. Bed Texture Characterization

At both sites, I collected pebble count samples ($n \geq 100$ [*Wolman,* 1954]) during base flow conditions immediately downstream of XSA, XS1, XS2, and XS3. I collected multiple samples along each cross section. Each sample was from an area with lateral widths of 3 m to 6 m and position that corresponds to the tracer deployment intervals (see Tracer Monitoring). The stream-wise length of a sample area was approximately 6 m. The results are averaged for each cross section in Figure 3 and mean of the cross section averages is presented in Table 1. Pebble counts performed after the two largest flows in 2011 indicate some minor changes in bed texture at R40. At this site the percent sand increased from 3% in 2010 to about 15% in 2011. In general, the bed exhibits a coarse texture with gradual lateral and longitudinal variations and insignificant patchiness.

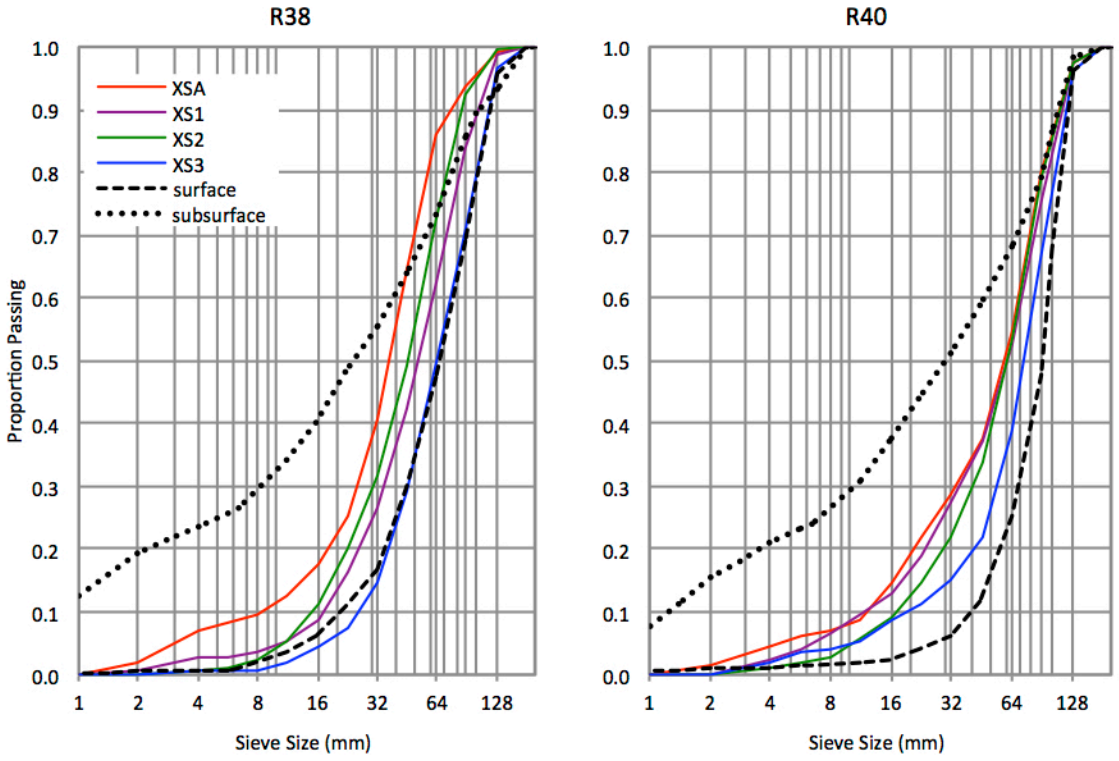

Figure 3. Bed grain size cumulative distributions along cross sections from pebble counts (solid) and from composited bulk samples (dashed) using square sieves. (Left) At R38 the pebble counts D_{50} ranged between 36 mm and 64 mm and show more variability than (Right) at R40 where they ranged from 60 mm and 72 mm and the samples are coarser.

I collected bulk samples in February 2011 from three locations at R38 and four at R40. These samples were divided into a surface stratum (R38, 3 samples with a composited weight of 77 kg; R40, 4 samples with a composited weight of 86 kg) and subsurface (R38 and R40 composited weights of 204 kg and 249 kg, respectively). The composited results are presented in Table 1 and illustrated in Figure 3.

D. Hydraulic Modeling

1. Description

Because directly measuring the hydraulic conditions above each tracer is impractical I relied on a 2-dimensional (2D) hydraulic model to generate simulations of peak flows

that provide the local τ that acted on each tracer. The monitored peak flows are simulated using the Flow and Sediment Transport for Morphological Evolution of Channels (FaSTMECh) computational model developed by the U.S. Geological Survey as a component of their Multi-Dimensional Surface Water Modeling System (MD-SWMS) [*Nelson and Smith*, 1989; *Nelson et al.*, 2003; *Barton et al.*, 2005; *McDonald et al.*, 2005]. This model predicts WSE, flow depth, and cross-stream and stream-wise vectors for the depth-averaged velocity and boundary shear stress along a channel-centered curvilinear grid. To do so, it uses vertically and Reynolds-averaged equations that account for mass and momentum conservation [see *Nelson et al.*, 2003]. As boundary conditions I input channel topography, discharge, WSE at the downstream limit, and roughness. In addition to the 2D horizontal grid computation is a quasi-third dimensional submodel that uses the grid node's computed depth-averaged velocity ($\bar{u}$) to predict the vertical structure of horizontal velocity vectors at discrete depths as they result from the eddy viscosity [see *Nelson and McDonald*, 1996]. This submodel accounts for cross-stream flow vectors thereby providing a refinement to the boundary shear stress calculation [*Nelson and Smith*, 1989; *Nelson et al.*, 1993; *McLean et al.*, 1999].

Assumptions of FaSTMECH include that the flow is steady and unvarying over short time periods and that there exist negligible vertical accelerations. Second, it assumes adequate representation of turbulence is provided by converting Reynolds stresses to shear using an eddy viscosity that is vertically averaged from a profile defined by having its bottom 20% of flow depth parabolic and the remainder of the water column being constant. Here the vertically averaged lateral eddy viscosity (LEV) is determined from the reach averages of $\bar{u}$ and depth (h) as described by *Barton et al.* [2005]:

$$LEV = 0.01 \times \langle \bar{u} \rangle \times \langle h \rangle \quad (2)$$

where the angle brackets indicate reach averaged values and over bar indicates depth average. Third, the model assumes that compared with the stream-wise bed stress, corresponding to the increasing shear with depth as a result of flow drag against the bed, the lateral and normal stresses resulting from lateral channel boundaries are negligible. The depth average vertical shear is related to $\bar{u}$ using a simple drag closure. Local solutions are determined numerically using a finite difference algorithm at each node defined by the curvilinear grid's intersections. For additional information on the model's underlying equations more complete details are provided by *Nelson et al.* [2003].

The total boundary shear stress (τ_b) is computed for each wetted grid node as the combination of its skin friction (τ_{sf}) and form drag (τ_{fd}) components ($\tau_b = \tau_{sf} + \tau_{fd}$). It is the τ_{sf} component of τ_b that is imposed on individual grains and responsible for their entrainment and transport. Because the study sites are in straight sections with simple and gradual relief, the τ_b (referred to as τ hereafter) is assumed to be overwhelmingly dominated by the τ_{sf} and, therefore, the τ_{fd} is not included in the calculations.

The curvilinear, computational grid is specified by digitizing the channel's centerline and inputting the desired number cells laterally and longitudinally. The result is a grid with constant width but whose stream-wise cell lengths are equal in straight sections, shortened on the inside of curves, and lengthened on the outside of curves (hence, curvilinear). Consideration is given for the need to include the wetted width of the channel within the grid, positioning of the channel centerline and selecting a grid width to avoid overlapping cells on inside of tight bends, and a cell count optimized to provide

sufficient resolution (nodal spacing) and perform within computational memory limitations.

2. Hydraulic Model Development

The 2400 m length of model domain (Figure 1, left) topography is provided by a combination of aerial photogrammetry (generally found to produce vertical accuracy to within 30 cm [*Ayres Associates*, 1998]) outside of the primary channel (i.e., flood plains, relict secondary channels), RTK GPS and total station surveys (accurate to <2.0 cm) across the channel and secondary channels, and depth sounding surveys integrated with RTK GPS for underwater bathymetry (accurate to <2.5 cm). In addition, each of the sites tracer cross sections were resurveyed during tracer deployment and regular monitoring surveys with a linear density of one point per ~1 m. Topographic survey results indicate that the channel is stable with negligible differences. The survey point densities within the channel and overbank areas were approximately 1 point per 40 m^2 and 150 m^2, respectively. While measurements of channel bed and bank elevations were either along transects (RTK GPS surveys) or in zigzagging cross-channel pattern (depth sounding surveys), points in the overbank areas were an even grid (aerial photogrammetry). The MD-SWMS software was used to interpolate between the topography-surveyed points for each grid node by specifying a preference for stream-wise versus lateral topographic data, at 4 m to 1 m, respectively, so as to preserve the banks as grade breaks. The result of the interpolation process is a topographic base map at the resolution of the curvilinear grid nodal spacing (Table 2).

Table 2. Hydraulic model curvilinear grids dimensions.

Date mm/dd/yyyy	Flow m^3/s	Grid spacing m	Stream-wise nodes #	Lateral nodes #	Grid width m
01/05/2011	173	3.0	785	121	360
03/29/2011	201	3.0	785	121	360
07/08/2011	221	3.0	785	121	360
10/20/2011	20	1.0	2,427	101	100
05/24/2012	31	1.5	1,619	101	150

For assigning τ computed locally to each tracer for each of the flow levels I developed three grid configurations. The centerline remained consistent in each grid but the width and cell size increased with the simulated discharge. This was necessary to account for overbank and secondary channel flows in the January, March, and July 2011 flow simulations while providing a finer resolution prediction at lower flows. Though the flood flows have wider grid spacing it is still within the 3 m to 6 m spacing intervals of the tracers and therefore provides τ specific to each tracer interval.

The reach discharge was provided from the U.S. Bureau of Reclamation Friant Dam, daily-averaged flow releases and a gaged tributary daily-averaged flow (Cottonwood Creek) records [*San Joaquin River Restoration Program*, 2015]. Both the dam and confluence are located approximately 9.5 km upstream of R40. A second tributary, Little Dry Creek, connects with the San Joaquin River mainstem within the R38 study site between XS4 and XS5. However, tracers had not been deployed at the one cross-section (XS5) downstream of this confluence when it was flowing and therefore it was not necessary to account for this tributary's contribution.

3. Hydraulic Model Calibration

I use the water surface elevations (WSE) and flow velocity (u) measurements (see Flow Monitoring) to calibrate and validate the hydraulic models. Using the discharge as input

for each peak flow simulation, the primary tuning parameter is the hydraulic roughness parameter C_d where:

$$C_d = \left[\left(\ln\left(\frac{h}{z_0}\right) - 1\right)/\kappa\right]^{-2} \quad (3)$$

and h is the flow depth, z_0 is the roughness length (D_{50}/30), and κ is von Karman's constant (0.408) [*McDonald et al.*, 2005]. For each flow simulation a first approximation of LEV and C_d was made using the hydraulic measurements and reach average D_{50} with Eqs. (2) and (3), respectively. To start, the C_d is applied uniformly throughout the domain and upon model convergence the initial reach average h and $\bar{u}$ is used to recalculate LEV, which is input to the model, and C_d is then further adjusted so as to minimize the difference in root mean squared error (RMSE) of the simulated versus measured WSE. When the WSE's RMSE is minimized the predicted $\bar{u}$ and h throughout the wetted domain are again averaged and the final LEV is calculated (Eq. 2) and input as a secondary refinement. The C_d is then further tuned to provide additional precision. Upon minimization of WSE RMSE with a spatially uniform C_d the resulting simulated h values are used to vary C_d spatially, which tends to improve WSE RMSE by <25% (Table 3).

Table 3. Hydraulic models calibration input and performance criteria. Four peak flows were monitored for water surface elevations (WSE), depth, and velocity. The 8 July 2011 peak flow was not monitored for depth or velocity and is simulated with the 29 March 2011 calibration results.

		Calibration Criteria			WSE RMSE	
Date	Q	C_d	LEV	WSE	Constant C_d	Variable C_d
mm/dd/yyyy	m^3/s		m^2/s	n	m	m
01/05/2011	173	0.0197	0.027	14	0.038	0.035
03/29/2011	201	0.0183	0.014	9	0.062	0.059
07/08/2011*	221	0.0183*	0.014*	51*	0.197*	0.216*
10/20/2011	20	0.0280	0.040	35	0.085	0.054
05/24/2012	31	0.0110	0.059	46	0.027	0.027

Note: * WSE determined post hoc from high water indicators (e.g., silt lines and snagged debris). Instead of tuning C_d to these less precise WSE the calibrated C_d and LEV from the 29 March 2011 model were used. The result was a greater RMSE that indicated consistent under prediction of the surveyed high water marks by an average of 22 cm. However, the more accurate pressure transducers recordings indicated a difference of only 4.5 cm and 0.11 cm, using the constant and variable C_d, respectively. *n* = number of surveyed points.

Flow and WSE were collected at the sites during each monitored peak flow event. In three cases (5 January, 20 October 2011, and 25 May 2012) WSE and flow were measured on the day of the monitoring period's flow peak and therefore additional adjustment of the calibrated model was not required to account for higher flows. On 29 March 2011 a high flow (201 m^3/s) was surveyed for WSE and flow. However, the Spring-Summer 2011 peak flow occurred on 8 July at 221 m^3/s and its indicators of high water level were subsequently surveyed in August 2011. Therefore, in this case a model was calibrated and validated using the 29 March 2011 data and its C_d and LEV were then used to simulate the subsequent higher peak flow. In doing so, the higher flow simulation was validated using the high water marks and pressure transducer. The less accurate high water marks indicated higher WSE (average of 0.22 m) than the simulation while the transducer measurements were in excellent agreement (±0.0011 m). Validation of the performance of the calibrated model results is provided as Appendix J.

E. Defining Tracer Activity

Only tracers that I observed to be members of the loose and unconstrained surface layer were included in the analysis. As the deployed tracers were left in place subsequent to monitored flows, overtime some of the tracers became embedded or buried. Tracers that exhibited such evidence of incorporation into the constraining subsurface layer either by embeddedness of ≥50% or burial beneath other surface material were excluded from the analysis. Furthermore, as it is impossible to tell when embedding took place (e.g., during waxing or waning flows), all tracers noted as embedded or buried before or after a monitored flow were excluded, whether or not they moved.

I determined entrainment and immobility by comparing each tracer's surveyed position before and after each peak flow. Those that moved downstream >15 cm were designated entrained, and those within 15 cm of their previous position were designated immobile. I recovered 81% to 100% of the tracers that were surveyed prior to each flow. After excluding tracers that were buried, embedded, or along the channel margins a total of 570 and 315 tracers at R38 and R40, respectively, remained for delineating entrainment thresholds (Table 4). For each monitored flow each tracer is assigned the τ computed by FaSTMECH from the computational grid node closest to the tracer's original location.

Table 4. Included (entrained or stable) and excluded (buried, embedded, or margin) tracers. Buried or embedded tracers are not exclusive of tracers found within 3 m of the channel margins, or vice versa.

Site	D_i	Entrained	Stable	Buried or Embedded	Margin
R38	32 mm	42	36	63	91
R38	45 mm	56	57	96	117
R38	64 mm	55	77	90	125
R38	90 mm	33	84	68	128
R38	128 mm	31	99	34	117
R40	32 mm	17	21	37	42
R40	45 mm	19	30	36	35
R40	64 mm	20	56	34	50
R40	90 mm	13	58	21	56
R40	128 mm	10	71	9	49

F. Results

I use binary designations of immobile (Y_i = 0, where Y_i refers to the proportion entrained) and entrained (Y_i = 1) tracers as a function of the local average boundary shear stress, τ, calculated by the 2D hydraulic model (plotted as plus symbols in Figure 4), to define the change in the Y_i by using binomial logistic regression. The purpose of the regression is to

fit a logit model to the transformed data that provides an estimate of the probability of entrainment from the shear stress where the logit is a continuous criterion on which linear regression is conducted using the maximum likelihood estimation to minimize the variance in the error in the prediction and estimate the regression coefficients. To fit a logit function using linear regression analysis, the binary data is converted to continuous data by determining the probability of entrainment from the binary data in increments of the independent variable. The result is a fitted model that describes the probability of entrainment of a grain in a grain size fraction with changes in the value of the τ. The logit model is a quantile function that relates continuous variables (e.g., τ) to a dichotomous dependent variable (e.g., immobile versus entrained) with the assumption that the tracer statuses are independent of one another, the dependent variable has mutually exclusive binary categories that completely describe their entrainment status (i.e. a particle has either moved or it has not), and that there exists a linear relationship between the Y_i and the logit transformed τ. The resulting equations are of the form:

$$Y_i = \frac{1}{1+e^{-(B+C\tau)}} \quad (4)$$

where '*B*' and '*C*' are regression derived coefficients (Table 5) [*Sharma*, 1996 p. 320]. The logistic distribution closely resembles the cumulative normal distribution while being computationally simpler. This is important because the frequency of $\tau_{c,i}$ values of individual grains on the bed is often normally distributed [Chapter 2]. In this regard, (4) provides a prediction of the probability of entrainment for a grain, which here is extended to imply an estimate of the average proportion of tracers in a grain size fraction that will be entrained (Y_i) for a given τ. As a result, the trend described by (4) defines the trend in partial entrainment for a grain size fraction as a function of τ beyond the range of the

shear stresses that acted on the tracers. This functionality is useful for estimating the τ that is capable of moving larger proportions of larger grains that did not approximate full entrainment (e.g., the τ_f value from the largest grain size).

Table 5. Results of binary logistic regression (4) for the proportion of tracers entrained as a function of shear stress (Pa). Statistics include the standard error (StErr) in the coefficient, Wald's criteria (z-value), and probability that the shear stress is significantly associated with the probability of entrainment (p-value). Results indicate that the coefficients are significantly different from zero at a significance level of <0.05.

Site	D_i	Term	Coefficient	StErr	z-value	p-value
R38	32 mm	B	-5.44	1.42	-3.83	1.27E-04
		C	0.217	0.0526	4.13	4.63E-05
	45 mm	B	-3.65	0.834	-4.37	1.25E-05
		C	0.140	0.0296	4.74	2.11E-06
	64 mm	B	-4.56	0.971	-4.70	2.58E-06
		C	0.152	0.0322	4.74	2.17E-06
	90 mm	B	-4.45	0.989	-4.50	6.94E-06
		C	0.128	0.0320	3.99	6.64E-05
	128 mm	B	-4.11	0.914	-4.49	6.98E-06
		C	0.109	0.0303	3.61	3.12E-04
R40	32 mm	B	-5.30	2.06	-2.57	1.02E-02
		C	0.195	0.0714	2.72	6.48E-03
	45 mm	B	-4.50	1.55	-2.91	3.61E-03
		C	0.146	0.0506	2.88	3.93E-03
	64 mm	B	-7.10	2.05	-3.46	5.44E-04
		C	0.223	0.0673	3.31	9.22E-04
	90mm	B	-5.40	1.53	-3.52	4.38E-04
		C	0.148	0.0498	2.96	3.05E-03
	128mm	B	-5.32	1.51	-3.52	4.40E-04
		C	0.131	0.0497	2.64	8.33E-03

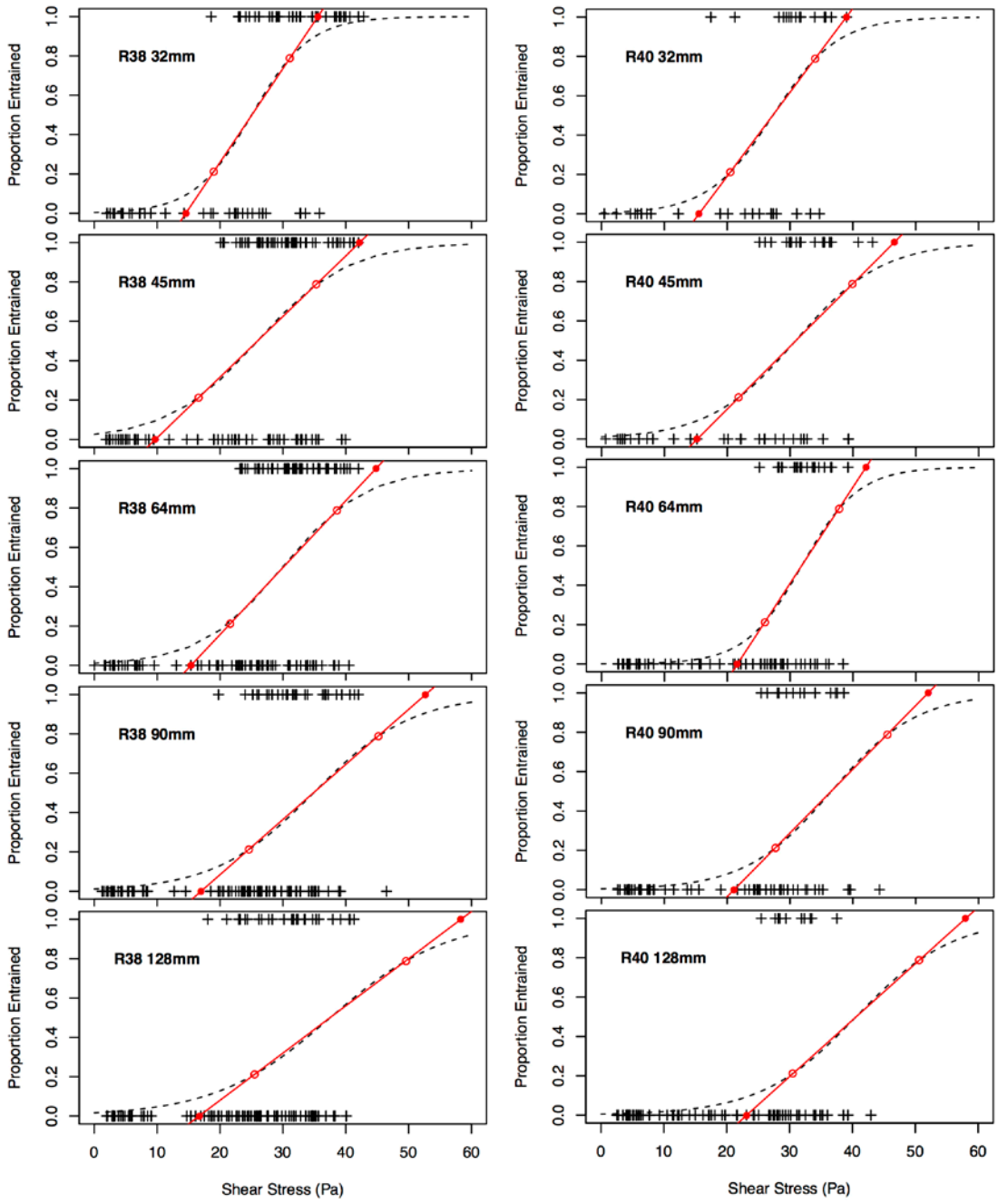

Figure 4. Binary logistic plots of mobility as a function of τ. Entrained (Y_i=1) and immobile (Y_i=0) tracers versus their experienced maximum τ are plotted as plus symbols. The distribution of plus symbols indicate that an increasing proportion of the grains become entrained with increasing shear stress. The resulting logistic regression is illustrated as the dashed line. Maximum curvature in Y_i with τ are indicated by hollow red circles and are used to define a linear increasing trend in partial entrainment (red line) as well as the $\tau_{c,i}$ and $\tau_{fe,i}$ values (solid red circles) outside of which the change in Y_i is negligible.

The logit model describes a symmetrical distribution that closely approximates the cumulative normal distribution and that provides useful features for describing characteristics of the trends in grain entrainment. The logistic regression trends indicate an increasing Y_i with increasing τ for each grain size fraction (Figure 4), as expected. Due to the asymptotic tails of the distribution of the logit model and the linear regression reliance on the incremental probability of entrainment, the trends begin to increase before the τ value in which the tracers are entrained. The trend line then continues to increase nearly linearly through the range of τ values that entrained the tracers, and the fitted logit model that extends beyond the range of the τ that acted on the tracers, thereby predicting an asymptotic approach to Y_i=1. This is useful because, even though I monitored flood flows in excess of five times the bankfull flow, only the smallest grain size fractions of the tracers experienced τ values approaching $\tau_{f,i}$. Therefore, the logistic regression provides an approximation of the Y_i as a function of τ values in excess of those that were measured, thereby providing a way to approximate the τ_f value for the bed. Furthermore, the logit model provides a trend that generally agrees with the tracer entrainment with increasing τ.

I use the range in τ values where, as indicated by the logit model, a nearly linear increase in Y_i occurs to provide indicators of the limits of the partial entrainment domain. In order to provide deterministic values of $\tau_{c,i}$ and approximations of $\tau_{f,i}$, I used the second derivative of (4), such that:

$$\frac{d^2Y_i}{d\tau^2} = \frac{e^{-(B+C\tau)}C^2\left(-1-e^{-(B+C\tau)}\right)+2e^{-2C\tau-2B}C^2}{\left(1+e^{-(B+C\tau)}\right)^3} \quad (5)$$

to define the linear trend by determining the τ values associated with the Y_i maximum (Y_i=0.212) and minimum (Y_i=0.788) acceleration and deceleration in Y_i as a function of τ

(Figure 4). The range within these Y_i values includes the majority (approx. 62%) of the distribution. From the logit model trend, Y_i values that are increasingly less than and greater than the maxima and minima of $d^2Y_i/d\tau^2$ become increasingly less dependent on the τ. The asymptotic tails that become increasingly horizontal outside these limits indicate this. Therefore, I linearized the trends in Y_i as a function of τ from the maxima and minima of $d^2Y_i/d\tau^2$ and extrapolated to Y_i=0 and 1 in order to define a range in τ values where the Y_i is more strongly dependent on the τ value.

I use the linearized trend in Y_i as a function of τ to approximate the partial entrainment trend and to quantify its domain. The τ value at which the linearized trend intersects Y_i=0 is used to define the $\tau_{c,i}$. This definition is consistent with observations from flume and field experiments (see Figure 2(b) in *Parker et al.* [1982]; Figure 6 in *Wilcock and Crowe* [2003]; Figure 2.46 in *Wilcock et al.* [2009]) that document an abrupt, steep, and steady increase in fractional transport rates with $\tau > \tau_{c,i}$.

The logit model predicts that as the τ increases above the $\tau_{c,i}$ value a greater proportion of the bed becomes entrained and the rate of increase in Y_i begins to decrease at a increasing rate with increasing τ in excess of those capable of producing a Y_i>0.788. This asymptotic approach to the hypothetical $\tau_{f,i}$ value with increasing Y_i, as described by the logit model, is a realistic tendency that is observed in (i) transport-based experiments that demonstrate trends in fractional transport rates that also increase at a decreasing rate as the proportion of a grain size fraction in transport becomes more equal with its proportion of the bed surface [*Wilcock and McArdell*, 1993] and (ii) distributions of grain resistance measurements that also have asymptotic tails [*Buffington et al.*, 1992; *Johnston et al.*, 1998; Chapter 2]. However, the τ values from the monitored floods are

only capable of entraining more than 91% of the tracers for the 32 mm class at site R38 (Figure 4) and, presumably because of the small number of tracers and the high probability of entrainment, all of them were entrained. I expect that if additional tracers were placed in sufficient quantities a similar asymptotic tendency would have been detected. However, this asymptotic characteristic makes the determination of the $\tau_{f,i}$ value impractical. Because of this, I extended the linearized trend to define the τ value where Y_i=1 to provide an approximation of the full entrainment threshold shear stress, $\tau_{fe,i}$, from the tracer entrainment measurements. Although the definition of $\tau_{c,i}$ from the linearized trend estimates the critical threshold for the onset of entrainment, the definition of $\tau_{fe,i}$ is more arbitrary. In this regard, $\tau_{fe,i}$ only approximates a τ value at which the proportion entrained becomes increasingly less dependent on the τ value. In this way, I provide two reference points for describing practical values for the outer limits of the partial entrainment domain.

The linearly determined $\tau_{c,i}$ and $\tau_{fe,i}$ are equal to values where (4) produces Y_i= 0.093 and 0.907. Although this suggests <20% probability of entrainment is unaccounted for by the bounds of $\tau_{c,i}$ and $\tau_{fe,i}$, mobile and immobile tracers, respectively, were not found to fall outside these limits. This observation is more meaningful for the lower bound, $\tau_{c,i}$, where a larger number of tracer observations occurred and at which the lower tail of the logistic distribution is in disagreement with trends in mobility that suggest an abrupt onset of grain motion, followed by a rapid and steady increase with increasing τ. At τ values with $\tau > \tau_{fe,i}$, however, the lack of immobile tracers is more likely a result of the high probability of entrainment and the low occurrence of tracers experiencing such high shear stresses. But even though the $\tau_{fe,i}$ values are not indicative of the actual

threshold $\tau_{f,i}$ they provide a consistent way to compare the limits of the partial entrainment domain. For example, with increasing grain size (i) $\tau_{c,i}$ and $\tau_{fe,i}$ values increase, either of which is indicative of selective entrainment of smaller grain sizes, and (ii) the range of τ that produces partial entrainment increases (i.e., where Y_i is at $0 < Y_i < 1$) (Figure 5).

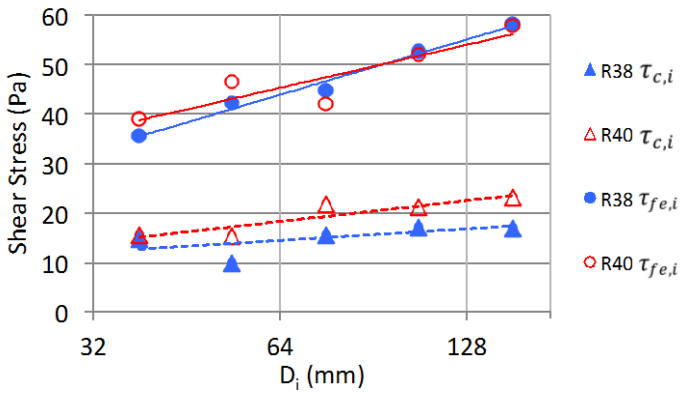

Figure 5. Thresholds shear stress as a function of grain size fraction. Power function trend lines of the thresholds are fitted using OLS regression to illustrate (i) the increase in the τ required to begin entrainment of a D_i, and (ii) the increasing difference between the $\tau_{c,i}$ and $\tau_{fe,i}$ values with increasing grain size. The $\tau_{fe,128mm}$ values, just under 60 Pa, are suggestive of the full entrainment threshold of the bed at both sites.

The rate of increase in Y_i with τ, as shown in Figure 4, varies between D_i depending on the shear stress at which Y_i=0.50, $\tau_{[50],i}$. I demonstrate this by comparing the rate of increase in Y_i with τ between the various D_i when the τ in the logit model of each grain size fraction is normalized by $\tau_{[50],i}$. The $\tau_{[50],i}$ value is computed by solving (4) for $\tau_{[50],i}$ with Y_i=0.50 and algebraically reorganizing, such that:

$$\tau_{[50],i} = \log_{e^{-C}}(e^{B}) \quad (6)$$

When the τ within the logistic regression equation is normalized by the corresponding $\tau_{[50],i}$ value, the cumulative frequency distributions collapse to a single dimensionless

curve (Figure 6). This collapse is similar to that observed by *Wilcock and McArdell* [1997, figure 3d] from flume experiments while using log-normal distributions.

Table 6. Extrapolated threshold shear stress values as plotted on Figure 5, shear stress at which $Y_i = 0.5$ ($\tau_{[50],i}$) from Figure 4 and (6), and the threshold Shields stress values as plotted in Figure 7.

Site	D_i (mm)	$\tau_{c,i}$ (Pa)	$\tau_{fe,i}$ (Pa)	$\tau_{[50],i}$	$\tau^*_{c,i}$	$\tau^*_{fe,i}$
R38	32	14.6	35.6	25.0	0.0237	0.0579
	45	9.7	42.2	26.0	0.0112	0.0486
	64	15.4	44.8	30.0	0.0125	0.0365
	90	17.0	52.7	34.9	0.0098	0.0303
	128	16.7	58.3	37.5	0.0068	0.0237
R40	32	15.5	39.0	27.3	0.0253	0.0634
	45	15.2	46.6	30.9	0.0175	0.0536
	64	21.6	42.1	31.9	0.0176	0.0342
	90	21.1	52.0	36.6	0.0121	0.0299
	128	23.2	58.0	40.6	0.0094	0.0236

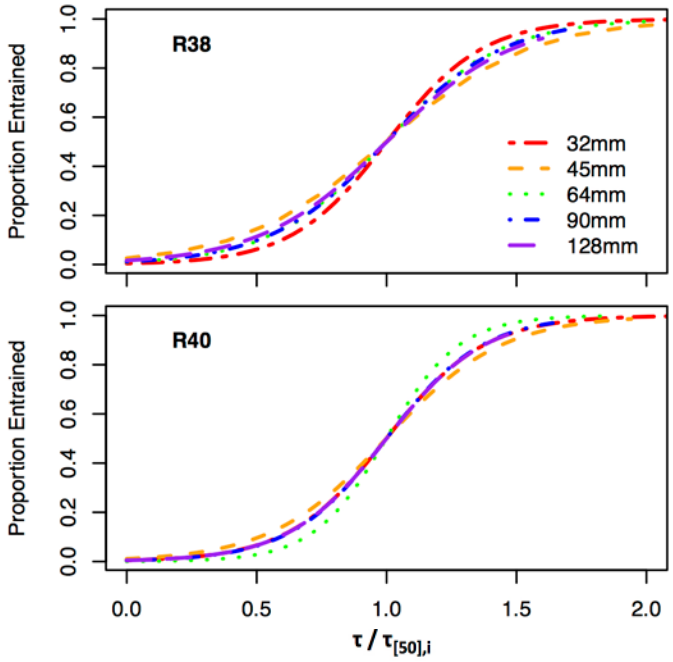

Figure 6. Proportion of grain size fractions entrained as logit functions of $\tau/\tau_{[50],i}$. By normalizing the independent variable in Figure 4 the trends are shown to collapse, thereby indicating a similarity in the change in Y_i with changes in τ.

A consistent difference between the thresholds is shown explicitly in Figure 7, where power functions are fit by ordinary least squares (OLS) regression to the $\tau^*_{c,i}$ and $\tau^*_{fe,i}$ values (Table 6), such that:

$$\tau^*_{g,i} = \alpha_g \left(\frac{D_i}{D_{50}}\right)^{-\beta_g} \quad (7)$$

where subscripted 'g' refers to either the critical or the approximation of the full entrainment threshold; superscripted '*' refers to the Shields stress from (1); and α and β are the empirically determined coefficients. This equation is referred to as the hiding function because it describes the degree to which smaller grains are relatively less mobile than larger grains, in part due to the smaller grains hiding in the lee of larger grains [*Parker et al.*, 1982; *Andrews*, 1983]. Originally, I regressed the thresholds against relative grain size, D_i/D_{50}, for the sites separately and these results are presented in Table 7. However, the site specific coefficients for the critical threshold are not significantly different (ANCOVA comparisons between site specific α_c and β_c produce p-value = 0.7 and 0.5, respectively) and, therefore, their measured $\tau^*_{c,i}$ were combined to determine the reach-averaged $\tau^*_{c,i}$ trend with relative grain size (Figure 7). While the β_f values are not significantly different between sites (p-value=0.3) the α_{fe} values are significantly different (p-value=0.003), and therefore the datasets are not combined to produce a reach-averaged hiding function for the $\tau^*_{fe,i}$.

Table 7. Hiding function coefficients, regression statistics, and 95% confidence interval (CI) of the slope and intercept coefficients. Refer to (7) for hiding function format. Probability values (p-values) indicate the probability that the trend line is independent of the relative grain size.

			Regression Results				α 95% CI	
Site	Threshold	n	α	β, 95% CI	R^2	P-value	Upper	Lower
R38	τ^*_c	5	0.0166	0.761 ±0.624	0.834	3.03E-02	0.0252	0.0109
	τ^*_{fe}	5	0.0505	0.650 ±0.082	0.995	1.35E-04	0.0533	0.0478
R40	τ^*_c	5	0.0174	0.675 ±0.289	0.949	5.04E-03	0.0202	0.0150

	τ_{fe}^*	5	0.0434	0.738 ±0.237	0.970	2.18E-03	0.0491	0.0384
Both	τ_c^*	10	0.0170	0.738 ±0.217	0.885	5.06E-05	0.0194	0.0149

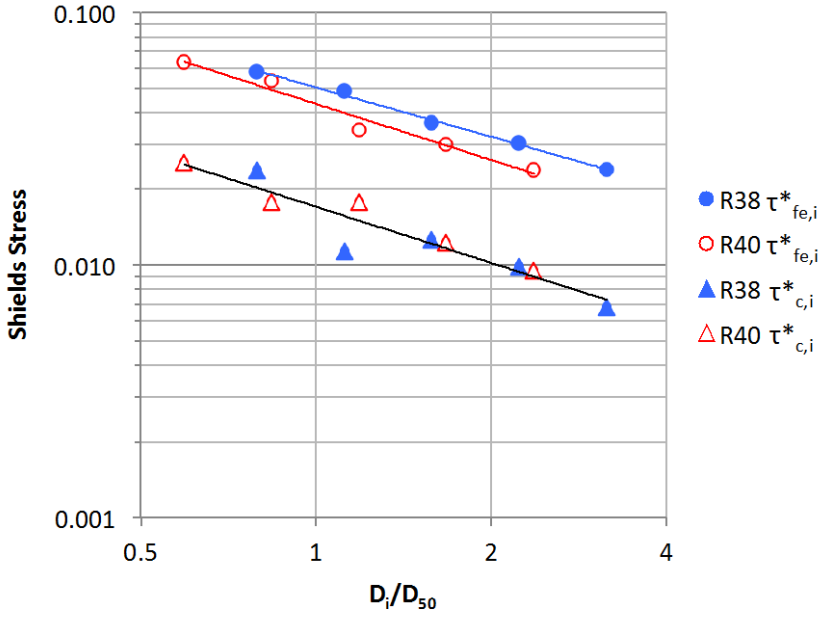

Figure 7. Threshold Shields stress as a function of relative grain size. The fractional incipient entrainment thresholds trend line is the result of the combination of both sites measurements (n=10) as their individual regression models intercepts and slopes were not significantly different (ANCOVA p-values > 0.5), while the intercepts were significantly different for their $\tau_{fe,i}$ trends (p-value=0.004). Regression coefficients and statistics are presented in Table 7.

The β_g values of 0.65 to 0.76 are within the range of 0.65 to 1.0 that have been observed by others (*Andrews*, 1983; *Buffington and Montgomery*, 1997; *Whittaker and Potts*, 2007). This coefficient is referred to as the hiding factor as it describes the degree to which smaller grains are more difficult to entrain than would be suggested by (1) in part due their being on the leeward side of larger grains that provide shelter from the flow. Deviation of a β_g value from unity indicates the degree to which the threshold of entrainment is a function of grain size relative to the median grain size of the bed, such that a β_g value less than unity indicates that the value of τ_g increases with relative grain

size but at a rate that is less than linear, and that the "hiding effect" is less effective. The measured β_g values are found to be significantly different from unity (Table 7), thereby providing strong indication that selective entrainment of smaller grains occurs at the study sites. With increasing τ, therefore, smaller grains become entrained before larger grains and become fully entrained before larger grains as well. Moreover, the suggested equivalence in the β_c and β_f values (ANCOVA p-values>0.59) implies that the "hiding effect" does not diminish with τ over the range $\tau_c < \tau < \tau_f$. Thus, an average β_g value of 0.71 is appropriate for application across the study sites.

The α_g coefficient values (Table 7) are comparable to measurements by others but have noteworthy distinctions. For instance, at both sites the α_c values of 0.017, which are indicative of $\tau^*_{c,50}$, are less than the typically assumed $\tau^*_{c,50}$ values of 0.03 to 0.06 and are at the low end of the range of $\tau^*_{c,50}$ values of between 0.01 and 0.2 observed by other researchers [*Buffington and Montgomery*, 1997]. This result indicates that on the study reach entrainment begins at a lower τ than has been typically observed elsewhere.

The α_f coefficient values, which are indicative of $\tau^*_{f,50}$, are similar to the measurements by others when considering the relative difference with $\tau^*_{c,50}$. The ratio of $\tau^*_{fe,50}/\tau^*_{c,50}$, whose values are provided by the ratio of the α coefficients (Table 7), is 3.0 and 2.5 at R38 and R40, respectively. But the force balance predictions from smaller bed areas at sites R38 and R40 indicate factor differences of 2.2 and 2.3, respectively (Chapter 2, see figure 10). *Wilcock and McArdell* [1997] found a ratio of 2.0 when defining thresholds in terms of the 10th and 90th percentiles of a log-normal distribution of mobile fractions like those in Figure 6. *Konrad et al.* [2002, see figure 9] who used a normal distribution fitted to entrainment measurements irrespective of grain size

measured the same ratio. Similarly, *Church and Hassan* [2002] used reference transport-based methods on a natural river bed to quantify the thresholds and reported a factor of 2 difference in full mobilization from initial mobilization; where full mobilization begins at the τ value that produces the proportion of a grain size fraction in transport that is equal to its proportion of the bed surface. However, others have measured factor differences from transport-based methods of 2.5 to 3.0 [see *Rainato et al.*, 2014].

The differences between the thresholds measured herein and the often-reported factor difference of 2 might be caused by differences in the range of grain size distributions as measured at the study sites (Figure 3). If the hiding function α_g coefficients (Table 7) are virtually constant over a bar form, as is implied by the conclusions of *Konrad et al.* [2002], then variation in the D_{50} along the bar will result in a greater $\tau^*_{fe,50}/\tau^*_{c,50}$ value when the mobility is measured over the bar. To test the magnitude of this effect, I used the $\tau^*_{c,50}$ as provided by the α coefficients (Table 7), and assumed the factor two difference with $\tau^*_{fe,50}$ (i.e., $\alpha_f = 2\alpha_c$). I calculated the $\tau_{c,50}$ and $\tau_{fe,50}$ values by using (1) for the maximum and minimum D_{50} values along each bar at the field site (Figure 3). From the minimum site specific D_{50} values the $\tau_{c,i}$ decreases and from the site specific maximum D_{50} the $\tau_{fe,i}$ increases, such that the range in D_{50} values produces site specific α_{fe}/α_c of 3.4 and 2.5 at R38 and R40, respectively, that would otherwise be a factor of 2.0 if the D_{50} were constant. Therefore, the variation in bed texture across the site where tracers are deployed appears to affect the threshold measurements when using tracers. However, it should be noted that there is no reason why a similar result would not be observed from using other methods to estimate entrainment. The only way around this effect would be to ensure the bed area is of uniform texture. From this simple explanation

it would seem that the difference in the $\tau^*_{c,50}$ and $\tau^*_{fe,50}$ measurements between the sites is due to the difference in variability in the D_{50} across the sites. Furthermore, the two-fold factor difference between the $\tau_{c,50}$ and $\tau_{fe,50}$ appears to hold for the different beds as indicated by the force balance predictions that are based on measurements from smaller bed areas with less variability in the D_{50}.

G. Discussion

Gravel- to cobble-sized tracer entrainment monitoring coupled with the 2D hydraulic model provides a way to quantify each of the facets of entrainment. By using a logit model as a function of τ to describe the probability of entrainment, I predict the trend in partial entrainment for the D_i from the logistic distribution (Figure 4). This distribution closely resembles the cumulative normal distribution that is found to describe the probability of entrainment from field studies by *Konrad et al.* [2002] using bed tags and *Chapter 2* using a force balance model to predict the distribution in the resistance of grains to movement downstream. This is a deviation from *Wilcock and McArdell* [1997] who describe the trend as log-normal and who supported it by noting that *Johnston* [1996] measured log-normal distributions of the coefficient of friction for D_i on gravel beds. However, although I also found that the coefficient of friction is log-normally distributed at the study sites, I found that using these values to compute the τ^*_c from a force balance model results in normal distributions of τ^*_c for each D_i [Chapter 2]. Thus, the appropriate theoretical distribution for describing the change in Y_i with τ is the untransformed normal distribution. Therefore, the logit model provides a reasonable approximation for the change in the probability of entrainment.

Using hiding functions (7) to define the limits of the domain of partial entrainment, I confirm the measurements of entrainment between the two study sites. I use the fitted logistic regression models predictions of probability of entrainment with increasing τ to approximate the thresholds of entrainment, from which I computed the $\tau^*_{g,i}$ and plotted them against D_i/D_{50} (Figure 7). The resulting hiding functions are generally similar between the sites with only minor but significant differences in the α_{fe} coefficients of the regression equations for $\tau^*_{fe,i}$ as a function of D_i/D_{50} (Table 7). I demonstrate that this difference is explained by the variation in the D_{50} at the sites, as the greater α_{fe} at Site R38 corresponds with its greater variability in D_{50}. Furthermore, by accounting for the difference in variation in the D_{50} I also find that it is plausible for there to be a two-fold difference between $\tau_{c,i}$ and $\tau_{fe,i}$, which is similar to differences measured by others from entrainment [*Wilcock and McArdell*, 1997; *Konrad et al.* 2002], force balance predictions [Chapter 2], and transport-based measurements [*Church and Hassan*, 2002; *Wu and Yang*, 2004]. However, there is no known explanation for such a rigid constancy to occur. Indeed, others have presented data that suggests larger differences [*Rainato et al.*, 2014], although it is uncertain whether they accounted for or otherwise controlled the variability in the D_{50}. Regardless, the similarity in the difference between $\tau^*_{c,i}$ and $\tau^*_{fe,i}$, as measured herein, with that reported by others provides support for the results and the method, and encourages research into the physical controls on the seemingly well constrained difference between $\tau^*_{c,i}$ and $\tau^*_{fe,i}$.

Constancy in the difference in τ_c and τ_{fe} between D_i is demonstrated by the collapse in the logistic regression equations of Y_i as a function of $\tau/\tau_{[50],i}$ (Figure 6). This collapse indicates that a constant variance normal distribution characterizes the partial entrainment

domain across several D_i. A similar collapse was also reported by *Wilcock and McArdell* [1997, see figure 3d] that illustrated a collapse in their log-normal fitted curves of Y_i as a function of $\tau/\tau_{[50],i}$. Their flume experiment consisted of a much sandier bed with between 30% and 60% sand on the bed surface and gravel up to 64 mm in diameter. The larger difference in their bed sediment with that of the much coarser bed at sites R38 and R40 strongly suggests that the collapse commonly occurs. Therefore, these results indicate that the partial entrainment domain is well constrained by a theoretical distribution whose variance scales with $\tau_{[50],i}$. Furthermore, the consistency of the collapse provides support for the regression equation computed $\tau_{fe,i}$ values that depended on extrapolation beyond the range of τ that were monitored by the tracers.

By comparing measurements of $\tau^*_{c,50}$ by others, the tracer measured $\tau^*_{c,50}$ values, as indicated by the α_c value of 0.017 (Table 7), are unusually low. The *Buffington and Montgomery* [1997] compilation of screened $\tau^*_{c,50}$ values measured with the reference, largest grain, and visual methods typically range from 0.025 to 0.086 [*Buffington and Montgomery*, 1997]. Explanation of this range of $\tau^*_{c,50}$ values as opposed to a constant value would perhaps depend on a variable $\tau^*_{c,50}$. This possibility is supported by a reported trend in $\tau^*_{c,50}$ as a function of channel slope. Researchers have quantified the trend from field measurements of the reference transport rate [*Mueller et al.*, 2005, see figure 4; *Prancevic and Lamb*, 2015, see figure 2], as well as using various methods in the field and laboratory [*Lamb et al.*, 2007, see figure 1]. From their regression equations of $\tau^*_{c,50}$ as a function of slope, the study reach average slope of 0.0007 predicts $\tau^*_{c,50}$ values of 0.023, 0.016, and 0.024, respectively. Given that all the data used by *Mueller et al.* and *Prancevic and Lamb* and most of the data from *Lamb et al.* were from the

reference transport-based method an over prediction should be anticipated based on greater $\tau^*_{c,50}$ values from reference-transport as compared to those from visually detected entrainment [*Wilcock and McArdell*, 1997; *Buffington and Montgomery*, 1997]. Even so, their predictions are about the tracer-measured value thereby providing strong support to the results. At the same time, *Lamb et al.* noted that "…an obvious lack of data for $S < 10^{-3}$"…"is likely due to the bed being sand covered in natural rivers…" Thus, these gravel-bed mobility results provide additional support as they extend the trend in $\tau^*_{c,50}$ with slope.

The trend in $\tau^*_{c,i}$ with D_i is indicated by the hiding coefficient (β), which I measured to be in closer agreement to equal mobility ($\beta = 1$) than dependence solely on the D_i value ($\beta = 0$). However, smaller tracers were entrained at lower $\tau_{c,i}$ values and in greater proportions at equivalent τ values than larger tracers (Figure 5). In regards to other methods of estimating entrainment, this detection of selective entrainment is an important finding; as the other methods are biased to produce results that either suggest equal mobility or selective entrainment. *Wilcock* [1988] evaluated the transport-based methods estimation of the trend in $\tau_{c,i}$ with D_i and found that $\tau_{c,i}$ values determined from the largest grain in transport are more likely to result in β_c values of roughly 0.5 but can produce ambiguous results if transport approximates equal mobility or if all grain sizes are in transport. Furthermore, *Wilcock* [1992] argues that the largest grain method is less dependable as it (i) requires sampling D_i that are the smallest proportion of the transport grain size distribution, and (ii) is often performed using equipment that are biased toward collecting smaller grains. In regards to the reference-transport method, *Wilcock* [1988] found that the reference transport method is more likely to result in values closer to unity.

Wilcock and McArdell [1997] explicitly observed that the reference transport method produced β_c closer to unity than their tracer entrainment observations, thereby demonstrating a reference-transport methodological bias toward equal mobility. Each of these difficulties is overcome using tracers: (i) The $\tau_{c,i}$ are determined from extrapolating the trend in Y_i versus τ, (ii) the grain size of the tracers is known, and (iii) the trends in $\tau_{c,i}$ with D_i are not limited by the availability of larger immobile grains or a narrow range in $\tau_{c,i}$ values.

The explanation for these trends in entrainment lies in the relationship between the grains exposure to flow and their frictional resistance. Each grain on a water-worked bed exerts resistance to the downstream force applied by flow. The resistance is provided by the submerged weight of the grain and frictional resistance from its geometric position against neighboring grains [*Wiberg and Smith*, 1987]. Additionally, larger grains can shelter smaller grains from the flow forces [*Kirchner et al., 1990*]. But the larger grains are more likely (i) to experience greater drag forces as they protrude into higher velocity flow with a larger exposed area [*White*, 1940; *Fenton and Abbott*, 1977] and (ii) to have less resistance provided by smaller surrounding grains, which allow the larger grains to topple over them [*Wiberg and Smith*, 1987]. The combination of these factors can counter the absolute resistance effect of weight [*Raudkivi*, 1998]. Thus, only when the forces of the flow exceed the forces holding a grain in place will it begin to move. Furthermore, because of the innumerable geometric positions a grain can have on a mixed bed, grains of a given size have a wide distribution of resistance [*Johnston et al.*, 1998; Chapter 2]. Therefore, individual grains of a D_i will begin to move over a range of flow levels imposing τ in excess of the $\tau_{c,i}$ value.

These physical controls of entrainment are apparent in the trends that define the domain of partial entrainment. These trends are displayed in the tracer entrainment results that are supported by consistencies between sites, corresponding measurements of mobility, and similarity with the observations of other researchers. Here, I review the results of each quantified facet of entrainment and discuss mechanical explanations for the results.

1. Partial Entrainment Domain

The partial entrainment trend with increasing τ reflects the mechanics that control the Y_i. The Y_i is controlled by the fluctuating flow force acting on the grains, in the grains' reinforcement against the force of the flow, and in their exposure to the flow. The resistance to movement is quantified by $\phi = \tan^{-1}\left(F_d/F_g\right)$ where ϕ is termed the friction angle, F_d is the minimum downstream directed force that is capable of moving the grain, and F_g is the submerged weight of the grain [*García*, 2008]. These variables were surveyed as part of a companion study [Chapter 2] and used to calculate the applied τ_c^* for individual grains using the force balance model of *Wiberg and Smith* [1987]. Some of the Chapter 2 findings are described here as they explain the mechanics and trends in the tracer results.

As reported in Chapter 2, the force balance model predicted a range of τ_c^* for each D_i that are normally distributed and similar to those described by the logit model (4) [Chapter 2, figure 9]. This strongly suggests that the mechanism explaining the trend in Y_i with increasing τ is the variability in the resistance to flow of the grains as described by *Wiberg and Smith* [1987].

The distributions of $\tau^*_{c,i}$ values from the tracer results are consistently less than the equivalently defined values predicted from the force balance model. The consistency is indicative of the similarity between the measurements. A simple adjustment to the force balance predicted τ^*_c by a site-specific constant factor results in their distributions aligning with those of the tracers [Chapter 2, figure 10]. The factor difference associates with the degree of turbulent fluctuation [Chapter 2, figure 8]. This finding implies that the time-average τ is not responsible for entrainment and suggests the maximum hydraulic forces provided by turbulent sweeps against the bed are responsible for the difference between the coupled values of τ and Y_i from the tracer measurements and the distributions of force balance calculated τ^*_c. This mechanism is explained by the turbulence of the flow, where turbulence is expressed by the variability in the instantaneous depth-averaged velocity relative to the shear velocity. The fluctuation caused by this variability results in forces in excess of their average acting on the grains and, therefore, the distribution of applied forces from velocities in excess of their average are responsible for entrainment. As a result, the distribution of resistance to the applied force from the flow of a D_i provides the primary explanation for the trends in Y_i with increasing τ (Figure 4).

2. Incipient Entrainment of the Bed

The flow conditions immediately before the first grains begin to move define the moment of incipient motion and the critical entrainment threshold of the bed. Because a mixed bed affects mobility, different D_i are closer to equally mobile than that suggested by their absolute size. Because the least reinforced grains are generally the most likely to move, those grains define the onset of entrainment [*Kirchner et al.*, 1990; *Buffington et al.*,

1992; *Johnston et al.*, 1998; Chapter 2]. However, as grain size decreases, the probability of being sheltered in the leeward side of a larger grain is greater. In addition, those grains that are more effectively sheltered often offer the least frictional resistance to a downstream-directed force [Chapter 2, Appendix A]. As a result, the τ_c^* values for D_i are greater than indicated by their lowest frictional resistance. This observation provides some support for truncating the lower tail of the logistic distributions with the linear determination of $\tau_{c,i}^*$ (Figure 4). Meanwhile, the coarser grains are not characterized as sheltered from flow by other large grains but neither does the lower tail of the distribution of force balance calculated and adjusted τ_c^* values extend beyond the values of $\tau_{c,i}^*$ as linearly determined from the tracers. Therefore, the $\tau_{c,i}^*$ provided by the linearized trend may also be justified for the larger grains though the mechanism for truncating the lower tail of their $\tau_{c,i}^*$ distribution is uncertain.

3. Full Entrainment

Generally similar to the onset of entrainment, there is also a flow strength at which full entrainment of a grain size fraction occurs [*Stelczer*, 1981]. In this case, it requires the flow strength to exceed the resistance of the most reinforced and least exposed grains on the bed. However, as discussed previously, the asymptotic trend in Y_i with increasing τ indicates that a $\tau_{f,i}$ value can only provide a statistical approximation of Y_i=1. This suggests that the upper tail of the frictional resistance to entrainment distributions, as described by the fractional distributions of τ_c^* from the force balance calculations [Chapter 2], controls the rate of change in Y_i with increasing τ toward a Y_i=1. Therefore, the most resistant grains on the bed as defined by the *Wiberg and Smith* [1987] force balance model define the τ_f.

Although some of the smaller D_i may have experienced full entrainment, the flows were not great enough to fully entrain the larger D_i (Figure 4). Therefore, as exhibited by the tracers, the sites did not experience shear stresses at levels capable of fully entraining the largest grain sizes or of complete bed entrainment. This observation is in agreement with research findings that gravel beds are rarely completely mobilized [*Haschenburger and Wilcock*, 2003]. However, the logit model provides a way to approximate $\tau_{f,i}$ from the trends in Y_i with increasing τ from tracer entrainment at $\tau < \tau_{f,i}$. The predicted $\tau_{f,i}$ are supported by (i) the tracer results that were consistent between sites (Figure 7), (ii) consistencies in the variance describing the trend in Y_i with τ (Figure 6), and (iii) force balance predictions that align with the logit models from regression of Y_i with τ [Chapter 2, figures 9 and 10]. As a result, the bed's τ_f is able to be approximated from the $\tau_{fe,i}$ of the largest grain size fraction on the bed (i.e., the 128 mm grain size class), which is well approximated by the trend in partial entrainment as described by Y_i as a logit function of τ and distributions of the applied τ_c for the largest D_i predicted by the force balance model.

4. Selective Entrainment

Because the weight of a grain scales directly with the cube of its diameter, a smaller grain requires less force to move [*Newton*'s Second Law]. However, hydraulic forces acting on a bed can be variably distributed on its grains depending on the bed roughness, where greater roughness indicates deeper pockets between grains that are indicative of greater ϕ. In addition, the ϕ is also affected by grain packing. For example, if the bed is composed of grains of size *d* and the top of each grain is at equal levels then the τ would be equally divided onto each grain. If the bed were uneven with some grains more

elevated than others, the elevated grains would bear a greater proportion of the τ as they are more exposed to the flow velocities that increase away from the bed surface. In addition, the elevated grains would have smaller ϕ_i values than grains on the packed bed as their contact with neighboring grains would be lower. Indeed, *White* [1940] found that rough beds have τ_c values about half that of smooth beds. Now, if the bed were composed of smaller grains d_1 and larger grains d_2, the different packing conditions again would influence their mobility. In the case, where both d_i tops are at equal elevations d_1 would experience greater forces from flows relative to their size. In addition, their ϕ_1 values would be less than the d_2 grains, thereby making d_1 more mobile. With a rough bed surface, though, the d_2 are more elevated into the flow profile and their resistance is reduced due to its contacts with supporting grains no longer as high, providing lower ϕ_2 values while receiving a greater portion of the flows forces. The d_1, on the other hand, are more likely to receive reduced flow forces as they are sheltered in the lee of the d_2, and to have greater ϕ_1 values due to their positioning lower against the d_2. Therefore, adjustments in packing affect bed mobility such that rough, mixed beds will deviate from direct dependence on grain weight and become more equally mobile.

H. Conclusions

I quantified the facets of entrainment from tracer monitoring methods and calibration of a 2D model. The tracer monitoring results in which the local τ value provided from a 2D hydraulic model allow the probability of entrainment to be described as a logit function of the τ and to be delineated for several D_i. Consistency in the Y_i versus τ trends between D_i provides support for the measurements. Additional support is provided by confirmation of the measurements between two sites and an alternative method that relied

on predicting the τ_c^* from the *Wiberg and Smith* [1987] force balance model that used measurements of ϕ as input.

The entrainment thresholds are quantified using the Shields stress as a function of relative grain size. Most of the coefficients of the hiding functions for the critical Shields stress as a function of relative grain size are not significantly different between sites. The range in the partial entrainment domain, defined as between the critical threshold, where the probability of entrainment is low, and an approximation of the full entrainment threshold, where the probability is high, is different between sites. However, a simple explanation is provided by the difference in the range of bed textures found at the sites. Also, the measured $\tau_{c,50}$ values are at the lower end of the range of values reported elsewhere but are supported by the trend in $\tau_{c,50}$ values with channel slope. Therefore, the presented method is verified between sites and provides applied practitioners a simple means to definitively measure and predict fractional entrainment.

Each of the facets of entrainment was quantified from tracer movements and immobility and explained using theoretical principles. The change in partial entrainment of a grain size fraction was determined from the change in the Y_i with increasing τ. Logit models of τ delineate its effect on Y_i and provide a prediction of the probability of entrainment of a grain. The logistic distribution of τ_c is used to provide the $\tau_{c,i}$ and an approximation of the τ_f that is extended to D_i that were not nearly fully entrained. In doing so, the τ capable of fully entraining the bed is approximated. Furthermore, I found that the probability of entrainment with increasing τ for a range of D_i may be described by a single $\tau_{[50],i}$ and its variance thereby providing additional diagnostic support to entrainment measurements in the absence of full entrainment. Therefore, the results

indicate that the physical controls and drivers of entrainment appear to be well defined and thus encourage further research, development, and use of theoretical-based models for predicting bed load transport rates.

Lastly, the measured low $\tau^*_{c[50]}$ values for entrainment emphasizes the value of measuring this metric. Although many methods of estimating the mobility of the bed exist, the mobility aspect of interest must be considered when choosing a method. Here, I present a method for quantifying the different facets of entrainment that should prove useful for managing benthic disturbance and salmon incubation habitat maintenance.

I. References

Andrews, E. D. (1983), Entrainment of gravel from naturally sorted riverbed material, *Geological Society of America Bulletin, 94*, 1225-1231.

Ayres Associates (1998), Topographic and Bathymetric Surveys for the San Joaquin River from Friant Dam to Gravelly Ford (RM 267 to RM 229), prepared for Bureau of Reclamation, Fresno, California.

Barton, G. J., R. R. McDonald, J. M. Nelson, and R. L. Dinehart (2005), Simulation of flow and sediment mobility using a multidimensional flow model for the white sturgeon critical habitat reach, Kootenai River near Bonners Ferry, Idaho, U.S. Geological Survey, Reston, VA.

Biggs, B. J. F., M. J. Duncan, A. M. Suren, and J. R. Holomuzki (2002), The importance of bed sediment stability to benthic ecosystems, in *Gravel-bed Rivers V*, edited by M. P. Mosley, pp. 423-449, New Zealand Hydrological Society, Inc., Wellington, New Zealand.

Buffington, J. M., and D. R. Montgomery (1997), A systematic analysis of eight decades of incipient motion studies, with special reference to gravel-bed rivers, *Water Resour. Res., 33(8),* 1993-2029.

Buffington, J. M., W. E. Dietrich, and J. W. Kirchner (1992), Friction angle measurements on a naturally formed gravel stream bed: Implications for critical boundary shear stress, *Water Resour. Res., 28(2),* 411-425, doi:10.1029/91WR02529.

Church, M., and M. A. Hassan (2002), Mobility of bed material in Harris Creek, *Water Resour. Res., 38(11),* 1237, doi:10.1029/2001WR000753.

Einstein, H. A. (1950), The bedload function for sediment transport in open channel flows, Tech. Bull. 1026, U. S. Department of Agriculture, Soil Conservation Service, Washington, D.C.

Fenton, J. D., and J. E. Abbott (1977), Initial movement of grains on a stream bed: The effect of relative protrusion, *Proc. R. Soc. London A. Math. Phys. Sci., 352(1671),* 523-537.

García, C., H. Cohen, I. Reid, A. Rovira, X. Ubeda, and J. B. Laronne (2007), Processes of initiation of motion leading to bed load transport in gravel-bed rivers, *Geophysical Research Letters, 34,* L06403, doi:10.1029/2006GL028865.

García, M. H. (2008), Sediment transport and morphodynamics, Ch. 2 in M. H. García (ed.), *Sediment Engineering: Processes, measurements, modeling, and practice, ASCE*, Reston, Va, pp. 21-163.

Gessler, J. (1971), Beginning and ceasing of sediment motion, in H. W. Shen (ed.), *River Mechanics,* Fort Collins, CO, pp. 7:1-22.

Gilbert, G. K. (1914), The transport of debris by running water, *U.S. Geological Survey Professional Paper 86*, 263 p.

Hammond, F. D. C., A. D. Heathershaw, and D. N. Langhorne (1984), A comparison between Shields' threshold criterion and the movement of loosely packed gravel in a tidal channel, *Sedimentology, 31*, 51-62.

Haschenburger, J. K., and P. R. Wilcock (2003), Partial transport in a natural gravel bed channel, *Water Resour. Res., 39(1)*, 1020, doi:10.1029/2002WR001532.

Johnston, C. E. (1996), Particle friction angle variability of five natural water-worked gravel mixtures, MA thesis, University of Colorado at Boulder.

Johnston, C. E., E. D. Andrews, and J. Pitlick (1998), In situ determination of particle friction angles of fluvial gravels, *Water Resour. Res., 34(8)*, 2017-2030, doi:10.1029/98WR00312.

Kirchner, J. W., W. E. Dietrich, F. Iseya, and H. Ikeda (1990), The variability of critical shear stress, friction angle, and grain protrusion in water-worked sediments, *Sedimentology, 37*, 647-672, doi:10.1111/j.1365-3091.1990.tb00627.x.

Komar, P. D. (1987), Selective grain entrainment by a current from a bed of mixed sizes: a reanalysis, *J. of Sedimentary Petrology, 57(2)*, 203-2011.

Kondolf, G. M., and P. R. Wilcock (1996), The flushing flow problem: Defining and evaluating objectives, *Water Resour. Res., 3(2)*, 2589-2599.

Konrad, C. P., D. B. Booth, S. J. Burges, and D. R. Montgomery (2002), Partial entrainment of gravel bars during floods, *Water Resour. Res., 38(7)*, doi: 10.1029/2001WR000828.

Lamb, M. P., W. E. Dietrich, and J. G. Venditti (2008), Is the critical Shields stress for incipient motion dependent on channel-bed slope?, *Journal of Geophysical Research, 113*, F02008, doi:10.1029/2007JF000831.

Larrone, J. B., C. García, and I. Reid (2001), Mobility of patch sediment in gravel bed streams: Patch character and its implications for bedload, in *Gravel-bed Rivers V*, edited by M. P. Mosley, pp. 423-449, New Zealand Hydrological Society, Inc., Wellington, New Zealand.

Lavelle, J. W., and H. O. Mofjeld (1987), Do critical shear stress for incipient motion and erosion really exist?, *J. Hydr. Engrg., 113(3)*, 370-385.

McDonald R. R., J. M. Nelson, and J. P. Bennett (2005), Multidimensional Surface-water Modeling System User's Guide, USGS Techniques in Water Resources Investigations 11-B2, U.S. Geological Survey, Reston, VA, 156 pp.

McLean, S. R., S. R. Wolfe, and J. M. Nelson (1999), Predicting boundary shear stress and sediment transport over bed forms, *J. Hydraul. Eng.*, 125, 725-736, doi:10.1061/(ASCE)0733-9429(1999)125:7(725).

Meyer-Peter, E., and R. Müller (1948), Formulas for bed-load transport, Proceedings, 2nd Congress International Association for Hydraulic Research, Stockholm, Sweden, 39-64.

Miller, M. C., I. N. McCave, and P. D. Komar (1977), Threshold of sediment motion under unidirectional currents, *Sedimentology, 24(4)*, 507-527.

Mueller, E. R., J. Pitlick, and J. M. Nelson (2005), Variation in the reference Shields stress for bed load transport in gravel-bed streams and rivers, *Water Resour. Res., 41*, W04006, doi:10,1029/2004WR003692.

Neill, C. R. (1968), A reexamination of the beginning of movement of coarse granular bed materials, Report INT 68, Hydraulics Research Station, Wallingford, England.

Nelson, J. M., and J. D. Smith (1989), Flow in meandering channels with natural topography, in River Meandering, *Water Resour. Monogr. Ser., vol. 12*, edited by S. Ikeda and G. Parker, pp. 69– 102, AGU, Washington, D. C.

Nelson J. M., J. P. Bennett, and S. M. Wiele (2003), Flow and sediment transport modeling, in *Tools in Fluvial Geomorphology*, G. M. Kondolf and H. Piegay (eds), John Wiley & Sons, Chichester, 539–576.

Nelson, J. M., and R. M. McDonald (1996), Mechanics and modeling of flow and bed evolution in lateral separation eddies, report, Grand Canyon Environ. Stud., Flagstaff, Ariz.

Nelson, J. M., S. R. McLean, and S. R. Wolf (1993), Mean flow and turbulence fields over two-dimensional bed forms, *Water Resour. Res., 29*, 3935– 3953, doi:10.1029/93WR01932.

Paintal, A. S. (1971), Concept of critical shear stress in loose boundary open channels, *J. Hydr. Res., IAHR, 9*, 91-113.

Parker, G., and P. C. Klingeman (1982), On why gravel bed streams are paved, *Water Resour. Res., 18(5),* 1409-1423.

Parker, G., P. C. Klingeman, and D. L. McLean (1982), Bedload size distribution in paved gravel-bed streams, *J. Hydr. Div., ASCE, 108(4)*, 544-571.

Parker, G. (2008), Transport of gravel and sediment mixtures, Chapter 3 in García, M. H. (ed.), *Sediment Engineering: Processes, measurements, modeling, and practice, Manual 110, ASCE*, Reston, Va, pp. 165-251.

Prancevic, J. P., and M. P. Lamb (2015), Particle friction angles in steep mountain channels, *J. Geophys. Res. Earth Surf., 120,* 242-259, doi:10.1002/2014JF003286.

Rainato, R., L. Picco, L. Mao, J. Moretto, and M. A. Lenzi (2014), The extent of partial transport in a disturbed gravel-bed braided river (Piave River, North-eastern Italy), *Quaderni di Idronomia Montana, 32(1)*, 265-276.

Raudkivi, A. J. (1990), *Loose boundary hydraulics*, Pergamon Press, New York, pp. 28-43:1-538.

San Joaquin River Restoration Program (SJRRP) (2015), Flow data: Final daily average, U.S. Bureau of Reclamation and California Department of Water Resources, retrieved on October 8, 2015, from: http://restoresjr.net/flows/Data/index.html

Sharma, A. (1996), *Applied Multivariate Techniques*, John Wiley and Sons, Inc., New Jersey, pp. 493.

Shields, A. (1936), Änwendung der Ahnlichkeitsmechanik und der Turbulenzforschung auf die Geschiebebewegung, *Mitt. Preuss. Vers. Anst. Wasserb. Schiffb., 26*, 26 pp. (translated by W. P. Ott & J. C. van Uchelen, U.S. Department of Agriculture, Soil Conservation Service Coop Laboratory, California Institute of Technology).

Stelczer, K. (1981), *Bedload Transport: Theory and Practice*, Water Resources Publications, Littleton, CO, 295 pp.

Whitaker, A. C., and D. F. Potts (2007), Coarse bed load transport in an alluvial gravel bed stream, Dupuyer Creek, Montana, *Earth Surface Processes and Landforms, 32,* 1984-2004.

White, C. M. (1940), Equilibrium of grains on the bed of a stream, *Proc. R. Soc. London A. Math. Phys. Sci., 174*, 322-334.

Wiberg, P. L., and J. D. Smith (1987), Calculations of the critical shear stress for motion of uniform and heterogeneous sediments, *Water Resour. Res., 23(8)*, 1471-1480, doi:10.1029/WR023i008p01471.

Wilcock, P. R. (1988), Methods for estimating the critical shear stress of individual fraction in a mixed-size sediment, *Water Resour. Res., 24(7)*, 1127-1135.

Wilcock, P. R. (1992), Flow competence: A criticism of a classic concept, *Earth Surface Processes and Landforms, 17*, 289-298.

Wilcock, P. R. (1993), Critical shear stress of natural sediments, *J. Hydr. Engrg., 119(4)*, 491-505.

Wilcock, P. R., and J. C. Crowe (2003), Surface-based transport model for mixed-size sediment, *J. Hydr. Engrg.*, DOI: 10.1061/(ASCE)0733-9429(2003)129:2(120).

Wilcock, P. R., J. Pitlick, and Y. Cui (2009), Sediment transport primer estimating bed-material transport in gravel-bed rivers, Gen. Tech. Rep. RMRS-GTR-226, U. S. Department of Agriculture, Forest Service, Rocky Mountain Research Station, 78 p.

Wilcock, P. R., G. M. Kondolf, W. V. G. Matthews, and A. F. Barta (1996), Specification of sediment maintenance flows for a large gravel-bed river, *Water Resour. Res., 32(9)*, 2911-2921.

Wilcock P. R., and B. W. McArdell (1993), Surface-based fractional transport rates: Mobilization thresholds and partial transport of a sand-gravel sediment, *Water Resour. Res., 29(4)*, 1297-1312.

Wilcock P. R., and B. W. McArdell (1997), Partial transport of a sand gravel sediment, *Water Resour. Res., 33(1)*, 235-245.

Wolman, M. G. (1954), A method for sampling coarse river-bed material, *Eos Trans. AGU*, 35, 951-956.

Wong, M., and G. Parker (2006), Reanalysis and correction of bed-load relation of Meyer-Peter and Muller using their own database, *J. Hydr. Engrg., 132(11)*, 1159-1168.

Wu, F.-C., and K.-H. Yang (2004), A stochastic partial transport model for mixed-size sediment: Application to assessment of fractional mobility, *Water Resour. Res., 40*, W04501, doi:10.1029/2003WR002256.

Yalin, M. S., and E. Karahan (1979), Inception of sediment transport, *J. Hydraul. Div., ASCE, 105(11)*, 1433-1443.

J. Appendix

Model Performance

Water surface elevations for all high-flow events are well modeled as indicated by correlation coefficients ($r > 0.99$), and negligible average model bias (<2 cm) that is less than the accuracy of the survey equipment (Table A-1). Local bias is greatest in the 201 m^3/s model as it deviates from a unity slope by 8% while the other models are within 3% (Figure A-1). The mean bias is the average difference between the prediction and the measurement. The local bias is the deviation from perfect agreement between predicted and the measurement. The upstream pressure transducer provides the day's range in WSE. Although the narrowest range is associated with the least biased model (31.2 m^3/s) it does not have a consistent effect on the bias.

Table A-1. FaSTMECh calibration and WSE verification for the four monitored discharges.

		Water Surface Elevation					
Date	Discharge	Measured WSE Points	Correlation Coefficient	Mean Bias	Pressure Transducer WSE* (m)		
ddmmyyyy	m^3/s	#	r	m	mean	min	max
20102011	19.9	35	0.996	-0.012	87.432	-0.005	0.005
24052012	31.2	46	0.999	0.000	87.552	-0.003	0.003
5012011	173	14	0.996	-0.008	88.698	-0.049	0.031
3292011	201	9	0.991	0.014	88.843	-0.014	0.014

* Recorded WSE at 15 minute intervals. Day's mean WSE, Min = minimum WSE – mean WSE, max = maximum WSE – mean WSE.

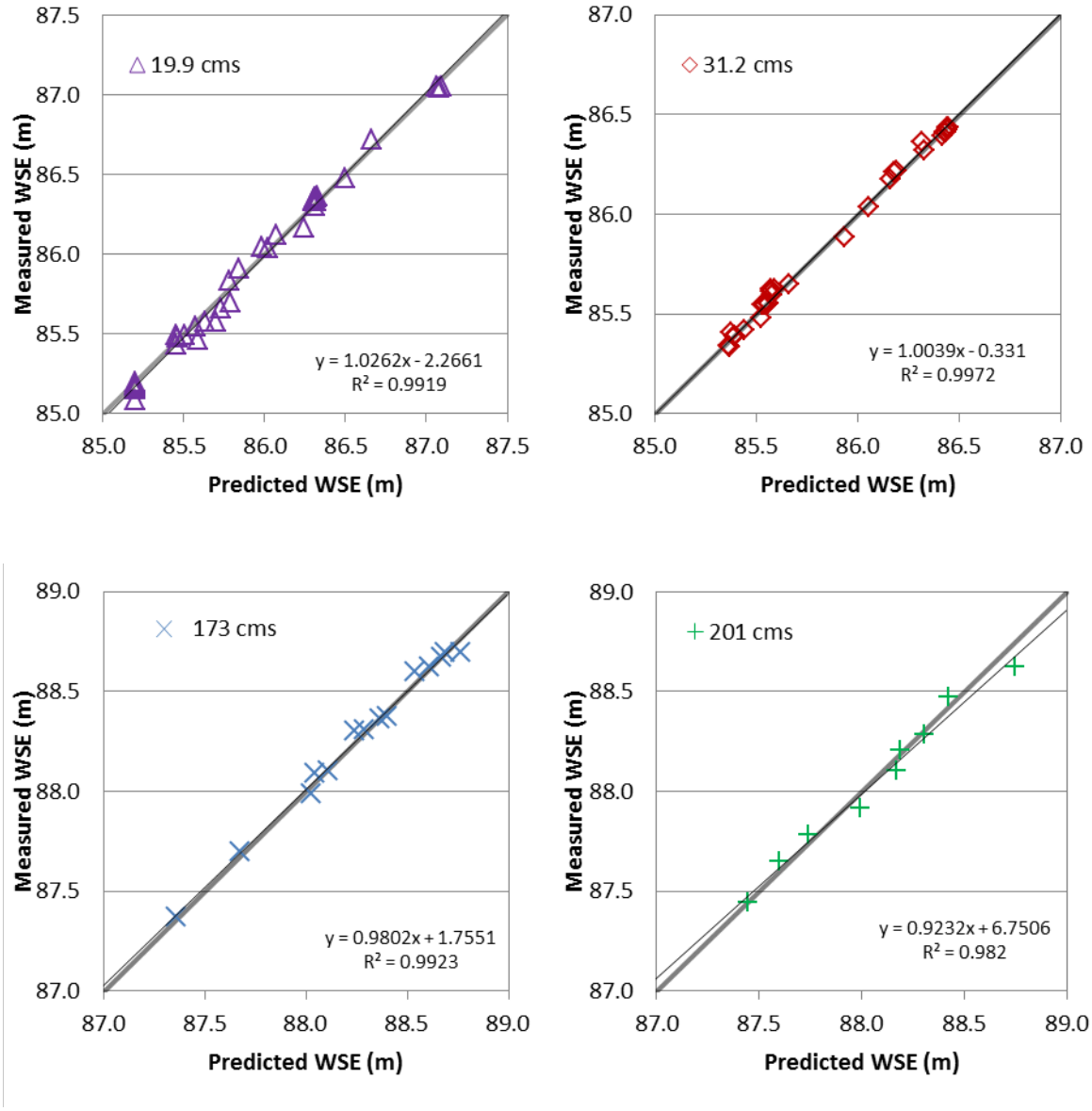

Figure A-1. Model verification of the four monitored high-flow events predicted versus measured water surface elevations. The one-to-one indicator of perfect agreement is provided as the heavier grey line with best-fit linear regression line provided as the thin black line.

Depth average velocity is biased but tends to be less so away from the tails (Figure A-2). In the case of the sub-bankfull flows the models over-predict slow water areas and under-predict faster water areas. The bias as expressed by the average residual error is less than 4% of the measured depth average velocity (Table A-2). The average bias is observed to become more negative with increasing discharge and the standard deviation

increases similarly. For the two over-bankfull flow models the bias is an under-prediction throughout the range of measured velocity. Therefore, the results indicate that the WSE are well correlated with negligible bias while the depth average flow velocity is more likely to be under predicted in areas more likely to experience gravel entrainment.

Table A-2. Verification of FaSTMECh predictions of depth average flow velocity.

		Velocity Verification				
Date	Discharge	Nodal Comparisons	Mean Bias	Standard Deviation	Average Residual	Correlation Coefficient
Ddmmyyyy	m^3/s	#	m/s		%	r
20102011	19.9	123	-0.001	0.079	-1.2	0.83
24052012	31.2	174	-0.032	0.119	-0.8	0.81
05012011	173	115	-0.086	0.185	-3.8	0.74
03292011	201	143	-0.128	0.302	-1.3	0.44

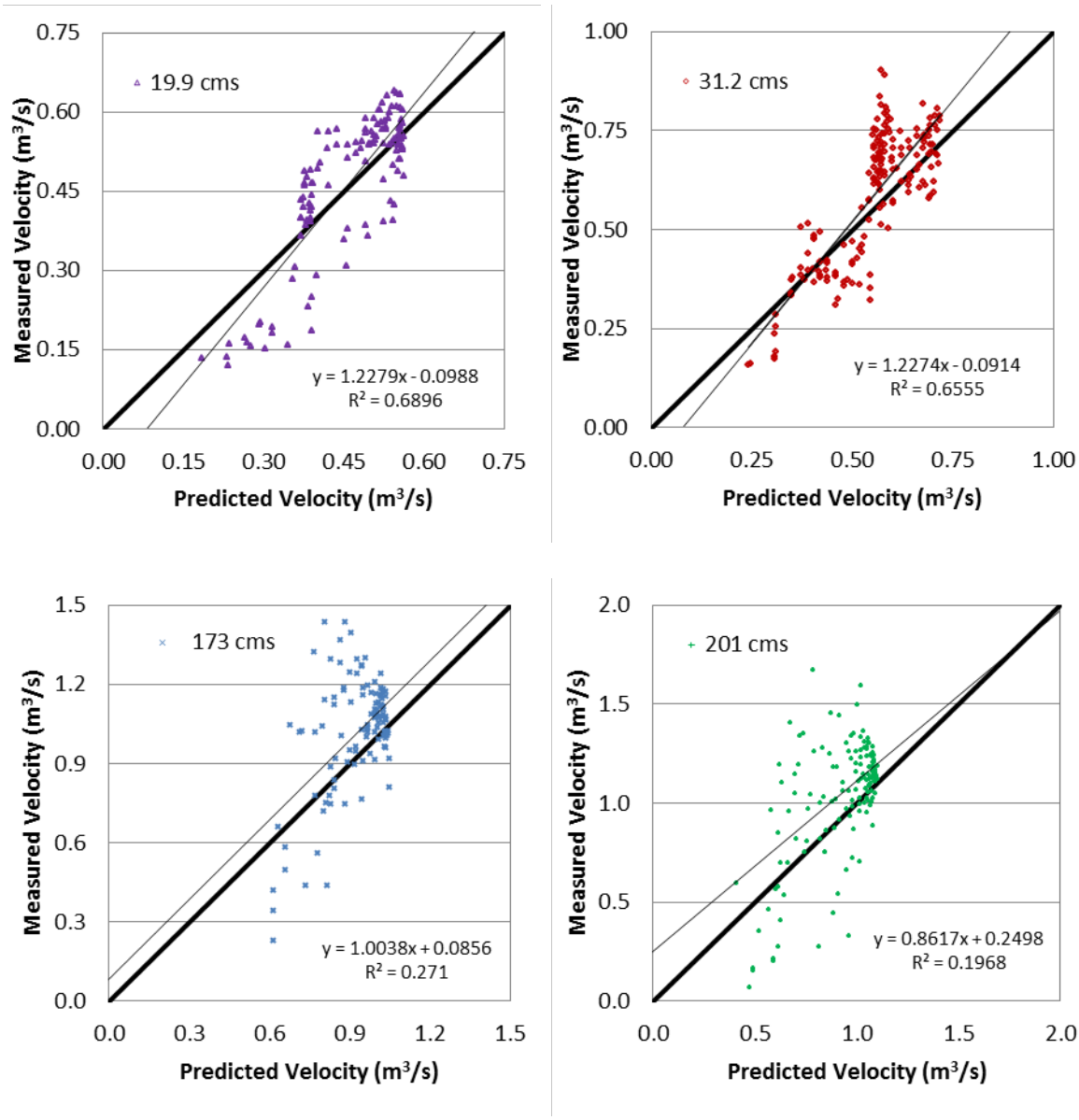

Figure A-2. Model verification of the four monitored high-flow events predicted versus measured depth average flow velocity. The one-to-one indicator of perfect agreement is provided as the heavier line with best-fit linear regression line provided as the thin line.

Lateral bias in the depth average flow velocity indicates the over-bank flow models provide an over-prediction along the channel margins where measured velocities are more erratic (Figure A-3). This is likely the result of submerged woody vegetation along the banks. Meanwhile the mid-channel area is much better approximated. Similar trends are seen in the sub-bankfull flow prediction and measured plots but the differences

are less extreme. These results suggest that the extremes in the differences from the predicted hydraulics, as exhibited in Figure A-2, can be reduced by excluding results from within 3 m of the channel margins and other roughness anomalies.

Lastly, the verification results suggest that there is a slight but consistent bias in the results. For each model run the velocity estimates under-predict the measured values as indicated by the bias and residuals summarized in Table A-2. These results suggest that in the tail-end of pools the velocity is underestimated on average by -3.8% to -0.8%

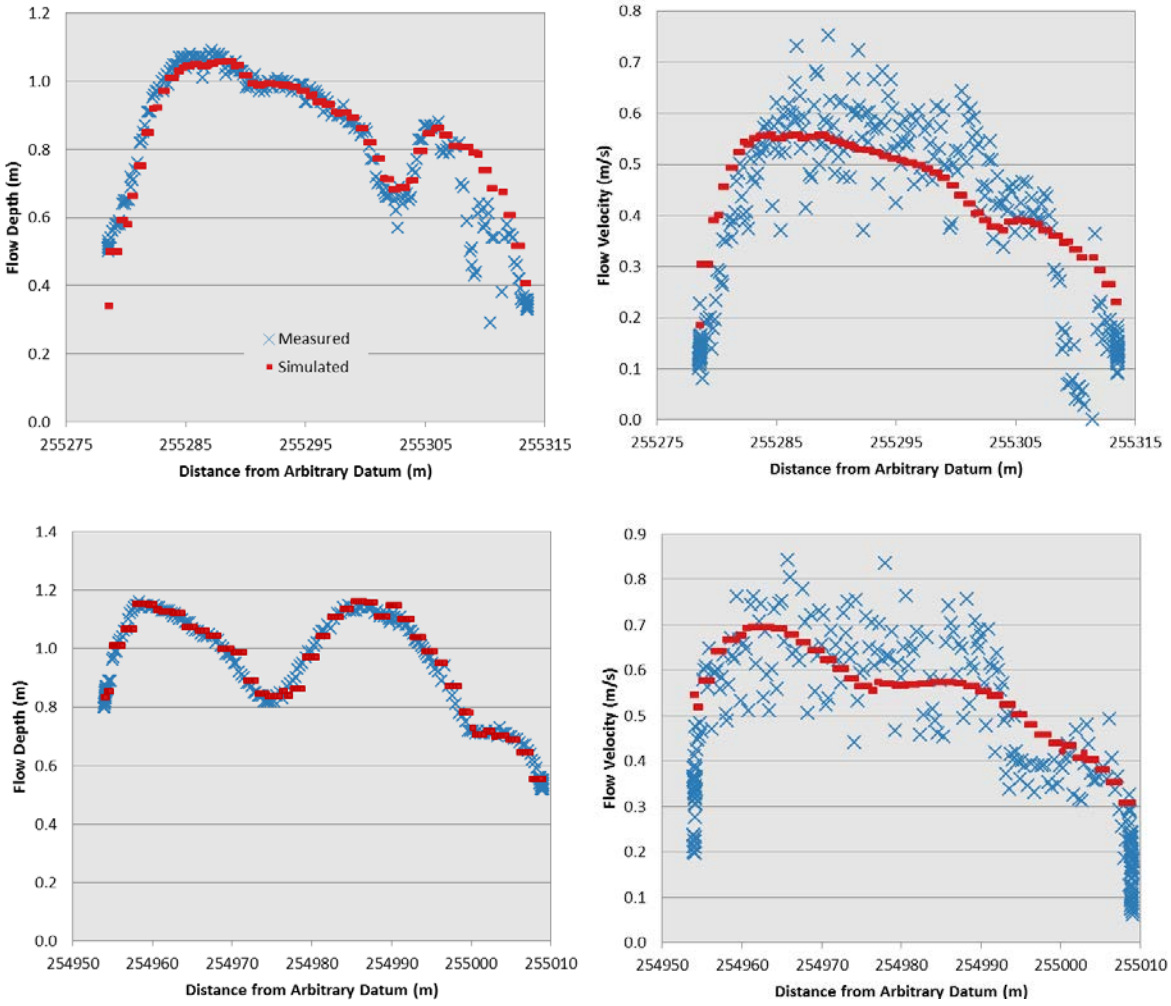

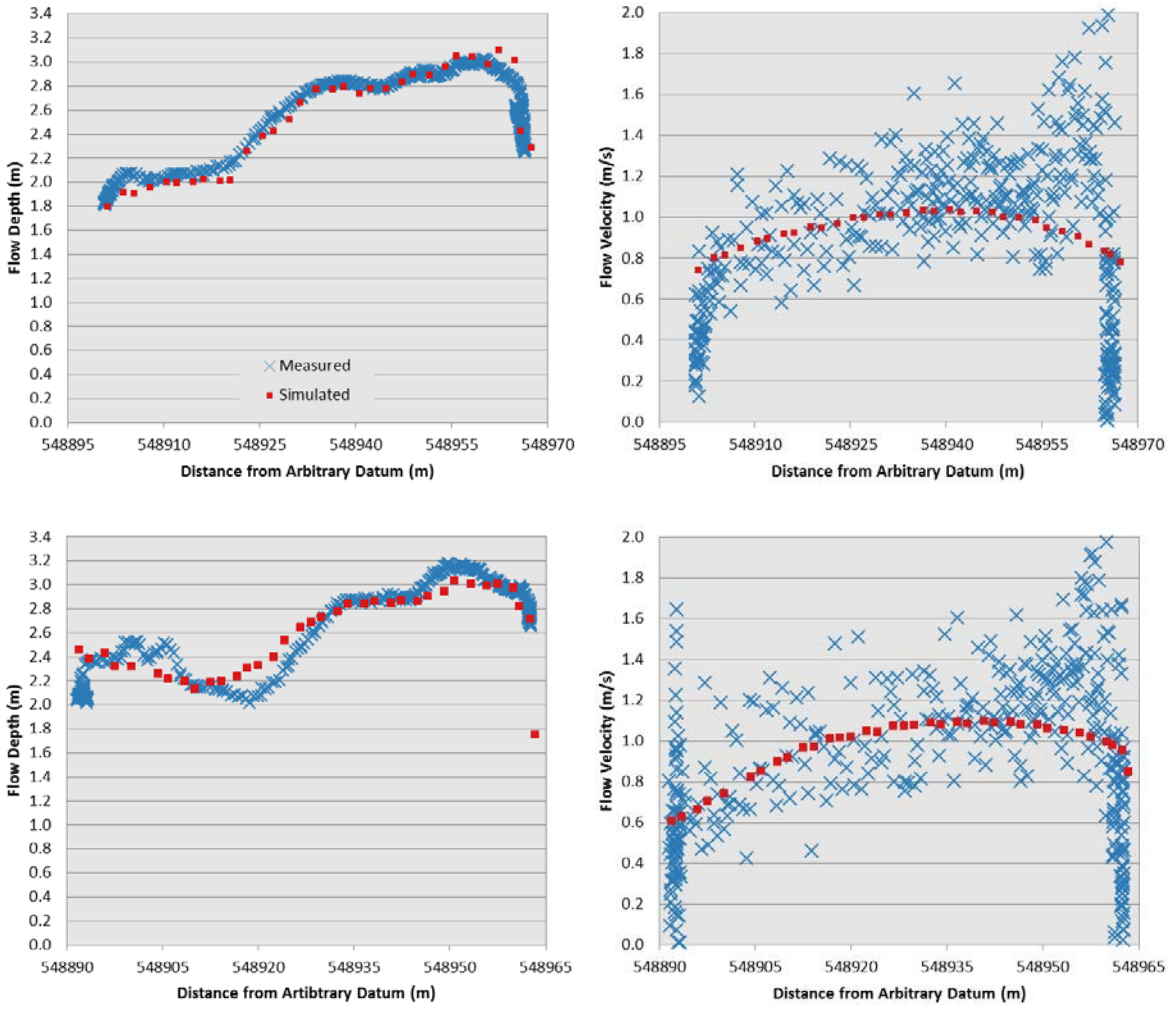

Figure A-3. Flow depth (left) and depth-averaged velocity (right). Individual measurements illustrate the breadth of scatter in the data. From top to bottom the modeled-measured panels are 20 October 2011 (ADP measured flow rate of 19.9 m^3/s), 24 May 2012 (ADP measured flow rate of 31.2 m^3/s), 5 January 2011 (USBR reported daily average flow rate of 173 m^3/s) and 29 March 2011 (USBR reported daily average flow rate of 201 m^3/s).

II. Variability in the Resistance to Entrainment of In Situ Grains Along a Gravel-bed

A. Introduction

The flow strength that begins to move grains on a bed is estimated for many aspects of river management, yet the fundamental resistance to downstream-directed forces of a grain on a natural streambed remains to be thoroughly characterized. Several physically based force balance models have been proposed for predicting the minimum flow strength required to dislodge a grain [*White*, 1940; *Komar and Li*, 1966; *Naden*, 1987; *Wiberg and Smith*, 1987; *James*, 1990; *Bridge and Bennett*, 1992]. Each of these models depends on the grain resistance as a primary variable, and while they hold promise for predicting sediment entrainment based on theoretical physics, they are not well tested. As part of an effort to characterize the variability in frictional resistance that is associated with local hydraulics and sedimentology, this study employs a force balance model to predict the flow strength necessary to entrain a grain. To do so, I rely on force gages to measure the frictional resistance properties of grains on a bed. These methods that focus on the specific moment when a grain becomes dislodged, i.e., entrained, are referred to as entrainment-based methods.

The frictional resistance of a grain is the force that is offered by its submerged weight and the surface over which the grain must roll or slide. This resistance can be measured at entrainment from an applied downstream-directed force F_d and the grain weight F_g where the bed surface is effectively horizontal. The ratio of these forces is the Coulomb coefficient of friction that is expressed in terms of a friction angle ϕ, such that:

$$\tan \phi = F_d / F_g \quad (1)$$

[see *García*, 2008].

Such ϕ values have been measured using randomly placed grains and observing their onset of displacement while on tilting boards with artificial rough surfaces [*Miller and Byrne*, 1966; *Li and Komar*, 1986], flume beds [*Kirchner et al.*, 1990], and natural beds [*Buffington et al.*, 1992]. More recently, handheld force gages have been used to measure ϕ values of *in situ* gravel [*Johnston et al.*, 1998] and boulders [*Prancevic and Lamb*, 2015] on natural beds. Each of these studies demonstrated an inverse relationship between the ϕ and relative grain size D_i/D_{50}, such that:

$$\phi_{[50],i} = e(D_i/D_{50})^{-f} \quad (2)$$

where subscripted '[50]' refers to the median value of the subscripted term; D is the grain diameter with subscripted '*i*' and '*50*' referring specifically to the values pertaining to the grain size class of interest and the median grain size of the bed, respectively; and '*e*' and '*f*' are the empirically derived intercept and slope coefficients from regression. Using force gage measurements from five different streams, *Johnston et al.* [1998] characterized the values of F_d/F_g for a D_i as log-normally distributed with no difference in variance between grain size classes. However, the variation in the frictional resistance of water-worked grains at different locations along a natural gravel bed has not been studied.

The variation in frictional resistance to particle entrainment along a channel is worthy of research most notably because the mobility of gravel-beds has been found to be more variable than previously thought [*Buffington and Montgomery*, 1997; *Mueller et al.*, 2005]. Factors that have been found to correspond to differences in mobility of gravel-

beds include differences in grain protrusion [*Fenton and Abbott*, 1977; *Kirchner et al.*, 1990], packing [*White*, 1940], sand content [*Wilcock*, 1998], sorting [*Wiberg and Smith*, 1987; *Buffington et al., 1992*; *Johnston et al.*, 1998; *Clayton*, 2010], and channel geometry [*Lamb et al.*, 2008]. Measuring the resistance to entrainment under variable sedimentological and hydraulic conditions should provide insight on these variables influence on entrainment mechanics.

The aforementioned measure of frictional resistance does not account for the effectiveness of the flow forces acting on the bed that are responsible for displacing a grain. Typically, the force of the flow that is required to entrain grains on the bed is quantified using time- and space-averaged shear stress T acting on the bed [*Shields*, 1936; *Buffington and Montgomery*, 1997]. *Shields* [1936] provided a theoretical-based relationship between the T value and the D to a dimensionless shear stress, referred to as the Shields stress T^* such that:

$$T^* = T/[Dg(\rho_s - \rho)] \quad (3)$$

where g is the gravitational acceleration, and ρ and ρ_s are the water and grain density, respectively [*Shields*, 1936]. The T value at which the grain will begin to move is referred to as the critical shear stress T_c and when used in the numerator of (3) provides the T_c^* for the *grain*, another measure of grain resistance. *Shields* used (3) to describe a constant T_c^* value for unisize beds of gravel size grains, thereby providing a practical tool for predicting the mobility of a bed.

More recently it has been found that on mixed beds the constant T^* is not a consistent predictor of the onset of entrainment of the various grain sizes. In the case where $T_{c,i}$ or $T_{c,i}^*$ is used to indicate a critical value for the *bed*, it refers to the T at which entrainment

of the most easily dislodged grains begins for the population of grains of size D_i. *Parker and Klingeman* [1982] found that on beds of mixed grain sizes the $T_{c,i}$ values are more nearly equal between D_i and therefore not well predicted by (3). Empirical data has been used that demonstrates an inverse relationship between $T^*_{c,i}$ calculated from (3) and the ratio of the grain size of interest and the median grain size of the bed, D_i/D_{50}, such that:

$$T^*_{c,i} = \alpha(D_i/D_{50})^{-\beta} \quad (4)$$

where α and β are the empirically determined intercept and exponent from regression, respectively [*Parker et al.*, 1982; *Andrews*, 1983]. The coefficient α provides the $T^*_{c,50}$ value, which has been found to be less variable than the $T^*_{c,i}$ value for smaller and larger grain sizes [*Wilcock and Southard*, 1988], thereby making it seemingly useful for comparing different beds. However, a compilation of eight decades of research from flumes and natural riverbeds has revealed measurements of α that vary by an order of magnitude [*Buffington and Montgomery*, 1997]. The exponent β is referred to as the "hiding factor" because it describes the degree to which $T^*_{c,i}$ is a function of the relative sizes of D_{50} and D_i, reflecting the exposure of the grains to the flows forces [*Andrews*, 1983; *Buffington and Montgomery*, 1997; *Whittaker and Potts*, 2007]. Equal $T_{c,i}$ between grain sizes are indicated by β=1, while $T_{c,i}$ values that are dependent on D_i and a constant $T^*_{c,i}$ in (3) are indicated by β=0. In general, reported β values from gravel beds typically range between 0.6 and 1, which indicates a closer approximation to equal T_c values with changing D_i [see compilation of documented hiding functions in *Buffington and Montgomery*, 1997]. Therefore, because of the demonstrated variation in the $T^*_{c,i}$ it is necessary to measure its value in order to predict entrainment.

However, the time- and space-averaged bed shear stress T that is typically used to calculate $T_{c,i}^*$ from (3) does not accurately account for the total applied shear stress τ acting on an individual grain that is responsible for its entrainment. *Celik et al.* [2010] demonstrated that fluctuations in the flow velocity in excess of the time-averaged velocity are associated a greater probability of grain entrainment. It follows that the total applied force acting on the grain must include the effects of fluctuating flow velocity. Furthermore, the flow forces acting on the bed are differentially applied to grains such that a larger grain protruding higher into the flow field will experience higher velocities and greater force as compared to a smaller grain than is suggested by a spatially averaged shear stress. Therefore, simple force balance equations that calculate the total force required to entrain a grain from frictional resistance must include the sum of direct forces acting on the grain, thereby providing the critical *applied* shear stress for a grain τ_c as opposed to a time- or space-averaged value.

Wiberg and Smith [1987] derived such a force balance model that predicts the τ_c^* for a grain as a function of its ϕ value and an unscaled, time-averaged flow velocity profile. Here, "time-average" refers to the average geometry of the profile over time and because it is unscaled it does not require input of measurements of the critical flow strength. Instead, the only value required that describes the "critical" condition is provided from the ϕ measurement. The model uses the assumption of a vertical profile of average velocity to predict the lift and drag forces required to displace a grain from its exposure to flow.

Wiberg and Smith [1987] and *Johnston et al.* [1998] compared this model's predictions of $\tau_{c,i}^*$ with the transport-based field measurements of $T_{c,i}^*$ reported by

Andrews and Erman [1986] and demonstrated correspondence between the measurements. However, there are reasons to believe the correspondence may be deceptive. First, *Wilcock and McArdell* [1997, figure 5] found explicitly that transport-based values of $T_{c,i}^*$ are greater than values produced from entrainment-based measurements using tracer grains, thereby suggesting that the $\tau_{c,i}^*$ values would also be expected to be less than the transport-based methods. Second, *Andrews and Erman* field measured T_c^* values were time-averaged shear stresses that do not include the effect of fluctuating flow velocity, while the model predicts the total applied τ_c^* value that should be greater than a time-averaged value. Third, both of the aforementioned studies relied on a drag coefficient C_D of 0.4 to 0.5 based on the settling velocity of spheres [*Schlichting*, 1979], whereas *Nelson et al.* [2001] and *Schmeekle et al.* [2007] more recently used a force transducer to obtain a drag coefficient of ~0.9 for gravel particles on a gravel bed. Each of these three important factors is significant in their effect on the predicted τ_c^*. This study incorporates these factors and while explicitly acknowledging the difference between averaged and total applied shear stress values when comparing the measurements and predictions of a grain's resistance to entrainment.

This study uses force gage measurements of ϕ and the *Wiberg and Smith* [1987] theoretical physics-based model to evaluate the variability in grain resistance from *in situ* gravel and cobble on bar forms along a 10 km reach of the San Joaquin River. This chapter adds to the limited body of documented *in situ* measurements of grain resistance, which are used to determine whether the measures of grain resistance vary significantly with differences in grain sizes, sand content, sorting, and flow velocities. Second, the different types of grain resistance measurements are evaluated to determine if they

provide a predictable mean and variance thereby allowing more robust methods to compare the variability in grain resistance between sites. Finally, I validate the *Wiberg and Smith* [1987] force balance model predicted $\tau^*_{c,i}$ values by comparing them to tracer entrainment results from Chapter 1 that were collected local to the sites where I surveyed the frictional resistance of grains. In doing so, I illustrate the correspondence between the fluctuating flow velocity and the difference between the T_c values and the *Wiberg and Smith* force balance model predicted τ_c values.

B. Study Sites

This study was performed on the San Joaquin River below Friant Dam (at river kilometer, Rkm, 430.5), near Friant, California (Figure 1, left). The study reach is gravel-bedded with a reach average slope of 0.0007 and a bankfull channel capacity of 42 m^3/s. Since the dam was installed in the 1940s, sediment from upstream has been impounded by the reservoir and the majority of the river flow has been diverted as part of the U.S. Bureau of Reclamation's Central Valley Project. The diversions have resulted in order of magnitude decreases in the base and average annual peak flow as compared to pre-dam conditions. As previously mentioned, several qualities of riverbeds and channels have been suggested to influence gravel-bed mobility. Here, the altered flow regime and unknown extent to which the subsequent adjustment to channel geometry and texture have equilibrated increase uncertainty about the current mobility of the bed material. Because the impetus for this research is driven by efforts to manage salmon spawning habitat [*Kondolf and Wilcock*, 1996; *Wilcock et al.*, 1996], this study focused on gravel bars that have suitable texture, flow velocity and depth for salmon spawning and where bed material entrainment should provide beneficial maintenance to their habitat.

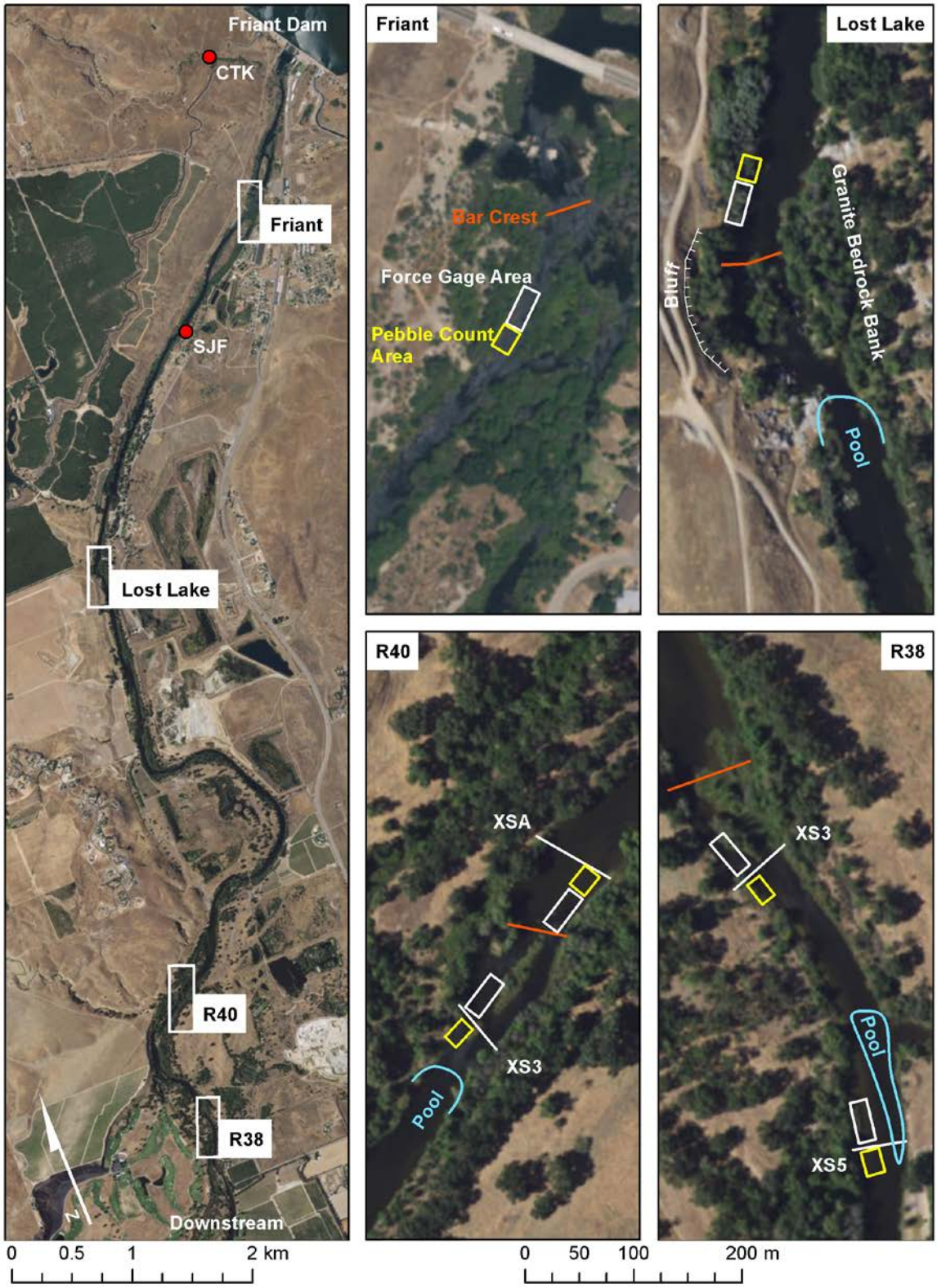

Figure 1: Study reach and site maps. Reach map (left) showing extent of each site subplot, as well as stream gages on the San Joaquin River (SJF) and a tributary, Cottonwood Creek (CTK). Subplots (right) indicate site identification, the bar crests (red line), pools (blue line), the bluff and bedrock bank at the Lost Lake site, and the locations of the force gage surveyed areas (white, rectangle) and their pebble count area

(yellow, smaller rectangle). For sites R40 and R38 the nearest monitoring cross-section is delineated as it is used in the site identification and for comparison with the companion study [Chapter 1]. The Little Dry Creek (LDC) confluence with the main-stem is also indicated.

Six locations were selected for force gage surveys of the gravel bed. At each location, areas were delineated where the bed material exhibited a consistent bed texture that was generally representative of the location and where base flow conditions allowed for easy access and low flow velocity (<0.3 m/s). Three areas were positioned downstream of a bar crest in riffle sections (Friant at Rkm 429.2, R40XS3 at Rkm 420.8, and R38XS3 at Rkm 419.6), two are upstream of a bar crest within pool tail-out sections (Lost Lake at Rkm 425.8 and R40XSA at Rkm 421.0), and another is located along a sandy gravel inside margin of a gentle bend (R38XS5 at Rkm 419.2). In general, the riffle areas exhibited a more packed grain structure with some imbricated grains and deeper intervening pockets between the larger grains. The pool tail-out areas generally exhibit greater protrusion of larger grains as they are resting on a more planar bed, and the sandy margin area is planar with sand supported gravel and cobbles whose grain tops, regardless of grain size, are nearly level with the bed. All sites have banks composed of alluvium except the Lost Lake site where flow is confined by higher banks as the river left bank is granitic bedrock and the right bank is an erosional scarp of a large bluff.

C. Methods

1. Grain Size Characterization

I performed pebble counts [*Wolman*, 1954] to define the grain size distribution of the bed surface immediately downstream of force gaged areas (Figure 1). I segmented pebble count areas into 3 m lateral widths by 10 m longitudinal lengths with the aid of a measuring tape that stretched across the channel along a boundary between the force gage

survey area and the pebble count area. In each pebble count segment I randomly selected at least 100 grains in a grid-like manner by side stepping after each sampled grain. I measured each grain using a steel template with standard ½-phi scale, square holes (gravelometer). The results of each pebble count segment are combined for each area and presented in Figure 2 and Table 1.

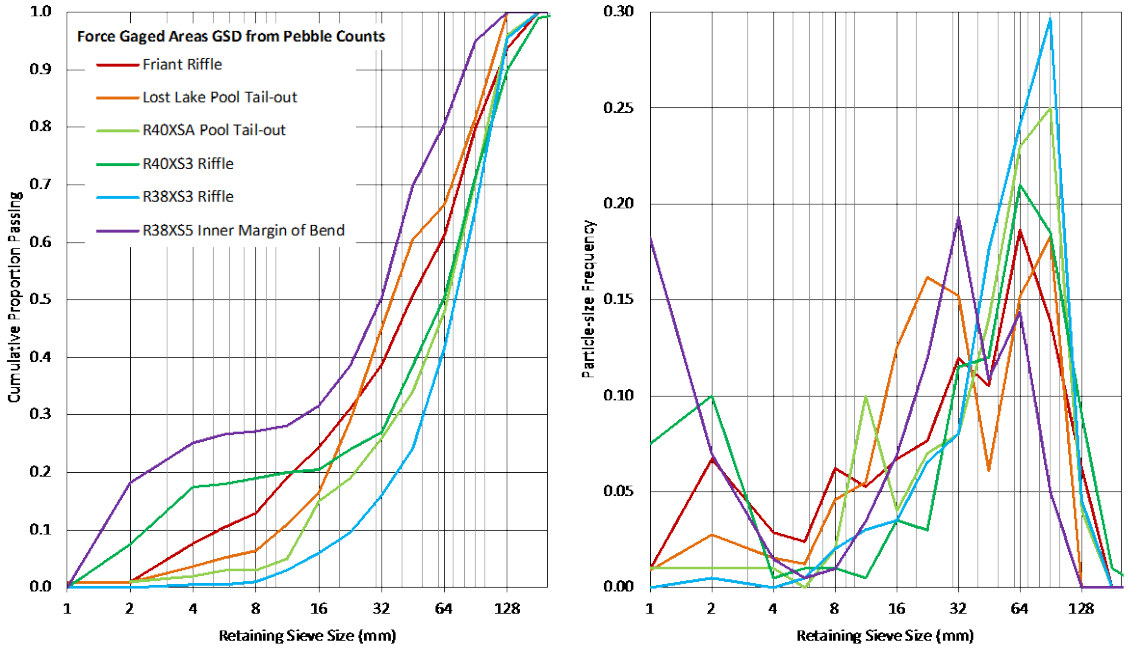

Figure 2: Grain size distributions from pebble counts associated with each force gage surveyed area. Cumulative distributions (left) indicate the proportion of the sampled grains that passed through each sieve size. Frequency distributions (right) indicate the fraction of the sample retained by each sieve size.

Although sediment supply is severely disrupted by the dam, several sources are present upstream of the study sites including a small tributary (Cottonwood Creek) upstream of the Friant riffle, some gully and bank erosion downstream of the Lost Lake site and upstream of R40, local bank erosion at R38, and a larger tributary (Little Dry Creek) between R38XS3 and R38XS5 (Figure 1). Presumably as a result of these sources, sand is present as veneers over the gravel-bed within the pools and is apparent as a secondary mode of sand size grains at site R38XS5 that is along the margin of a pool

(Figure 2). It is noted that site R38XS5 had the most sand and that site R40XS3 also had abundant sand on the riffle bed during this study. Although there is a general trend of decreasing D_{50} and increasing sand content on the riffles with increasing distance downstream of Friant Dam, the grain size distributions at the study sites do not exhibit this pattern (Table 1) but instead reflect the variability in the texture along this 10 km reach.

Table 1: Pebble count grain size distribution statistics.

Pebble Counts Site	D_{50} mm	D_{16} mm	D_{84} mm	Sorting phi-scale	Count #
Friant Riffle	44	9.5	100	1.7	209
Lost Lake Pool Tail-out	36	16	94	1.3	328
R40XSA Pool Tail-out	66	17	108	1.3	100
R40XS3 Riffle	63	3.6	114	2.2	200
R38XS3 Riffle	72	32	112	0.9	199
R38XS5 Sandy Margin	32	1.8	69	2.3	202

2. Frictional Resistance Measurements via Force Gage

To measure the minimum F_d capable of displacing *in situ* grains as a function of grain size, I divided the grain sizes into five classes whose retaining sieves were 32, 45, 64, 90, and 128 mm. The detection limit of the smallest force gage set the size limit of the smallest class that could be measured while the upper size limit was only limited by the largest grain sizes present on the bed (<180 mm). I used the force gages to measure approximately 100 grains of most of the size classes as *Johnston et al.* [1998] determined this was a sufficient sample size for efficiently minimizing the standard error of the estimate of the average frictional resistance of a grain size class.

I used Chatillon^{TM} push-pull, spring-resistant force gages to measure the F_d value of individual grains. I had a selection of gages with a maximum capacity and graduation accuracy of 1.00$\pm$0.01 kg, 2.25$\pm$0.05 kg, 4.50 $\pm$0.05 kg, 9.0$\pm$0.1 kg, and 18.0$\pm$0.2 kg.

At each site, measurement began at the upstream end of the survey area (Figure 1). I randomly selected each gaged grain by averting my eyes while gently pointing to the bed until my index finger detected a grain that I estimated to be greater than or within the 22.6 mm size class. I then examined the selected grain through an underwater viewing scope for its size and position to assess the appropriate capacity force gage. Selecting the appropriate gage was a balance between ensuring it had the capacity to measure the maximum force applied while at the same time minimizing the gage capacity so as to maximize the precision. Upon gage selection, I positioned the tip of the gage on the upstream side of the grain, oriented the gage downstream through the centroid of the grain in a bed parallel manner, and pushed until the grain moved from its resting position. The gage registered the maximum force applied. I measured the mass of the gaged grain to the nearest gram using a digital scale or, for grains >6 kg, by using a hanging scale ($\pm$0.1 kg) and bucket. I repeated this process for each randomly selected grain along an approximately 1 m wide longitudinal strip within each subplot. Upon completion of each strip, another was begun at the upstream end of the survey area and adjacent to the previous strip.

Other recorded attributes of the gaged grains included their size class measured with the gravelometer; longest, intermediate, and shortest axes (A-, B-, and C-axis, respectively) measured using calipers ($\pm$1 mm); axis parallel to the flow direction; axis normal to the bed; and a descriptive characterization of the greatest resistance to forces on the bed offered by neighboring particles. In order of most to least protection offered against displacement, these characterizations were: embedded, partially but loosely buried, imbricated, braced, sheltered, and loosely exposed (data are presented in

Appendix A). Because embedded and partially buried grains are likely to be loosened and uncovered before becoming entrained, these support types are generally assumed not to be indicative of the conditions in which they would be displaced and thus their measured frictional resistance is less meaningful to this study. Unless otherwise explicitly stated, embedded grains were excluded from the analysis and buried grains were only included at the R38XS5 site. Unlike the other sites, the gaged grains at R38XS5 were more often partially buried in loose sand that appeared to offer negligible support to the gaged grains thereby suggesting that the gravels might mobilize in the presence of the surrounding sand. Therefore, the force gage measurements of the gravel and cobble that were loosely buried in sand at R38XS5 were included in the analyses. I also used these characterizations of resistance to assess their relationship with the frictional resistance measurements, thereby providing a general understanding of how these visual observations relate to the mobility of a bed. The grain size and resistance data of the gaged grains are summarized in Appendix B, Table B-1.

3. Force Balance Predicted Resistance to Flow

I used the measurements collected during the force gage surveys with the force balance model provided by *Wiberg and Smith* [1987] to predict the τ_c^* of gaged grains, such that:

$$\tau_c^* = \frac{2}{(C_D A_x D_n / V)} \times \frac{1}{\langle f^2(z/z_o)\rangle} \times \frac{(\tan\phi \cos S - \sin S)}{[1+(F_L/F_D)\tan\phi]} \quad (5)$$

where S is the stream-wise slope of the bed; the drag coefficient C_D is 0.9 [*Nelson et al.*, 2001; *Schmeekle et al.*, 2007]; A_x is the cross-section of the grain that is normal to flow; D_n is the nominal diameter of the grain, equal to the diameter of a spherical grain with the same mass and ρ_s (2.65 cm^3/g); and V is the volume of the grain (V = mass/ρ_s). The expression within the angled brackets is the squared function for the cross-sectionally

averaged logarithmic vertical profile of velocity, u_z, with height above the bed z and the bottom roughness parameter z_o=$D_{50}/30$, such that in rough flow:

$$u_z = u_* f(z/z_o) = u_* \frac{1}{\kappa} \ln(z/z_o) \quad (6)$$

where $u_* = (\tau/\rho)^{0.5}$ is the shear velocity and κ=0.407 is von Kármán's constant. The drag and lift forces, F_D and F_L, are also dependent on the velocity profile such that:

$$F_D = \frac{1}{2} C_D \tau_c A_x \langle f^2(z/z_o) \rangle \quad (7)$$

$$F_L = \frac{1}{2} C_L \tau_c A_z [f^2(z_T/z_o) - f^2(z_B/z_o)] \quad (8)$$

where C_L is the lift coefficient of 0.2 [*Wiberg and Smith*, 1985], A_z is the cross-sectional area of the grain that is parallel to the bed, and z_T and z_B are the height above the bed of the top and bottom of the grain, respectively. The elevation datum, z=0, is considered to be the average elevation of the bed surface [*Wiberg and Smith*, 1987, figure 1].

The heterogeneity of bed grain sizes is reflected in several components of equation (5). First, the particle size of interest, D_n, appears in the denominator of the first term; secondly, the particle size of the surrounding bed influences the flow velocity through its effect on z_o in the second term [*Egiazaroff*, 1965; *Wiberg and Smith*, 1987]. Finally, the $\tan \phi$ in the third term reflects the interaction between the size of the particle of interest and the size of its downstream neighbor [*Wiberg and Smith*, 1987, figure 1] as well as the frictional resistance from its unspecified surrounding neighbors. In the original model, this frictional coefficient is specified as reflecting the relative size of the particle of interest and of the characteristic, uniform size of the population of bed particles.

4. Fluctuations in the Shear Stress

Testing the *Wiberg and Smith* [1987] force balance model's predictions of τ_c^* is a primary goal of this study. To accomplish this, I rely on the tracer entrainment results from

Chapter 1 to compare with the predictions. However, because equation (5) predicts the instantaneous dimensionless critical shear stress τ_c^* that can begin to move the gaged grains, it is different from the time-averaged value, T_c^*, used to quantify the tracers mobility. The T_c^* values were computed from (3) using a T value provided from a 2D flow model (see Chapter 1). In order to explain the difference between τ_c^* and T_c^*, I used measurements of u_z collected at three of the force gage survey sites (R40XSA, R40XS3, and R38XS3) where tracer entrainment had also been monitored. I measured flow velocity using a Sontek^{TM} S5 acoustic Doppler profiler (ADP) that floated over a position for approx. 90 s while measuring stream-wise u_z at multiple depths at 1 s intervals from its downward-directed acoustic beams. From each of these instantaneous 1 s intervals an array of velocity measurements and their depths provided a vertical profile of flow velocities. I used each profile to fit the power law velocity profile proposed by *Chen* [1991] that is derived from the law of the wall logarithmic profile, which provides the depth-averaged instantaneous flow velocity $\bar{u}$, where a single bar indicates the instantaneous depth-averaged value. From the compilation of ~90 $\bar{u}$ measurements at a position, I computed the time- and depth-averaged velocity $\bar{\bar{u}}$, distinguished by two bars.

From each sample of the field measured $\bar{u}$ and $\bar{\bar{u}}$, I calculated approx. 90 instantaneous shear stresses $\bar{\tau}$ and one time-averaged shear stress $\bar{\bar{\tau}}$. This was accomplished by solving for $\bar{u}_*$ and $\bar{\bar{u}}_*$ from the following relationships:

$$\frac{\bar{u}}{\bar{u}_*} = \frac{1}{\kappa}\ln\left(\frac{h}{ez_o}\right) \tag{9a}$$

$$\frac{\bar{\bar{u}}}{\bar{\bar{u}}_*} = \frac{1}{\kappa}\ln\left(\frac{h}{ez_o}\right) \tag{9b}$$

where here *e* refers to the base of the natural log and *h* is the flow depth [*Wilcock*, 1996]. The $\bar{\tau}$ and $\bar{\bar{\tau}}$ values are calculated by using the relationship between u_* and τ ($u_* = (\tau/\rho)^{0.5}$) and algebraically reorganizing (9a) and (9b) to solve for $\bar{\tau}$ and $\bar{\bar{\tau}}$, such that:

$$\bar{\tau} = \rho\left[\frac{\bar{u}\kappa}{\ln\left(\frac{h}{e z_o}\right)}\right]^2 \tag{10a}$$

$$\bar{\bar{\tau}} = \rho\left[\frac{\bar{\bar{u}}\kappa}{\ln\left(\frac{h}{e z_o}\right)}\right]^2 \tag{10b}$$

For each sample of approx. 90 $\bar{\tau}$ values, I used a truncated histogram of the frequency of the computed $\bar{\tau}$ values percentage in excess of the $\bar{\bar{\tau}}$ value (i.e., $100\%[(\bar{\tau}/\bar{\bar{\tau}}) - 1]$) to compute the root mean squared deviation (RMSD) (Appendix C). Because the distributions are approximately normal, the RMSD is the standard deviation of the $\bar{\tau}$ distribution. I used the standard deviation of $\bar{\tau}$ and the $\bar{\bar{\tau}}$ value from each sample to approximate values of $\bar{\tau}$ for a given percentile of their distributions. For each sample I computed an index of shear stress fluctuation (i.e., $100\%\left(\bar{\tau}_p - \bar{\bar{\tau}}\right)/\bar{\bar{\tau}}$, where subscripted '$p$' refers to a specific percentile value of $\bar{\tau}$) and plotted it as a function of $\bar{\bar{\tau}}$. I then included a plot of a similar relationship between the *Wiberg and Smith* [1987] force balance model predicted τ_c and the tracer entrainment measured T_c with an analogous determination of their percentage difference (i.e., $100\%(\langle\tau_{c50}\rangle - T_{50,[50]})/T_{50,[50]}$, where subscripted '50' refers to the value for the median grain size and subscripted '[50]' refers to the value of the variable that is capable of producing 50% entrainment) as a function of $T_{c50,[50]}$. The indexes were compared by varying the percentile of the index of shear stress fluctuation until it reasonably agreed with the index values provided by the differences from the force balance predictions with tracer entrainment. This comparison

between the time-averaged values and instantaneous values provides an assessment of the correspondence between the model predictions and the distribution of instantaneous flow fluctuation that contributed to the applied forces that entrained the tracer grains.

5. Analysis

My approach to describe the variability in grain resistance with location was to seek parameters that describe the distributions of the measurements and compare those parameters between grain sizes and locations. To do so, I considered the distributions of the measurements of resistance (i.e., ϕ_i, $\left(F_d/F_g\right)_i$, and $\tau_{c,i}^*$) and analyzed for consistency in their central tendency and variance. I used graphical methods to compare with the theoretical normal distribution as well as non-parametric testing to provide quantitative assessments of statistically significant differences from the theoretical distribution. Measurements that indicated non-random order were subsequently analyzed with: ordinary least squares (OLS) regression and a graphical approach to assess the trend in variance between the distributions; OLS regression and analysis of variance (ANOVA) to examine strength of correlations in the parameters of the distributions as functions of grain size; and analysis of covariance (ANCOVA) to test for significant differences between these trends at different sites. Lastly, I compared the predicted τ_c^* values to tracer-measured proportions of D_i entrained as a function of T^* to validate the force balance model, and discuss how the expressed variation is controlled by the bed and hydraulics at the sites.

D. Results

1. Frictional Resistance Variation

The distribution of the measured force of frictional resistance to movement values ($\phi_i, F_d/F_g$) is suggestive of the range of hydraulic forces necessary to entrain grains. The least resistant grains should be indicative of the grains first moved by the flow [*Miller and Byrne*, 1966; *Kirchner et al.*, 1990; *Buffington et al.*, 1992; *Johnston et al.*, 1998], and the most reinforced grains on the bed surface characterize the maximum flow strength necessary to entrain all the grains for a given grain size fraction. The range defined by these limits should define the range of the bed's resistance to movement.

a) Friction Angle

I began by examining the distribution of the ϕ_i values using quantile-quantile (q-q) plots. Overall, the within size class variability in the ϕ_i values ranges from approximately 10° to 90°. This range is comparable to the *Johnston et al.* [1998] force gage results but narrower than *Buffington et al.* [1992]. It is possible for a ϕ value to be greater than 90° when measured using tilting boards, as the grains can become lodged against grains that slightly overhang them [see *Kirchner et al.*, 1990 and *Buffington et al.*, 1992]. However, force gaging grains under this condition results in larger F_d/F_g values that when solving equation (1) for ϕ limits the range to ϕ values of $0° < \phi < 90°$ and effectively skews greater ϕ values as they asymptotically approach 90° with increasing F_d/F_g. As a result, the force gage measured ϕ values enter the *Wiberg and Smith* [1987] model more appropriately than values of ϕ>90° that produce tan ϕ values indicating declining frictional resistance with increasing ϕ. The effect of this is observed in q-q plots that do not strongly fit a normal distribution (Appendix E). Most of these plots illustrate a skew

in the uppermost quartile range of the data, indicating that they cannot be reliably predicted by a symmetrical distribution to describe the variability in grain resistance to entrainment within a grain size fraction.

Following previous research that consistently found average ϕ_i values to vary inversely with grain size by fitting the model to the variables as described by (2) [*Miller and Byrne,* 1966; *Li and Komar,* 1986; *Kirchner et al.*, 1990; *Buffington et al.*, 1992; *Johnston et al.*, 1998], I also examine the data for this trend. In general, the fitted trends in the median ϕ_i as a function of D_i/D_{50} generate values of *f* that are less than most of the previous researchers' findings (Appendix D, Table D-1). This indicates that the frictional resistance of the grains at the study sites is more similar between grain size fractions than have been measured on other beds thereby emphasizing the large variation in grain-to-grain interactions between sediment mixtures. The consistently low *f* values suggest this result is characteristic of the studied reach. At the same time, five of the six sites have values of this exponent that indicate a decreasing trend, as was found by the previous researchers. Only the median ϕ_i values from the sandy margin at R38XS5 increase with D_i/D_{50}, but this result is discounted by the ANOVA test results that yield a *p*-value = 0.12 thereby indicating that the trend is not significantly different from horizontal at a significance level of 0.05. The results from the Friant and R40XSA sites also indicate a lack of significance in their regression models (ANOVA p-values > 0.26) thereby emphasizing their low *f* values. Furthermore, the strength of the relationship between the $\phi_{50,i}$ and the D_i/D_{50} from these three sites is low (R^2<0.60), suggesting that the dependent variable is not a strong function of the grain size.

b) Coefficient of Friction

Frequency distributions of F_d/F_g values for a given D_i at a site are negatively skewed, thereby suggesting that they are log-normally distributed as was found by *Johnston et al.* [1998]. Hence, I also used the natural log-transformed F_d/F_g measurements to characterize the distribution of each D_i, for which q-q plots indicated are well approximated by the theoretical normal distribution (Appendix E). The Kolmogorov-Smirnov, K-S, nonparametric test indicated that all but one sample (R38XS5 45mm, *p*-value=0.04) of $\ln(F_d/F_g)_i$ values are not significantly different from the theoretical distribution with a significance level of 0.05 (Appendix E, Table E-1). Furthermore, in all but five samples of $\ln(F_d/F_g)_i$, the K-S test *p*-values are greater than those of the corresponding ϕ_i distribution K-S test results, indicating that distributions of $\ln(F_d/F_g)_i$ have a lower probability of difference from the theoretical distribution than ϕ_i distributions. These results support the findings of *Johnston et al.* [1998] and indicate that the distribution of $(F_d/F_g)_i$ can be approximated from the mean and standard deviation of the $\ln(F_d/F_g)_i$ distribution.

Power functions such as equations (2) and (4) are used to describe bed mobility as a function of D_i/D_{50} and typically produce strong inverse trends and R^2 values [see Appendix D, Table D-1; *Johnston et al.*, 1998; *Buffington and Montgomery*, 1998]. An analogous relationship using OLS regression to fit natural log functions to the mean of the natural log-transformed values, such that:

$$\langle ln(F_d/F_g)_i \rangle = a \ln(D_i/D_{50}) + b \qquad (11)$$

where angle brackets refer to the mean values of the term contained within, and 'a' and 'b' are the fitted coefficients of the regression, found a similar inverse trend at most of the sites (Figure 3), suggesting the frictional resistance provides a strong control on bed mobility. The same approach illustrates the trend of the variance with changes in relative grain size through the standard deviation of $\ln\left(F_d/F_g\right)_i$ as a function of the D_i/D_{50}, such that:

$$stdev\ of\ \ln\left(F_d/F_g\right)_i = c\ln(D_i/D_{50}) + d \tag{12}$$

where 'c' and 'd' are the fitted coefficients of the regression. In this case an inverse trend in the standard deviation with D_i occurs at all sites and is statistically significant at all sites except Friant and Lost Lake (p-values>0.07). This differs from the observations of *Johnston et al.* [1998] that found no trend in the variance of $\tan\phi_{i[50]}$ with D_i/D_{50}.

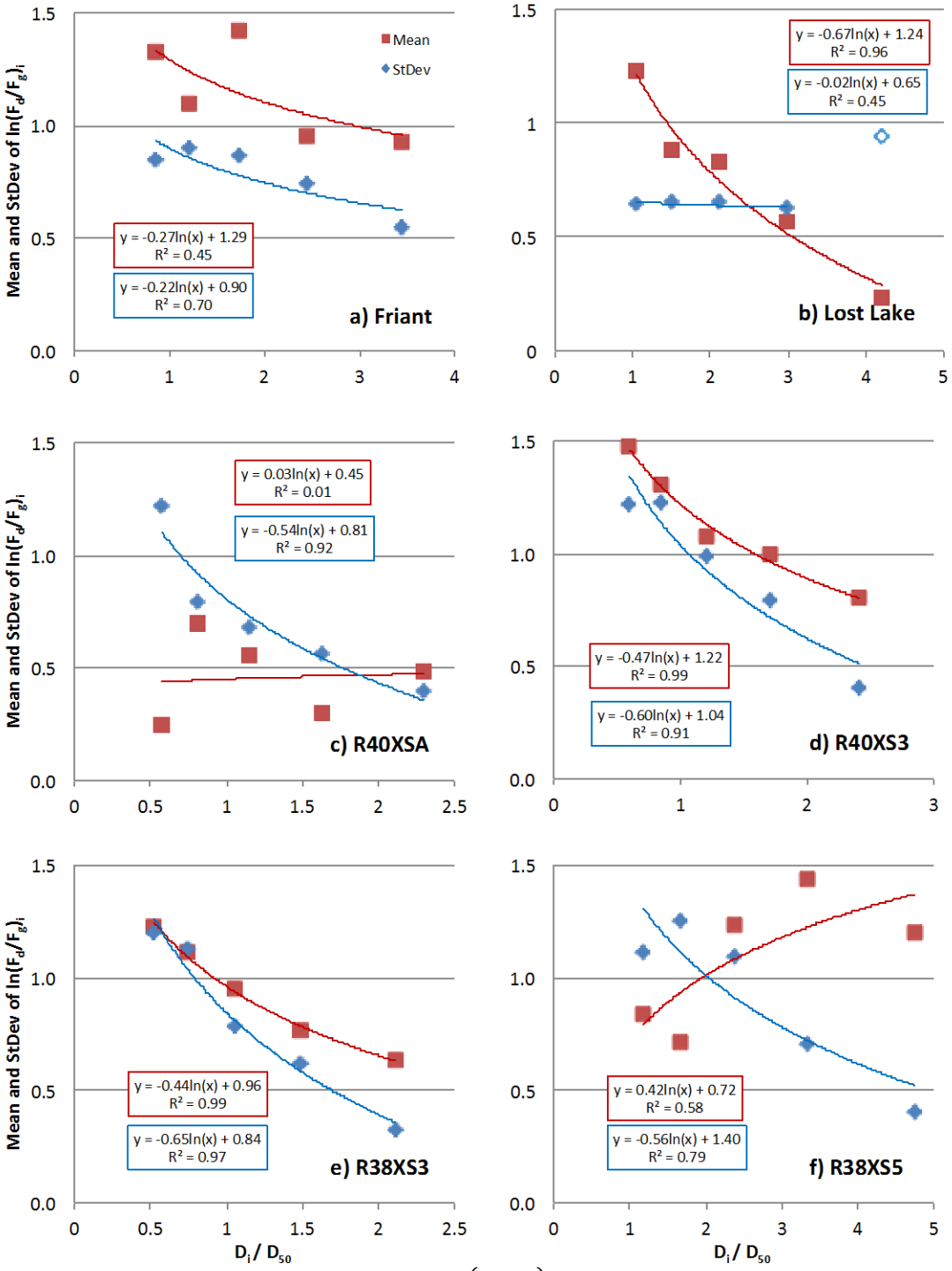

Figure 3. The parameters of the distributions of $ln\left(F_d/F_g\right)_i$ as functions of relative grain size. The mean values are colored red and the standard deviation values are blue. The OLS logarithmic function regression equation and trend line are provided with each plot and parameter.

The fitted trends to the $\ln\left(F_d/F_g\right)_i$ distribution parameters as functions of D_i/D_{50} demonstrate similarities and differences between the sites. Most notably, the riffle sites

(Friant, R40XS3, and R38XS3) all show inverse relationships for both mean and standard deviation. These relationships were strong (R^2>0.90) and statistically significant (ANOVA *p*-values<0.02) at the R40XS3 and R38XS3 sites, with the exception of the Friant site mean (R^2=0.45, *p*-value=0.22) and standard deviation (R^2=0.70, *p*-value=0.078) of $\ln\left(F_d/F_g\right)_i$ (Table 2). Also, the magnitude of the $\langle\ln\left(F_d/F_g\right)\rangle_{50}$, as indicated by the intercept coefficient b, tends to be greater at the riffle sites than at the other sites. However, the pool tail-out at Lost Lake site has an intercept value that is within the range of the riffle sites, thereby suggesting that this site bears some resemblance to the riffles.

Table 2. Intercept and slope coefficients of equations (11) and (12) that describe the trend in the normal distribution parameters of $\ln(F_d/F_g)_i$ as functions of D_i/D_{50} (see Figure 3). Standard error (±SE) of the coefficients and ANOVA test results probability (*p*-) values of the null hypothesis that the fit of the intercept-only model and the OLS regression model are equivalent; *p*-values less than a significance level of 0.05 indicates the model provides a better fit and a statistically significant trend as a function of D_i/D_{50}.

Site	Intercept±SE	Slope±SE	R^2	*p*-value	n
$\langle\ln\left(F_d/F_g\right)_i\rangle = a\ln(D_i/D_{50}) + b$					
Friant	1.29±0.19	-0.270±0.174	0.447	0.217	5
Lost Lake	1.24±0.09	-0.666±0.077	0.962	3.20E-03	5
R40XSA	0.45±0.22	0.026±0.196	0.006	0.901	5
R40XS3	1.22±0.04	-0.474±0.033	0.985	7.50E-04	5
R38XS3	0.96±0.02	-0.442±0.020	0.994	2.10E-04	5
R38XS5	0.72±0.22	0.416±0.204	0.580	0.135	5
$stdev\ of\ \ln\left(F_d/F_g\right)_i = c\ln(D_i/D_{50}) + d$					
Friant	0.90±0.10	-0.220±0.084	0.699	0.0778	5
Lost Lake	0.65±0.01	-0.021±0.016	0.450	0.329	4
R40XSA	0.81±0.10	-0.537±0.094	0.915	0.0107	5
R40XS3	1.04±0.12	-0.597±0.110	0.908	0.0122	5
R38XS3	0.84±0.07	-0.652±0.064	0.972	2.05E-0.3	5
R38XS5	1.40±0.18	-0.564±0.169	0.787	0.0446	5

The sandy margin and pool tail-out sites did not show these inverse trends in the distribution parameters as a function of D_i/D_{50} and their standard deviation of $\ln\left(F_d/F_g\right)_i$ did not covary with the mean values with changes in D_i/D_{50}. Additionally,

the measurements from the R40XSA and R38XS5 sites yield trends in the mean $\ln\left(F_d/F_g\right)_i$ that are neither statistically significant (p-values>0.13) nor as strongly correlated ($R^2 \leq 0.58$). These results indicate that the frictional resistance at the non-riffle sites is not as consistently dependent on the grain size.

Another similarity between the sites is an inverse relationship of the standard deviation of $\ln\left(F_d/F_g\right)_i$ with D_i. This relationship is statistically significant at four sites but not at the Friant and Lost Lake sites (Table 2). This supports the findings of *Kirchner et al.* [1990] and *Buffington et al.* [1992] who measured a slight decreasing trend in the variance of ϕ_i with grain size, rather than *Miller and Byrne* [1966] and *Johnston et al.* [1998] who characterized the variance in ϕ_i as equivalent between grain size fractions. Using the standard deviation of $\ln\left(F_d/F_g\right)_i$, my results show that the differences in the trends in variance, and lack thereof, appear to reflect real differences in the beds. These results indicate a tendency for the coarser grains to have less variation in their frictional resistance thereby suggesting reduced diversity in pocket geometries with increasing D_i. This should be expected as smaller gravel may rest against smaller or larger grains but with increasing D_i there are fewer larger grains to rest against.

Previous research on frictional resistance reported that the parameters of their distributions were related to grain size sorting σ [*Buffington et al.*, 1992; *Johnston et al.*, 1998]. I evaluate the same variables that were indicated to control the variability in frictional resistance to determine if they provide a possible explanation for the differences between sites. *Buffington et al.* [1992 figure 8] presented an inverse relationship between the median ϕ_i as a function of σ (Appendix D: Figure D-2) while *Johnston et al.* [1998 figure 7] found the average of the standard deviations of $\ln\left(F_d/F_g\right)_i$ to be an inverse

function of σ (Figure 4). Because I found that the standard deviation of $\ln(F_d/F_g)_i$ was not always constant with D_i, I used the *d* values in Table 2 as the dependent variable, which provides estimates of the average standard deviation of $\ln(F_d/F_g)_{50}$, where subscripted '50' refers to the value for the D_{50}, to plot with the data presented by *Johnston et al.* I found direct relationships using OLS linear regressions from both of their proposed relationships with the stronger being that presented by *Johnston et al.* (R^2=0.65). This trend is significantly different from a model without an effect from σ (ANOVA slope coefficient *p*-value=0.007) thereby suggesting that σ is a control on the variance in the frictional resistance. Although the result is contrary to that presented by *Johnston et al.*, the increasing variance in $\ln(F_d/F_g)_{50}$ with increasing σ is plausible as it may be explained by an increase in the variety of grain-to-grain positions that result from more abundant smaller and larger grain sizes.

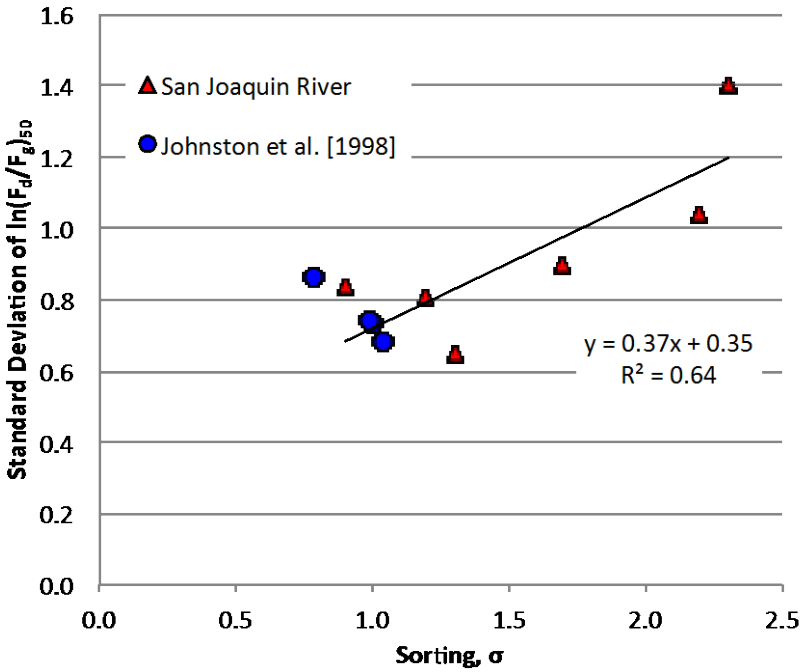

Figure 4. Correlation of the standard deviation of $\ln(F_d/F_g)_{50}$ as a function of the grain size sorting parameter as defined by *Blatt et al.* [1980]. Data points are from this study (n=6) and *Johnston et al.* [1998] (n=4). As was presented by *Johnston et al*. their average standard deviations of $\ln(F_d/F_g)_i$ are used here for the dependent variable. An OLS linear regression trend line is shown for the results of both studies datasets (n=10) (slope coefficient is significantly different from horizontal, *p*-value=0.007).

2. Grain Resistance to Flow

By themselves, the frictional resistance measurements provide the resistance to downstream displacement by a direct force F_d relative to the grain weight. However, flowing water exerts lift and drag forces on a grain that vary depending on the exposure of the grain to the forces exerted by the flow and to the intensity of the hydraulic forces. At the same time, the vertical profile of the flow velocity is affected by bed roughness elements thereby producing variability in the forces applied to different grains [*Wiberg and Smith*, 1987; *Kirchner et al.*, 1990]. In order to assess the resistance to movement of a grain from hydraulic forces acting on the bed, I applied equation (5) using the force gage survey measurements to compute the τ_c^* value for each gaged grain. The resulting

distributions of $\tau^*_{c,i}$ values were examined for normality as was done for the ϕ_i and $\ln\left(F_d/F_g\right)_i$ distributions using the q-q plots (Appendix E) and K-S test (Table E-1).

The distributions of $\tau^*_{c,i}$ values are well described by a normal distribution as the K-S tests indicate all the $\tau^*_{c,i}$ distributions are not significantly different from the theoretical distribution at a significance level of 0.05. This finding supports the tracer entrainment results in Chapter 1 that use the normal distribution to define the trend in the proportion of a D_i entrained with increasing $\overline{T}$. However, this result conflicts with the log-normally distributed frictional resistance as found herein and by *Johnston et al.* [1998]. Furthermore, others have found that transport-based measurements indicate that the amount of a D_i in transport relative to its proportion on the bed increases log-normally as a function of τ^*[*Wu and Yang*, 2004: Figure 15]. Lastly, this finding provides an ability to estimate the forces necessary to entrain bed material within a D_i using the mean and standard deviation of the $\tau^*_{c,i}$ from force gage surveys and encourages their comparison with the $T^*_{c,i}$ measured from tracers with the aspects of the entrainment domain, such as those presented in Chapter 1.

Figure 5 illustrates the cumulative distributions of the computed $\tau^*_{c,i}$ values for each D_i. The plots show that the distributions diverge with increasing τ^* from a nearly common origin. The divergence is such that the $\tau^*_{c,i}$ distributions steepen with increasing D_i, as found by *Buffington et al.* [1992], and that the average $\tau^*_{c,i}$ values, hereafter distinguished as $\langle\tau^*_{c,i}\rangle$, decrease with increasing D_i. Therefore, the force balance model predicts that all the force gaged grain size classes will begin to move at $\tau^*_{c,i}$ values that have a smaller difference than those required to move a given greater proportion of the grain size fractions. Moreover, the results suggest consistent trends in both the average

and standard deviation of the $\tau^*_{c,i}$ values that were not always observed in the frictional resistance measurements.

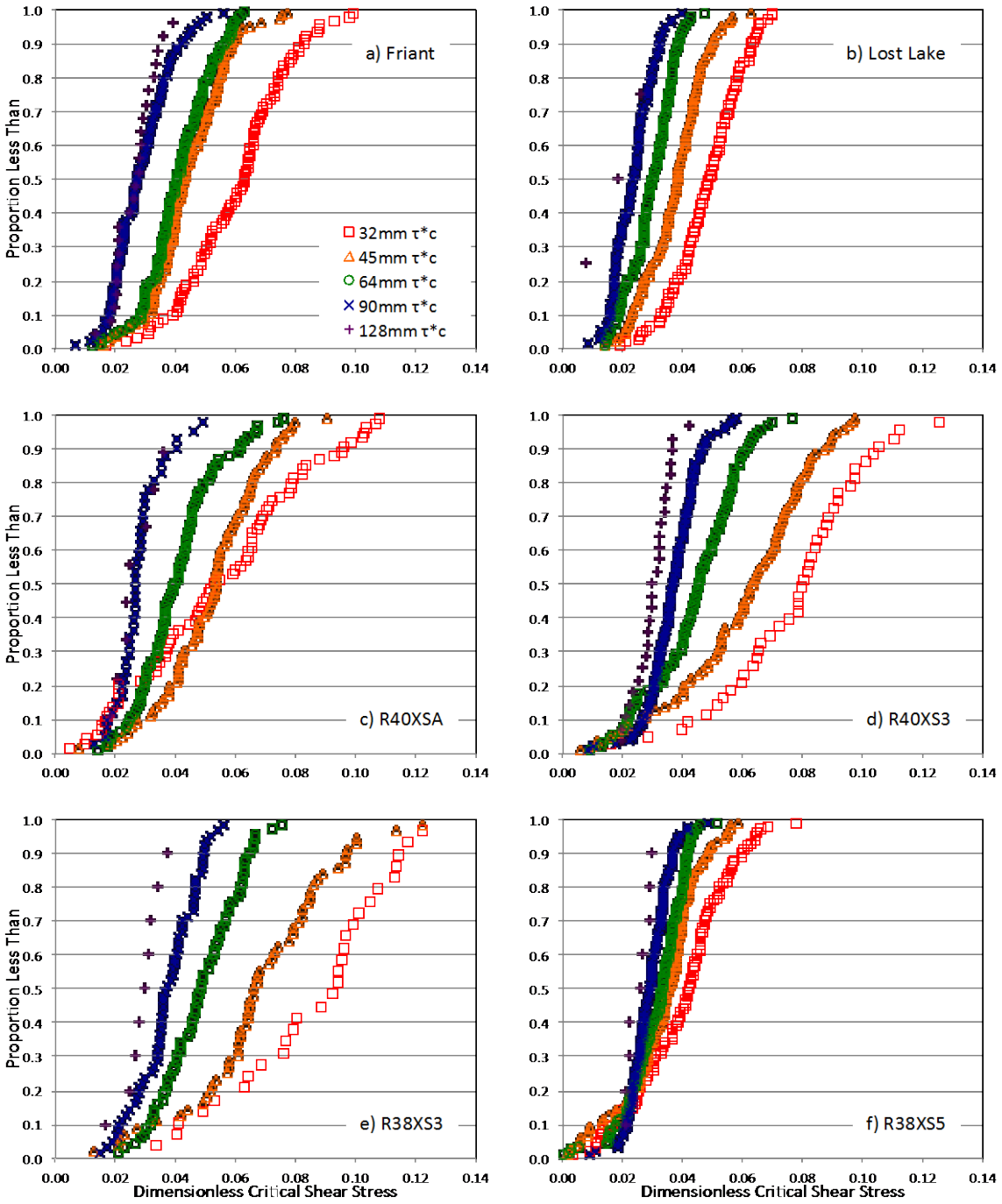

Figure 5. Cumulative distributions of grain resistance to downstream directed forces. Colors and symbols are unique to each grain size class (legend in plot a). Symbols indicate individual force gage measurements.

The systematic nature of the difference between the $\tau_{c,i}^*$ distributions with D_i suggests that both the mean and standard deviation of the distributions are functions of the D_i. The parameter values are fit to power functions using OLS regression that produce the hiding function (4) with the dependent variable equal to $\langle \tau_{c,i}^* \rangle$ (Figure 6). In addition, I use a similar model fit to the standard deviation of $\tau_{c,i}^*$, such that:

$$st.dev.of\ \tau_{c,i}^* = \gamma (D_i/D_{50})^{-\delta} \tag{13}$$

where 'γ' and 'δ' refer to the intercept and slope coefficient values from OLS regression. These models provide statistically significant (ANOVA p-values<0.01) and strong correlations (R^2>0.92) (Table 3).

The trends in both the mean and standard deviation of the $\tau_{c,i}^*$ are inverse functions of D_i/D_{50}. Trends in the $\langle \tau_{c,i}^* \rangle$ values have β values in (4) between 0.3 and 0.8 thereby indicating wide variability between sites that suggests a reach wide function is not appropriate. Values of β less than unity indicate that on average larger grains require greater flow strength to move than smaller grains. Five of the sites have β values between 0.6 and 0.8, which are (i) in agreement with trends in tracer entrainment from Chapter 1, shown on Figure 6c-e, and (ii) within the range commonly observed on gravel beds using transport-based methods [see *Buffington and Montgomery*, 1997]. Only the sandy margin site R38XS5 has a β value that is less than this range. Because the frictional resistance measurements at the Friant, R40XSA, and R38XS5 sites indicate a lack of a significant relationship with D_i, the force balance predicted $\tau_{c,i}^*$ values suggest that the effects of the grain exposure to the flow forces strongly impose the "hiding effect". This is illustrated by the consistent systematic trends on the $\tau_{c,i}^*$ distributions at each site. These effects will

be verified using the equation (5) predicted $\tau^*_{c,i}$ values from the R40XSA and R40XS3 sites and their comparison with the observed tracer entrainment results of Chapter 1.

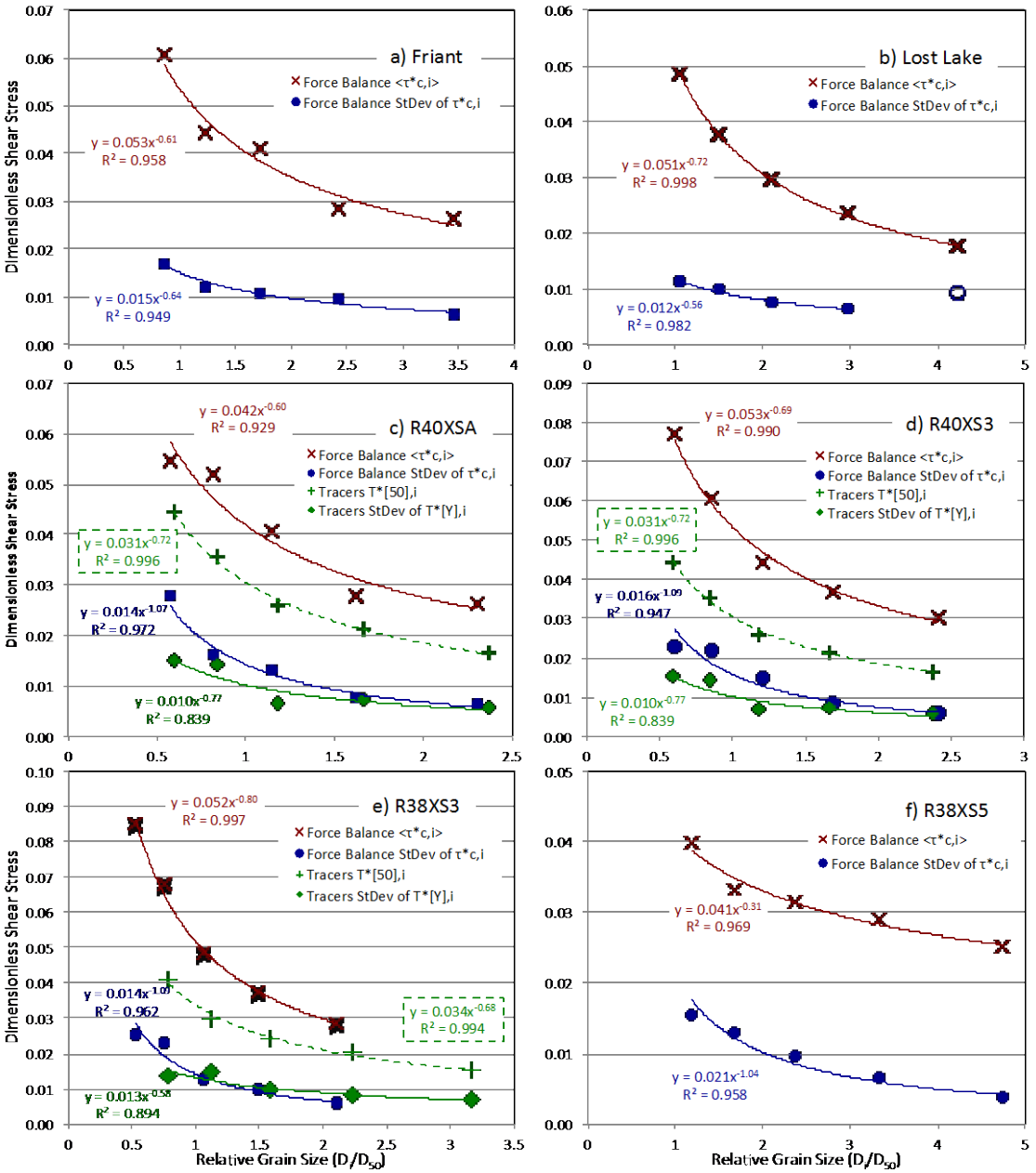

Figure 6. Trends in the parameters of the theoretical distribution of the $\tau^*_{c,i}$ obtained with the *Wiberg and Smith* [1987] model as functions of relative grain size. For the mean (red) and standard deviation of $\tau^*_{c,i}$ (blue) are fit with power functions. At Lost Lake the standard deviation of $\tau^*_{c,i}$ for the largest grain size class (128mm) was not included in the regression (indicated as a hollow circle symbol) because it was an outlier resulting from a small sample size (n=3). In addition, the tracer results from Chapter 1 were included with the appropriate sites. From the tracer entrainment results, the T^* values that provided 50% entrainment of a grain size fraction (green plus symbols), distinguished with '[50]' in the legend, are provided from Chapter 1: Table 6. The standard deviation of the frequency of tracers entrained as a function of the T^*, distinguished with '[Y]' in the legend, is also provided (green diamond symbols). This

standard deviation of $T^*_{[Y],i}$ was approximated from the logistic regression by using the square root of the variance, such that the variance is $\sigma_i^2 = \frac{1}{3}\pi^2(1/C_i)^2$ where 'C_i' is a coefficient of the logistic equation whose values are provided in Chapter 1, Table 5. As the logistic regression was performed in terms of T, the dimensionless form of the tracer measured $T_{[50],i}$ and the corresponding standard deviations were calculated using the Shields equation (3).

Table 4. Statistics of regression equations (4) and (13) for the mean and standard deviation of the $\tau^*_{c,i}$ values as functions of D_i/D_{50} (see Figure 6). The standard error ($\pm$SE) is provided for each coefficient. Statistical significance of the models are indicated by *p*-values<0.05.

Site	Intercept Coefficient	$\pm$SE	Slope Coefficient	$\pm$SE	R^2	*p*-value	n
$\langle\tau^*_{c,i}\rangle = \alpha(D_i/D_{50})^{-\beta}$							
Friant	0.0534	$\pm$0.0538	0.610	$\pm$0.073	0.958	3.65E-03	5
Lost Lake	0.0505	$\pm$0.0146	0.724	$\pm$0.016	0.999	2.57E-07	5
R40XSA	0.0418	$\pm$0.0491	0.603	$\pm$0.097	0.929	8.27E-03	5
R40XS3	0.0534	$\pm$0.0210	0.686	$\pm$0.040	0.990	4.36E-04	5
R38XS3	0.0518	$\pm$0.0133	0.798	$\pm$0.027	0.997	8.47E-05	5
R38XS5	0.0371	$\pm$0.0232	0.305	$\pm$0.032	0.969	2.35E-03	5
$St.Dev.of\ \tau^*_{c,i} = \gamma(D_i/D_{50})^{-\delta}$							
Friant	0.0151	$\pm$0.0629	0.641	$\pm$0.086	0.949	4.94E-03	5
Lost Lake	0.0118	$\pm$0.0372	0.560	$\pm$0.054	0.982	9.10E-03	4
R40XSA	0.0142	$\pm$0.0537	1.073	$\pm$0.106	0.972	2.03E-03	5
R40XS3	0.0158	$\pm$0.0775	1.086	$\pm$0.148	0.947	5.22E-03	5
R38XS3	0.0142	$\pm$0.0614	1.085	$\pm$0.125	0.962	3.21E-03	5
R38XS5	0.0209	$\pm$0.0916	1.035	$\pm$0.125	0.958	3.68E-03	5

The good fit of the parameters values to power functions of D_i/D_{50} allow them to be compared between sites with less ambiguity resulting from the minimized residuals. I use ANCOVA to test for significant differences in the regression coefficients of equation (4) (Appendix F, Table F-2). The results indicate that the hiding effect (β value) at site R38XS5 (sandy margin) is significantly less than the other sites (*p*-values<0.03), while it is not significantly different between the other sites (*p*-values>0.05).

The most suggestive clue to the cause of the difference between the R38XS5 site from the others is its greater sand content (Figure 2). With increasing sand content the pockets between grains become filled and subsequently deposited gravels are perched higher against downstream grains, thereby resulting in increasing frictional resistance values with D_i (see Figure 3f). As the tops of smaller grain sizes become more equal with

larger grains, the hiding effect reduces due to the greater exposure of smaller grains to the flow. With greater exposure and reduced ϕ values the smaller grains have lower $\langle \tau_{c,i}^{*} \rangle$ values. At the same time, due to filling of the pockets around larger grains they have greater frictional resistance to movement due deposition on their leeward side and less exposure to flow due to the deposition on their stoss side, thereby resulting in higher $\langle \tau_{c,i}^{*} \rangle$ values.

The magnitude of the $\langle \tau_{c,50}^{*} \rangle$ values, approximated by α in Table 4, are also significantly different between some sites (Appendix F, Table F-2). In this case, the riffle sites (Friant, R40XS3, and R38XS3) are not significantly different from one another (p-values > 0.15). However, the pool tail-out sites (Lost Lake and R40XSA) are marginally significantly different (p-value = 0.05). In general, at the riffles the $\langle \tau_{c,50}^{*} \rangle$ values are significantly greater than the pool tail-out sites (p-values < 0.02), with the exception of R38XS3 versus Lost Lake (p-value = 0.83). The $\langle \tau_{c,50}^{*} \rangle$ value of the Lost Lake site is greater than the other non-riffle sites and approaches the higher values of the riffle sites. Together these results indicate that the trend can be generalized across the riffles but at other locations there is greater diversity in the magnitude and trend of the $\langle \tau_{c,i}^{*} \rangle$ values. These results are supported by the observations in the $\langle \ln(F_d/F_g) \rangle_{50}$ (coefficient b, Table 2) as a function of D_i/D_{50} (Figure 3), which (i) tend to have a greater magnitude at the riffle sites, (ii) are not as consistently dependent on the D_i/D_{50} at the non-riffle sites, and (iii) show a high $\langle \ln(F_d/F_g) \rangle_{50}$ at the Lost Lake site similar to that of the riffles sites. It follows that bed texture maintenance processes are consistent at riffles due to more regular high flow strengths while other locations experience lower flow strengths that can result in a range of bed textures that correspond to more variable frictional resistance.

Furthermore, the more confined channel at the Lost Lake site may explain its similarity with the riffles as higher flow strengths occur more regularly due to a narrower channel and higher banks that cause greater flow velocities for a given flow as compared to the R40XSA and R38XS5 sites as witnessed during field monitoring of near bankfull flows.

The inverse relationships of the mean and standard deviation of $\tau_{c,i}^*$ with D_i/D_{50} generally suggests some amount of covariance between them. I check for covariance in these parameters by converting the $\tau_{c,i}^*$ values to $\tau_{c,i}$ using equation (3) (see Appendix G: Figure G-1), normalizing them by the corresponding $\langle\tau_{c,i}\rangle$ value, and plotting the resulting theoretical distributions (Figure 7). The results show that the majority of sites distributions of $\tau_{c,i}/\langle\tau_{c,i}\rangle$ collapse, thereby suggesting that a constant variance in the normal distribution of $\tau_{c,i}$ can describe the change in the proportion of a D_i that is entrained with increasing τ. Analogously, strong covariance was demonstrated in the entrainment measurements presented in Chapter 1 that found their distributions collapsed when the proportion of a grain size fraction entrained as a function of the T was normalized by the shear stress that produces 50% entrainment of the grain size fractions $T_{[50],i}$ [Chapter 1, figure 6]. However, at site R38XS5 and less so at site R40XS3, there is a systematic trend of decreasing variance with increasing D_i. This lack of collapse shows that their mean and standard deviation covary the least; these are also the two sites with the most sand (Figure 2). Therefore, these results indicate that the covariance in the mean and standard deviation of $\tau_{c,i}$ is a common attribute at riffle and pool tail-outs. However, a secondary sand mode appears to cause deviation from the covariance, such that coarser grains will have a narrower range of $\tau_{c,i}/\langle\tau_{c,i}\rangle$ than smaller grains. Indeed, strongly bimodal mixtures have been determined to have lower τ_c values for gravels [*Wilcock and*

Crowe, 2003]. The lack of covariance appears to be an expression of this effect in terms of the resulting change in the resistance of entrainment across the partial entrainment domain.

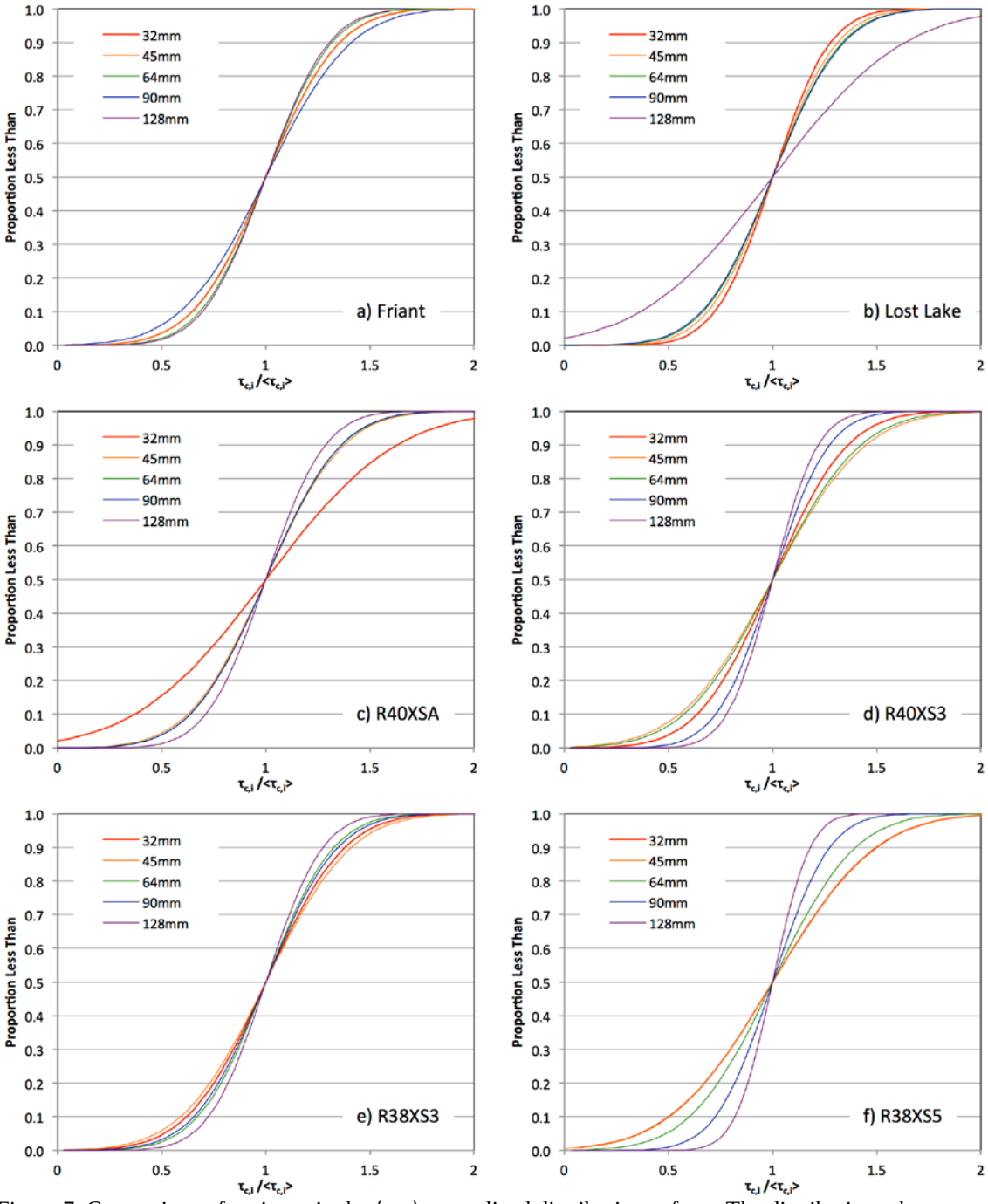

Figure 7. Comparison of variance in the $\langle\tau_{c,i}\rangle$ normalized distributions of $\tau_{c,i}$. The distributions shown are the resulting theoretical normal distributions using the mean and standard deviation of the normalized

distributions. The results shown include the variance of site Lost Lake for the 128 mm grain size class that was previously indicated to be an outlier.

3. Comparison of Force Balance Predictions and Tracer Entrainment

Because the *Wiberg and Smith* [1987] force balance model predicts the instantaneous τ_c^*, I examine the differences between the field-measured instantaneous and time-averaged flow strengths to see if they explain the difference between the force balance predicted $\langle\tau_{c,i}^*\rangle$ and the tracer entrainment measured $T_{[50],i}^*$, where subscripted '[50]' refers to the value that produced 50% entrainment of the tracers of size '*i*', shown in Figure 6c,d,e. Although these variables have similar definitions, such that the $\langle\tau_{c,i}^*\rangle$ is the τ^* capable of moving 50% of the force gaged grains of size '*i*', the predicted $\langle\tau_{c,i}^*\rangle$ values are consistently greater than the tracer defined $T_{[50],i}^*$ values. I suspect this is a result of using time-averaged τ values from the 2D flow model to indicate the flow strength that acted on the tracers. The greater instantaneous $\tau_{c,i}^*$ values could result from shear stress fluctuations that impose forces in excess of the time-averaged value as was found by *Celik et al.* [2010], which are not accounted for in the flow model.

To determine if the differences between $\langle\tau_{c,i}^*\rangle$ and $T_{[50],i}^*$ are attributed to temporal fluctuations in the τ value I convert them to $\langle\tau_{c,i}\rangle$ and $T_{[50],i}$ using (3) to compare them to $\bar{\tau}$ and $\bar{\bar{\tau}}$ that I calculated from (10a,b) using flow velocity measurements (see Methods). I use the percent difference between $\langle\tau_{c,50}\rangle$ (i.e., from the intercept coefficients presented Table 4) and $T_{50,[50]}$ from Chapter 1 (i.e., $100\%(\langle\tau_{c50}\rangle - T_{50,[50]})/T_{50,[50]}$) as a function of $T_{50,[50]}$ (solid symbols on Figure 8) to compare with the index of shear stress fluctuation (i.e., $100\%\left(\bar{\tau}_p - \bar{\bar{\tau}}\right)/\bar{\bar{\tau}}$) as a function of $\bar{\bar{\tau}}$ (hollow symbols on Figure 8) from each velocity measurement sample. By adjusting the percentile *p* of the distributions of $\bar{\tau}$

to get a $\bar{\tau}_p$ value from each of the $\bar{\tau}$ samples, I find that at about the 98th percentile of the $\bar{\tau}$ distribution (i.e., two standard deviations greater than the $\bar{\bar{\tau}}$) produces reasonable agreement with the percent difference between $\langle \tau^*_{c,50} \rangle$ and $T^*_{50,[50]}$. Therefore, the comparison indicates that the $\langle \tau^*_{c,i} \rangle$ values are within the upper tail of the $\bar{\tau}$ distribution.

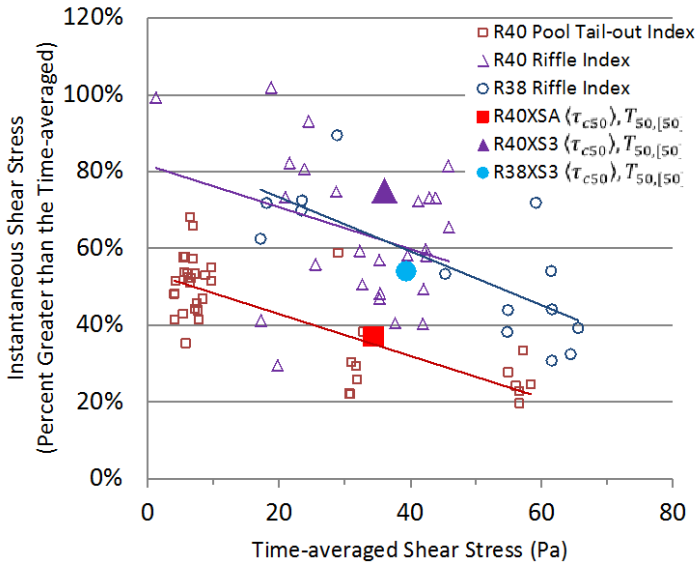

Figure 8: The index of shear stress fluctuation as a function of the time-averaged shear stress. The ordinate axis indicates the percent at which the instantaneous shear stress is in excess of the time-averaged shear stress. The velocity was measured within 50 m of three force gage sites while staying within the same morphologic zone. The hollow points indicate the 97.8 percentile values of the flow velocity-measured $\bar{\tau}$ distributions (i.e., two standard deviations greater than the $\bar{\bar{\tau}}$) as a percentage expressed by $100\%\,[(\bar{\bar{\tau}} + 2 \times RMSD\ of\ \bar{\tau}) - \bar{\bar{\tau}}]/\bar{\bar{\tau}}$ as a function of their $\bar{\bar{\tau}}$ values; which is referred to as the index of shear stress fluctuation. Their trends at each site are fitted using linear OLS regression, which illustrate similarity amongst the riffle sites (R40XS3 vs. R40 Riffle n=26 and R38XS3 vs. R38 Riffle n=14) and their difference with the pool tail-out site (R40XSA vs. R40 Crest-Pool Tail n=36). The relative difference between the force balance predicted $\langle \tau_{c,50} \rangle$ values and the tracer measured $T_{[50],50}$ values (i.e., $100\%(\langle \tau_{c50} \rangle - T_{50,[50]})/T_{50,[50]}$) are plotted as solid symbols as a function of the $T_{[50],50}$ values from the tracer measurements (Figure 6c,d,e).

Figure 8 illustrates similarity in the index of shear stress fluctuations at the riffle sites (R40XS3 and R38XS3) and a notable difference from the pool tail-out site R40XSA. These are also reflected in the differences between the $\langle \tau^*_{c,50} \rangle$ and $T^*_{50,[50]}$ of these sites. These results indicate that fluctuations in the shear stress have similar variance at the riffle sites and the variance at the pool tail-out site is less for a given time-averaged shear stress. Therefore, the riffles experience greater instantaneous shear stresses than the pool

tail-out for a given time-averaged shear stress, which supports the previous suggestion that bed texture maintenance processes are associated flow strength, as the greater instantaneous flow strengths correspond with less variation in the frictional resistance at the riffle sites relative to the other sites. Furthermore, the correspondence of the *Wiberg and Smith* [1987] model predictions of $\langle \tau^*_{c,50} \rangle$ with the index of shear stress fluctuations indicates that the model provides a reasonable approximation of the instantaneous $\langle \tau^*_{c,50} \rangle$.

In order to compare the distributions of the calculated $\tau^*_{c,i}$ from (5) with the distributions of the tracer measured $T^*_{c,i}$ values, I adjust the force balance model predictions of τ^*_c by the relative difference between the $\langle \tau^*_{c,50} \rangle$ and $T^*_{50,[50]}$ to approximate time-averaged values from the predicted critical dimensionless shear stress $\tilde{T}^*_c$, where the tilde indicates the adjusted τ^*_c that approximates the time-averaged value, such that:

$$\tilde{T}^*_c = \frac{\tau^*_c}{1+\left[\left(\langle \tau^*_{c,50} \rangle - T^*_{50,[50]}\right)/T^*_{50,[50]}\right]} \tag{14}$$

The distributions of $\tilde{T}^*_c$ for each D_i are compared to the tracer entrainment measured distributions of $T^*_{c,i}$ in Figure 9. The resulting distributions of adjusted values fit well with the theoretical distributions of the tracer-measured proportion entrained of each D_i as a function of T^*. Therefore, the tracer measurements appear to validate the *Wiberg and Smith* [1987] model predicted $\tau^*_{c,i}$ values and their resulting distributions.

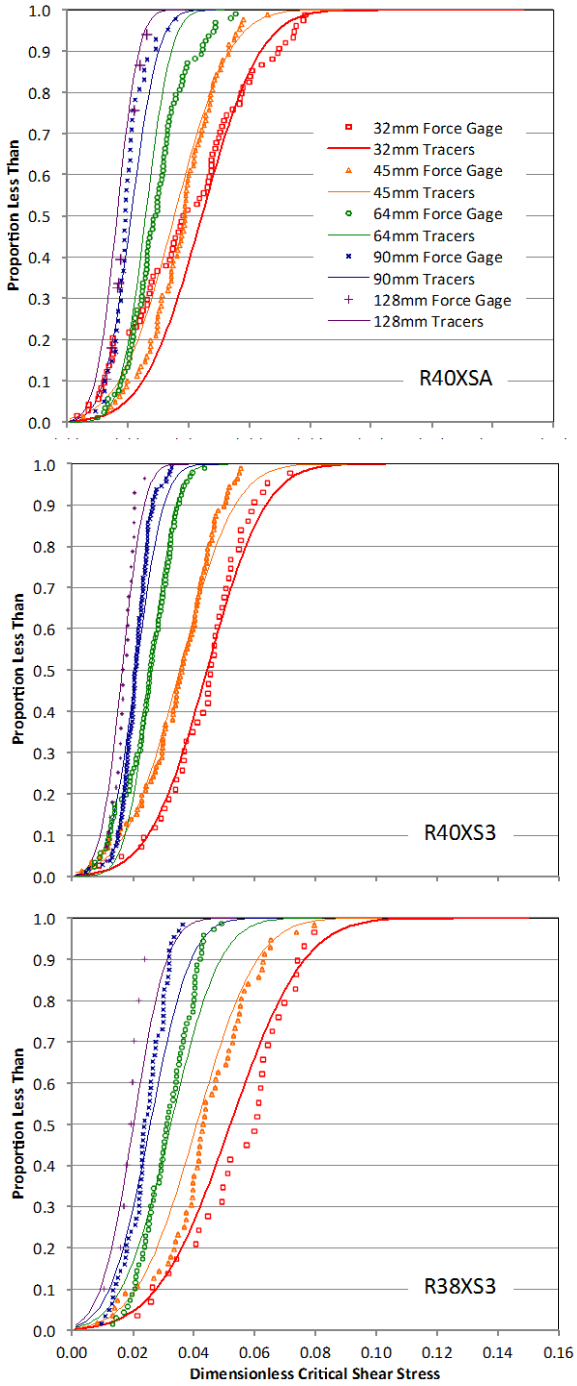

Figure 9. Approximations of the time-averaged, force balance predicted $\tilde{T}^*_{c,i}$ values (points) and entrainment measured theoretical distributions of $T^*_{c,i}$ (lines). The tracer measurements of fractional proportion entrained as functions of $T^*$are here being shown as indicative of the proportion of the grains within a size class entrained by values equal to or less than the T^*. As compared to the $\tau^*_{c,i}$ values in Figure 5c,d,e, each of the $\tilde{T}^*_{c,i}$ values shifted to the left thereby aligning with the $T^*_{c,i}$ distributions.

A test of the difference in the $\tilde{T}^*_{c,i}$ requires accounting for the effects of D_i/D_{50} on the $\tilde{T}^*_{c,i}$ distributions. I use hiding function plots for percentile values of $\tilde{T}^*_{c,i}$ in the tails of the

distribution to compare with those from the tracer entrainment measured distributions. The tails of the distribution of $\tilde{T}^*_{c,i}$ values are indicative of the thresholds of incipient and full entrainment for the D_i. I calculated the 9.3 and 90.7 percentile values from the $\tilde{T}^*_{c,i}$ distributions, distinguished as $\tilde{T}^*_{c[9],i}$ and $\tilde{T}^*_{c[91],i}$, respectively, to approximate the thresholds of entrainment (Figure 10). These percentile values are the same as those used to approximate the dimensionless shear stresses for onset of entrainment $T^*_{c,i}$ and full (91%) entrainment $T^*_{fe,i}$, respectively, from tracer entrainment measurements in Chapter 1. To compare the threshold measurements between the methods, I use hiding functions (4) fit using OLS regression for each threshold approximation from plots of these percentile values as functions of the D_i/D_{50}. The resulting trends exponent values generally range from -0.87 to -0.48 and indicate that smaller grains require lower τ to begin entrainment than larger grains. The intercepts of the regression equation for the trend in $\tilde{T}^*_{c[9],\mathrm{i}}$ as a function of D_i/D_{50} indicate the $\tilde{T}^*_{c,50}$ values and are between 0.018 and 0.021. These results are in general agreement with the measurements of the exponents values of -0.74 to -0.65 and $T^*_{c,50}$=0.017 from the tracers [Chapter 1], therefore they suggest that the predictions of the force balance model provide reasonable approximations of the distributions of $\tau^*_{c,i}$ values.

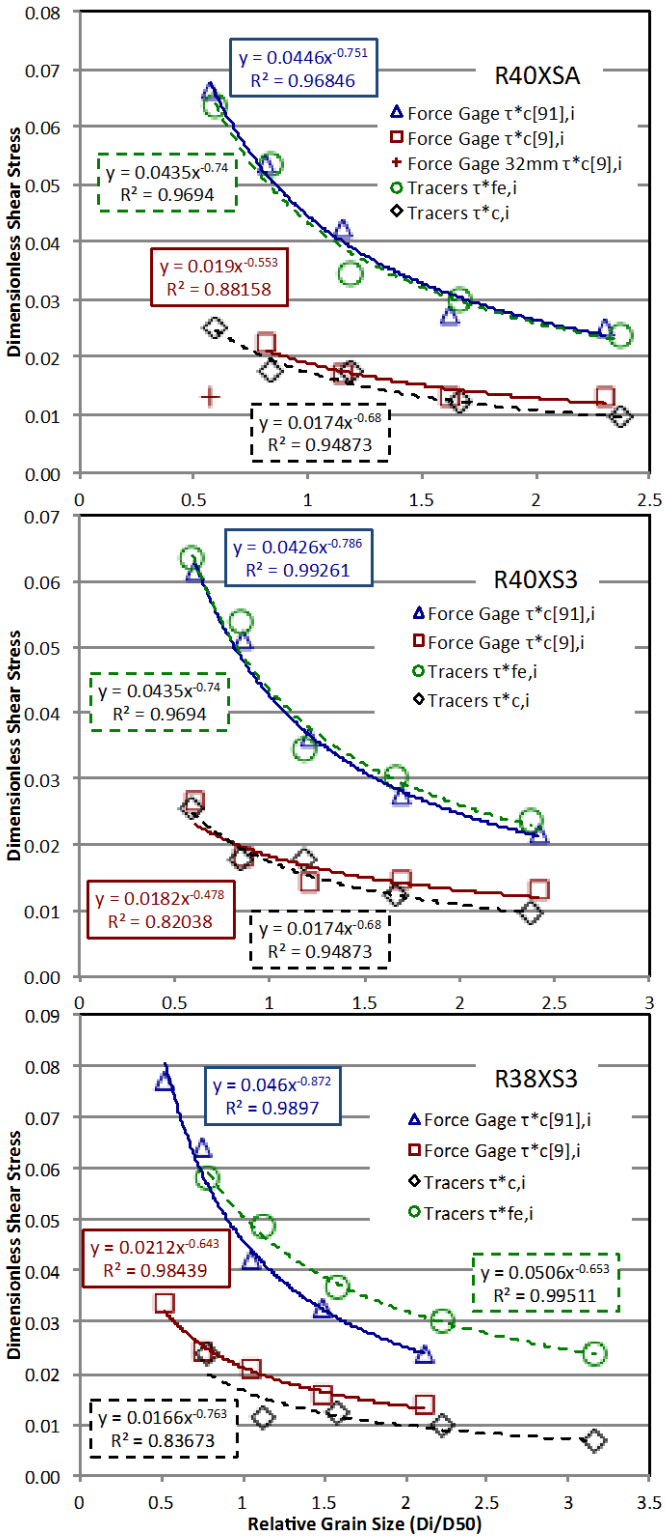

Figure 10. Force balance (adjusted to approximate time-averaged values) and tracer-measured trends of the approximations of the threshold dimensionless shear stresses. Power functions in the form of equation (4) fit by OLS regression are provided for each set of measurements. At site R40XSA the 32 mm grain size class was not included in the regression as it appears to be an outlier that possibly resulted from deposition of this grain size and finer subsequent to the tracer measurements.

I use ANCOVA tests to determine if the coefficients of the regression functions in Figure 10 are significantly different between the tracer and force balance results. The tests indicate that the coefficients are not significantly different (p-values>0.12) between the corresponding thresholds from R40 (tracers) vs. R40XSA (force balance) and vs. R40XS3 (force balance). Therefore, combining these data is justified to provide a hiding function that encompasses this riffle-pool tail-out section. However, the hiding functions that describe the site R38 tracer-measured $T^*_{c,i}$ and $T^*_{fe,i}$ values are less than and greater than those of the predicted $\tilde{T}^*_{c[9],i}$ and $\tilde{T}^*_{c[91],i}$ values, respectively. This is apparent in their significantly different intercepts (p-values<0.03). This narrowing of the range between the predicted thresholds supports the notion expressed in Chapter 1 that the greater difference between the tracer measured $T^*_{c,i}$ and $T^*_{fe,i}$ values at site R38 was due to the greater variation in grain size distributions as expressed by the D_{50} along the bar at this site. By force gage surveying a much smaller area – selected in part based on a consistent bed texture – than was covered by the tracer study at R38, the variation in the grain size distribution is undoubtedly reduced. As a result, the force gage survey results confirm the grain size variation explanation for the wider range between the thresholds from the tracer measurements. This also suggests that the force balance predicted $\tilde{T}^*_{c[9],i}$ and $\tilde{T}^*_{c[91],i}$ values, though different from the $T^*_{c,i}$ and $T^*_{fe,i}$ values at R38, appear to be accurate. Therefore, the *Wiberg and Smith* [1987] force balance model provides validated predictions of the distribution of τ^*_c values for grain size fractions and that are confirmed with the tracer entrainment measurements.

E. Discussion

I used force gages to measure the frictional resistance of grains. When coupled with the *Wiberg and Smith* [1987] force balance model (5) they provide the value of the applied τ_c^*. The distributions of τ_c^* for grain size fractions allow comparison with distributions of probability of entrainment with increasing τ^* from tracer measurements that are presented in Chapter 1. A difference between the force balance model predicted τ_c^* values and the tracer entrainment measurements is observed and attributed to the difference between the methods determination of the τ. I found that the majority of the difference is explained by shear stress fluctuations that are not accounted for by the time-averaged τ values used in the tracer study. A simple adjustment in the predicted τ_c^* values that corresponds to a quantile of the distribution of shear stress fluctuations is found to produce agreement with the tracer measurements. Therefore, the force gage method, as presented herein, allows the determination of the frictional resistance and critical shear stress of the grains on the bed.

When the flow forces and the measured distributions of frictional resistance of the grains are accounted for by using equation (5), all the sites exhibit normal distributions of $\tau_{c,i}^*$ (Figure 5), and the parameters of these distributions have statistically significant inverse relationships with grain size (Figure 6). In most cases, the variance in $\tau_{c,i}^*$ collapses when the $\tau_{c,i}^*$ values are normalized by their mean value (Figure 7), thereby indicating virtually parallel log-log linear relationships of $\tau_{c,i}^*$ as functions of grain size for any given pair of quantiles of the $\tau_{c,i}^*$ distributions at a site. These results indicate strong interdependence in the parameters defining the distribution of $\tau_{c,i}^*$ values between different grain sizes at a site. It follows that the parameters defining the distributions of

$\tau^*_{c,i}$ values therefore provide useful indices for comparing similarities and differences between grain sizes and sites.

My results suggest that the variance in $\tau^*_{c,i}$ is often dependent on the corresponding $\langle\tau^*_{c,i}\rangle$ value. By comparing $\langle\tau^*_{c,i}\rangle$ values between sites, I discover similarities and differences in their trends as a function of D_i/D_{50} that appear to correspond to their proximity to the bar crest. For instance, β values (Table 4) are not significantly different between the sites (excluding R38XS5 that had the lowest β value) thereby indicating that along the reach there were similar degrees of "hiding effects." However, the magnitude of the trends as expressed by the α value of (4) indicates greater $\langle\tau^*_{c,50}\rangle$ values at the riffle sites that are statistically significant at the Friant and R40XS3 sites. The pool tail-out sites, though, have more variability their $\langle\tau^*_{c,50}\rangle$ values and the sandy gravel bed at R38XS5 has the lowest $\langle\tau^*_{c,50}\rangle$ value (Figure 6). Thus, these differences in the equation (5) predicted $\tau^*_{c,i}$ values indicate variability in grain resistance that correlates with longitudinal position along the bars, such that the resistance to flow of grains on (i) the riffles are more equal with one another and greater than other locations; (ii) the pool tail-outs are less and more variable between sites; and (iii) patches of sandy gravel beds are the lowest and have greater variation in τ_c as a function of grain size.

Differences in $\langle\tau^*_{c,50}\rangle$ between the riffles and other sites are attributed to the variation in the shear stress fluctuation. This is supported by a greater variance in the $\bar{\tau}$ about the $\bar{\bar{\tau}}$ value on the riffles than at a pool tail-out (Figure 8) that corresponds with the greater $\langle\tau^*_{c,50}\rangle$ values at the riffles than the other sites (Figure 6). The strongest support though comes from the R40 sites. Here, the range of $\langle\tau^*_{c,i}\rangle$ values is different between the sites as indicated by $\langle\tau^*_{c,50}\rangle$ values of 0.042 and 0.053 at R40XSA and R40XS3 that are

significantly different. However, the adjustment that is supported by the difference between the sites index of shear stress fluctuation produces distributions of $\tau^*_{c,i}$ values that align well between the sites. Furthermore, when accounting for the relative grain size effect quantiles of the distributions that approximate the thresholds of entrainment are not significantly different (Figure 10). These results demonstrate the merits of using the time-averaged shear stress to characterize grain mobility from a constant $T^*_{c,50}$ along a barform with differences in bed texture and frictional resistance. In addition, they also indicate that the resistance of the grains on the bed adjusts to the amount of shear stress fluctuation, such that the instantaneous τ values in the upper tail of their distribution are responsible for entrainment. As such, the frictional resistance of the bed provides a measure of the shear stress fluctuation in excess of the time-averaged value that is associated with the bed. Moreover, the force gage measurements and *Wiberg and Smith* [1987] model provides the means of quantifying this difference.

Differences in frictional resistance measurements correspond to differences in shear stress fluctuation. The average and standard deviation of $\ln\left(F_d/F_g\right)_i$ values at the riffle sites are inversely dependent on D_i/D_{50} (Figure 3), but this is not the case at the other sites. The average $\ln\left(F_d/F_g\right)_i$ values at the R40XSA and R38XS5 sites do not indicate significant dependence on D_i/D_{50}, nor does the standard deviation of $\ln\left(F_d/F_g\right)_i$ values at the Lost Lake site. These results indicate variability in grain organization along a bar form. If the difference between the index of shear stress fluctuation measured at the non-riffle versus riffles sites is indicative of the difference between similar types of locations elsewhere, then it would explain the greater variability in grain resistance at the non-riffle sites. This, together with typically greater $\langle\ln\left(F_d/F_g\right)_{50}\rangle$ values at the riffle sites (Figure

3), indicates that the higher instantaneous shear stresses functions to organize the grains in more resistive positions. Higher magnitudes of instantaneous τ encourage this process by inducing greater flow velocities closer to the bed, thereby entraining less resistive grains, creating deeper pockets in which remaining grains are better restrained, and thereby increasing their $\langle \ln(F_d/F_g)_{50} \rangle$ values (Table 2). With lower instantaneous τ, on the other hand, grains can accumulate in the pockets between larger grains, creating a smoother bed surface of grains in less resistive positions as is indicated by the smaller $\langle \ln(F_d/F_g)_{50} \rangle$ values from the R40XSA and R38XS5 sites.

The Lost Lake site exhibited the strongest dependence in the $\langle \ln(F_d/F_g)_i \rangle$ on D_i/D_{50}, which indicates a strong water-worked effect on grains at this pool tail-out site (Figure 3). A more confined channel at this site affects hydraulics so that the τ increases at a greater rate with discharge than at the other sites. This creates greater flow forces for a given flow level as compared to the other non-riffle sites, which may be sufficient to flush pockets in the absence of the greater variance in instantaneous τ that is observed at riffles that have similarly strong dependencies. However, the difference in the rate of change in τ with discharge appears to affect the variance in $\ln(F_d/F_g)_i$ with D_i/D_{50} differently than it does at the riffle sites. Here, the standard deviation in $\ln(F_d/F_g)_i$ does not depend on D_i/D_{50}. Further research is necessary to explain the relationship between the variance in $\ln(F_d/F_g)_i$ with D_i/D_{50} with variable relationships between τ as a function of discharge.

Where shear stress fluctuation is low and there is a high influx of sand, there is potential for pockets to accumulate sand, which has been found to affect the mobility of

gravels on a gravel bed [*Ikeda and Iseya*, 1988; *Wilcock*, 1998]. The bed surface at R40XS3 and R38XS5 contained ~10% and ~20% sand, respectively (Figure 2). Using flume experiments, *Wilcock and Crowe* [2003] found that similar concentrations of sand on gravel beds are associated with lower τ_c^* for gravels. I examine the grain resistance at these sites to determine if sand content affects mobility of gravels differently at a site with higher shear stress fluctuations (R40XS3) and a site where a significantly lower $\langle\tau_{c,50}^*\rangle$ value is assumed to be associated with lower shear stress fluctuations (R38XS5) (Figure 6). Although the $\langle\tau_{c,50}^*\rangle$ values at these sites are in agreement with this relationship, the variance in $\tau_{c,i}$ values was more independent of the $\langle\tau_{c,i}\rangle$ at these two sites than is the case for the other sites that had unimodal to weakly bimodal grain size distributions (Figure 7). Furthermore, as the variance is greatest at the R38XS5 site the variance of the $\tau_{c,i}$ distributions are also the least dependent on the $\langle\tau_{c,i}\rangle$. Therefore, while the difference in $\langle\tau_{c,i}^*\rangle$ can be explained by shear stress fluctuations, the sand appears to affect the variance in the $\tau_{c,i}$ distributions. The reduced variance of larger grains sizes with increasing sand content appears to describe an effect on the probability of entrainment with increasing τ that appears to explain the enhanced mobility of gravel by sand as observed by *Wilcock and Crow*e [2003].

Wilcock [1992] found grain size heterogeneity as expressed by bimodal grain size distributions to correspond with a reduction in the hiding factor, β. I found this to be the case at the R38XS5 site, which has the largest secondary mode in its grain size distribution (Figure 2) and a β value that is significantly smaller (β=0.31) than the other sites (Figure 6). Because the $\tau_{c,i}$ values for the *bed* at this site more closely approximate a constant τ^* value where β=0 than a constant τ value where β=1, the tendency toward

equal mobility of gravel beds observed in transport-based measurements [*Parker and Toro-Escobar*, 2002] is at least partly explained by the combined effects of frictional resistance and exposure to hydraulic forces. Furthermore, it demonstrates that grain resistance, as defined by the *Wiberg and Smith* [1987] force balance predicted $\tau^*_{c,i}$, along this gravel-bedded reach is capable of local adjustment that results from effects of local grain size sorting (Figure 4) that does not significantly correlate with the magnitude of the frictional resistance distributions (Appendix D, Figure D-2). Instead, the degree of sorting more strongly determines the effect of the dependence of the variance of $\tau_{c,i}$ on $\langle\tau_{c,i}\rangle$ such that the variance becomes less dependent on $\langle\tau_{c,i}\rangle$ with greater sand concentrations (Figure 7). Therefore, the coupled force gage and force balance model produce distributions of $\tau^*_{c,i}$ that detect the effects of grain size heterogeneity on the degree of the hiding effect.

F. Conclusions

Using force gages to measure the frictional resistance of in situ grains on a bed, I find that the *Wiberg and Smith* [1987] force balance model predicts valid values of the instantaneous $\tau^*_{c,i}$. Although the predictions differ from the $T^*_{c,i}$ measured from tracers in Chapter 1, the difference from the time-averaged values are demonstrated to correspond to the variance in temporal shear stress fluctuations. A simple factor adjustment, that is shown to correspond to this variance, to the predicted $\tau^*_{c,i}$ values results in distributions of $\tau^*_{c,i}$ values that when accounting for D_i/D_{50} agree with the tracer gravel-cobble entrainment measurements from Chapter 1.

The measurements of the ϕ_i, $\ln\left(F_d/F_g\right)_i$, and $\tau^*_{c,i}$ values demonstrate a range of values for a grain size fraction. This range is indicative of the domain of partial entrainment where some grains are entrained at a given flow strength while others are not. However, as was found by *Johnston et al*, [1998] the ϕ_i values are not symmetrically distributed thereby not being well characterized by the parameters of the normal distribution. The measurements of $\ln\left(F_d/F_g\right)_i$, and $\tau^*_{c,i}$, on the other hand, are not significantly different from the normal distribution. Therefore, these measurements provide a mean and variance that adequately describes their distributions thereby allowing more robust methods to compare the variability in grain resistance as a function of grain size that can be compared between sites.

The average and standard deviation of $\ln\left(F_d/F_g\right)_i$ vary with differences in grain size, sand content, sorting, position along a barform, and hydraulics. Both the mean and standard deviation of $\ln\left(F_d/F_g\right)_i$ are affected by the sand content. Sites with a secondary mode in their grain size distribution consisting of sand (Figure 2) are associated with $\langle\ln\left(F_d/F_g\right)_i\rangle$ values that are less of a function of grain size than sites without a strong secondary mode of sand (Table 2). Grain size sorting corresponds directly with changes in the standard deviation of $\ln\left(F_d/F_g\right)_{50}$ (Figure 4). These observations offer an entrainment-based explanation for observations of enhanced gravel mobility with increasing sand content. There are also significant differences in frictional resistance along the studied reach, as quantified by differences in mean and standard deviation of $\ln\left(F_d/F_g\right)_i$ values as functions of D_i/D_{50} (Figure 3). Riffle sites exhibited $\langle\ln\left(F_d/F_g\right)_i\rangle$ values that are inversely related to grain size and that covary with the standard deviation

of $\ln\left(F_d/F_g\right)_i$. Non-riffle sites tend to have more variable mean and standard deviation of $\ln\left(F_d/F_g\right)_i$values as a function of D_i/D_{50}. These differences along a barform correspond to differences in the variance in shear stress fluctuations that were measured at three sites (Figure 8).

The variability in the predicted mean and standard deviation of the $\tau^*_{c,i}$ is also found to depend on grain size, sand content, position along a barform, and hydraulics. In most cases, the standard deviation of $\tau^*_{c,i}$ covaries with the $\langle\tau^*_{c,i}\rangle$ value (Figure 7). However, with increasing sand content this covariance diminishes such that the variance becomes dependent on grain size, with the variance in $\tau_{c,i}/\langle\tau_{c,i}\rangle$ of larger grains becoming narrower and smaller grains becoming wider. Additionally, a reduced dependence of $\langle\tau^*_{c,i}\rangle$ on D_i (Figure 6f) is ascribed to the sand content as expressed by a strong secondary mode in the grain size distribution. The $\langle\tau^*_{c,i}\rangle$ values tend to be higher on the riffles than the other locations (Table 4), which is demonstrated to be associated with the variance in the shear stress fluctuation that differs between riffles and a pool tail-out (Figure 8).

Symbol	Definition
a	Slope coefficient in equation (11) (pages 20-21).
ADP	Acoustic Doppler profiler (page 15).
ANCOVA	Analysis of covariance (page 17).
ANOVA	Analysis of variance (page 17).
A_x	Cross-sectional area of the grain that is normal to flow (page 13).
A_z	Cross-sectional area of the grain that is parallel to the bed (page 14).
b	Intercept coefficient in equation (11) (pages 20-21).
c	Slope coefficient in equation (12) (page 21).
'c' subscripted	Refers to the 'critical' value (page 3).
C_D	Drag coefficient (page 6).
C_L	Lift coefficient; assumed equal to 0.2 (page 14).
d	Intercept coefficient in equation (12) (page 12).
D	Grain diameter (page 2).
D_i/D_{50}	Relative grain size (page 2).
D_n	The nominal diameter of the grain. This diameter is equal to that of a spherical grain with the same mass and ρ_s (2.65 cm^3/g) as the gaged grain (page 13).
e	In the text this term refers to the intercept coefficient of equation (2) (page 2). However, in two instances it is in reference to the base of the natural logarithm and is specifically noted in each case: equations (9a,b) and (10a,b) (page 16).
f	Slope coefficient of equation (2) (page 2).
F_d	Downstream-directed force (page 1).
F_D	The drag force imposed by the flow on a grain, see equation (7) (page 14).
F_g	The force imposed by the grain due to its weight (page 1).
F_L	The lift force imposed by the flow on a grain, see equation (8) (page 14).
$f^2(z/z_o)$	The generic reference to an unscaled function of the vertical profile of velocity (page 13).
g	The gravitational acceleration 9.81 m/s^2 (page 3).
h	Flow depth (page 16).
'i' subscripted	References a value specific to a grain size class (page 2).
K-S	Kolmogorov-Smirnov nonparametric statistical test (page 20).
n	Number of samples or data points.
OLS	Ordinary least squares (page 17).
p-	Probability (page 21).
'p' subscripted	Refers to a percentile of the cumulative distribution (pages 16 and 35).
q-q	Quantile-quantile (page 18).
Rkm	River kilometer (page 7).
RMSD	Root mean squared deviation (page 16).
R^2	Coefficient of determination (page 17).
S	Stream-wise slope (page 13).
SE	Standard error (pages 23 and 31).
u	Depth-averaged flow velocity (page 13).
$\bar{u}$	Instantaneous depth-averaged flow velocity (page 15).
$\bar{\bar{u}}$	Time- and depth-averaged flow velocity (page 15).
u_z	Flow velocity at a specified height, z, above the bed (page 14).
u_*	Shear velocity, $= (\tau/\rho)^{0.5}$, used as the scaling parameter of the vertical profile of velocity to compute u_z (page 14).
V	The volume of the grain (V = mass/ρ_s) (page 13).
z	Height above the bed (page 14).
z_B	The height above the bed of the bottom of the grain (page 14).
z_T	The height above the bed of the top of the grain (page 14).
z_o	Bed roughness parameter herein set equal to $D_{50}/30$ (page 14).
'50' subscripted	References a value specific to the median grain size of the bed (pages 2, 16, and

without brackets	25).
'[Y]' subscripted	Refers to the proportion of tracers entrained or the probability of entrainment as a function of τ or τ^* from Chapter 1 (page 30).
'[9]' subscripted	Refers to the 9.3 percentile of the distribution of force balance predicted $\tau^*_{c,i}$ values. This percentile was defined in Chapter 1 to approximate the τ^*_c of a grain size fraction from the linearization of the proportion entrained as a function of τ and the line's intercept at zero percent entrained (page 35-36).
'[50]' subscripted	Refers to the median value of the subscripted term (page 2, 16, 30, and 35).
'[91]' subscripted	Refers to the 90.7th percentile of the distribution of force balance predicted $\tau^*_{c,i}$ values. This percentile of the τ_c distributions was defined in Chapter 1 to approximate the full entrainment of a grain size fraction as defined by a linearization of the proportion entrained as a function of τ and its intercept at 100% entrained. It is acknowledged that this value is not a precisely defined threshold but rather an index value that provides a point for comparison for an otherwise indeterminate threshold. At about this percentile further increases in fractional proportion entrained is less a function of τ as the proportion entrained asymptotically approaches 1 with increasing τ (page 35-36).
$\langle angle\ brackets \rangle$	Refers to the mean value of the term within them (page 21).
α	Intercept coefficient of the hiding function, see equation (4) (page 4).
β	Slope coefficient, referred to as the hiding factor of the hiding function, see equation (4) (page 4).
γ	Intercept coefficient of equation (13) (page 29).
δ	Slope coefficient of equation (13) (page 29).
κ	von Kármán's constant of 0.407 (page 14).
ρ	The density of water 1.00 g/cm^3 (page 3).
ρ_s	The grain density 2.65 g/cm^3 (page 3).
σ	Grain size sorting (page 24).
τ	Shear stress acting on the bed (page 5).
τ_c	The critical shear stress. The minimum shear stress that will begin to displace a grain (page 5).
τ^*	Dimensionless shear stress, also referred to as the Shields stress. See equation (3) (page 3).
τ^*_c	The dimensionless critical shear stress; also referred to as the critical Shields stress. The minimum dimensionless shear stress that will begin to move a grain or a bed of grains (page 5). Herein, this refers to the instantaneous value as predicted the Wiberg and Smith [1987] model (pages 13 and 15).
$\bar{\tau}$	Instantaneous shear stress computed from depth-averaged flow velocity measurements (page 15).
$\bar{\bar{\tau}}$	Time-averaged shear stress computed from depth-averaged flow velocity measurements (page 15).
$\tilde{T}^*_{c[9],i}$	Refers to the force balance predicted $\tau^*_{c,i}$ values that have been adjusted to approximate the time-averaged value of $\tau^*_{c,i}$ that is indicative of incipient entrainment of the grain size class *i* as defined by the tracer results in Chapter 1 (page 35).
T^*	Refers to the dimensionless shear stress that is specifically from the tracer entrainment measurements of Chapter 1. These are predicted time-averaged values from a 2-dimensional flow model (page 3).
T^*_c	The critical dimensionless shear stress as determined from the tracer measurements of Chapter 1. These are the predicted time-averaged values from a 2-dimensional flow model (page 3, 15, and 35).
$T^*_{fe,i}$	The dimensionless shear stress that is able to entrain 91% of grain size class *i* as determined from the tracer measurements of Chapter 1. These are the predicted time-averaged values from a 2-dimensional flow model (page 35).
$\tilde{T}^*_{c[91],i}$	The force balance model predicted dimensionless shear stress that have been

	adjusted to approximate the time-averaged value of $\tau^*_{fe,i}$ that approximates full entrainment of the grain size class *i* as defined by the tracer results in Chapter 1 (page 35).
ϕ	Friction angle such that $\phi = \tan^{-1}(F_d/F_g)$ (page 1).

G. References

Andrews, E. D. (1983), Entrainment of gravel from naturally sorted riverbed material, *Geological Society of America Bulletin, 94*, 1225-1231.

Andrews, E. D., and D. C. Erman (1986), Persistence in the size distribution of surficial bed material during an extreme snowmelt flood, *Water Resour. Res., 22(2)*, 191-197.

Blatt, H., G. Middleton, and R. Murray (1980), *Origin of Sedimentary Rocks*, pp. 48-79, Prentice-Hall, Englewood Cliffs, N. J.

Bridge, J. S., and S. J. Bennett (1992), A model for the entrainment and transport of sediment grains of mixed sizes, shapes, and densities, *Water Resour. Res., 28(2)*, 337-363.

Buffington, J. M., and D. R. Montgomery (1997), A systematic analysis of eight decades of incipient motion studies, with special reference to gravel-bed rivers, *Water Resour. Res., 33(8)*, 1993-2029.

Buffington, J. M., W. E. Dietrich, and J. W. Kirchner (1992), Friction angle measurements on a naturally formed gravel stream bed: Implications for critical boundary shear stress, *Water Resour. Res., 28(2)*, 411-425.

Bunte, K., and S. R. Abt (2001), Sampling surface and subsurface particle-size distributions in wadable gravel- and cobble-bed streams for analyses in sediment transport, hydraulics, and streambed monitoring, *Gen. Tech. Rep. RMRS-GTR-74*,

Fort Collins, CO: U.S. Department of Agriculture, Forest Service, Rocky Mountain Research Station, 428 p.

Celik, A. O., P. Diplas, C. L. Dancey, and M. Valyrakis (2010), Impulse and particle dislodgement under turbulent flow conditions, *Physics of Fluids, American Institute of Physics, 22*, doi:10.1063/1.2285433.

Chen, C. L. (1991), Unified theory on power laws for flow resistance, *Journal of Hydraulic Engineering, ASCE, 117(3)*, 371-389.

Clayton, J. A. (2010), Local sorting, bend curvature, and particle mobility in meandering rivers, *Water Resour. Res., 46*, W02601, doi:10.1029/2008WR007669.

Egiazaroff, I. V. (1965), Calculation of nonuniform sediment concentrations, *J. Hydraul. Div. Am. Soc. Civ. Eng., 91(HY4)*, 225-247.

Fenton, J. D., and J. E. Abbott (1977), Initial movement of grains on a stream bed: The effect of relative protrusion, *Proc. R. Soc. London A. Math. Phys. Sci., 352(1671)*, 523-537.

García, M. H. (2008), Sediment transport and morphodynamics, in *Sedimentation Engineering: Processes, Measurements, and Practice*, edited by M. H. García., pp. 21-163, ASCE, Reston, VA.

Ikeda, H., and F. Iseya (1988), Experimental study of heterogeneous sediment transport, *Environmental Research Center Paper, 12*, 50 pp.

James, C. S. (1990), Prediction of entrainment conditions for nonuniform noncohesive sediments, *J. Hydraul. Res., 28*, 25-41.

Johnston, C. E., E. D. Andrews, and J. Pitlick (1998), In situ determination of particle friction angles of fluvial gravels, *Water Resour. Res., 34(8)*, 2017-2030, doi:10.1029/98WR00312.

Kirchner, J. W., W. E. Dietrich, F. Iseya, and H. Ikeda (1990), The variability of the critical shear stress, friction angle, and grain protrusion in water-worked sediments, *Sedimentology*, 37, 647-672.

Komar, P. D., and Z. Li (1986), Pivoting analysis of the selective entrainment of sediments by shape and size with application to gravel threshold, *Sedimentology, 33*, 425-436.

Kondolf, G. M., and P. Wilcock (1996), The flushing flow problem, *Eos Trans. AGU, 73*, 239.

Lamb, M. P., W. E. Dietrich, and J. G. Venditti (2008), Is the critical Shields stress for incipient motion dependent on channel-bed slope?, *Journal of Geophysical Research, 113*, F02008, doi:10.1029/2007JF000831.

Li, Z., and P. D. Komar (1986), Laboratory measurements of pivoting angles for applications to selective entrainment of gravel in a current, *Sedimentology, 33*, 413-423.

Miller, R. L., and R. J. Byrne (1966), The angle of repose for a single grain on a fixed rough bed, *Sedimentology, 6*, 303-314.

Mueller, E. R., J. Pitlick, and J. Nelson (2005), Variation in the reference shields stress for bed load transport in gravel-bed streams and rivers, *Water Resour. Res., 41*, W04006, doi:10.1029/2004WR003692.

Naden, P. (1987), An erosion criterion for gravel-bed rivers, *Earth Surf. Processes Landforms, 12*, 83-93.

Nelson, J. M., M. W. Schmeeckle, and R. L. Shreve (2001), Turbulence and particle entrainment, in *Gravel-Bed Rivers V*, edited by M. P. Mosley, pp. 221 – 240, New Zealand Hydrological Society, Wellington, New Zealand.

Parker, G. and C. M. Toro-Escobar (2002), Equal mobility of gravel in streams: The remains of the day, *Water Resour. Res., 38(11),* 1264, doi:10.1029/2001WR000669.

Parker, G., and P. C. Klingeman (1982), On why gravel bed streams are paved, *Water Resour. Res., 18(5),* 1409-1423.

Parker, G., P. C. Klingeman, and D. G. McLean (1982), Bedload and size distribution in paved gravel-bed streams, *Journal of Hydraulic Engineering, 108(4),* 544-571.

Prancevic, J. P., and M. P. Lamb (2015), Particle friction angles in steep mountain channels, *J. Geophys. Res. Earth Surf., 120,* 242-259, doi:10.1002/2014JF003286.

Shields, A. (1936), Änwendung der Ahnlichkeitsmechanik und der Turbulenzforschung auf die Geschiebebewegung, *Mitt. Preuss. Vers. Anst. Wasserb. Schiffb., 26*, 26 pp. (translated by W. P. Ott & J. C. van Uchelen, U.S. Department of Agriculture, Soil Conservation Service Coop Laboratory, California Institute of Technology).

Schlichting, H. (1979), *Boundary-Layer Theory*, McGraw-Hill, 817 pp.

Schmeeckle, M. W., J. M. Nelson, and R. L. Shreve (2007), Forces on stationary particles in near-bed turbulent flows, *J. Geophys. Res., 112*, F02003, doi:10.1029/2006JF000536.

Whitaker, A. C., and D. F. Potts (2007), Coarse bed load transport in an alluvial gravel bed stream, Dupuyer Creek, Montana, *Earth Surface Processes and Landforms, 32*, 1984-2004.

White, C. M. (1940), The equilibrium of grains on the bed of a stream, *Proc. R. Soc. London A, 174*, 322-338.

Wiberg, P. and J. D. Smith (1985), A theoretical model for salting grains in water, *J. Geophys. Res., 90*, 7341-7354.

Wiberg, P. and J. D. Smith (1987), Calculations of the critical shear stress for motion of uniform and heterogeneous sediments, *Water Resour. Res., 23*, 1471-1480.

Wilcock, P. R. (1992), Experimental investigation of the effect of mixture properties on transport dynamics, in *Dynamics of Gravel Bed Rivers*, edited by P. Billi et al., pp. 24-39, John Wiley, New York.

Wilcock, P. R. (1996), Estimating local bed shear stress from velocity observations, *Water Resour. Res., 32(11)*, 3361-3366.

Wilcock, P. R. (1998), Two-fraction model of initial sediment motion in gravel-bed rivers, *Science, 280*, 410-412.

Wilcock, P. R., and J. C. Crowe (2003), Surface-based transport model for mixed-size sediment, *Journal of Hydraulic Engineering, 129(2)*, 120-128.

Wilcock, P. R., and J. P. Southard (1988) Experimental study of incipient motion in mixed size sediment, *Water Resour. Res., 24*, 1137-1151.

Wilcock, P. R., G. M. Kondolf, W. V. G. Matthews, and A. F. Barta (1996), Specification of sediment maintenance flows for a large gravel-bed river, *Water Resour. Res., 32(9)*, 2911-2921.

Wilcock P. R., and B. W. McArdell (1997), Partial transport of a sand gravel sediment, *Water Resour. Res., 33(1),* 235-245.

Wolman, M. G (1954), A method of sampling coarse river-bed material, *Transactions, AGU, 35(6),* 951-956.

Wu, F.-C., and K.-H. Yang (2004), A stochastic partial transport model for mixed-size sediment: Application to assessment of fractional mobility, *Water Resour. Res., 40,* W04501, doi:10.1029/2003WR002256.

Appendix A: Grain Positioning and Frictional Resistance Box Plots

The position of each gaged grain was characterized by its support against and among neighboring grains. Categorizing the grains required assignment based on the assumed greatest support provided. For example, a gaged grain may have been sheltered from flow by a larger grain immediately upstream but also braced against a larger grain than itself on its downstream side. Which of these provided the most support was assumed to be in the following order of decreasing support: embedded, loosely buried, imbricated, braced, sheltered, and loosely exposed.

In general, smaller grains tended to be more likely to be sheltered than larger grains while larger grains were more likely to be loosely exposed or embedded than smaller grains. The following boxplots illustrate the relationship of these support categorizations with grain resistance and grain size (Figure A-1). An example of this is that sheltered grains tend to have the lowest resistance to movement and therefore their frictional resistance is expressed at the lower tail of the distribution. But because they are sheltered their frictional resistance to movement is not as well represented by the predicted flow strength that is able to mobilize them. This hiding effect likely truncates the lower tail of the distribution of critical Shields stress values predicted from the force balance such that the effective resistance to entrainment of those smaller grains in the lower tail of the distribution is greater than the predicted values.

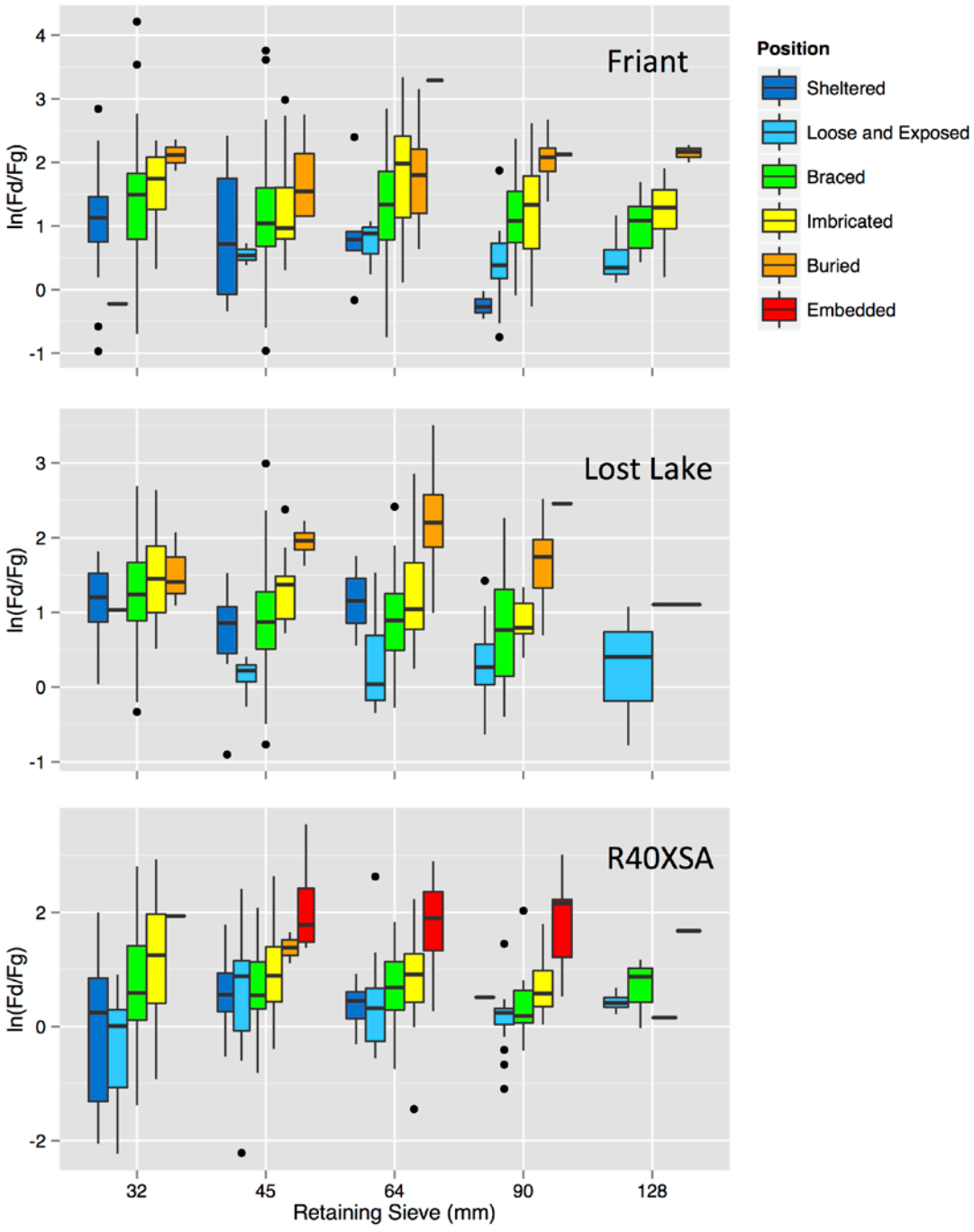
Friant
Lost Lake
R40XSA
ln(Fd/Fg)
Retaining Sieve (mm)
32
45
64
90
128
Position
Sheltered
Loose and Exposed
Braced
Imbricated
Buried
Embedded

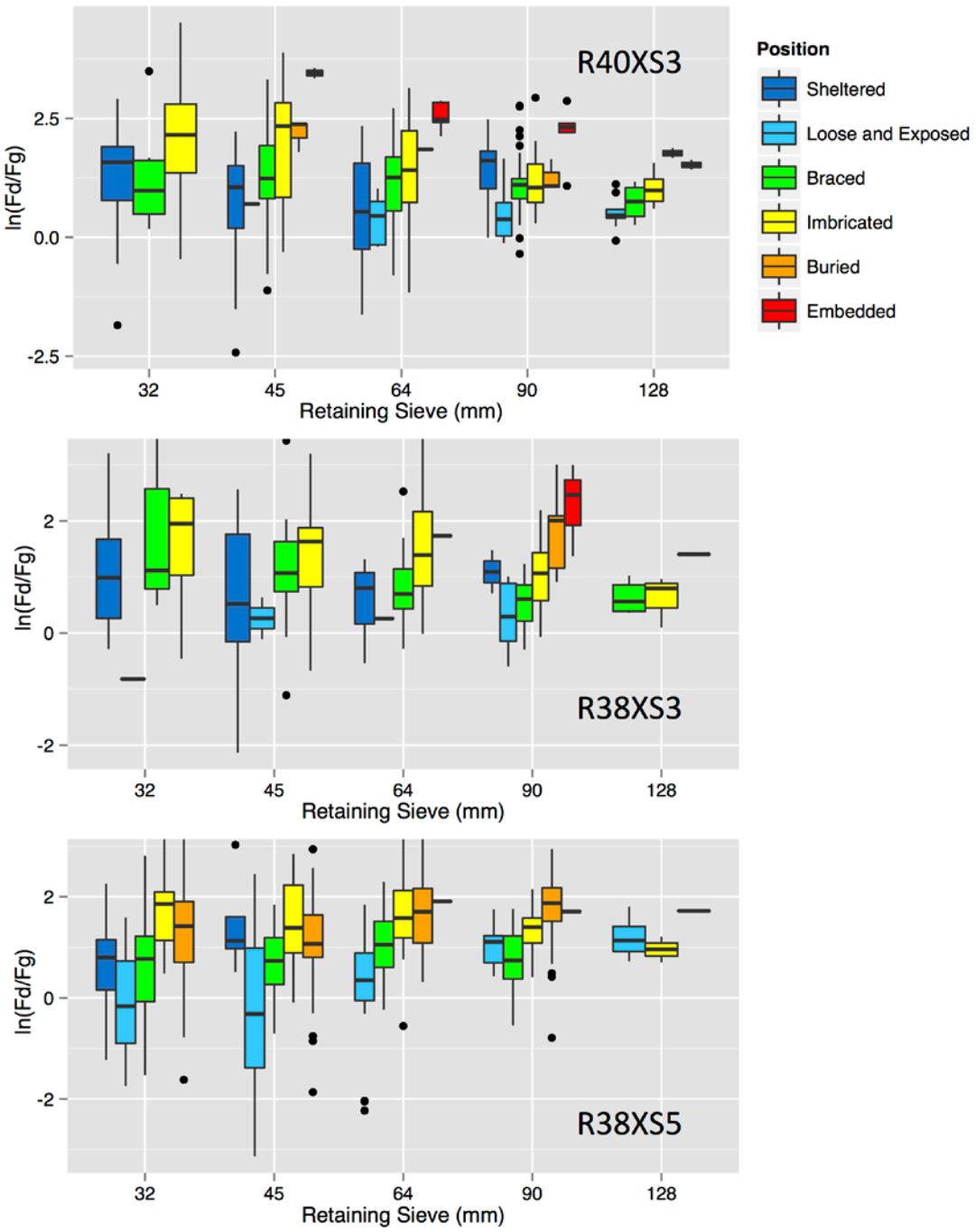

Figure A-1. Support categorization boxplots. Characteristics of the distribution of frictional resistance of each support type (color) are shown for each grain size fraction (abscissa) and site (plots). The vertical limits of the boxes indicate the first and third quartiles, the thick horizontal bar indicates the median value, the whiskers indicate the extent of measurements beyond the inner quartile range but within 1.5 times the interquartile range, and the dots indicate outliers that are beyond the range of the whiskers. In cases when (i) no measurements were collected there is no box or bar shown; and (ii) only one measurement was made only a bar is shown.

Appendix B: Summary of Force Gaged Grain Size and Resistance

Table B-1: Measures of grain size and resistance for each grain size class. Resistance measurements do not include embedded or buried gaged grains, except for R38XS5 that does include buried grains (see main body of report in Methods). The geometric center of each size class is given from $D_i = 10^{\left[\left(\log D_r - \log D_p\right)/2\right]}$ where D_r and D_p are the largest retaining and smallest passing sieves, respectively [*Bunte and Abt*, 2001]. Sorting is computed from $\sigma = 3.32[(\log D_{84} - \log D_{16})/4 + (\log D_{95} - \log D_5)/6.6]$ where the subscripted numbers refer the percentile of the grain size distribution [*Blatt et al.*, 1980].

Size class	32 mm	45 mm	64 mm	90 mm	128 mm
Geometric center of class (mm)	38	54	76	107	152
Friant (Riffle), D_{50}=44 mm, σ=1.7					
Mean nominal diameter (mm)+/-stdev	44 +/- 5	60 +/- 7	82 +/- 10	117 +/- 14	153 +/- 17
Mean A-axis (mm) +/- stdev	65 +/- 12	88 +/- 18	121 +/- 25	166 +/- 32	210 +/- 35
Mean B-axis (mm) +/- stdev	47 +/- 5	66 +/- 8	90 +/- 11	129 +/- 16	165 +/- 17
Mean C-axis (mm) +/- stdev	28 +/- 6	38 +/- 9	52 +/- 12	77 +/- 16	104 +/- 19
Number of F_d measurements	89	103	124	88	24
Median ϕ_i(degrees) +/- stdev	77 +/- 14	69 +/- 14	76 +/- 13	67 +/- 14	69 +/- 11
Mean ln(F_d/F_g)$_i$ +/- stdev	1.3 +/- 0.8	1.1 +/- 0.9	1.4 +/- 0.9	1.0 +/- 0.7	0.93 +/- 0.54
Mean $\tau^*_{c,i}$ +/- stdev	0.060 +/- 0.017	0.044 +/- 0.012	0.041 +/- 0.011	0.028 +/- 0.010	0.027 +/- 0.006
Lost Lake (Pool Tail-out), D_{50}=36 mm, σ=1.3					
Mean nominal diameter (mm)+/-stdev	44 +/- 5	58 +/- 8	87 +/- 9	111 +/- 12	153 +/- 7
Mean A-axis (mm) +/- stdev	65 +/- 14	85 +/- 18	129 +/- 23	157 +/- 23	199 +/- 18
Mean B-axis (mm) +/- stdev	46 +/- 5	62 +/- 9	93 +/- 10	123 +/- 15	164 +/- 5
Mean C-axis (mm) +/- stdev	30 +/- 6	37 +/- 9	55 +/- 11	72 +/- 15	103 +/- 10
Number of F_d measurements	108	96	88	77	3
Median ϕ_i (degrees) +/- stdev	74 +/- 11	67 +/- 13	67 +/- 13	58 +/- 14	56 +/- 24
Mean ln(F_d/F_g)$_i$ +/- stdev	1.2 +/- 0.6	0.88 +/- 0.65	0.82 +/- 0.65	0.57 +/- 0.62	0.23 +/- 0.94
Mean $\tau^*_{c,i}$ +/- stdev	0.048 +/- 0.011	0.037 +/- 0.010	0.030 +/- 0.008	0.023 +/- 0.006	0.017 +/- 0.009
R40XSA (Pool Tail-out), D_{50}=66 mm, σ=1.2					
Mean nominal diameter (mm)+/-stdev	43 +/- 4	59 +/- 6	82 +/- 10	115 +/- 13	160 +/- 12
Mean A-axis (mm) +/- stdev	63 +/- 10	85 +/- 14	115 +/- 17	163 +/- 32	218 +/- 24
Mean B-axis (mm) +/- stdev	46 +/- 6	65 +/- 7	92 +/- 12	124 +/- 16	164 +/- 14
Mean C-axis (mm) +/- stdev	28 +/- 6	38 +/- 8	53 +/- 12	78 +/- 15	115 +/- 22
Number of F_d measurements	73	81	92	40	8
Median ϕ_i (degrees) +/- stdev	56 +/- 25	64 +/- 16	59 +/- 15	52 +/- 13	56 +/- 10
Mean ln(F_d/F_g)$_i$ +/- stdev	0.24 +/- 1.21	0.69 +/- 0.80	0.56 +/- 0.68	0.29 +/- 0.57	0.49 +/- 0.40
Mean $\tau^*_{c,i}$ +/- stdev	0.054 +/- 0.028	0.052 +/- 0.016	0.041 +/- 0.013	0.028 +/- 0.008	0.026 +/- 0.006
R40XS3 (Riffle), D_{50}=63 mm, σ=2.2					
Mean nominal diameter (mm)+/-stdev	45 +/- 4	58 +/- 6	83 +/- 11	117 +/- 14	151 +/- 14
Mean A-axis (mm) +/- stdev	65 +/- 9	84 +/- 13	119 +/- 23	165 +/- 25	205 +/- 26
Mean B-axis (mm) +/- stdev	51 +/- 6	63 +/- 8	91 +/- 12	132 +/- 15	166 +/- 13
Mean C-axis (mm) +/- stdev	27 +/- 6	38 +/- 9	55 +/- 13	74 +/- 16	102 +/- 19
Number of F_d measurements	42	87	92	113	27
Median ϕ_i (degrees) +/- stdev	79 +/- 18	74 +/- 20	73 +/- 18	69 +/- 14	65 +/- 9
Mean ln(F_d/F_g)$_i$ +/- stdev	1.5 +/- 1.2	1.3 +/- 1.2	1.1 +/- 1.0	1.0 +/- 0.8	0.80 +/- 0.40
Mean $\tau^*_{c,i}$ +/- stdev	0.077 +/- 0.023	0.061 +/- 0.022	0.044 +/- 0.015	0.037 +/- 0.009	0.030 +/- 0.006
R38XS3 (Riffle), D_{50}=72 mm, σ=0.9					
Mean nominal diameter (mm)+/-stdev	45 +/- 4	60 +/- 8	84 +/- 11	114 +/- 14	154 +/- 12
Mean A-axis (mm) +/- stdev	70 +/- 15	93 +/- 16	126 +/- 23	161 +/- 28	211 +/- 31
Mean B-axis (mm) +/- stdev	49 +/- 6	68 +/- 8	97 +/- 11	128 +/- 13	168 +/- 12
Mean C-axis (mm) +/- stdev	25 +/- 5	34 +/- 10	49 +/- 12	71 +/- 16	103 +/- 18
Number of F_d measurements	28	55	69	62	9
Median ϕ_i (degrees) +/- stdev	71 +/- 19	71 +/- 19	66 +/- 13	65 +/- 13	63 +/- 8
Mean ln(F_d/F_g)$_i$ +/- stdev	1.2 +/- 1.2	1.1 +/- 1.1	0.95 +/- 0.79	0.77 +/- 0.61	0.63 +/- 0.32
Mean $\tau^*_{c,i}$ +/- stdev	0.085 +/- 0.025	0.068 +/- 0.023	0.048 +/- 0.013	0.037 +/- 0.010	0.029 +/- 0.006
R38XS5 (Inside Margin of Bend), D_{50}=32 mm, σ=2.3					
Mean nominal diameter (mm)+/-stdev	43 +/- 5	58 +/- 8	84 +/- 9	114 +/- 13	151 +/- 6
Mean A-axis (mm) +/- stdev	64 +/- 12	86 +/- 17	121 +/- 20	156 +/- 25	203 +/- 17
Mean B-axis (mm) +/- stdev	47 +/- 5	65 +/- 8	92 +/- 11	121 +/- 14	150 +/- 7
Mean C-axis (mm) +/- stdev	28 +/- 6	36 +/- 9	55 +/- 11	82 +/- 16	113 +/- 17
Number of F_d measurements	99	105	119	94	9
Median ϕ_i (degrees) +/- stdev	68 +/- 22	68 +/- 23	75 +/- 18	77 +/- 11	73 +/- 6
Mean ln(F_d/F_g)$_i$ +/- stdev	0.84 +/- 1.1	0.71 +/- 1.2	1.2 +/- 1.1	1.4 +/- 0.7	1.2 +/- 0.4
Mean $\tau^*_{c,i}$ +/- stdev	0.040 +/- 0.015	0.033 +/- 0.013	0.031 +/- 0.010	0.029 +/- 0.006	0.025 +/- 0.004

Appendix C: Fluctuations in the Shear Stress

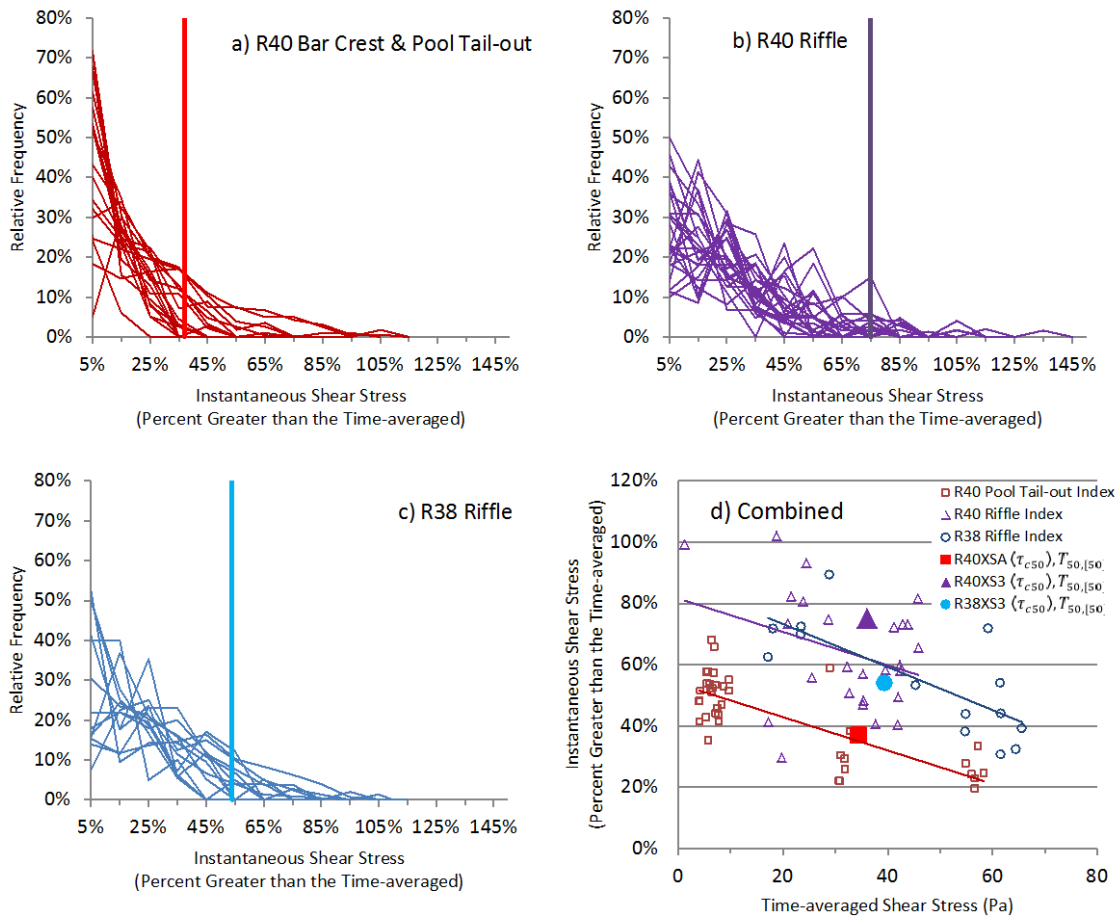

Figure C-1: Instantaneous shear stress (i.e., fluctuations) calculated from flow velocity measurements distributions and comparison to the time-averaged. Plots a-c show truncated histograms of the relative frequency of measurement values as a function of the standardized instantaneous shear stress (i.e., $100\%\ (\bar{\tau} - \bar{\bar{\tau}})/\bar{\bar{\tau}}$, approx. 90/2 measurements of $\bar{\tau}$ per sample) for $\bar{\tau}$ in excess of the $\bar{\bar{\tau}}$ (one $\bar{\bar{\tau}}$ value per sample). Results are shown from the velocity measurement samples (n) from random locations in the vicinity of site (a) R40XSA from R40 Crest-Pool Tail (n=36), (b) R40XS3 from R40 Riffle (n=26), and (c) R38XS3 from R38 Riffle (n=14). A histogram of each sample is represented by the fine lines and each fine line represents a sample of approx. 90 $\bar{\tau}$ values computed from depth-averaged velocity measurements that was collected over a 90 second time interval at a fixed position. The histogram is separated into bins of 10% widths with centers at 5%, 15%, etc. The $\bar{\bar{\tau}}$ value for each sample of velocity measurements has an abscissa value of 0%. The bottom right panel (d, same as Figure 8) shows the 97.8th percentile of the instantaneous shear stress fluctuations in the τ values, as expressed by the index of shear stress fluctuation where $100\%\ [(\bar{\bar{\tau}} + 2 \times RMSD\ of\ \bar{\tau}) - \bar{\bar{\tau}}]/\bar{\bar{\tau}}$, as a function of $\bar{\bar{\tau}}$ (hollow symbols) and whose trend is illustrated with fitted lines from OLS linear regression. The force balance predicted $\langle \tau_{c,50} \rangle$ values are used to compute the percentage difference with the tracer entrainment measured $T_{50,[50]}$ values (i.e., $100\%(\langle \tau_{c50} \rangle - T_{50,[50]})/T_{50,[50]}$) and are plotted as a function of $T_{50,[50]}$. These percentages are plotted as (i) vertical lines on plots a-c for reference, and (ii) solid symbols on plot d.

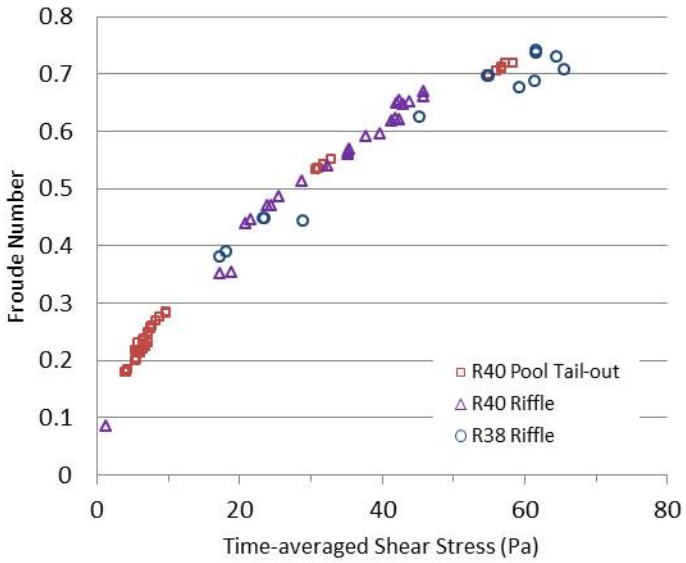

Figure C-2. Trend in Froude number with increasing time-averaged shear stress. Flow velocity measured time-averaged shear stresses, same as in Figure C-1d, are compared against the Froude number *Fr* that is calculated from the flow velocity *u* and depth *h* measurements, such that: $Fr = \bar{\bar{u}}/(hg)^{0.5}$. The results demonstrate that the flow becomes less tranquil with increasing shear stress. The data collapse contrasts with the wide range and differences between sites with the instantaneous shear stress relative to the time-averaged shear stress in Figure C-1d.

Appendix D: Friction Angles

D-1. Variation within a Grain Size Class

The variance of frictional resistance is illustrated using the inter-quartile values of the ϕ_i distributions about its median value as a function of the relative grain size, D_i/D_{50} (Figure D-1). These plots illustrate a skew in the distributions such that the upper quartile range tends to be narrower than that of the lower quartile. This deviation from symmetry is also detected on quantile-quantile (q-q) plots (Appendix E). Overall, the within size class variability in the ϕ_i values range from approximately 10° to 90°. This range is comparable to *Johnston et al.* [1998] force gage results but narrower than *Buffington et al.* [1992]. It is possible for a ϕ value to be greater than 90° as were measured by *Kirchner et al.* [1990] and *Buffington et al.* [1992] using tilting boards to determine the angle at which a grain moved. But by solving (1) for ϕ the range is limited to ϕ values of $0° < \phi < 90°$. This limitation truncates and affects the skew of the greater ϕ values thereby causing them to asymptotically approach 90° as F_d/F_g approaches infinity. Thus, the force gage measured ϕ_i values are not well characterized by a symmetrical distribution.

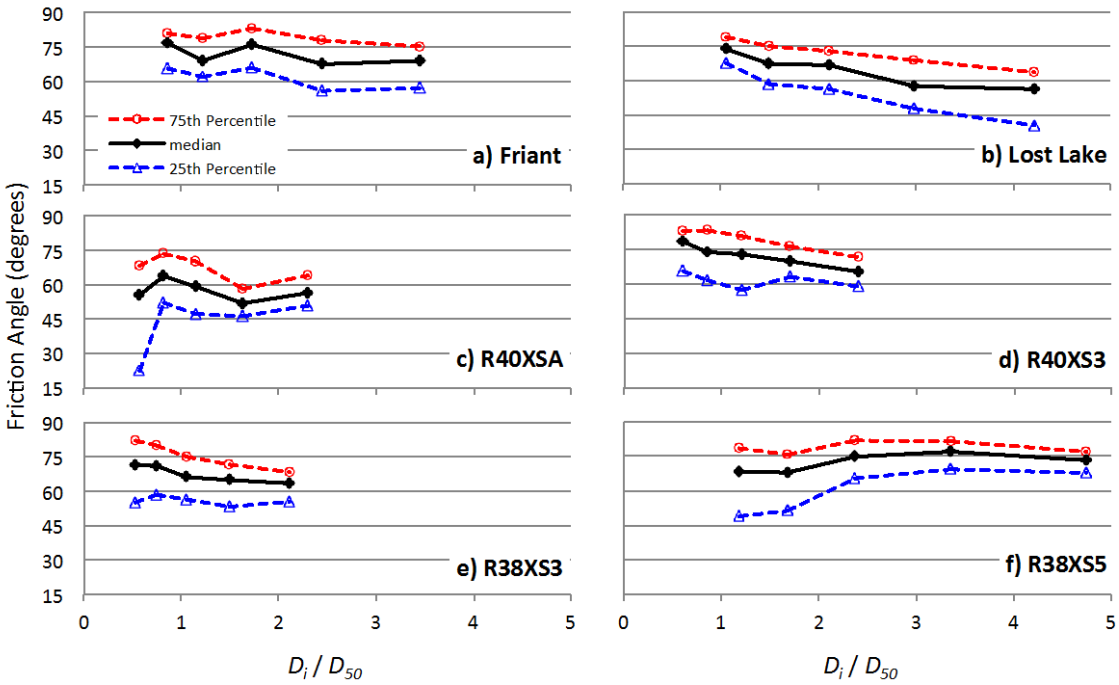

Figure D-1: Friction angle trends as a function of the relative grain size. The median (black), upper quartile (red), and lower quartile (blue) friction angles are shown for the relative grain sizes of five size classes.

D-2. Variation Between Grain Size Classes

I fitted the median ϕ_i values as a function of D_i/D_{50} to produce equations of the form of equation (2) using OLS regression. These regression models were compared with those of previous researchers [*Miller and Byrne*, 1966; *Li and Komar*, 1986; *Kirchner et al.*, 1990; *Buffington et al.*, 1992; *Johnston et al.*, 1998] that used equation (2) to define their average ϕ_i. The value of the intercept coefficient *e* is the approximation of the $\phi_{i,50}$, where subscripted '50 refers to the value for grains equal in size to that of the D_{50}, and provides an index for comparing magnitudes between sites. The value of *f* quantifies the degree of change in $\phi_{i,50}$ with D_i such that greater *f* coefficients indicate that larger grain sizes are less resistant.

In general, the fitted trends in $\phi_{i,50}$ as a function of D_i/D_{50} generated values of *f* that are less than those found by most of the previous researcher's findings (Table D-1). The consistently low *f* values suggest this result is characteristic to the studied reach and

implies variation exists in the range of $\phi_{i,50}$ values beyond which was previously reported. At the same time, most of these coefficients indicate a decreasing trend as was found by the previous researchers. Only the $\phi_{i,50}$ values from the sandy margin at site R38XS5 increases with D_i/D_{50}. But this result is discounted by an ANOVA test that yielded a *p*-value = 0.13 thereby indicating that the trend is not significantly different from horizontal at a significance level of 0.05. The results from the Friant and R40XSA sites also indicate the lack of significance in their regression models (*p*-values > 0.26). Furthermore, the strength of the relationship between the $\phi_{50,i}$ and the D_i/D_{50} from these three sites are low as indicated by their relatively low coefficients of determination, R^2<0.60, thereby indicating that the $\phi_{50,i}$ values are not dependent on the grain size.

Table D-1. Coefficients of equation (2) that describe the trend of the $\phi_{50,i}$with D_i/D_{50}. Standard error (SE) of the coefficients and ANOVA test results probability (*p*-) values of the null hypothesis that the fit of the intercept-only model and the OLS regression model are equal; *p*-values less than α=0.05 indicate the model provides a better fit and suggests a significant trend in $\phi_{50,i}$ as a function of D_i/D_{50}.

	$median\ of\ \phi_i = e(D_i/D_{50})^{-f}$ (2)					
Friction Angle Study	*e* (degrees)	*e* SE (degrees)	*f*	*f* SE	R^2	*p*-value
Present Study, San Joaquin River, CA						
Friant	74.3	1.0	0.068	0.050	0.39	0.262
Lost Lake	74.4	1.0	0.20	0.031	0.93	0.007
R40XSA	57.6	1.0	0.050	0.074	0.13	0.551
R40XS3	73.6	1.0	0.12	0.015	0.96	0.004
R38XS3	67.6	1.0	0.094	0.015	0.96	0.008
R38XS5	67.4	1.0	-0.079	0.037	0.59	0.127
***Johnston et al.* [1998]**						
Pacific Creek, WY	61.9	0.8	0.28	0.03	0.94	NA
Van Duzen River, CA	49.1	1.1	0.45	0.05	0.92	NA
Sagehen Creek, CA	51.6	1.2	0.30	0.05	0.86	NA
Colorado River, CO	55.5	1.3	0.14	0.04	0.98	NA
***Buffington et al.* [1992]**						
Wildcat Creek, CA: D_{50}=4.1 mm	60	$\pm$1	0.26	0.02	0.99	NA
Wildcat Creek, CA: D_{50}=11.4 mm	51	$\pm$1	0.28	0.01	0.99	NA
Wildcat Creek, CA: D_{50}=14.0 mm	54	$\pm$1	0.21	0.05	0.91	NA
Wildcat Creek, CA: D_{50}=14.5 mm	46	$\pm$1	0.21	0.04	0.92	NA
Wildcat Creek, CA: D_{50}=45.0 mm	52	$\pm$1	0.24	0.04	0.93	NA
***Kirchner et al.* [1990]**						
Poorly sorted natural grains, flume bed	55.2	NA	0.31	NA	0.91	NA
Poorly sorted natural grains, unworked bed	66.1	NA	0.46	NA	0.99	NA
***Li and Komar* [1986], used mean ϕ_i as the dependent variable in (2)**						
Well-sorted, crushed basalt, artificial bed	51.3	NA	0.33	NA	0.98	NA
Well-sorted, spheres, artificial bed	20.4	NA	0.75	NA	0.99	NA
Well-sorted, ellipsoidal grains, artificial bed	31.9	NA	0.36	NA	0.87	NA
***Miller and Byrne* [1966] from *Kirchner et al.* [1990]**						
Poorly sorted, crushed quartzite, artificial bed	63.8	NA	0.28	NA	0.96	NA
Nearshore sand, artificial bed	57.3	NA	0.30	NA	0.98	NA
Poorly sorted glass spheres, artificial bed	45.7	NA	0.32	NA	0.91	NA
Well-sorted glass spheres, artificial bed	44.9	NA	0.44	NA	0.99	NA

D-3. Variation due to Grain Size Sorting

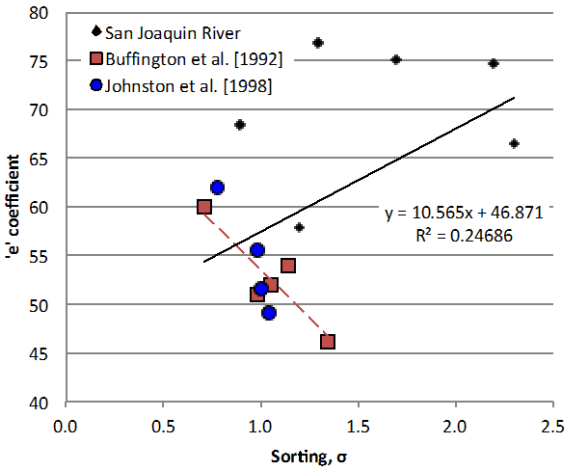

Figure D-2. Correlation of the '*e*' coefficient (Table D-1) as a function of the grain size sorting parameter as defined by *Blatt et al.* [1980]. Data is from this study, *Buffington et al.* [1992], and *Johnston et al.* [1998]. Linear regression trend lines are shown as presented by *Buffington et al.* (red dashed line, n=5) and from the results the three studies datasets (solid black line and linear equation, n=15, *p*-value=0.06).

Appendix E: Comparisons of Measures of Grain Resistance with the Theoretical Normal Distribution

The cumulative distributions of ϕ, $\ln(F_d/F_g)$, and τ_c^* for each grain size class (indicated by the largest retaining sieve size) at each site is compared with the standard theoretical normal distribution; where an abscissa value of zero is equal to the mean and unit distances from the mean are in standard deviations. Alignment of the measurements (points) with the diagonal line would indicate perfect agreement between the sample and theoretical distributions and deviation from the line indicates difference from the normal distribution. The results of Kolmogorov-Smirnov (K-S) normality tests that correspond to each these plots are provided in Table E-1.

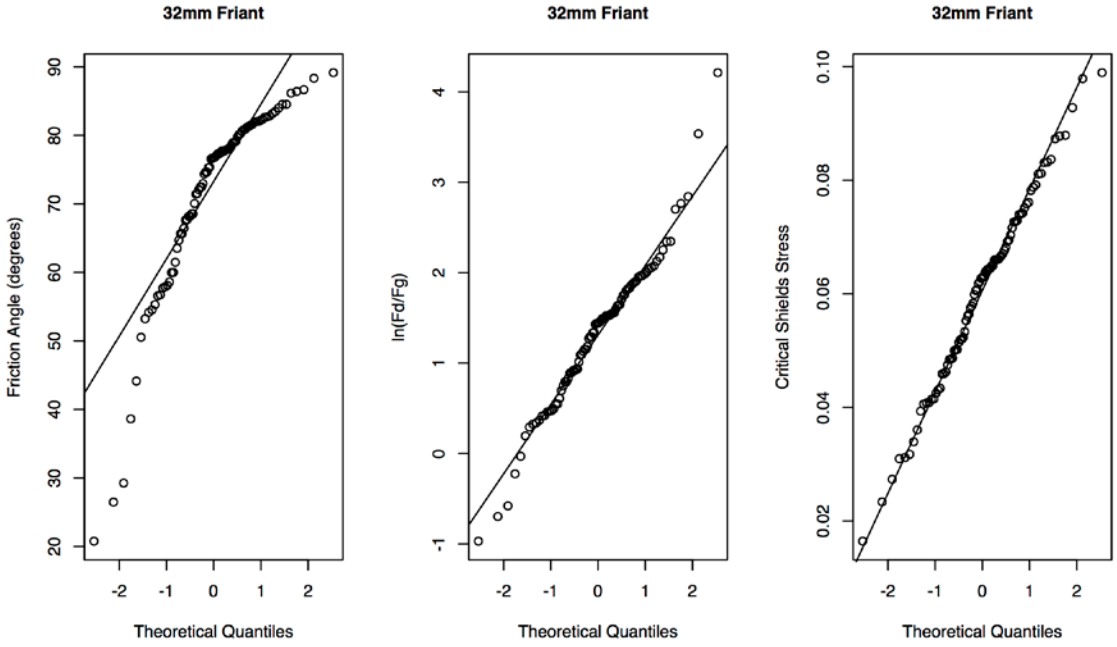
32mm Friant
Friction Angle (degrees)
Theoretical Quantiles
32mm Friant
ln(Fd/Fg)
Theoretical Quantiles
32mm Friant
Critical Shields Stress
Theoretical Quantiles

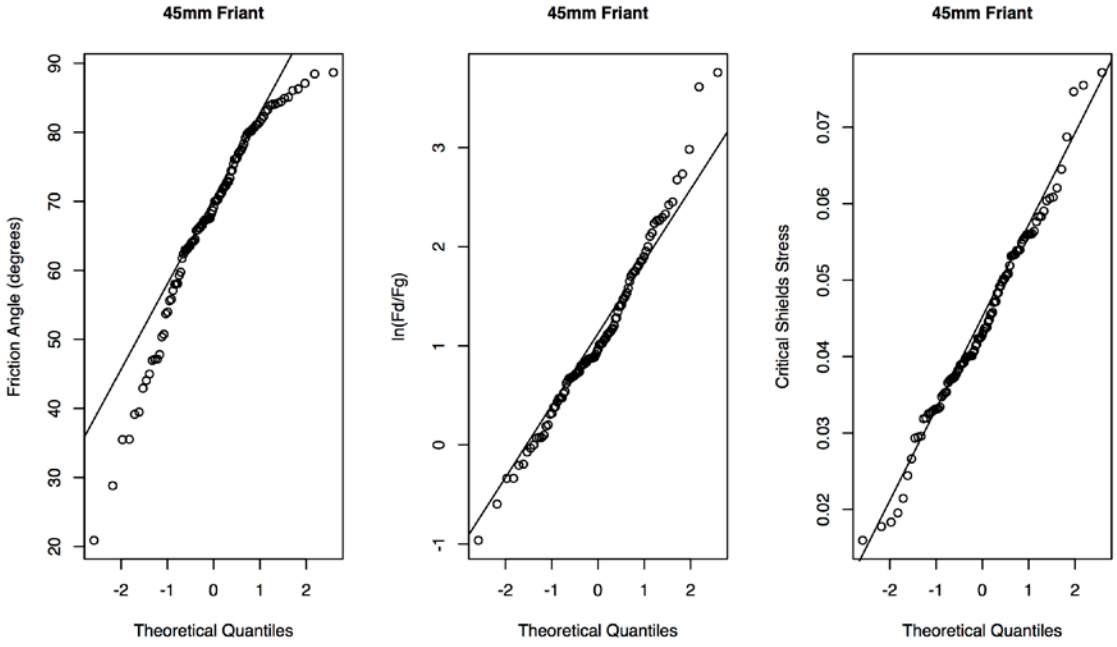
45mm Friant
Friction Angle (degrees)
Theoretical Quantiles
45mm Friant
ln(Fd/Fg)
Theoretical Quantiles
45mm Friant
Critical Shields Stress
Theoretical Quantiles

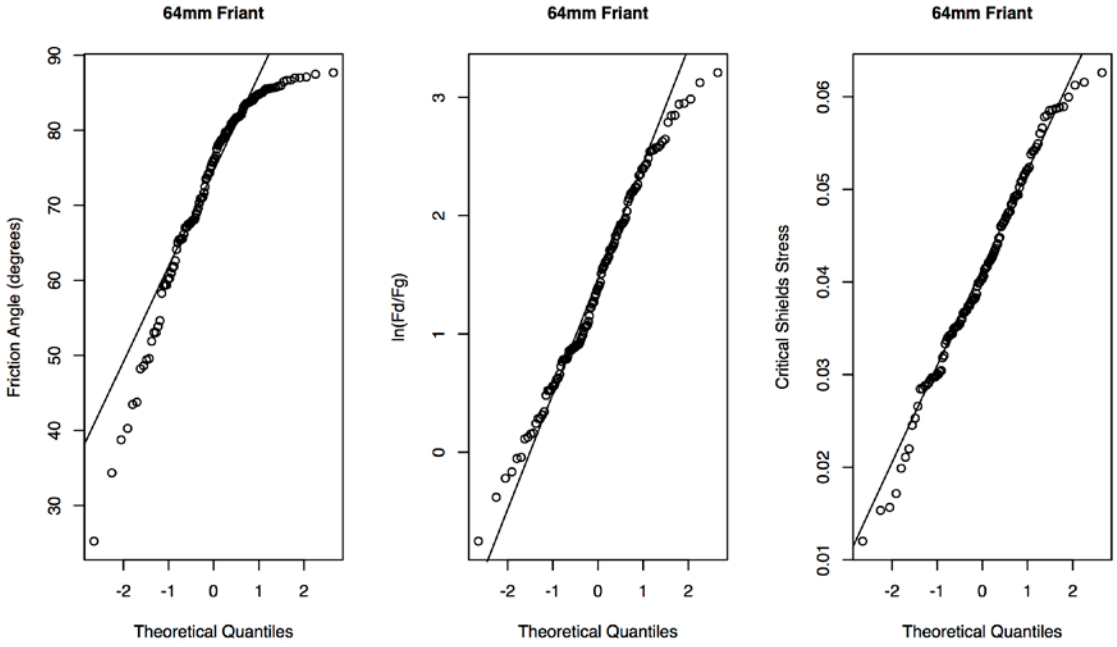
64mm Friant
Friction Angle (degrees)
Theoretical Quantiles
64mm Friant
ln(Fd/Fg)
Theoretical Quantiles
64mm Friant
Critical Shields Stress
Theoretical Quantiles

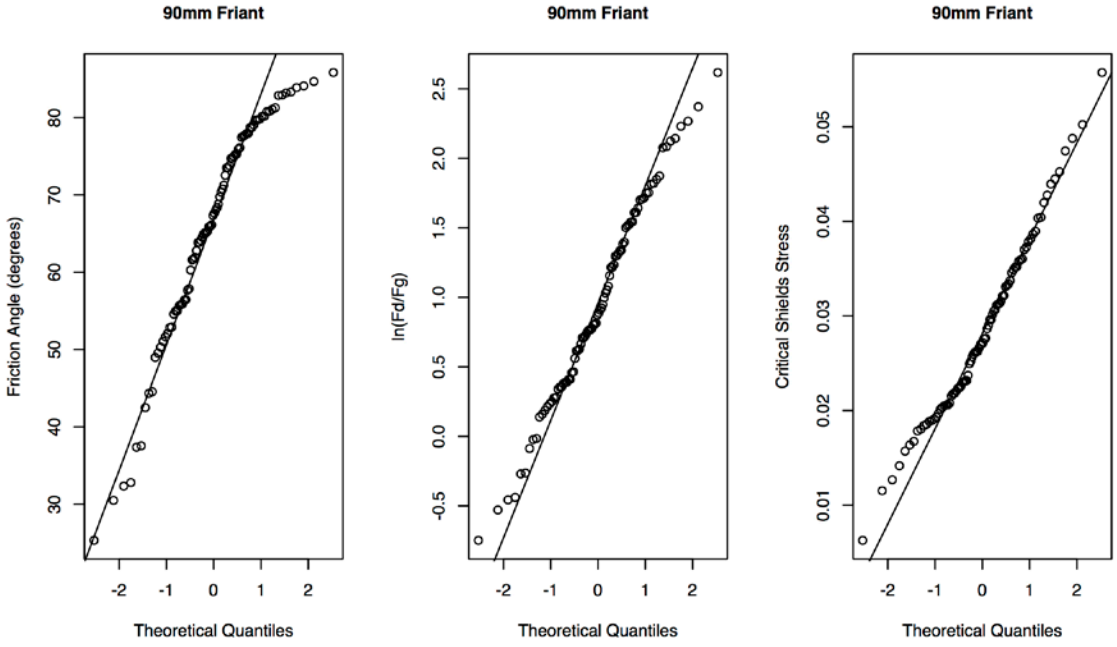
90mm Friant
Friction Angle (degrees)
Theoretical Quantiles
90mm Friant
ln(Fd/Fg)
Theoretical Quantiles
90mm Friant
Critical Shields Stress
Theoretical Quantiles

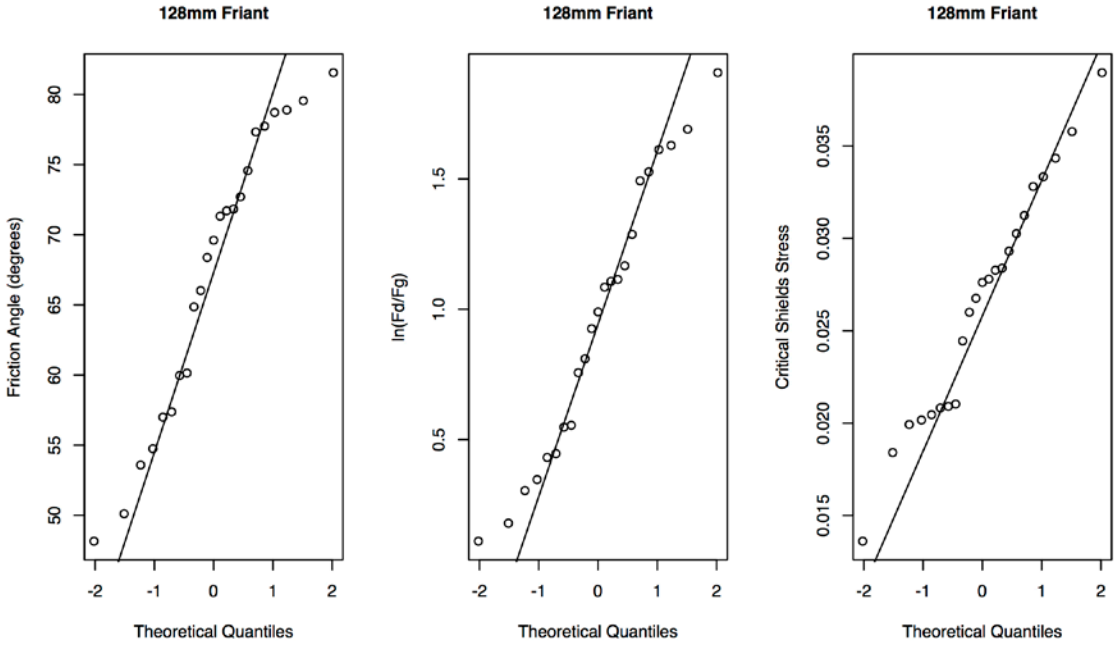
128mm Friant
Friction Angle (degrees)
Theoretical Quantiles
128mm Friant
ln(Fd/Fg)
Theoretical Quantiles
128mm Friant
Critical Shields Stress
Theoretical Quantiles

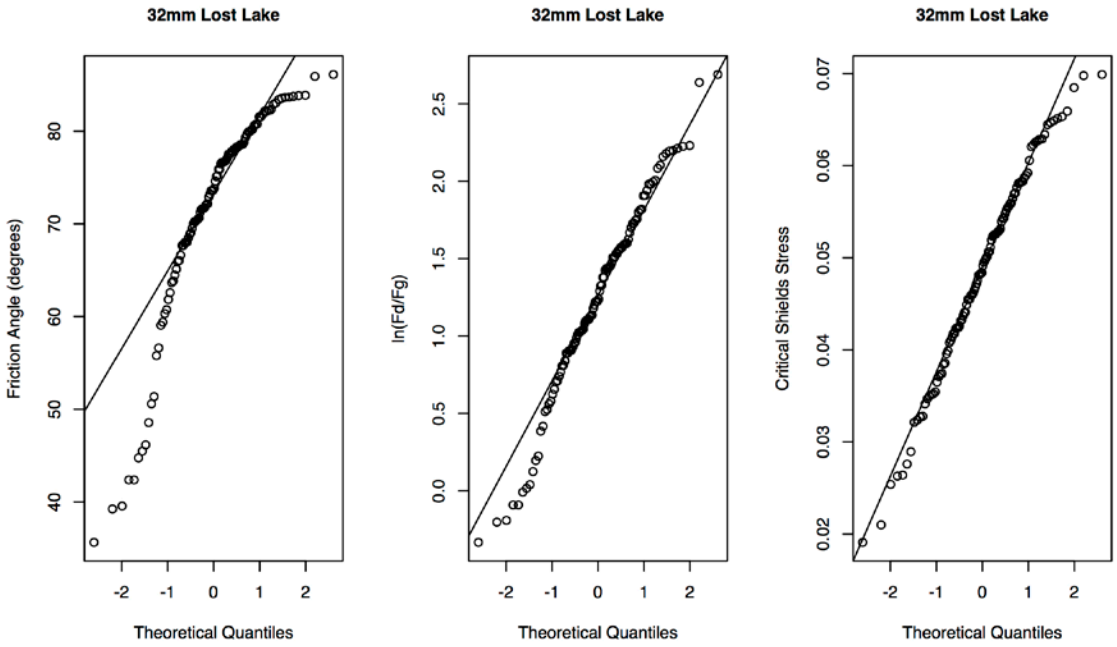
32mm Lost Lake
Friction Angle (degrees)
Theoretical Quantiles
32mm Lost Lake
ln(Fd/Fg)
Theoretical Quantiles
32mm Lost Lake
Critical Shields Stress
Theoretical Quantiles

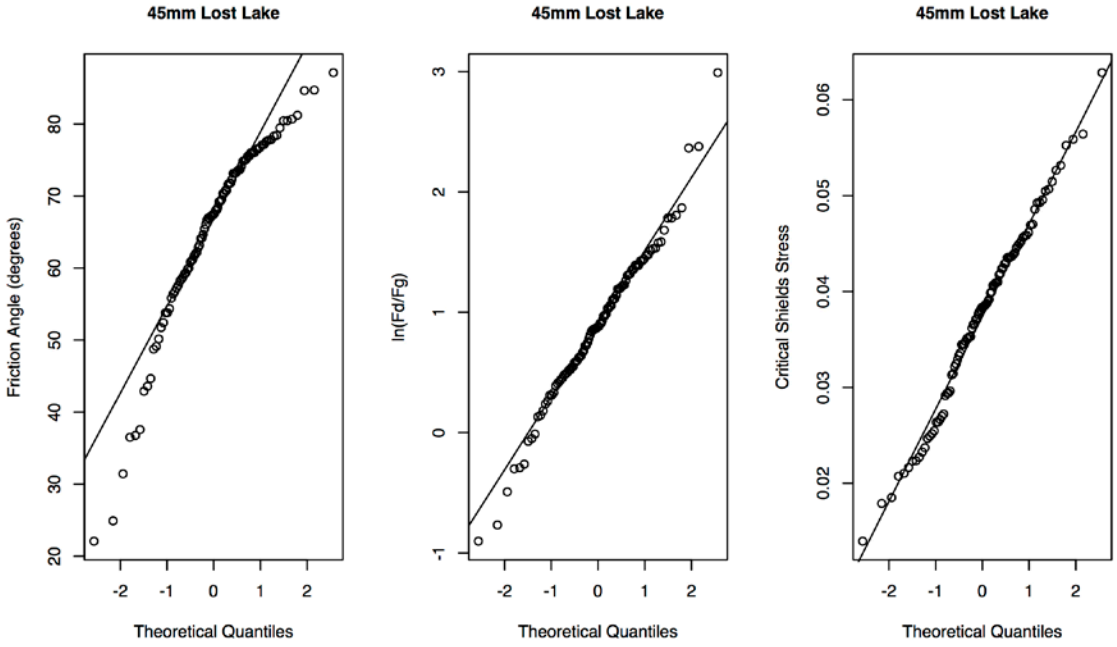
45mm Lost Lake
Friction Angle (degrees)
Theoretical Quantiles
45mm Lost Lake
ln(Fd/Fg)
Theoretical Quantiles
45mm Lost Lake
Critical Shields Stress
Theoretical Quantiles

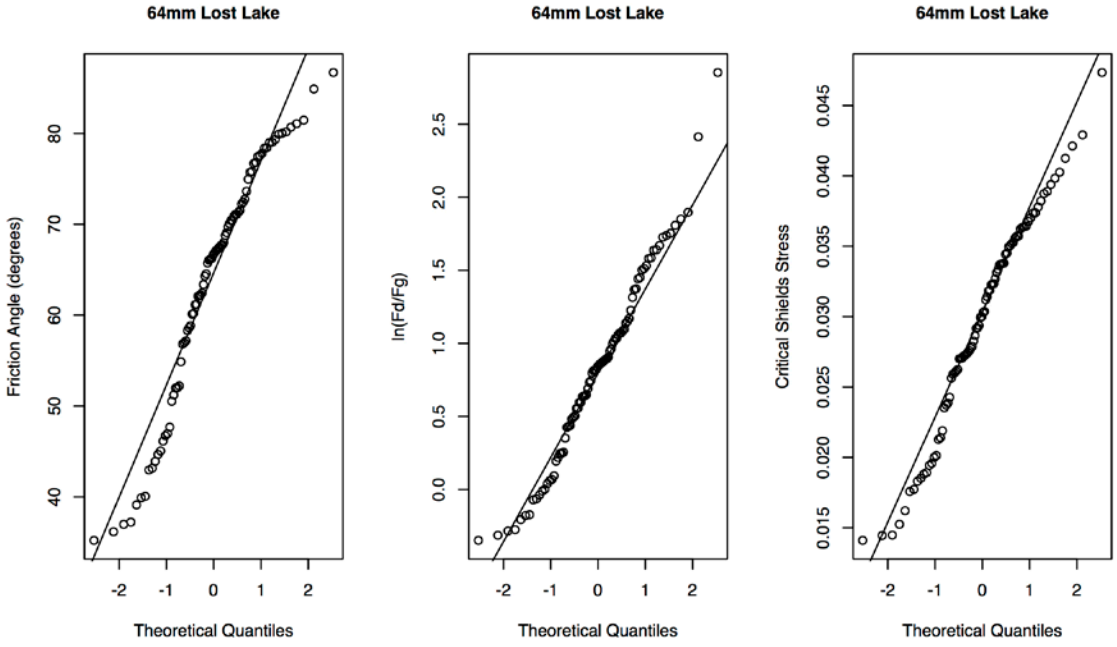
64mm Lost Lake
Friction Angle (degrees)
Theoretical Quantiles
64mm Lost Lake
ln(Fd/Fg)
Theoretical Quantiles
64mm Lost Lake
Critical Shields Stress
Theoretical Quantiles

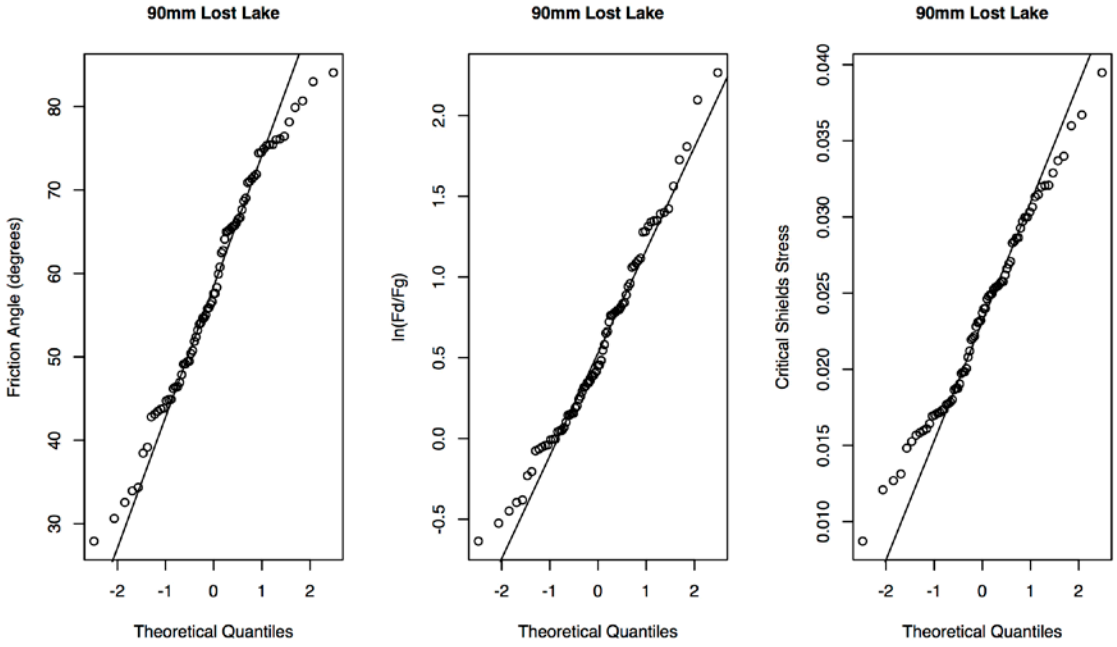
90mm Lost Lake
Friction Angle (degrees)
Theoretical Quantiles
90mm Lost Lake
ln(Fd/Fg)
Theoretical Quantiles
90mm Lost Lake
Critical Shields Stress
Theoretical Quantiles

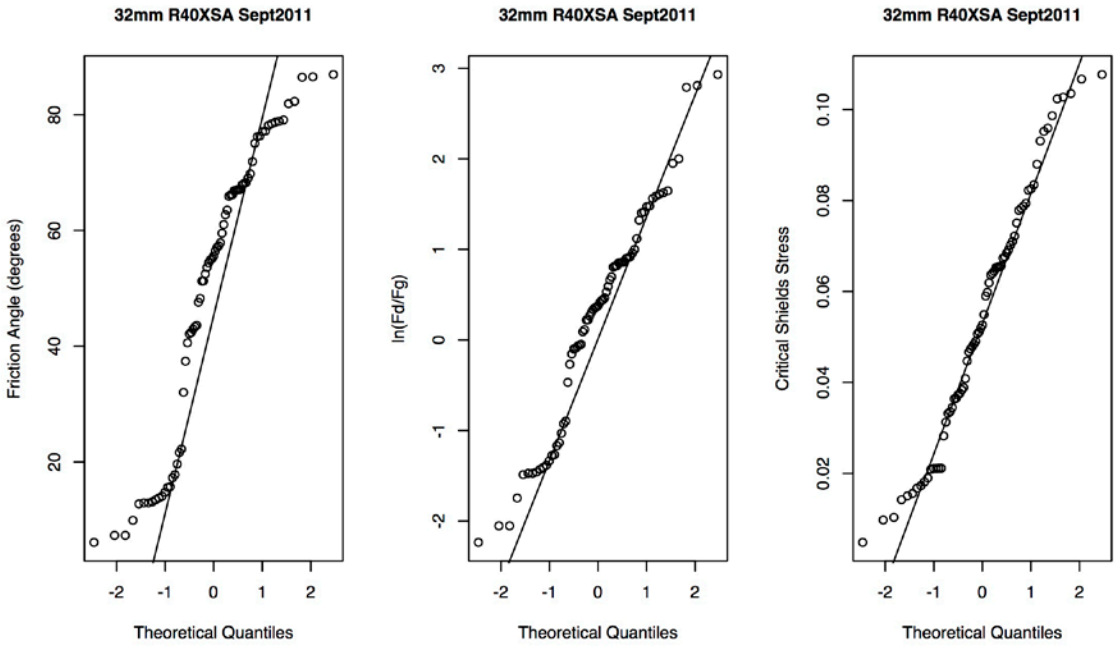
32mm R40XSA Sept2011
Friction Angle (degrees)
Theoretical Quantiles
32mm R40XSA Sept2011
ln(Fd/Fg)
Theoretical Quantiles
32mm R40XSA Sept2011
Critical Shields Stress
Theoretical Quantiles

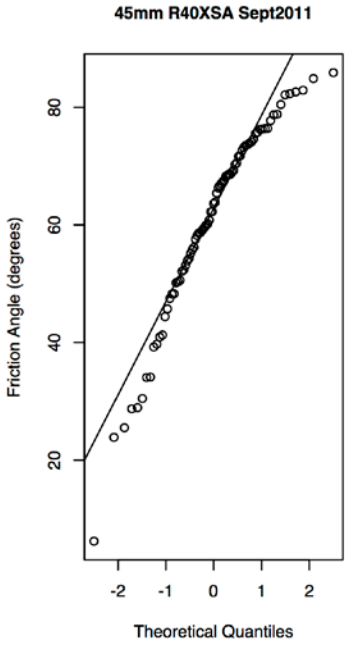
45mm R40XSA Sept2011
Friction Angle (degrees)
Theoretical Quantiles

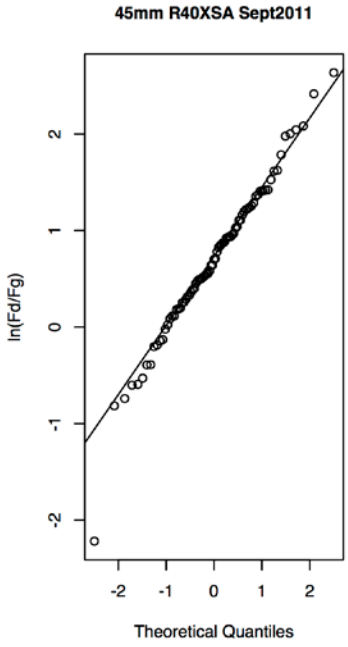
45mm R40XSA Sept2011
ln(Fd/Fg)
Theoretical Quantiles

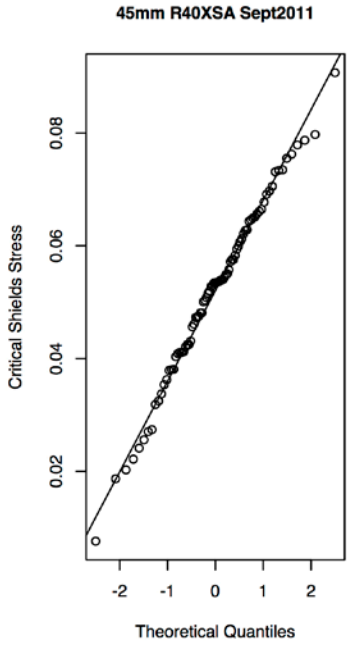
45mm R40XSA Sept2011
Critical Shields Stress
Theoretical Quantiles

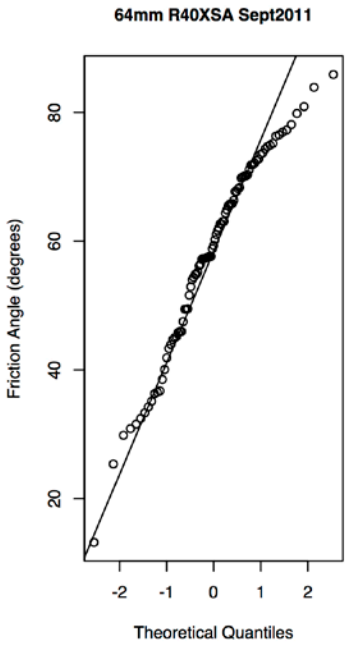
64mm R40XSA Sept2011
Friction Angle (degrees)
Theoretical Quantiles

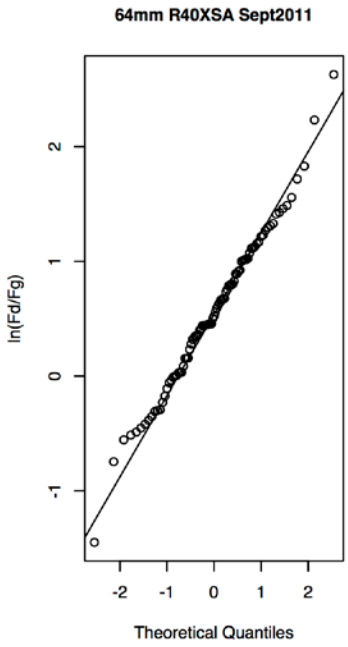
64mm R40XSA Sept2011
ln(Fd/Fg)
Theoretical Quantiles

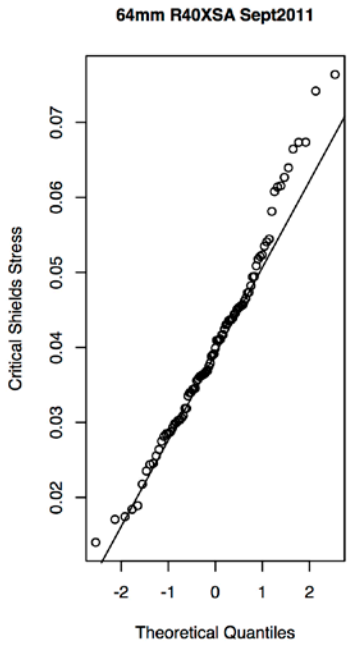
64mm R40XSA Sept2011
Critical Shields Stress
Theoretical Quantiles

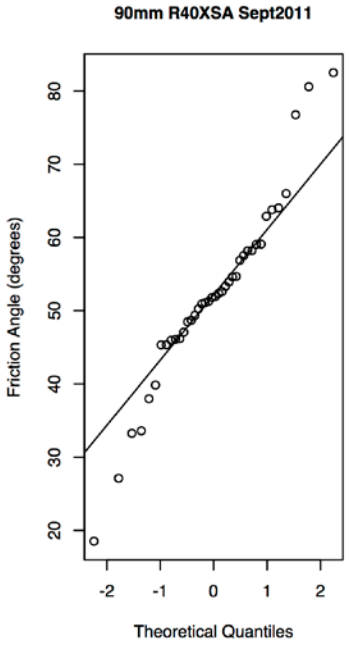
90mm R40XSA Sept2011
Friction Angle (degrees)
Theoretical Quantiles

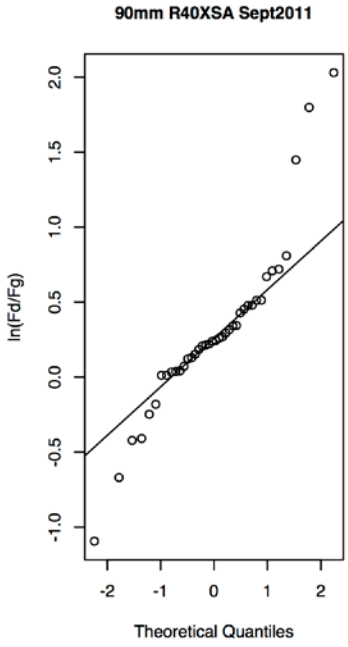
90mm R40XSA Sept2011
ln(Fd/Fg)
Theoretical Quantiles

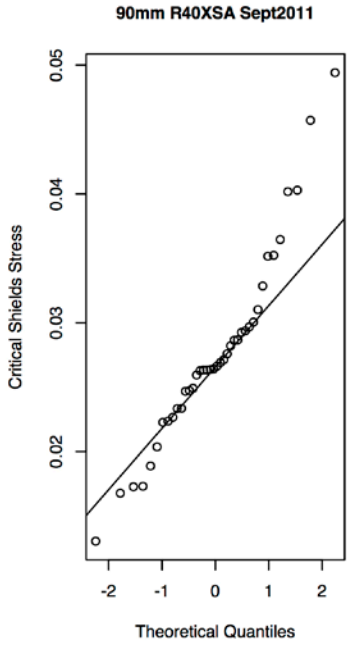
90mm R40XSA Sept2011
Critical Shields Stress
Theoretical Quantiles

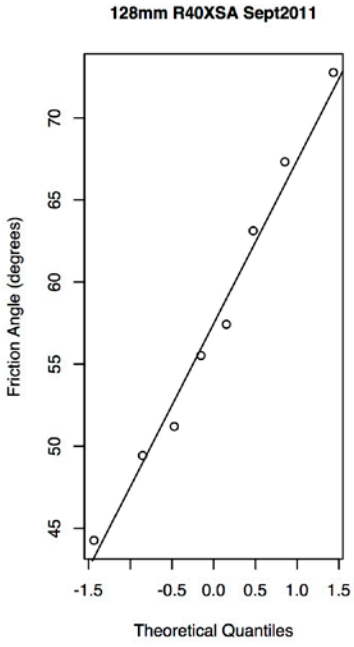
128mm R40XSA Sept2011
Friction Angle (degrees)
Theoretical Quantiles

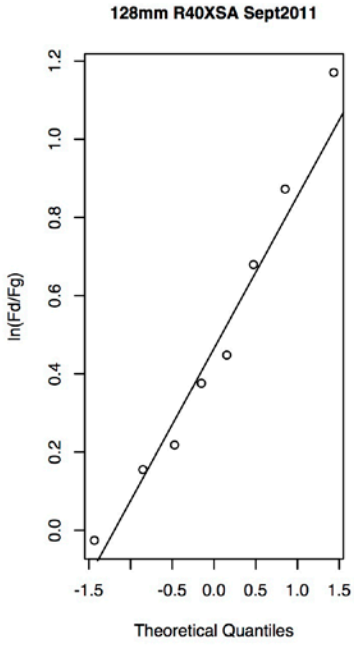
128mm R40XSA Sept2011
ln(Fd/Fg)
Theoretical Quantiles

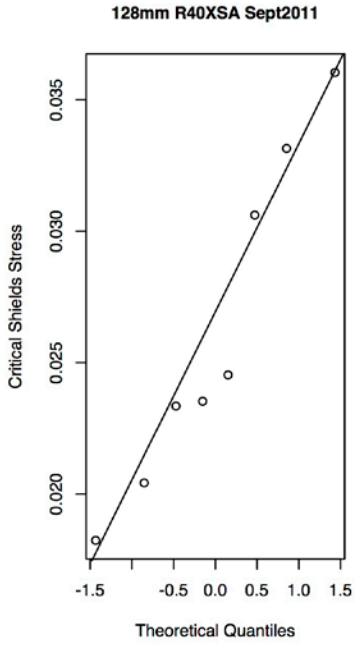
128mm R40XSA Sept2011
Critical Shields Stress
Theoretical Quantiles

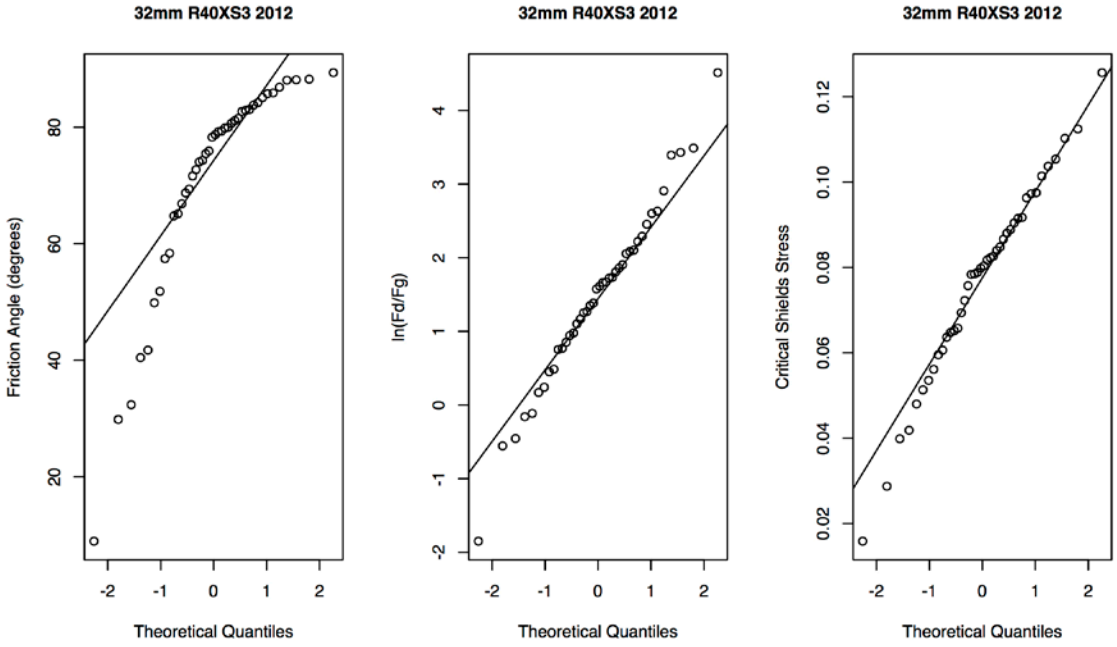
32mm R40XS3 2012
Friction Angle (degrees)
Theoretical Quantiles
32mm R40XS3 2012
ln(Fd/Fg)
Theoretical Quantiles
32mm R40XS3 2012
Critical Shields Stress
Theoretical Quantiles

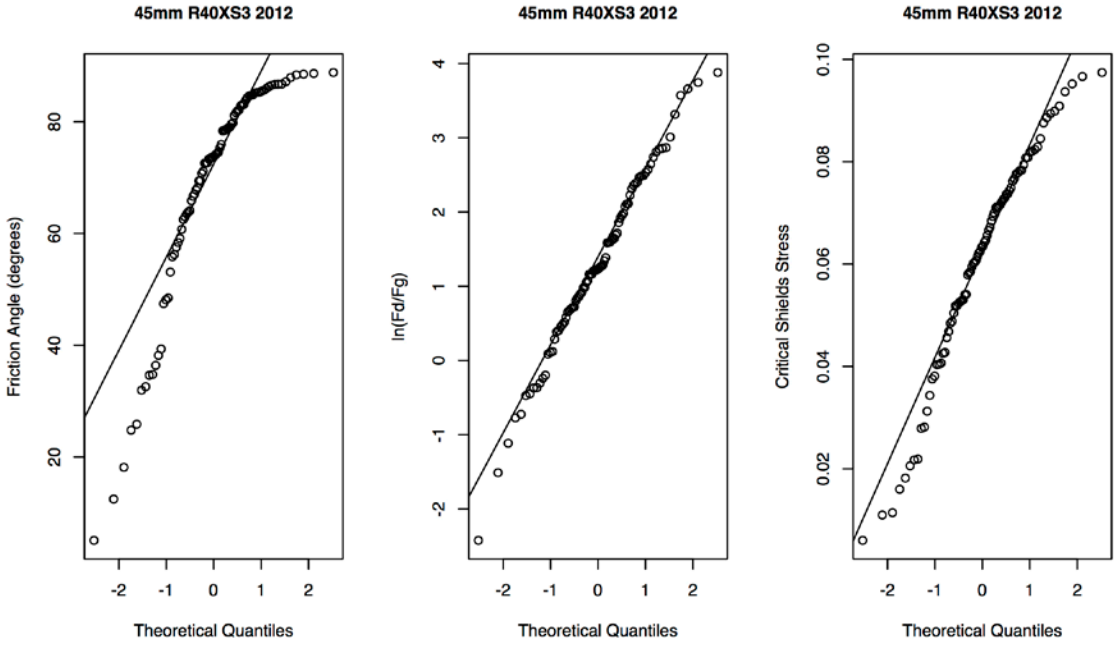
45mm R40XS3 2012
Friction Angle (degrees)
Theoretical Quantiles
45mm R40XS3 2012
ln(Fd/Fg)
Theoretical Quantiles
45mm R40XS3 2012
Critical Shields Stress
Theoretical Quantiles

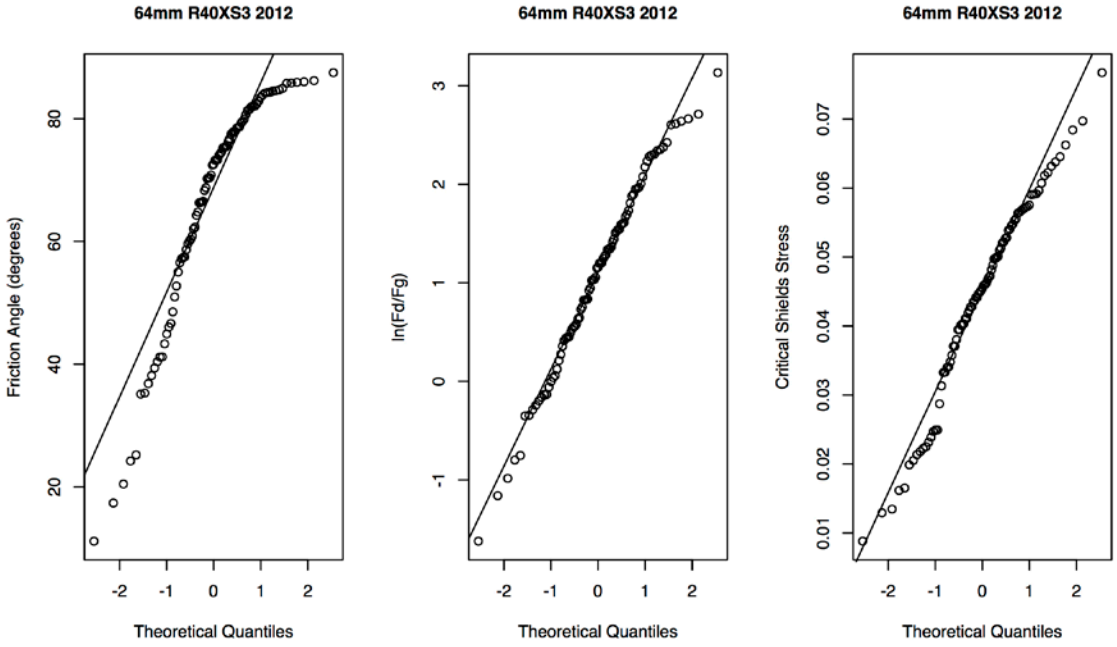
64mm R40XS3 2012
Friction Angle (degrees)
Theoretical Quantiles
64mm R40XS3 2012
ln(Fd/Fg)
Theoretical Quantiles
64mm R40XS3 2012
Critical Shields Stress
Theoretical Quantiles

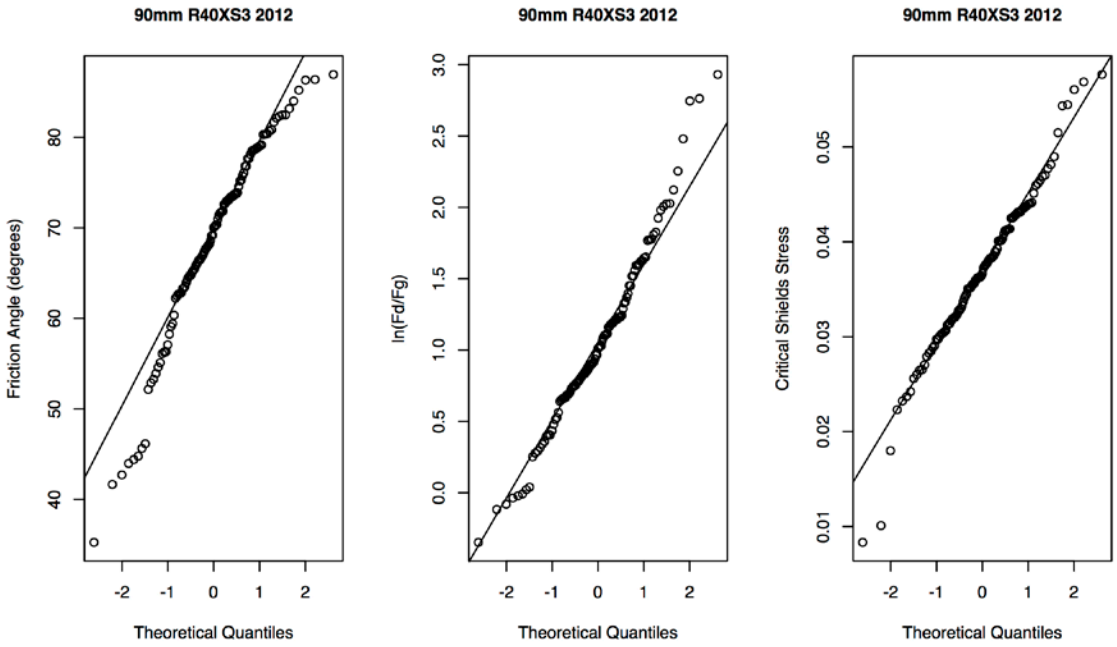
90mm R40XS3 2012
Friction Angle (degrees)
Theoretical Quantiles
90mm R40XS3 2012
ln(Fd/Fg)
Theoretical Quantiles
90mm R40XS3 2012
Critical Shields Stress
Theoretical Quantiles

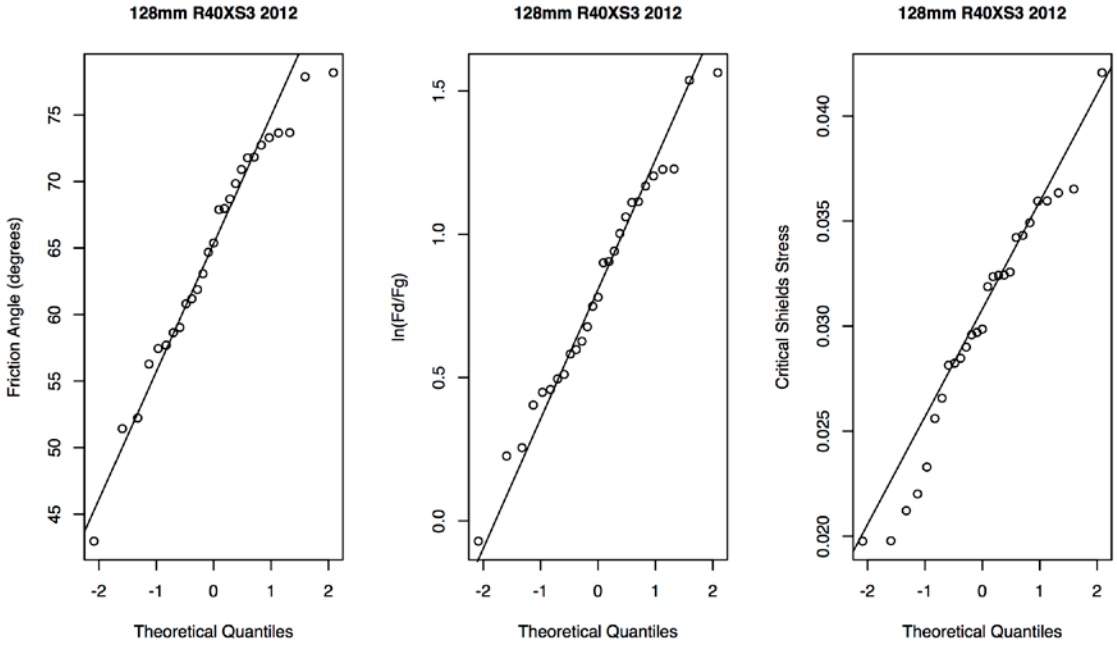
128mm R40XS3 2012
Friction Angle (degrees)
Theoretical Quantiles
128mm R40XS3 2012
ln(Fd/Fg)
Theoretical Quantiles
128mm R40XS3 2012
Critical Shields Stress
Theoretical Quantiles

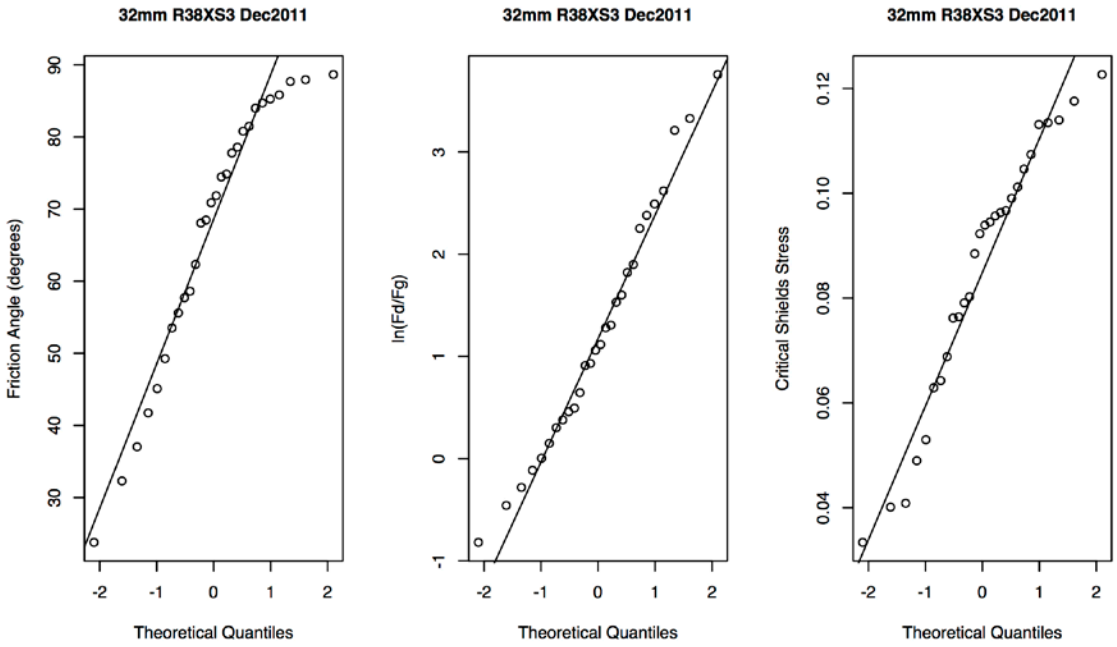
32mm R38XS3 Dec2011
Friction Angle (degrees)
Theoretical Quantiles
32mm R38XS3 Dec2011
ln(Fd/Fg)
Theoretical Quantiles
32mm R38XS3 Dec2011
Critical Shields Stress
Theoretical Quantiles

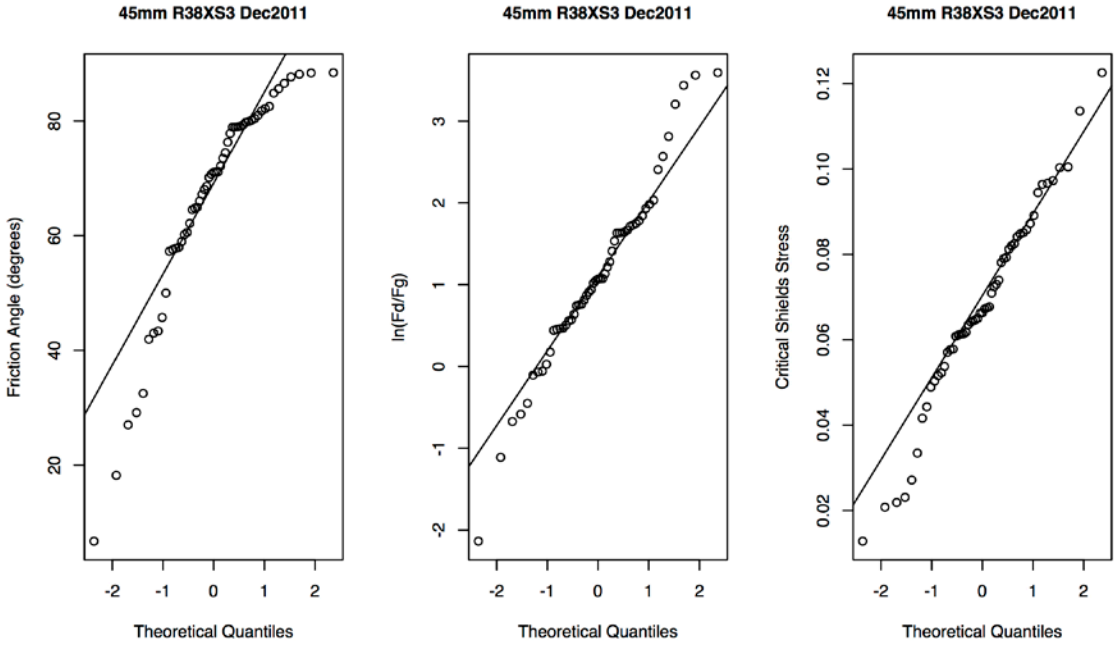
45mm R38XS3 Dec2011
Friction Angle (degrees)
Theoretical Quantiles
45mm R38XS3 Dec2011
ln(Fd/Fg)
Theoretical Quantiles
45mm R38XS3 Dec2011
Critical Shields Stress
Theoretical Quantiles

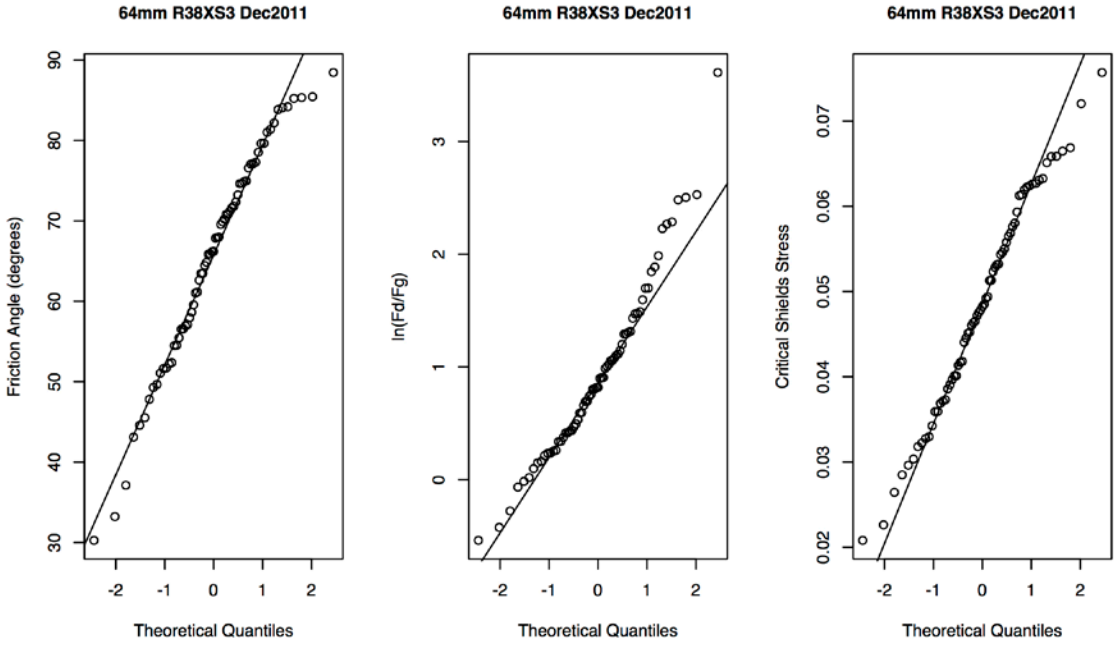
64mm R38XS3 Dec2011
Friction Angle (degrees)
Theoretical Quantiles
64mm R38XS3 Dec2011
ln(Fd/Fg)
Theoretical Quantiles
64mm R38XS3 Dec2011
Critical Shields Stress
Theoretical Quantiles

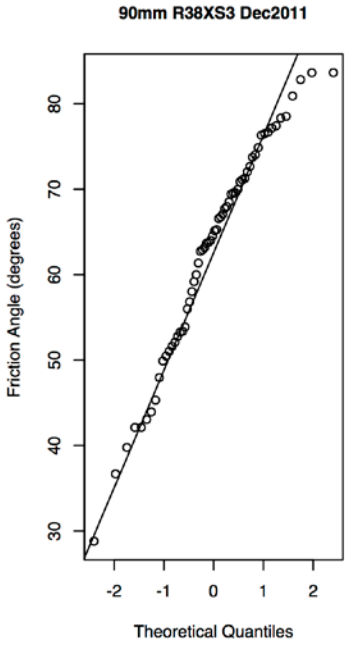
90mm R38XS3 Dec2011
Friction Angle (degrees)
Theoretical Quantiles

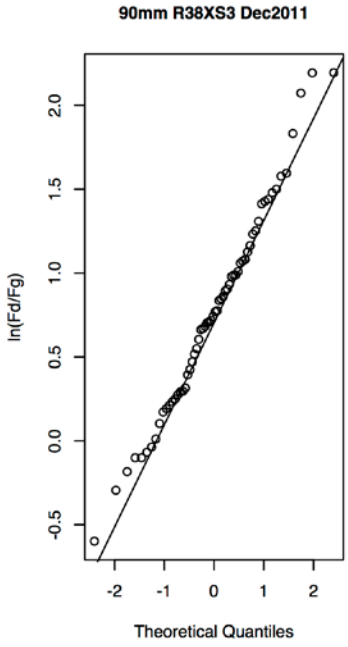
90mm R38XS3 Dec2011
ln(Fd/Fg)
Theoretical Quantiles

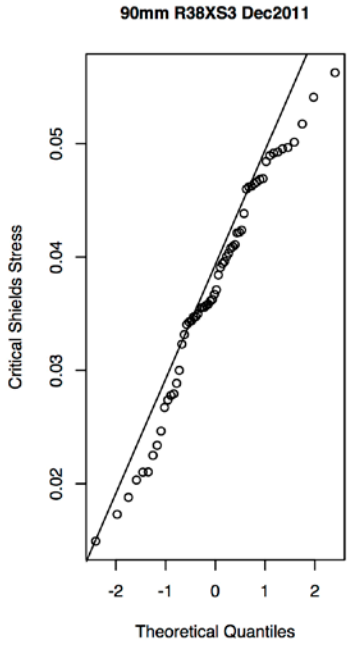
90mm R38XS3 Dec2011
Critical Shields Stress
Theoretical Quantiles

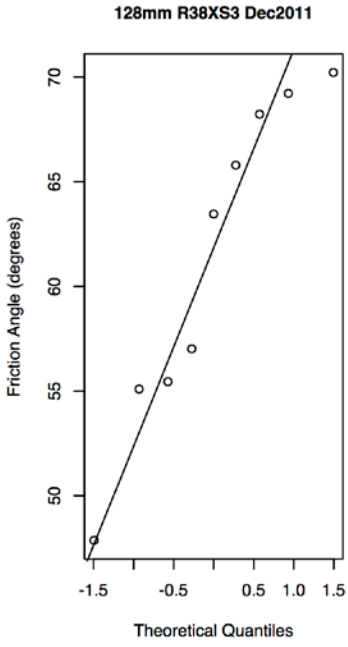
128mm R38XS3 Dec2011
Friction Angle (degrees)
Theoretical Quantiles

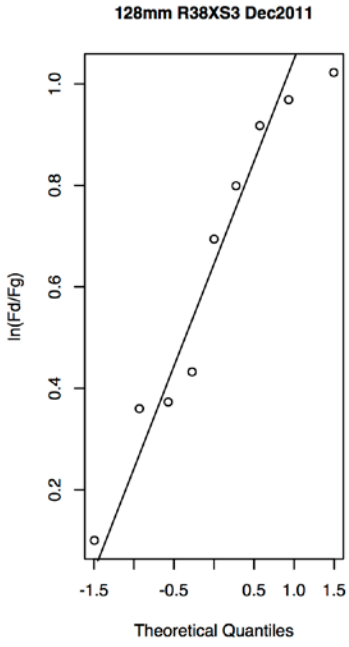
128mm R38XS3 Dec2011
ln(Fd/Fg)
Theoretical Quantiles

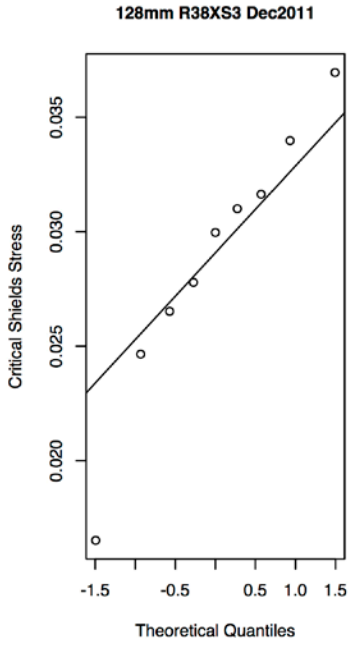
128mm R38XS3 Dec2011
Critical Shields Stress
Theoretical Quantiles

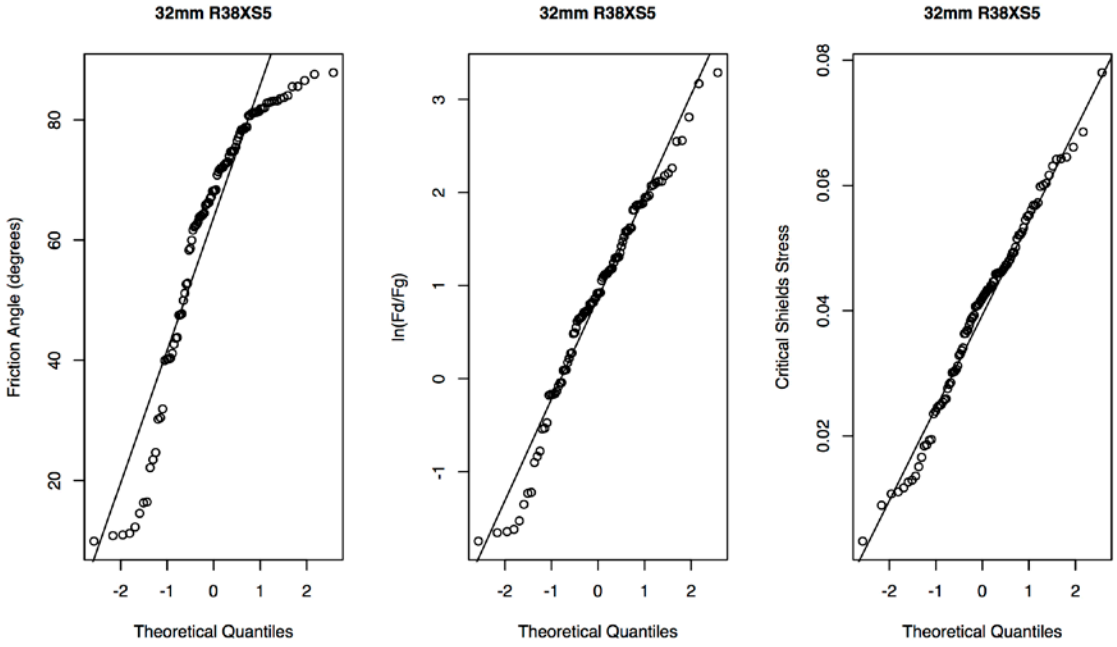
32mm R38XS5
Friction Angle (degrees)
Theoretical Quantiles
32mm R38XS5
ln(Fd/Fg)
Theoretical Quantiles
32mm R38XS5
Critical Shields Stress
Theoretical Quantiles

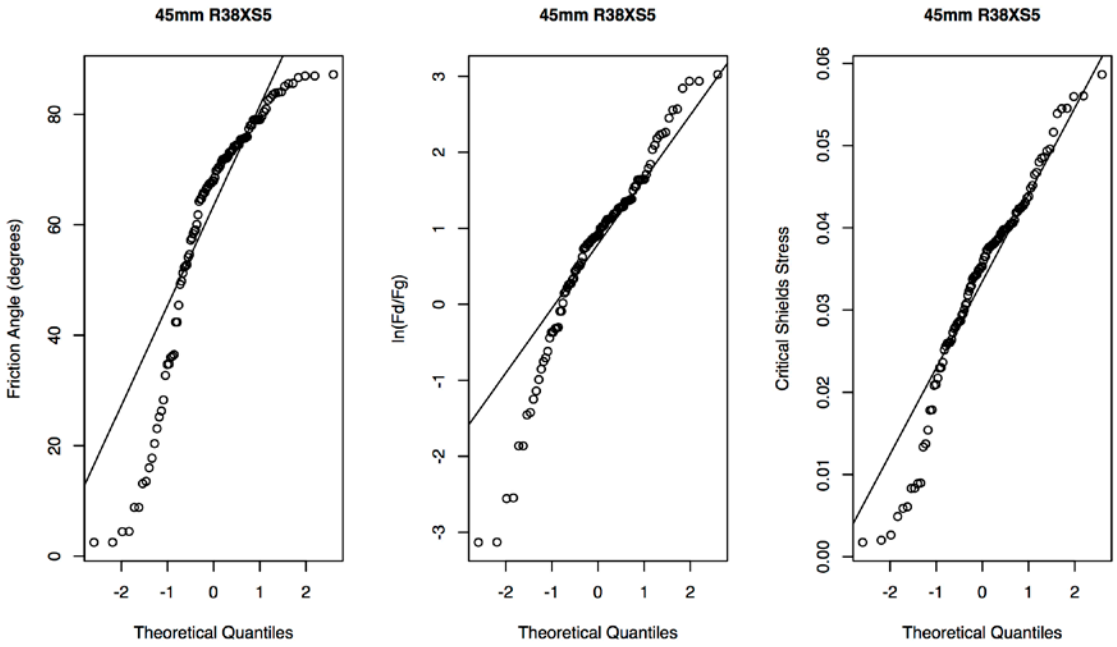
45mm R38XS5
Friction Angle (degrees)
Theoretical Quantiles
45mm R38XS5
ln(Fd/Fg)
Theoretical Quantiles
45mm R38XS5
Critical Shields Stress
Theoretical Quantiles

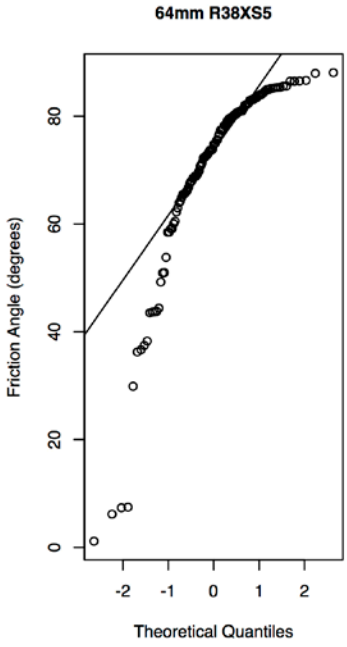
64mm R38XS5
Friction Angle (degrees)
Theoretical Quantiles

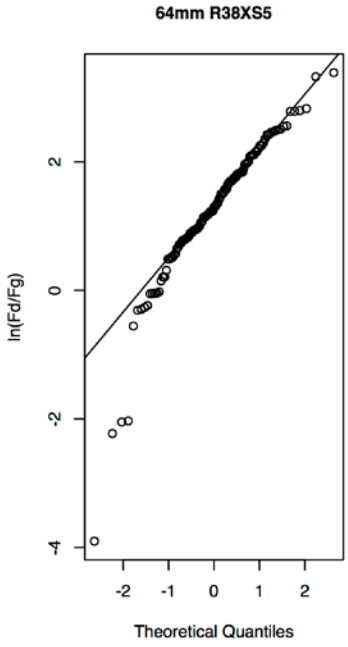
64mm R38XS5
ln(Fd/Fg)
Theoretical Quantiles

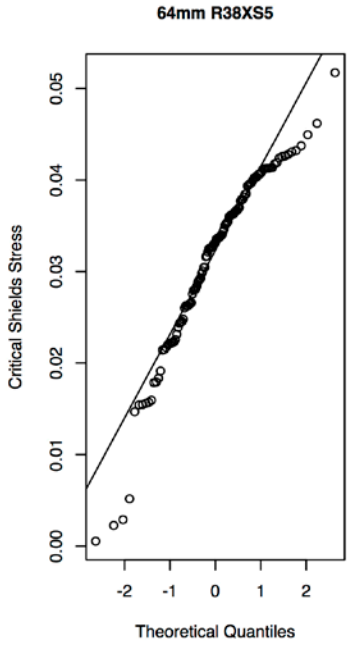
64mm R38XS5
Critical Shields Stress
Theoretical Quantiles

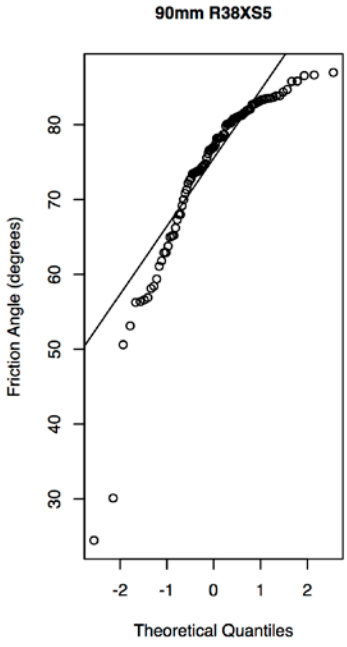
90mm R38XS5
Friction Angle (degrees)
Theoretical Quantiles

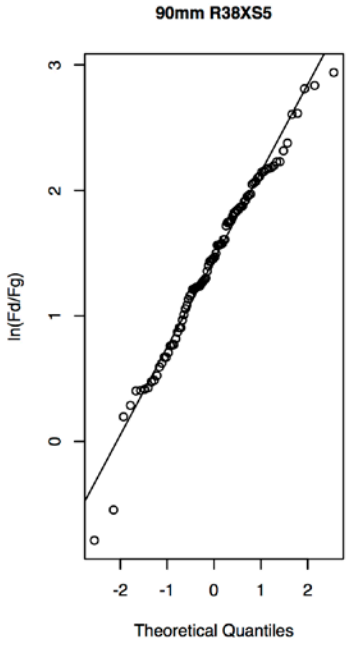
90mm R38XS5
ln(Fd/Fg)
Theoretical Quantiles

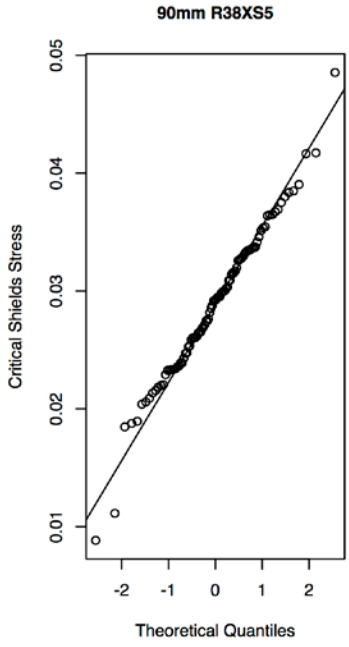
90mm R38XS5
Critical Shields Stress
Theoretical Quantiles

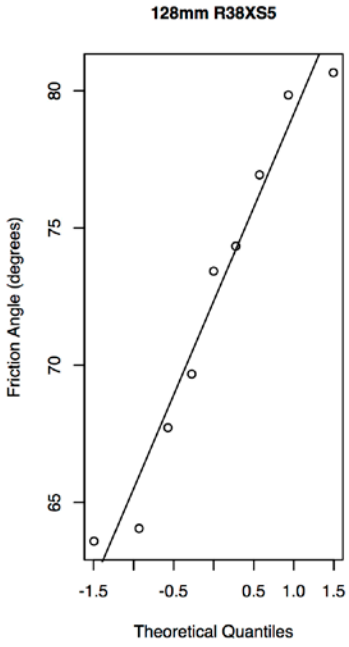
128mm R38XS5
Friction Angle (degrees)
65
70
75
80
-1.5
-0.5
0.5
1.0
1.5
Theoretical Quantiles

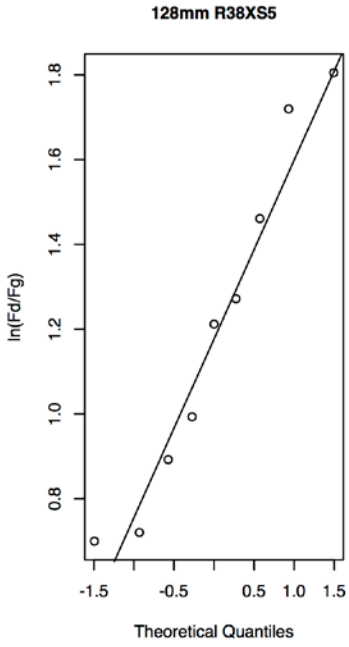
128mm R38XS5
ln(Fd/Fg)
0.8
1.0
1.2
1.4
1.6
1.8
-1.5
-0.5
0.5
1.0
1.5
Theoretical Quantiles

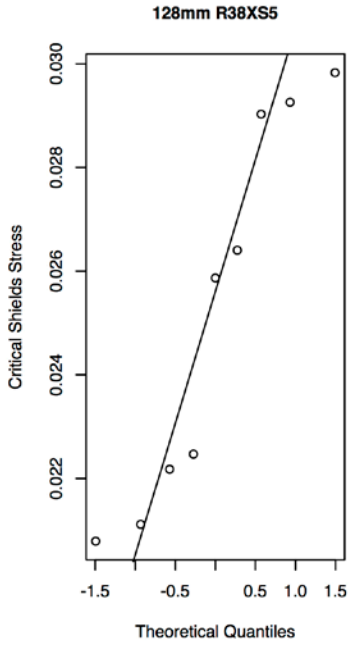
128mm R38XS5
Critical Shields Stress
0.022
0.024
0.026
0.028
0.030
-1.5
-0.5
0.5
1.0
1.5
Theoretical Quantiles

Table E-1. Kolmogorov-Smirnov (K-S) normality test result *p*-values for each gaged grain size class and the different measures of grain resistance. Each sampled grain size class is indicated by its retaining sieve size. The test results p-values that are less than a significance level of 0.05, thereby indicating significant difference from the theoretical distribution, are indicated in red font.

	K-S test p-values		
Sample	ϕ_i	$\ln(F_d/F_g)_i$	$\tau^*_{c,i}$
Friant			
32mm	0.0102	0.631	0.751
45mm	0.184	0.349	0.850
64mm	0.0304	0.628	0.979
90mm	0.264	0.875	0.490
128mm	0.751	0.831	0.589
Lost Lake			
32mm	0.0369	0.809	0.902
45mm	0.201	0.923	0.873
64mm	0.174	0.951	0.765
90mm	0.571	0.508	0.692
128mm	NA	NA	NA
R40XSA			
32mm	0.160	0.519	0.550
45mm	0.341	0.948	0.890
64mm	0.611	0.995	0.638
90mm	0.344	0.154	0.284
128mm	0.994	0.960	0.704
R40XS3			
32mm	0.100	0.991	0.536
45mm	0.0151	0.972	0.610
64mm	0.0287	0.968	0.566
90mm	0.401	0.363	0.807
128mm	0.798	0.993	0.902
R38XS3			
32mm	0.630	0.975	0.493
45mm	0.273	0.687	0.715
64mm	0.867	0.672	0.782
90mm	0.441	0.967	0.580
128mm	0.946	0.911	0.989
R38XS5			
32mm	0.00605	0.303	0.432
45mm	0.000611	0.0437	0.186
64mm	0.00373	0.190	0.120
90mm	0.0135	0.814	0.996
128mm	0.993	0.988	0.709

Appendix F: Statistical Tests on Regression Functions

ANCOVA Test Results

I use ANCOVA tests to determine if the slope and intercept coefficients are significantly different between power functions of median ϕ_i versus D_i/D_{50} of the different sites fit by OLS regression. The regression coefficients and statistics are presented in Table D-1. The upper right half of Table F-1 presents the results for the comparison of the slope coefficients *f*. The lower left half of the table is the results for the comparison of the intercept coefficients *e*. The sites being compared in each cell are indicated by the left-most column and top-most row. *P*-values less than 0.05 indicate that the paired coefficient values are significantly different. The test results indicate the slope of the trends in the median ϕ_i as a function of D_i/D_{50} is significantly different or nearly so when comparing site R38XS5 with the other sites, and between the Lost Lake and R38XS3 sites. Comparison of the magnitude of the trends indicates that site R40XSA and R38XS3 are both significantly different from the other sites. These results are not given much weight due to the lack of a predictable distribution of ϕ_i values as compared to other measures of grain resistance.

Table F-1: ANCOVA test *p*-values from comparison of paired sites corresponding regression coefficients, where the power function provided by OLS regression is of the form: $median\ of\ \phi_i = e(D_i/D_{50})^{-f}$. Yellow highlighted sites indicate those with significantly different coefficients. Gray shaded cells are not applicable to a test for significant difference in the intercept due to the exponent values that are significantly different.

ANCOVA intercept test *p*-value	ANCOVA slope test *p*-values					
Site	Friant	Lost Lake	R40XSA	R40XS3	R38XS3	R38XS5
Friant	1	0.0760	0.8169	0.3001	0.6939	0.0577
Lost Lake	0.0618	1	0.1084	0.0867	0.0207	0.0011
R40XSA	0.0089	0.0101	1	0.3142	0.5799	0.1740
R40XS3	0.3047	0.3752	0.0018	1	0.1048	0.0018
R38XS3	0.0086	0.1337	0.0148	0.0002	1	0.0052
R38XS5	0.8478	0.0604	0.0018	0.6752	0.1557	1

I performed ANCOVA tests to determine if the slope and intercept coefficients are significantly different (significance level of 0.05) between OLS regression fit power functions of $\langle \tau_{c,i}^{*} \rangle$ versus D_i/D_{50} of the different sites. The regression coefficients and statistics are presented in Table 4. The upper right half of Table F-2 are the results from the slope tests and the lower left half of the table is the results from the intercept tests. The results indicate that differences between the coefficients of the trends in the $\langle \tau_{c,i}^{*} \rangle$ as a function of D_i/D_{50} are related to morphology (i.e., position along a barform). The slope coefficients are significantly different when comparing the R38XS5 site with the others (p-values<0.03). The intercept coefficients are significantly different when comparing riffles with pool tails (p-values<0.02), or the riffles (excluding R38XS3) with the margin (p-values<0.02). The intercept coefficients are not significantly different when comparing the riffles sites (p-values>0.15) or pool tail-out sites (p-values>0.96). These results indicate that there are significant differences in the force balance computed average critical Shields stress value for the D_{50} of the bed and its trend with relative grain size that is dependent on geomorphic location along a channel. See text in the main body of Chapter 2 for the further discussion of the relevance of these results.

Table F-2: ANCOVA test *p*-values from comparison of paired sites corresponding regression coefficients, where the regression function is: $\langle \tau^*_{c,i} \rangle = \alpha (D_i/D_{50})^{-\beta}$, where the null hypothesis is that the coefficients are equal between regression models of paired sites. At a significance level of 0.05 the coefficients are significantly different when *p*-value<0.05. Yellow cells indicate an apparent inconsistency in the difference of riffles from the other sites. Gray shaded cells are not applicable to a test for significant difference in the intercept due to the β values that are significantly different.

		ANCOVA slope test *p*-values					
		Friant	Lost Lake	R40XSA	R40XS3	R38XS3	R38XS5
ANCOVA intercept test *p*-values	Friant	1	0.180	0.959	0.397	0.052	8.87E-03
	Lost Lake	0.015	1	0.264	0.417	0.056	2.28E-05
	R40XSA	4.65E-03	0.053	1	0.459	0.100	0.026
	R40XS3	0.525	0.019	0.002	1	0.059	3.01E-04
	R38XS3	0.156	0.826	0.012	0.186	1	2.17E-05
	R38XS5	0.020	0.641	0.817	0.024	0.117	1

I performed ANCOVA tests to determine if the slope and intercept coefficients are significantly different between OLS regression fitted power functions of the standard deviation of $\tau^*_{c,i}$ versus D_i/D_{50} of the different sites. The regression coefficients and statistics are presented in Table 4. The upper right half of Table F-3 contains the results from the slope tests; the lower left half of the table contains the results from the intercept tests. The results indicate that differences between the slope of the trends in the standard deviation of $\tau^*_{c,i}$ as a function of D_i/D_{50} appear to be related to stream-wise position. The slope coefficients are significantly different when comparing the upstream most two sites with the other four sites (*p*-values<0.05). However, the slope coefficients are not significantly different when comparing the four downstream most sites (*p*-values>0.78). The intercept coefficients are not significantly different between sites R40XSA, R40XS3, and R38XS3 (*p*-values>0.25) thereby indicating that in these cases the standard deviation trend is equal in magnitude and interaction with the dependent variable. The intercept coefficients are significantly different when comparing the Friant and Lost Lakes sites (*p*-value = 0.008) and the R38XS5 site with the R40XSA, R40XS3, and R38XS3 sites (*p*-values < 0.03). These results are not considered very informative though as the standard

deviation is found to covary with the mean of $\tau_{c,i}$ and therefore these results are less useful than those of distributions of $\tau_{c,i}$ values that are normalized by the $\langle \tau_{c,i} \rangle$ values.

Table F-3: ANCOVA test *p*-values from comparison of paired sites corresponding regression coefficients, where the regression function is: Standard Deviation of $\tau^*_{c,i} = \gamma(D_i/D_{50})^{-\delta}$. Gray shaded cells are not applicable to a test for significant difference in the intercept due to the exponents that are significantly different.

		ANCOVA slope test *p*-values					
		Friant	Lost Lake	R40XSA	R40XS3	R38XS3	R38XS5
ANCOVA intercept test *p*-value	Friant	1	0.547	0.0191	0.0387	0.0253	0.0406
	Lost Lake	7.62E-03	1	0.0174	0.0460	0.0273	0.0399
	R40XSA	0.103	0.769	1	0.941	0.940	0.822
	R40XS3	0.362	0.697	0.257	1	0.995	0.795
	R38XS3	0.154	0.840	0.974	0.272	1	0.781
	R38XS5	0.662	0.066	3.33E-03	0.0233	5.72E-03	1

Appendix G: The Applied Shear Stress

To illustrate the predicted τ necessary to move the gaged grains I calculated the τ_c by solving for the numerator in the Shields equation (3) using the computed τ_c^* values from equation (5) and the nominal diameter (the diameter of a sphere of equal weight and density) of each gaged grain. For calculations of τ_c^* using equation (5) see Methods section of the main body of this report. The cumulative distributions of the $\tau_{c,i}$ values are presented as points in Figure G-1. The plots include the theoretical cumulative normal distribution curves of the $\tau_{c,i}$ values that were determined from their mean and standard deviation. The plots illustrate the consistent approximation of the theoretical distribution with the $\tau_{c,i}$ values.

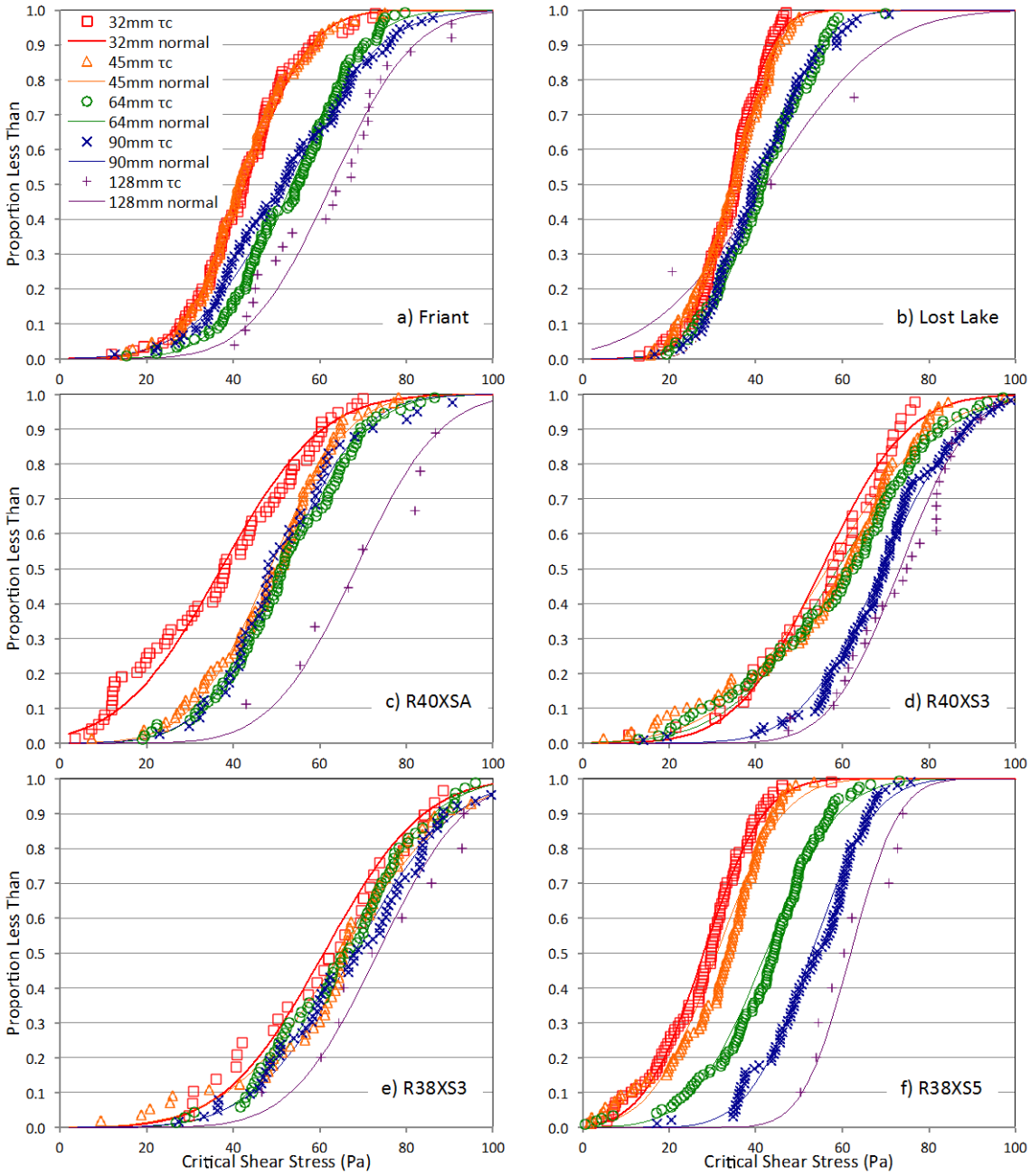

Figure G-1. Cumulative distributions of the force balance computed $\tau_{c,i}$ values. Colors and symbols are unique to each grain size class (legend on plot a). Symbols indicate the values of τ_c computed from individual force gage measurements. Lines are the theoretical normal distributions determined from the mean and standard deviation of the $\tau_{c,i}$ values. Differences in the means of the $\tau_{c,i}$ distributions at a site were tested using one-way ANOVA and *post hoc* using Tukey HSD (Appendix G: Tables G-2 and G-3). There is a significant effect of grain size class on the mean $\tau_{c,i}$ at all sites except R38XS3.

The distributions of $\tau_{c,i}$ values show consistencies between grain size fractions. The values of $\tau_{c,i}$ are consistently greater for larger grain sizes, which is contrary to the results of *Kirchner et al.* [1990] and *Buffington et al.* [1992]. The difference from these

studies is likely due to the gaging of *in situ*, water-worked grains as opposed to their reliance on randomly placed test grains. Their test grains were more likely to settle in shallower pockets that provide less resistance to downstream directed forces than *in situ* grains whose positions during emplacement were more likely to persist when provided greater resistance to flow forces and therefore settled in reinforce positions against stable protruding grains. Therefore, because the force balance computed $\tau_{c,i}$ distributions are validated by the tracer grain entrainment, this difference in the measurements of grain resistance from randomly placed test grains indicates that randomly placed test grains are probably not directly comparable to the mobility of water-worked beds.

When the values of $\tau_{c,i}$ are normalized by the $\langle \tau_{c,i} \rangle$ the distributions tend to collapse thereby indicating strong covariance between the mean and standard deviation with changes in grain size (Figure 7). Only the normalized $\tau_{c,i}$ distributions at the R40XS3 and R38XS5 sites showed significant difference between the majority of their paired comparisons of the distributions by grain size class (*F*-test results in Appendix G, Table G-1). This result is expressed by the increasing variance with decreasing grain size. It appears as though the variability in the variance between sites is related to the presence of a secondary mode in the grain size distribution that is composed of sand. Sites R40XS3 and R38XS5 have the most sand in their grain size distributions (Figure 2). Furthermore, for sites with less than 10% sand on the bed the normalized $\tau_{c,i}$ distributions collapse, such that the variance at the Friant site is well collapsed though it has the third largest amount of sand (~5%). Therefore, though the standard deviation of $\tau_{c,i}$ covaries with the $\langle \tau_{c,i} \rangle$ (Figure 7) this covariance can be reduced by the presence of a secondary mode of sand in the grain size distributions.

Table G-1. Two-tailed *F*-test results between paired distributions of $\tau_{c,i}/\langle\tau_{c,i}\rangle$. Because the distributions of $\tau_{c,i}$ are not significantly different from the normal distribution it is appropriate to use two-tailed *F*-tests to determine if the variance in the distributions between pairs of grain size fractions is equal. The results indicate that most sites show few differences between grain sizes while sites R40XS3 and R38XS5 show signs of systematic differences as larger grains are significantly different from smaller grains. I compared the distributions of all combinations of the distributions of the grain size classes at a site. The tables below are matrices of *p*-values from the paired grain size fractions distributions with the grain size classes indicated on the top row and left most column of cells. With a significance level of 0.05, a *p*-value<0.05 indicates the null hypothesis is rejected and the alternative hypothesis, i.e., that the variances are not equal (red font), is accepted.

Table G-1a. Friant Riffle Site.

	128mm	90mm	64mm	45mm	32mm
128mm	1	0.102	0.866	0.410	0.401
90mm		1	7.61E-03	0.146	0.175
64mm			1	0.235	0.235
45mm				1	0.964
32mm					1

Table G-1b. Lost Lake Pool Tail-out Site. As noted in the main document, the variance of the 128mm distribution is an outlier that is likely a result of the small sample size of n=3.

	128mm	90mm	64mm	45mm	32mm
128mm	1	0.0736	0.0614	0.0373	0.0136
90mm		1	0.818	0.390	0.0472
64mm			1	0.518	0.0715
45mm				1	0.246
32mm					1

Table G-1c. R40XSA Pool Tail-out Site. As noted in the main document, the variance of the 32mm distribution is an outlier that is likely a real difference from the other distributions caused by recent deposition of small gravel on the pool tail.

	128mm	90mm	64mm	45mm	32mm
128mm	1	0.541	0.535	0.473	0.0350
90mm		1	0.979	0.839	3.11E-04
64mm			1	0.770	9.90E-07
45mm				1	8.59E-06
32mm					1

Table G-1d. R40XS3 Riffle Site. As noted in the main document, the significant difference in the variances at this site may be the result of the secondary mode of sand in the grain size distribution.

	128mm	90mm	64mm	45mm	32mm
128mm	1	0.201	3.18E-04	1.22E-04	8.60E-03
90mm		1	1.12E-05	1.19E-06	0.0215
64mm			1	0.616	0.256
45mm				1	0.132
32mm					1

Table G-1e. R38XS3 Riffle Site.

	128mm	90mm	64mm	45mm	32mm
128mm	1	0.503	0.630	0.232	0.346
90mm		1	0.649	0.205	0.545
64mm			1	0.0811	0.328
45mm				1	0.682
32mm					1

Table G-1f. R38XS5 Inner Margin of a Gentle Bend. As noted in the main document, the significant difference in the variances at this site may be the result of the secondary mode of sand within the grain size distribution.

	128mm	90mm	64mm	45mm	32mm
128mm	1	0.204	0.0215	4.93E-03	4.84E-03
90mm		1	2.40E-04	2.39E-08	2.67E-08
64mm			1	0.0235	0.0232
45mm				1	0.973
32mm					1

Another apparent characteristic of the grain resistance that is illustrated in Figure G-1 are tendencies for some grain size classes distributions of $\tau_{c,i}$ to be equivalent with others. For example, the $\tau_{c,i}$ distributions from the Friant site (Figure G-1a) shows the 32 mm and 45 mm size classes as having equivalent distributions as is also the case for the 64 mm and 90 mm size classes. The 128 mm size class, however, has a distribution that is distinct with τ_c values of any given quantile being greater than the other classes. To test for significant differences between these distributions at each site, I used one-way ANOVA to compare the influence of grain size on the $\langle\tau_{c,i}\rangle$ by testing the null hypothesis that the $\langle\tau_{c,i}\rangle$ values do not differ between the grain size classes at a significance level of 0.05 (Table G-2). Except for site R38XS3 whose $\langle\tau_{c,i}\rangle$ range between 60 Pa and 75 Pa (p-value=0.34), the results indicated a significant effect of grain size on the $\langle\tau_{c,i}\rangle$ at each site (p-value$<3.6\times10^{-9}$).

Table G-2. One-way ANOVA test results to determine if the mean of the $\tau_{c,i}$ values is significantly different between at least one pair of grain size fractions from the site.

Site	*p*-value
Friant	4.70E-16
Lost Lake	1.69E-09
R40XSA	1.17E-10
R40XS3	3.56E-09
R38XS3	0.339
R38XS5	<2E-16

A *post hoc* test was then performed using the Tukey's Honest Significant Differences method to test for differences between the paired comparisons of $\langle\tau_{c,i}\rangle$ at the five sites with significant differences (Table G-3). The results indicate that those grain size classes with $\tau_{c,i}$ distributions that are not significantly different are well illustrated in Figure G-1. Furthermore, the $\langle\tau_{c,i}\rangle$ values from the R38XS5 site are all significantly different except for the comparisons of the two smallest grain size classes and the two largest grain size classes. Therefore, these tests support the conclusion that there are clusters of grain sizes that exhibit equal $\langle\tau_{c,i}\rangle$ at many of the sites and that at the R38XS3 riffle site all of the force gage measured grain size classes have virtually equal $\langle\tau_{c,i}\rangle$.

Table G-3: Tukey Honest Significant Difference test results. I performed a post hoc test using Tukey's Honest Significant Difference (HSD) method to determine which grain size class-paired $\tau_{c,i}$ distributions at a site were significantly different. At a significance level of 0.05, significant differences between the mean $\tau_{c,i}$ values of paired grain size fractions is indicated by p-values<0.05 (red font). Shaded test results indicate that 128 mm grains at the Lost Lake site are not represented by a sufficient sample size (n=3). Therefore, the results from those comparisons are much less likely to be representative of the $\tau_{c,i}$ of the population of 128 mm grains on the bed at this site. Overall, these results indicate a clustering of grain sizes with equivalent mean $\tau_{c,i}$ values at most sites, and that virtually all values of $\langle\tau_{c,i}\rangle$ are significantly different at the sandy margin site (R38XS5).

Table G-3.Tukey HSD post hoc test results.

Site	Compared D_i	*p*-value
Friant	45mm-32mm	1.000
	64mm-32mm	3.00E-07
	90mm-32mm	2.88E-05
	128mm-32mm	<1.0E-7
	64mm-45mm	<1.0E-7
	90mm-45mm	8.20E-06
	128mm-45mm	<1.0E-7
	90mm-64mm	0.985
	128mm-64mm	0.018
	128mm-90mm	8.98E-03
Lost Lake	45mm-32mm	1.000
	64mm-32mm	3.40E-06
	90mm-32mm	2.30E-05
	128mm-32mm	0.560
	64mm-45mm	6.90E-06
	90mm-45mm	4.03E-05
	128mm-45mm	0.562
	90mm-64mm	1.000
	128mm-64mm	0.999
	128mm-90mm	0.999
R40XSA	45mm-32mm	1.13E-04
	64mm-32mm	<1.0E-7
	90mm-32mm	5.42E-05
	128mm-32mm	1.50E-06
	64mm-45mm	0.522
	90mm-45mm	0.861
	128mm-45mm	5.38E-03
	90mm-64mm	0.999
	128mm-64mm	0.039
	128mm-90mm	0.040
R40XS3	45mm-32mm	0.996
	64mm-32mm	0.791
	90mm-32mm	1.29E-04
	128mm-32mm	3.14E-04
	64mm-45mm	0.883
	90mm-45mm	6.00E-06
	128mm-45mm	1.47E-04
	90mm-64mm	3.68E-04
	128mm-64mm	1.74E-03
	128mm-90mm	0.802
R38XS3	45mm-32mm	0.881
	64mm-32mm	0.869
	90mm-32mm	0.460
	128mm-32mm	0.392
	64mm-45mm	1.000
	90mm-45mm	0.910
	128mm-45mm	0.702
	90mm-64mm	0.888
	128mm-64mm	0.689
	128mm-90mm	0.917
R38XS5	45mm-32mm	0.361
	64mm-32mm	<1.0E-7
	90mm-32mm	<1.0E-7
	128mm-32mm	<1.0E-7
	64mm-45mm	<1.0E-7
	90mm-45mm	<1.0E-7
	128mm-45mm	<1.0E-7
	90mm-64mm	<1.0E-7
	128mm-64mm	2.72E-05
	128mm-90mm	0.192

III. Variability of Hydraulic Conductivity in Artificial Redds with Fine Sediment Accumulation and Bed Load Transport

A. Introduction

Salmon populations are imperiled throughout much of their historic range [*Nehlsen et al.,* 1991; *Huntington et al.,* 1996; *Shea and Mangel,* 2001; *WWF,* 2001; *Youngson et al.,* 2002; *Montgomery,* 2003; *Lackey et al.,* 2006; *Moyle et al.,* 2008]. One of the contributing causes of salmon population declines is reduced productivity of salmon incubation habitat [*Lichatowich,* 1999; *Katz et al.,* 2012], a factor of which is fine sediment deposition in the salmon nest, termed a redd [*Chapman,* 1988; *Reiser,* 1998; *Greig et al.,* 2005]. Fine sediment concentration within the redd inversely correlates with egg survival [*Lotspeich and Everest,* 1981; *Tappel and Bjornn,* 1983; *Chapman,* 1988; *Young et al.,* 1991; *Bennett et al.,* 2003; *Greig et al.,* 2005] and with the ability to conduct flow, referred to as the hydraulic conductivity, through the interstitial space between the gravels of the redd [*Zimmerman and Lapointe,* 2005]. It follows that the hydraulic conductivity also inversely correlates with egg survival [*Tagart,* 1976; *McCuddin,* 1977].

Fine sediment in spawning gravels may occur due to the initial concentration of fines during the deposition of the bar-forming gravel [*Kondolf et al.,* 1993] or as a result of subsequent deposition from transported sediment collecting in the void spaces between the gravel particles [*Beschta and Jackson,* 1979; *Lisle,* 1989; *Lisle and Lewis,* 1992]. Increasing stream flow results in an increased sediment transport rate. The sediment transport flux during incubation acts to deliver and deposit fine sediment that reduces the

hydraulic conductivity of the redd. Because sediment accumulated in a redd is directly related to the sediment transport flux that is dependent on the flow level, hydraulic conductivity can vary over time and with flow. The degree and rate at which the hydraulic conductivity decreases as a result of sediment transport during incubation season flow levels is examined as part of this study.

There are several mechanisms through which fine sediment negatively affect the incubation habitat quality [*Malcolm et al.,* 2008]. Fine sediment concentrated in the intergranular spaces clog flow pathways, thereby reducing hydraulic conductivity [*Freeze and Cherry,* 1979]. Reduced hydraulic conductivity decreases the interstitial flow velocity within the redd thereby reducing ventilation, which is necessary for providing oxygenated water and removing metabolites. Additionally, fine organic sediments can consume oxygen, via bio-chemical oxygen demand, reducing that available to the eggs. Fine sediment can also affect salmon production by clogging pathways that the hatched alevins use to emerge from the redd [*Crisp,* 1993]. Therefore, depending on the mechanism, fine sediment deposition on the redd can cause the incubating eggs to suffocate [*Sowden and Power,* 1985; *Peterson and Quinn* 1996], the embryos to experience a reduced rate of development [*Silver et al.,* 1963; *Shumway et al.,* 1964], or the juvenile fish to become entombed by the fine sediment seal [*Koski,* 1966; *Bjornn,* 1969; *Phillips et al.,* 1975].

Although others, noted above, have found a relationship between fine sediment accumulation and hydraulic conductivity with egg survival, there is less certainty about the degree to which these habitat quality characteristics may change during an incubation cycle. For example, by how much does hydraulic conductivity change over the duration

of an incubation period? How does that change correspond with changes in flow and accumulated sand? To explore these questions, I constructed artificial redds at five locations along an 18 km gravel-bedded reach and monitored sand accumulation and near-bed sediment transport under different flow conditions to quantify the effect on hydraulic conductivity.

This study aims to answer the following questions. To what extent does the hydraulic conductivity within artificially created redds change with varying flow conditions? How does this change in hydraulic conductivity relate to the fine sediment accumulation and sediment delivery from bed load transport that result from changes in flow? I also explore how differences in the grain size composition – that might be altered during the redd construction process – of the redd backfill affect these relationships. From these relationships I demonstrate that local bed load transport rates can be useful for predicting the effect of flow on the hydraulic conductivity of the redd and for estimating its influence on salmon egg survival.

B. Study Sites

The study was located on the San Joaquin River within 18 km downstream of Friant Dam with five sites positioned between the Highway 41 Bridge and North Fork Bridge (Figure 1). Each site is nearly equidistant from the next up- or downstream site with Site A at river kilometer (RKm) 430, Site B at RKm 426, Site C at RKm 422, Site D at RKm 417, and Site E at RKm 412. At each site, I constructed two sediment-free artificial redds less than 25 m upstream of a riffle crest within the pool tail-out (Figure 2). The redds were approximately halfway between the thalweg and a bank where flows were at least 0.3 m deep and velocity was 0.3 to 1 m/s during typical spawning and incubation flow levels

(approx. 10 m^3/s). The study reach is at an average slope of 0.0007 and bankfull flow capacity is approx. 42 m^3/s. Channel and flow characteristics at each study site are summarized in Table 1. The bed surface at all sites is predominantly coarse gravels. These conditions are within suitable ranges for Chinook salmon in California's Central Valley rivers [*Aceituno*, 1990, 1993; *Gard*, 1997; *Kondolf and Wolman*, 1993]. To ensure sites are generally representative of the pool tail-out and comparable to one another, each location was without anomalous influences on flow and sediment transport from woody debris, boulders, bedrock out crops, vegetation, and banks. Spawning Chinook salmon utilized all five sites in water year (WY) 2013 and 2014 [*SJRRP*, 2016] (Figure 2). My site selection criteria are therefore considered representative of spawning habitat as determined by the fish.

Table 1. Site Characteristics. Shear stress values are calculated from flow velocity and depth measurements at the sites.

				Q = 10 m^3/s			Q=19 m^3/s		
Site Id	Location (km)	D_{50} mm	Channel Width M	Depth m	Slope	Shear Stress Pa	Depth m	Shear Stress Pa	Slope
A	430	103	40	0.79	0.0004	3.1	0.76	7.7	0.0010
B	426	34	37	0.52	0.0005	2.6	0.62	6.6	0.0011
C	422	42	60	0.61	0.0002	1.1	0.72	3.2	0.0004
D	417	57	55	0.52	0.0008	3.8	0.69	8.4	0.0012
E	412	44	70	0.43	0.0005	2.3	0.58	6.9	0.0012

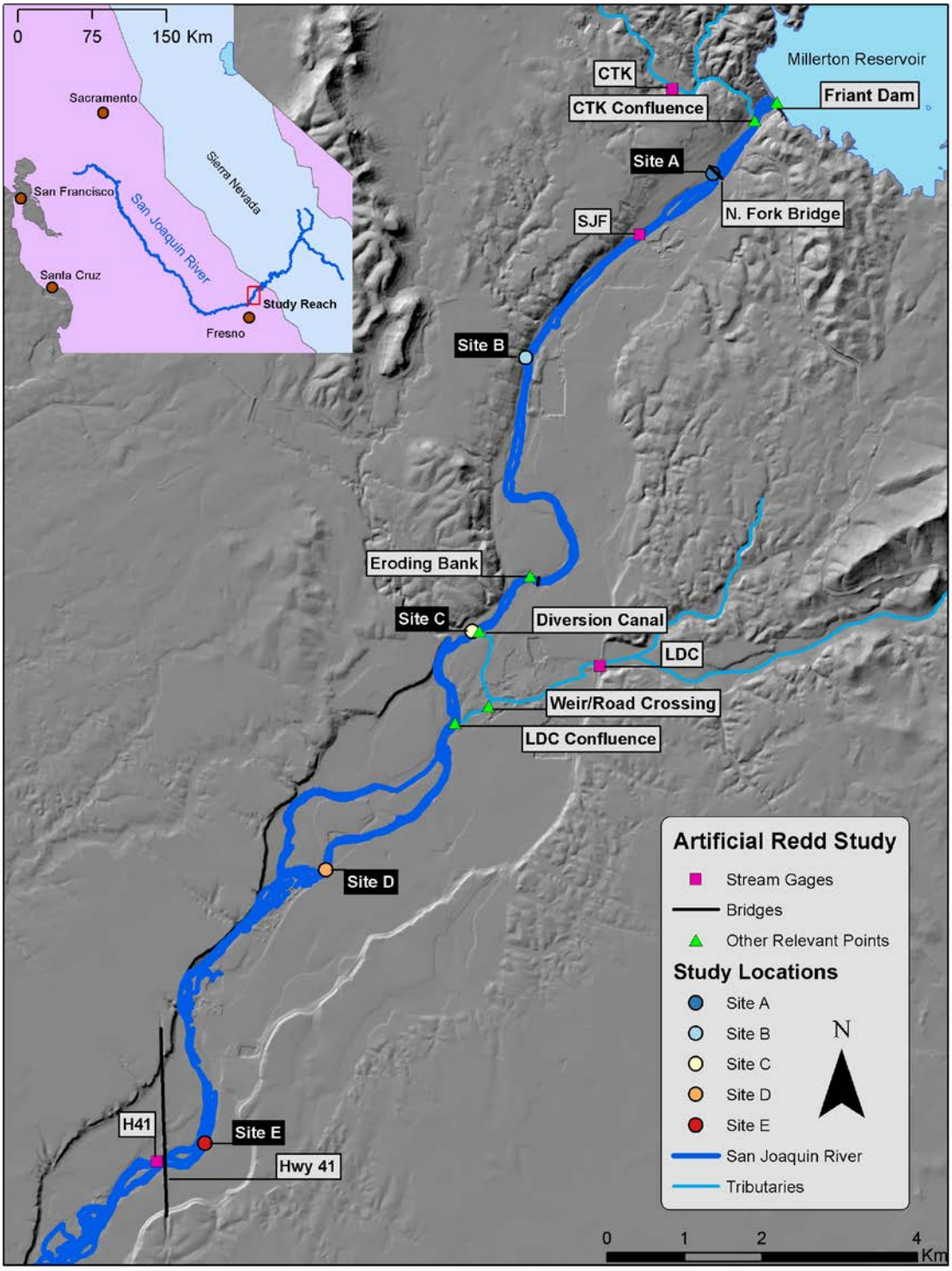

Figure 1. Reach map and pertinent locations mentioned in the text, including: artificial redd study sites, stream gages, highway (Hwy) 41 and North Fork bridges, a weir/road crossing, confluences with creeks and a diversion canal, and an eroding channel bank that is the largest known source of sand to this reach. The stream gages are on Cottonwood Creek (CTK), San Joaquin River below Friant (SJF), Little Dry Creek (LDC), and San Joaquin River below Highway 41 (H41).

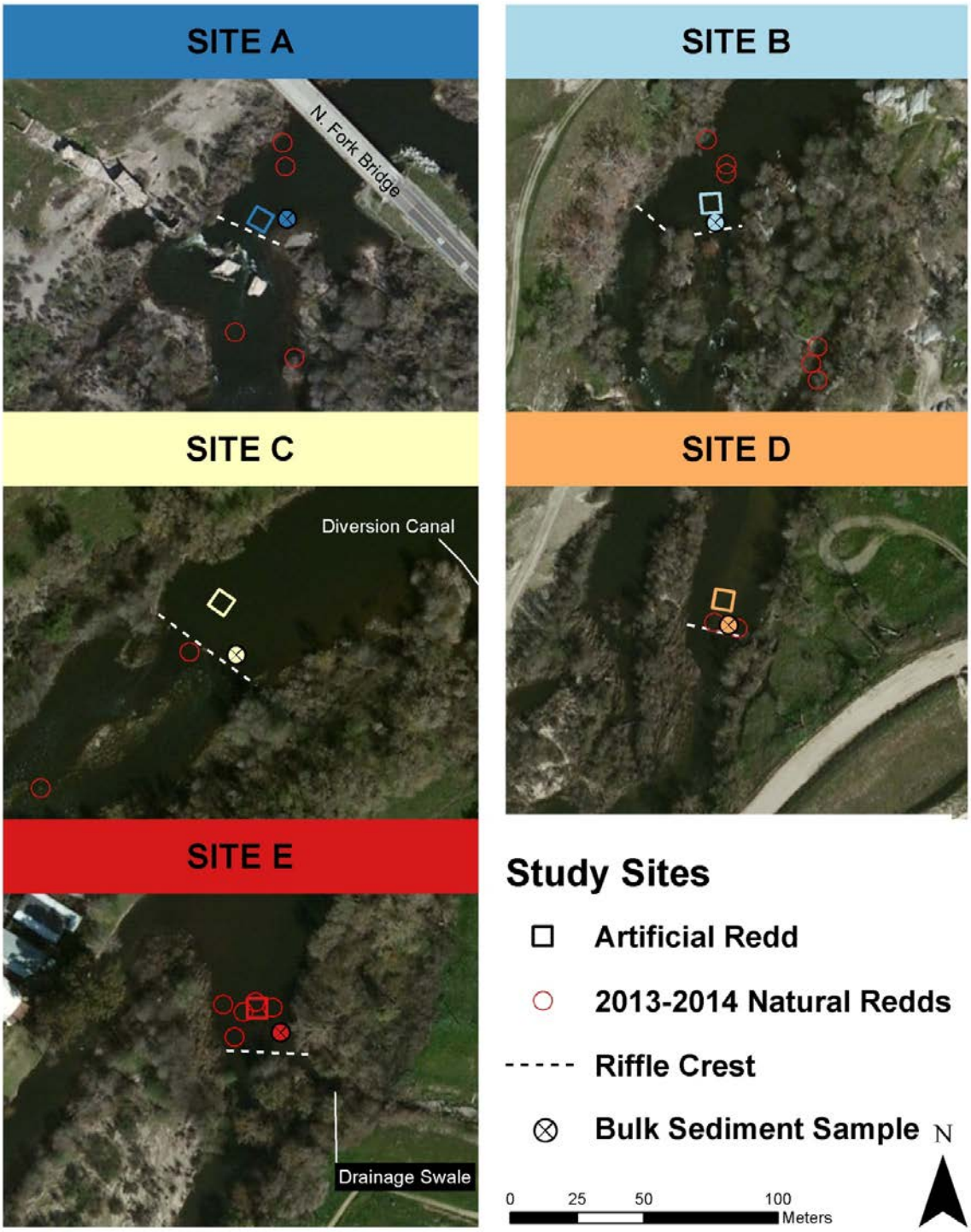

Figure 2. Aerial photographs of the study sites show the channel features around each artificial redd location at a discharge of 10 m^3/s, with the riffle crest and local manmade features noted. Natural redds created by Fall-run Chinook salmon in the late fall and early winter of WY 2013 and 2014 [*SJRRP*, 2016] and bulk bed material sample locations are also identified.

I conducted artificial redd experiments and associated monitoring at the five sites during WY 2012 and 2013. Three artificial redd experiments occurred with Experiment 1

from November 2011 through April 2012, Experiment 2 from April 2012 through May 2012, and Experiment 3 from November 2012 through March 2013. Experiments 1 and 3 were performed when flow levels ranged within typical incubation season levels that are considered base flows of 3 m^3/s to 10 m^3/s, while Experiment 2 was performed during greater flow levels of as much as 32 m^3/s that on average have been exceeded every 6 years during the Fall-run Chinook salmon incubation season. Figure 3 illustrates the combined daily average discharge as measured from Friant Dam and a stream gage on Cottonwood Creek [*SJRRP*, 2014] and the durations of each artificial redd monitoring experiment. The combined minimum daily average flow monitored was 2.6 m^3/s on December 7 and 8, 2011. The combined maximum daily average flow monitored was 31.4 m^3/s on May 13 and 15, 2012. Little Dry Creek drains into the San Joaquin River within the study reach (see Figure 1) and flowed for a total of 50 days in WY 2012 to 2013 [*SJRRP*, 2014] (Figure 3, bottom). Although Little Dry Creek has a natural confluence downstream of Site C, during the study its flows were diverted through a diversion canal that joins with the San Joaquin River immediately upstream of Site C. Therefore, Little Dry Creek contributions to flow are used for Sites C, D, and E.

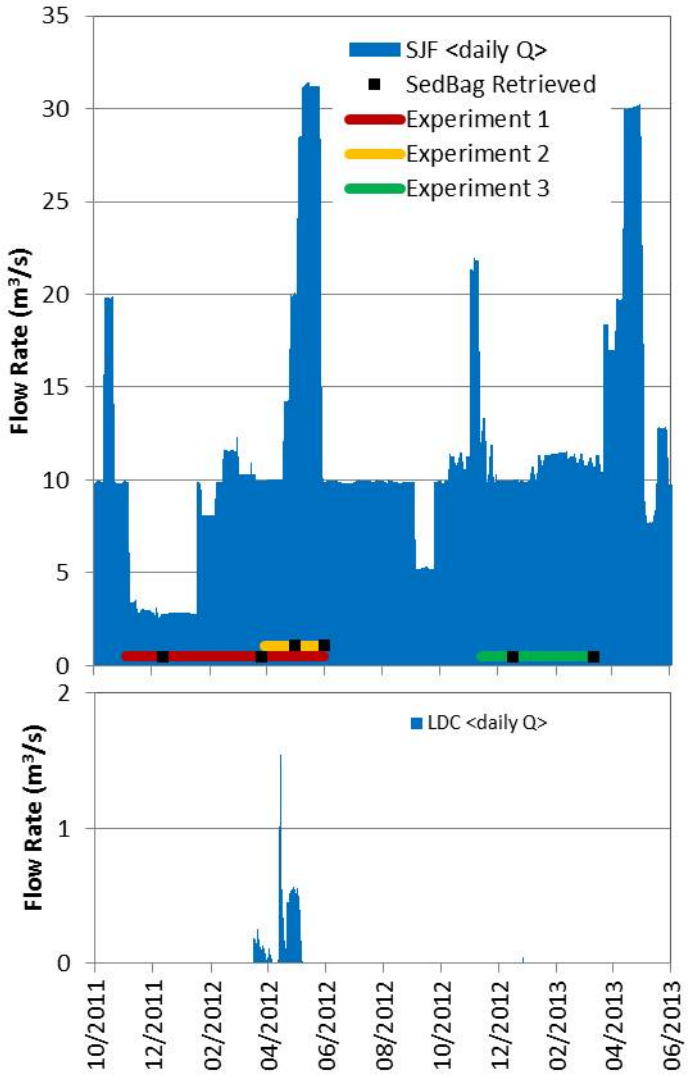

Figure 3. Hydrographs and monitoring experiment periods. (Top) The artificial redd monitoring periods (horizontal lines), and sediment bag retrieval events (black squares) are plotted with the daily average flow levels at the SJF gage (blue, vertical bars) [*SJRRP*, 2014]. Artificial redd monitoring experiments are distinguished by their colors. (Bottom) The daily average flow measured by the LDC gage provides the additional flow contributed to the main-stem via the diversion canal immediately above Site C.

C. Methods and Materials

1. Bed Material Characterization

To characterize the differences in grain size composition between the sites, I used a McNeil sampler [*McNeil and Arnell,* 1964] to collect a sample of the bulk bed material that extends to a depth of 0.3 m and is about 0.021 m^3 in volume. I sieved samples from each site (Figure 2) using screen sizes that are in half-phi increments [see *Bunte and Abt,*

2001]. As the coarser grain size fractions are more difficult to accurately represent with manageable sample sizes, I truncated the grain size distributions at 0.025 m to illustrate the differences between the lower tails of the distributions thereby avoiding the influence of the more ambiguous coarser limb (Figure 4). The sediment composition of Site A is the most distinctly different as it has about a quarter as much sand as the other sites. In general, Site C has the finest sediment, which may be a result of Little Dry Creek and an eroding bank approximately 1 km upstream that supply sand to the channel (Figure 1). Site D has a coarse sand mode that is a similar proportion of the bulk bed sample as that found at Site C, but otherwise its cumulative grain size distribution is more similar to Sites B and E. It follows that the bed at Site A is expected to have greater hydraulic conductivity as its intergranular spaces are relatively void of finer grains and the other sites are expected to have a lower hydraulic conductivity with more subtle differences between them.

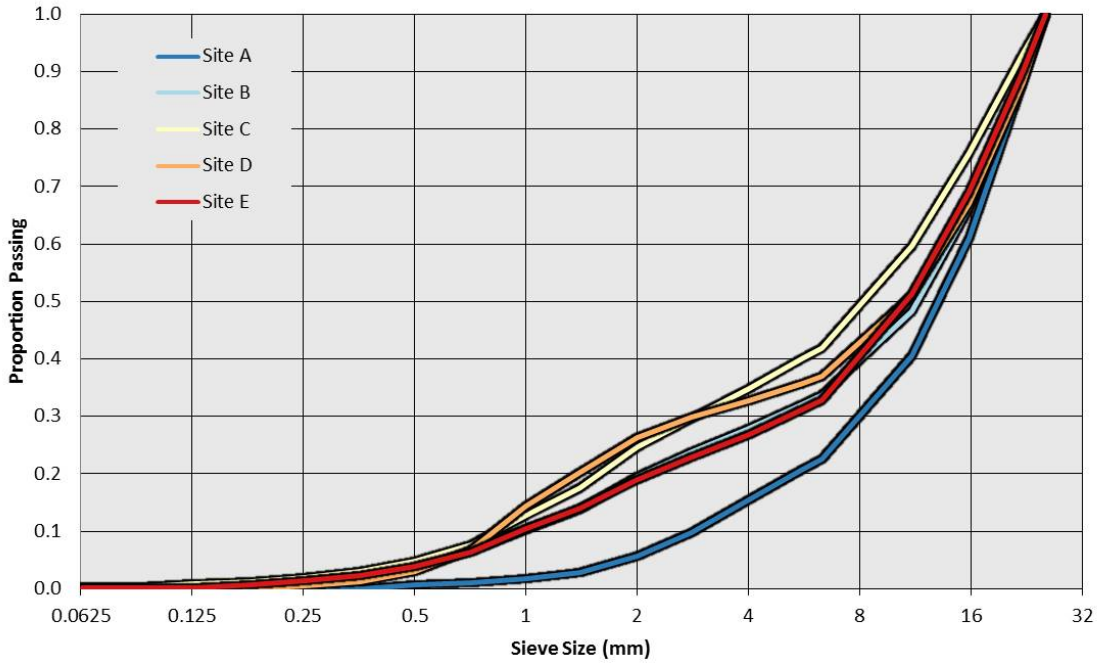

Figure 4. Truncated cumulative distribution of grain sizes from the bed at each study site. The bed material at all sites contains grain size fractions as large as 128 mm to 180 mm and median grain sizes that range

from 28 mm to 59 mm. Here, the bulk bed material samples are truncated at 25 mm to focus on the lower tail of the grain sizes that reduce the interstitial porosity of the larger gravel and cobble.

2. Experimental Design

For each of three experiments and at every site, I installed and monitored two artificial redds that mimicked the physical attributes of Chinook salmon incubation habitat (Figure 5). I placed excavated sediment in a mound immediately downstream of the redd to resemble the tail-spill of a natural redd. At the bottom of every redd excavation pit, I placed a collapsed sediment bag that I buried in nearby-sourced bed material cleansed of smaller grains using a 6.4 mm sieve (referred to as “sieved” backfill). At all the sites, I installed a scour chain between the two redd excavation pits. I installed piezometers (i) in separate pits around the periphery of the redds in Experiment 1 and backfilled with nearby-sourced bed material (referred to as “unsieved”), and (ii) within the redd excavation pit during Experiments 2 and 3 and backfilled with “sieved” bed material. As shown in Figure 5, I positioned the piezometers in different configurations for each experiment (i) to allow different backfill treatments to be monitored or (ii) to increase the number of measurements.

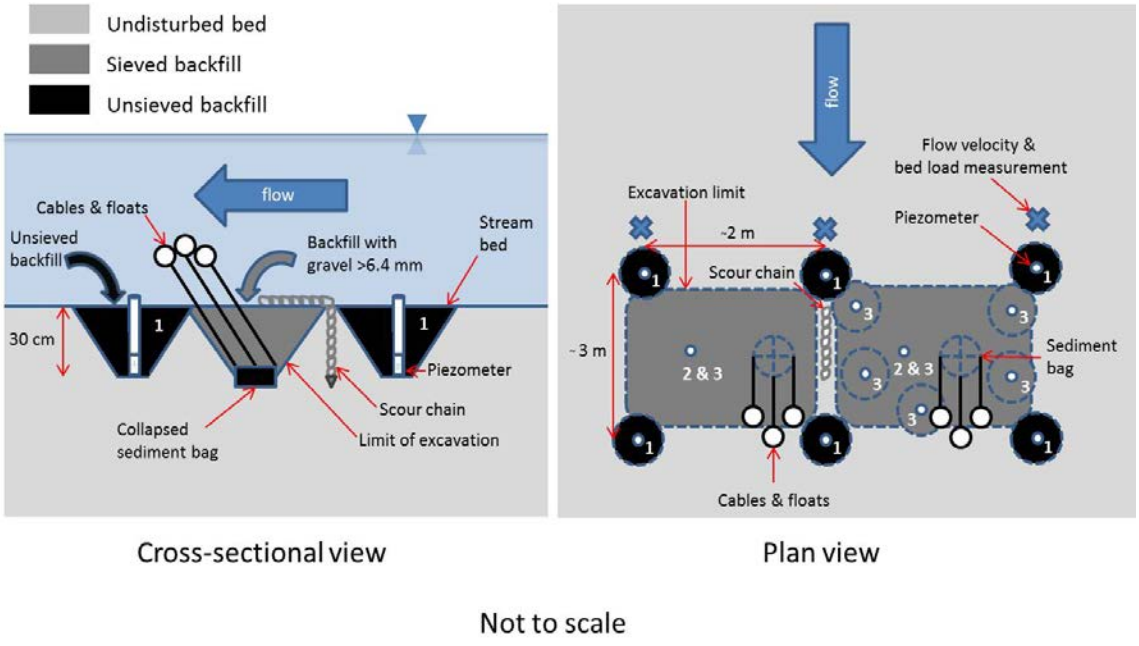

Figure 5. Generalized artificial redd experimental setup. The experiment number (in white font) indicates the piezometer positions for each experiment and the shading in the excavation pit indicates the type of backfill material. The bed topography (e.g., tail-spill and slight depression over the sediment bag) and the piezometer(s) in the sediment bag pit are not shown on the cross-sectional view for clarity. The sizes and shapes of the pits differ due to the size of the excavation that was necessary to install the monitoring instruments.

I used (i) the sediment bags to retrieve samples of fine sediment that accumulated within the redd; (ii) the piezometers to measure hydraulic conductivity around the egg pocket; and (iii) the scour chain to detect erosion and deposition of gravel on the redd. I used different backfill treatments around the piezometers to determine how the initial conditions influence hydraulic conductivity. At each site and for each experiment I constructed two artificial redds each containing a sediment bag so that they could be retrieved at two different instances in time. I measured surface flow velocity and sediment transport in close proximity to each artificial redd at flows ranging from 3 to 29 m^3/s using an acoustic Doppler velocimeter (ADV) and a Helley-Smith hand-held bed load sampler. Although water quality parameters (i.e., dissolved oxygen, electrical conductivity, and temperature) and surface flow characteristics were measured as part of

this study (Appendices A and B), their results were not found to clearly indicate changes in the incubation habitat quality caused by the accumulating sediment.

3. Sediment Bags

I collapsed and buried two impermeable sediment bags under approx. 30 cm of sieved backfill, such that one was within each of the paired artificial redds (Figure 5). The sediment bags had a 26 cm diameter circular steel frame to hold the bag open and attached to cables with floats for relocating and bag retrieval. At various times throughout each experiment, I retrieved the bags by lifting them with a hoist through the overlying sediment. As the sediment bag was hoisted, it captured the column of overlying sediment. I removed the first of the paired sediment bags (located towards the left when facing downstream, i.e., river left) 32 to 41 days after installation. I retrieved the second after an additional 105 days in Experiment 1, 30 days in Experiment 2, and 84 days in Experiment 3 to monitor differences in sediment accumulation from variable cumulative sediment transport. Sediment samples were transferred to sealed buckets and transported to a laboratory for sieve analysis. Sediment bag sample sieve results are tabulated and illustrated in Appendix C.

4. Piezometers

I used the piezometers to measure hydraulic conductivity and water quality parameters from within the artificial redd and surrounding bed substrate [*Terhune,* 1958; *Barnard and McBain,* 1994] at various times during the experiments. I constructed the piezometers out of PVC pipe with: an inside diameter of 34 mm and outer diameter of 42 mm; a total length of 380 mm including its top's slip-cap; a bottom capped with a shortened slip-cap glued in place; and perforated with 48 x 3.2 mm diameter holes in 16

columns of 3 holes with each column offset, covering a length of the piezometer that is from 73 mm to 13 mm from its bottom end. These design specifications fall between those of *Terhune* [1958] and of *Barnard and McBain* [1994]. Since both of these referenced studies laboratory-calibrated their design piezometer and produced similar hydraulic conductivity as a function of inflow results (Figure 6) [see *Barnard and McBain,* 1994] even with the slight differences in their piezometers, the intermediate design used herein is believed to also function according to the same calibrated graph.

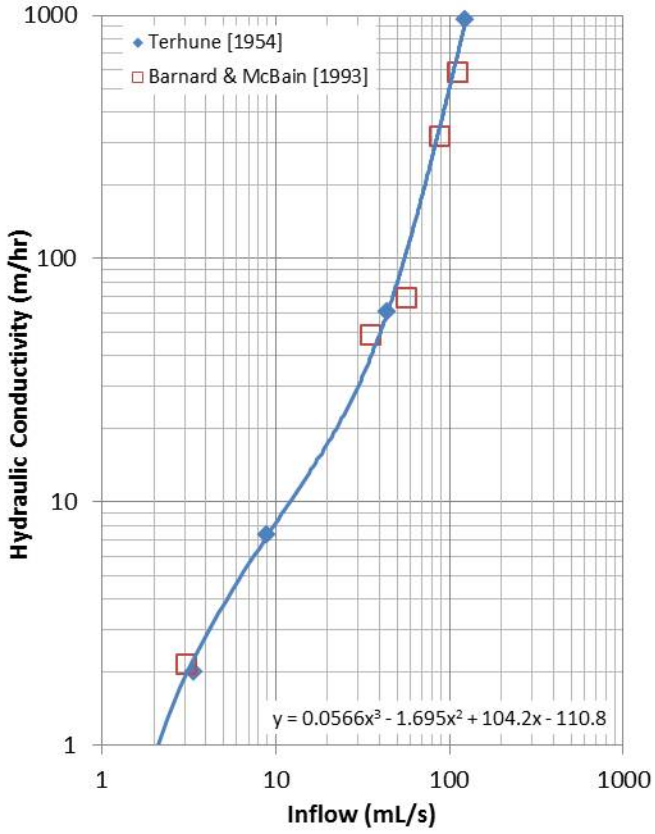

Figure 6. Laboratory produced inflow to hydraulic conductivity curve. Data points are from previous researchers' calibration measurements from their piezometer designs and laboratory-determined hydraulic conductivity [*Terhune*, 1954; *Barnard and McBain*, 1994]. The curve is fit by a nonlinear least squares regression and the resulting equation is used for converting hydraulic conductivity from the piezometer inflow rate.

I installed the piezometers in different positions during each experiment as expressed by the numbers next to the piezometers in Figure 5. I placed the screened end of the piezometers at about 30 cm below the final grade of the artificial redd surface and backfilled the pit with unsieved bed material during Experiment 1 and sieved bed material during Experiments 2 and 3 as indicated by shading in Figure 5. The backfill treatments provided two distinctly different levels of small granule content that can result from gravel cleansing during a natural redd construction process. I used the different backfill types to examine the difference in hydraulic conductivity resulting from different degrees of backfill cleansing. I found that a 6.4 mm sieve removed all the sand grains with less effort spent on sieving than smaller sieve sizes. Unsieved backfill more likely resembled the existing bed material grain size distributions that had 10% to 30% sand content as shown in Figure 4. I placed six piezometers around the periphery of the artificial redds in Experiment 1 and I left them in place through Experiment 2 to determine the extent of further change in hydraulic conductivity with additional time and increased flow levels. During Experiment 2, I installed two piezometers at each site alongside the sediment bags. During Experiment 3, I installed seven piezometers at each site with two placed next to the sediment bags and the other five installed in positions arranged in a downstream pointing chevron. Because they were later disturbed as part of other efforts that are not pertinent to this study, I only used these five piezometers for the first two hydraulic conductivity-monitoring events of Experiment 3.

Hydraulic Conductivity

I calculated the hydraulic conductivity within the interstitial environment of the artificial redds from the flow rate into the piezometer when the hydraulic head within the

piezometer is reduced by 2.5 cm below that of the stream surface following the method of *Terhune* [1958]. To do this, I attached a riser pipe to the piezometer that extends the piezometer to above the water surface level. I extracted the water within the piezometer with a battery-powered pump, maintaining the depressed hydraulic head, and filled a graduated cylinder. The hydraulic head depression of 2.5 cm was (i) attained by submerging the probe of the pump 2.5 cm below the water surface, (ii) detected by the slurping sound from the probe tip when it was pulling from the air and water interface, and (iii) maintained by holding the probe steady with a vice-grip held on the top of the piezometer. I determined the inflow rate from the amount of time required to remove 2 L of water from the piezometer.

I measured inflow rate into the piezometers on multiple days during each artificial redd experiment to determine the change in hydraulic conductivity with time at each piezometer. Typically, I made measurements immediately after installing the artificial redds and every 2-4 weeks thereafter. I used these inflow rates in the regression equation provided in Figure 6 to calculate the hydraulic conductivity for each measurement following the methods of *Terhune* [1954]. See Appendix D for tabulated piezometer monitoring data.

Finally, I factored the effect of water temperature on kinematic viscosity into each measurement of hydraulic conductivity so as to standardize all measurements to 10 degrees Celsius [*Terhune,* 1958] (Appendix D). I used the daily median water temperatures measured at the stream gages at SJF and H41 [*CDEC,* 2015a, b] to linearly extrapolate (Site A) and interpolate (Site B, Site C, Site D, and Site E) water temperatures, using RKm as the independent variable. Occasionally, I measured water

temperature in the surface flow and hyporheic zone via the piezometers that ranged from 11 to 19 °C (n=90). I used these data to compare with the linearly interpolated estimations of water temperature at each site. The difference between the field measured and linearly estimated temperature produced viscosity factors that averaged 1% greater than the actual viscosity (mean and median), with errors ranging from -2% to 9%. The observed range of error (<10%) is believed to be within the error of the overall hydraulic conductivity determination and is therefore not suspected to limit the accuracy of hydraulic conductivity calculations.

5. Bed Load Transport Sampling

I measured bed load transport rates to quantify sediment transport to the artificial redds. I collected bed load samples while wading using a Helley-Smith handheld bed load sampler with a 7.6 cm square orifice, 3.22 expansion ratio, and 0.25 mm mesh sample bag. Typically, I collected samples over a duration of 30 minutes at one or more positions at the head of the redd (Figure 5). On occasion, I collected samples over a longer duration (up to 1,280 minutes) or in one case a shorter sampling duration (20 minutes) to determine if the 30 minute samples are sufficient to capture the average transport rate. The bed load transport measurements did not reveal any consistent difference resulting from either lateral position or duration. See Appendix E for the bed load sampling notes and tabulated sieve results.

D. Results

1. Fine Sediment Accumulation

I use the sediment bags – all of which monitored accumulation in sieved backfill during all the experiments – to determine the amount of sediment finer than 6.4 mm that

accumulates over various flow levels and durations. By using a 6.4 mm sieve I avoided having residual sand in the cleansed backfill thereby allowing the measurements of accumulated sand to be unambiguously related to the bed load transported samples, which are predominantly composed of sand. I retrieved the first sediment bags from each site after about a month of deployment and retrieved the second sediment bags at a later date and whose duration of deployment is variable between experiments (see Methods). The second sediment bag (i) from Site A during Experiment 1 was lost and no sample is available, and (ii) from Site B during Experiment 2 was disturbed by constant vigorous shaking for the duration of the experiment due to an object attaching to its cables that results in an anomalous measurement (shown in Figure 7).

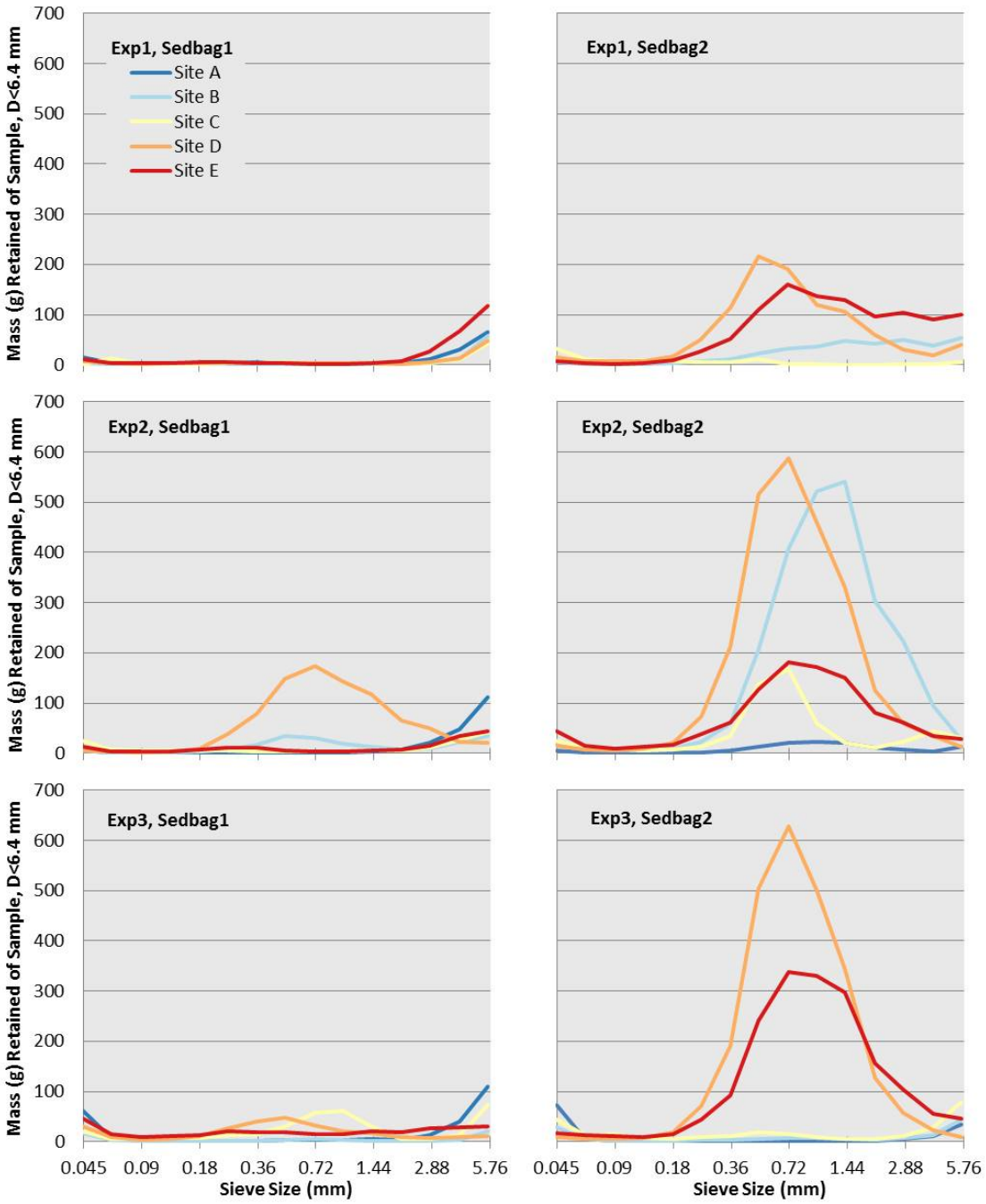

Figure 7. The grain size distributions of accumulated sediment finer than 6.4 mm measured using the sediment bags. The grain sizes are divided into half-phi intervals and the mass retained on each sieve are presented. Note that there is no second sediment bag sample from Site A during Experiment 1 and the second sediment bag sample measurements from Site B during Experiment 2 are anomalous due disturbance of the artificial redd.

The mass of grain size gradations finer than 6.4 mm in the sediment bag samples is illustrated in Figure 7 to show the differences in the grain size distributions and amounts of the sediment accumulation. The distributions consistently have a mode at about 0.72

mm and range from 0.18 mm to 2.88 mm (i.e., sand). There are also larger grains within the samples and whose distributions suggest that their presence results from incompletely cleansed backfill. By ranking the sites using the magnitude of the mode in the distributions, I avoid the ambiguity associated with the presence of these residual larger grains. These rankings indicate that the first sediment bag (Sedbag1) samples contain more sporadic and typically much smaller quantities of sand due the combination of the shorter deployment durations and lower flow levels that transport less sediment to the redds. The second sediment bag (Sedbag2) samples generally have more sand than the first, as they were often deployed longer and experienced greater flow levels.

In general, greater amounts of sediment accumulation correspond with longer duration and higher flow but neither of these factors on their own consistently explains the differences. The only appreciable amount of sand in the first sediment bag is from Site D during Experiment 2, while all the second sediment bag samples from Experiment 2 contain noticeable amounts of sand, except Site A. Additionally, even though flows are much greater during Experiment 2 (Q_{max}=31.4 m^3/s) the amount of sand accumulation at Site D is nearly equivalent with Experiment 3 (Q_{max}=13.3 m^3/s) and the accumulation at Site E is greatest during Experiment 3. Also, it is evident that Experiment 1 has less sediment accumulation at Sites D and E than Experiment 3 even though during both experiments the flow was at baseflow levels and the deployment of the second sediment bags from Experiment 1 lasts a month longer than those of Experiment 3. Therefore, the relationships between the amounts of sediment accumulation due to either the duration or flow level are not clearly discerned from Figure 7. These effects are more clearly distinguished in subsequent sections below.

The depth to which the accumulated sand penetrated the backfill of the redds was not explicitly observed. However, I did observe sand filled spaces between the backfill gravel and cobble on the surface of most of the redds by the end of the Experiments 1 and 2 (see photographs in Appendix F). This was not the case at Site A and B where the surface of the redds remained clean coarse gravel and cobble. At Site A the lack of sand on the surface is explained by a negligible amount of sand accumulation (Table 2). However, in the second sediment bag sample from Site B during Experiment 2 there was an abundance of accumulated sediment. Here, the shaking sediment bag cables appears to have caused the infiltrating sediment to penetrate deeper thereby leaving the backfill relatively clean on the redd surface and allowing more sediment to accumulate than might otherwise. From these results, I suspect that normally accumulated sand concentrates near the surface as opposed to distributing through the backfill.

Table 2. Accumulated sediment. Sieve results are included in Appendix C. Notes: NA = data not available. * = anomalous measurement.

	Accumulated Sediment (g)					
Site	Experiment 1		Experiment 2		Experiment 3	
Id	SedBag1	SedBag2	SedBag1	SedBag2	SedBag1	SedBag2
A	156	NA	204	129	261	138
B	93	358	211	2464*	67	138
C	100	97	155	597	352	279
D	106	1001	883	2476	284	2502
E	266	1026	173	1033	312	1771

Overall, sand accumulation varies fairly consistently between the sites, especially when considering samples collected over longer duration or higher flows. The amounts of accumulated sediment (Table 2) indicate that (i) Site D and Site E consistently have the most, (ii) Site A and B more often have the least (i.e., excluding the anomalous measurement at Site B from Experiment 2), and (iii) Site C has a variable ranking. This variability at Site C appears to be due to the flow level, as during Experiment 2 it has a

nearly equivalent amount of sand as Site E while during the other experiments it contains a negligible amount (i.e., < 500 g).

2. Hydraulic Conductivity

I used piezometers to measure the hydraulic conductivity beneath approx. 30 cm of the backfill. I use the hydraulic conductivity measured from each piezometer to evaluate its variability with time and location (Figure 8). Generally, the measurements from a site on a given date range by up to 0.5 to 1.5 orders of magnitude, which indicates conductivity is highly variable. Despite the variability between measurements at a location, the values demonstrate that the artificial redd backfill became less permeable with time in both backfill types. In most cases, the conductivity decreases by an order of magnitude over the course of an experiment.

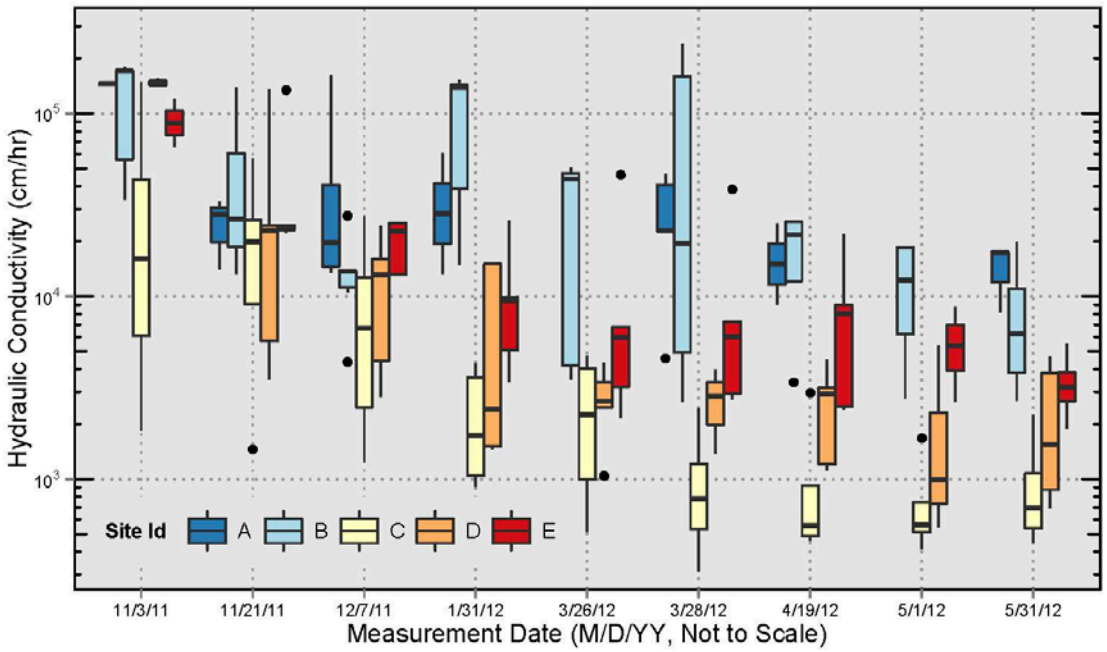
Hydraulic Conductivity (cm/hr)
10^5
10^4
10^3
Site Id
A
B
C
D
E
11/3/11
11/21/11
12/7/11
1/31/12
3/26/12
3/28/12
4/19/12
5/1/12
5/31/12
Measurement Date (M/D/YY, Not to Scale)

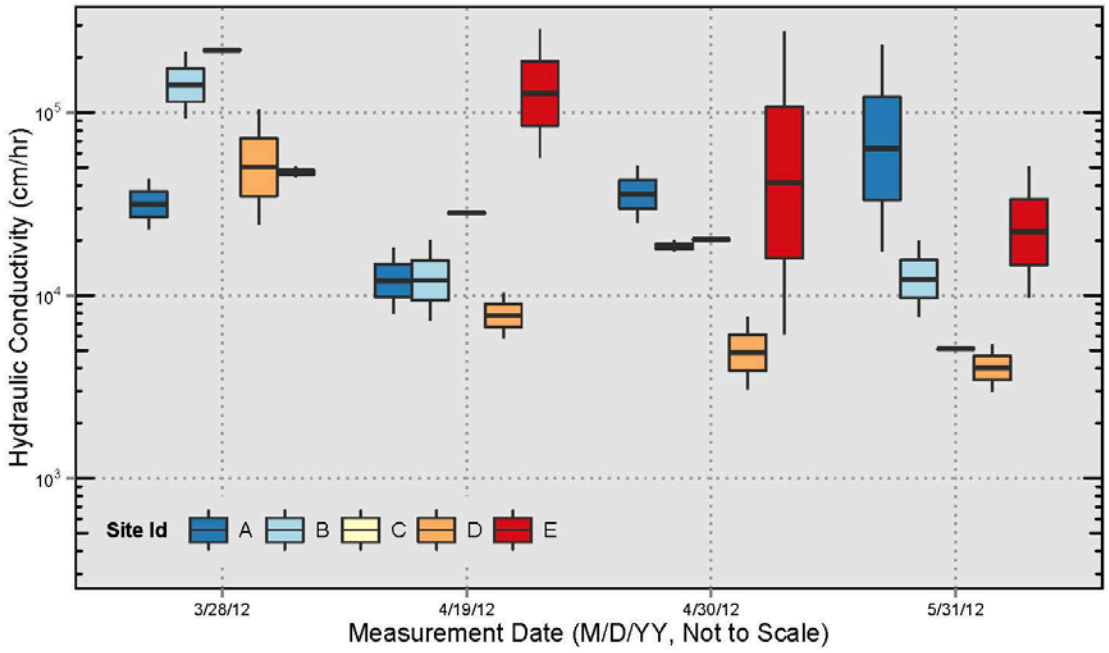
Hydraulic Conductivity (cm/hr)
10^5
10^4
10^3
Site Id
A
B
C
D
E
3/28/12
4/19/12
4/30/12
5/31/12
Measurement Date (M/D/YY, Not to Scale)

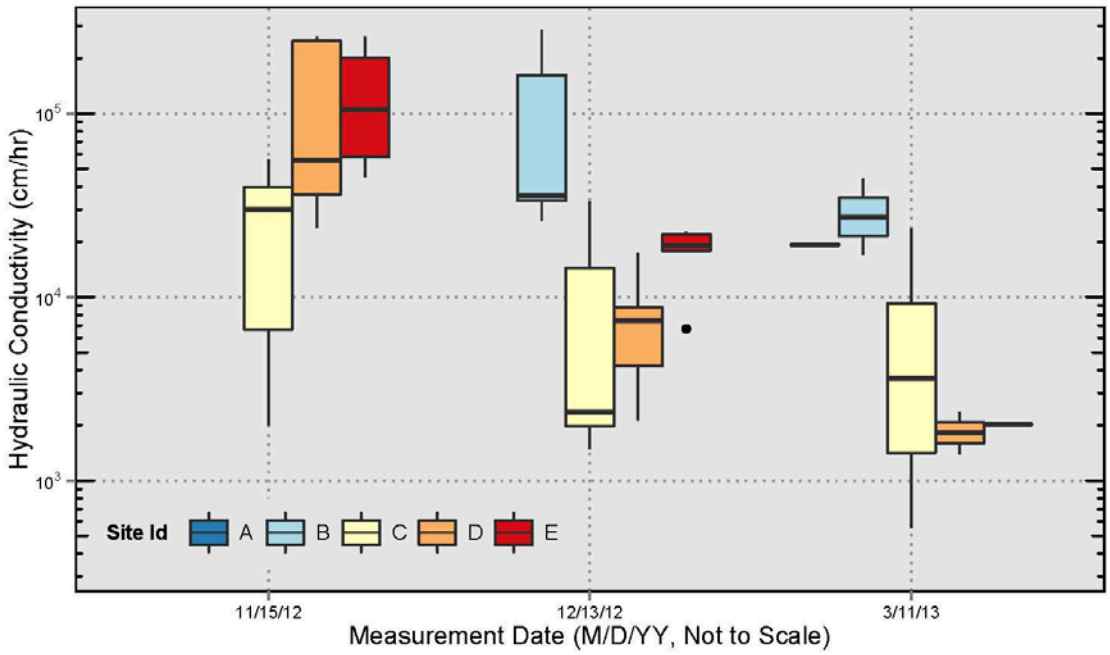

Figure 8. Hydraulic conductivity monitoring during (Top) Experiment 1 with unsieved backfill over seven months the first five months of which have low to typical incubation season flow levels of 2.6 to 12 m^3/s; (Middle) Experiment 2 with sieved backfill over 2 months of greater than normal incubation season flow levels of as much as 31 m^3/s; and (Bottom) Experiment 3 with sieved backfill over 4 months of typical incubation season flow levels of 9.9 to 13 m^3/s. These box and whisker plots illustrate the distribution of hydraulic conductivity measurements at a site (color and horizontal position) that were collected on each sampling date. The vertical limits of the boxes indicate the first and third quartiles, the thick horizontal bar indicates the median value, the whiskers indicate the extent of measurements beyond the inner quartile range but within 1.5 times the interquartile range, and the dots indicate outliers that are beyond the range of the whiskers. In cases when (i) no measurements were collected there is no box or bar shown; (ii) only one measurement was made only a bar is shown; and (iii) only two measurements were made the box and whiskers are of equal length and symmetrical about the bar and the data points are indicated by the end of the whiskers.

In general, for a given site the different backfill types and flow levels do not appear to produce distinguishable differences in the *range* of hydraulic conductivities. As indicated by the boxes and whiskers of each plot in Figure 8, for any given site the initial conductivity measurements have similar range of magnitudes during Experiment 1 with unsieved backfill as compared with Experiments 2 and 3 from sieved backfill. Also, for any given site after equivalent durations the range of conductivities is generally similar regardless of the differences in flow conditions experienced during the experiments. Only the conductivities from Experiment 2 at Site E appear noticeably higher and deviate from

this general observation. However, it is not immediately apparent as to how accumulating sediment may be confounding these very general observations. The differences in the *average* conductivity caused by flow levels are compared below in the context of accumulating sediment and bed load transport.

In general, the hydraulic conductivities vary consistently with location and time. The two upstream-most sites (Sites A and B) exhibit the highest conductivities throughout the experiments. The sandiest site (Site C) generally exhibits the lowest conductivity throughout Experiment 1 and the three downstream-most sites (Sites C, D, and E) generally have the lowest conductivity at the end of the Experiments 2 and 3. Although the conductivity decreases at all sites, there are instances of increased conductivity at Site B during Experiment 1 that appears to be due to measurement variability. Measurement variability may also be responsible for the lack of a decreasing conductivity during Experiment 2 at Sites A and E, which had low initial conductivities and abnormally high conductivities, respectively. Otherwise, over the duration of an incubation period of about 60 days, the hydraulic conductivity typically decreases by about an order of magnitude from its initial condition.

The decrease in hydraulic conductivity of the unsieved backfill is limited as it stabilizes at all sites during Experiment 1. The measurements from the last two months of Experiment 1 that coincide with those of Experiment 2 confirm this observation. At this time, the conductivity within the unsieved backfill is stable. At the same time, in the more recently installed piezometers of Experiment 2 that are in sieved backfill the conductivity decreases thereby demonstrating continuation of the processes that cause decreasing conductivity. Because the processes that cause the hydraulic conductivity to decrease

were ongoing, the stability in conductivity within the Experiment 1 piezometers suggest that the accumulation process was no longer effective in substantially reducing the conductivity of the unsieved backfill after the end of March 2012.

I use the differences in these stabilized hydraulic conductivities between sites, as shown in Figure 8 (top), to determine if the differences in the bed material along the study reach have an appreciable effect. To test for significant differences in the conductivities, I use one-way analysis of variance (ANOVA) with hydraulic conductivity being the dependent variable and site for the independent variable. Results indicate that the null hypothesis, in which the measurements are not significantly different between sites, can be rejected, and that there is a significant difference in the mean hydraulic conductivity between at least two sites (p-value=3.0×10^{-7}). I examine for difference between paired sites using a *post-hoc* Tukey honest significant difference (HSD) test (Appendix G, Figure G-1). Results indicate that there is not a significant difference between the unsieved backfill, equilibrated conductivities between Sites A and B (p-value=0.92), Sites C and D (p-value=0.96), Sites C and E (p-value=0.13), and Sites D and E (p-value=0.41), and that Sites C, D, and E are significantly different from Sites A and B (p-values<0.05).

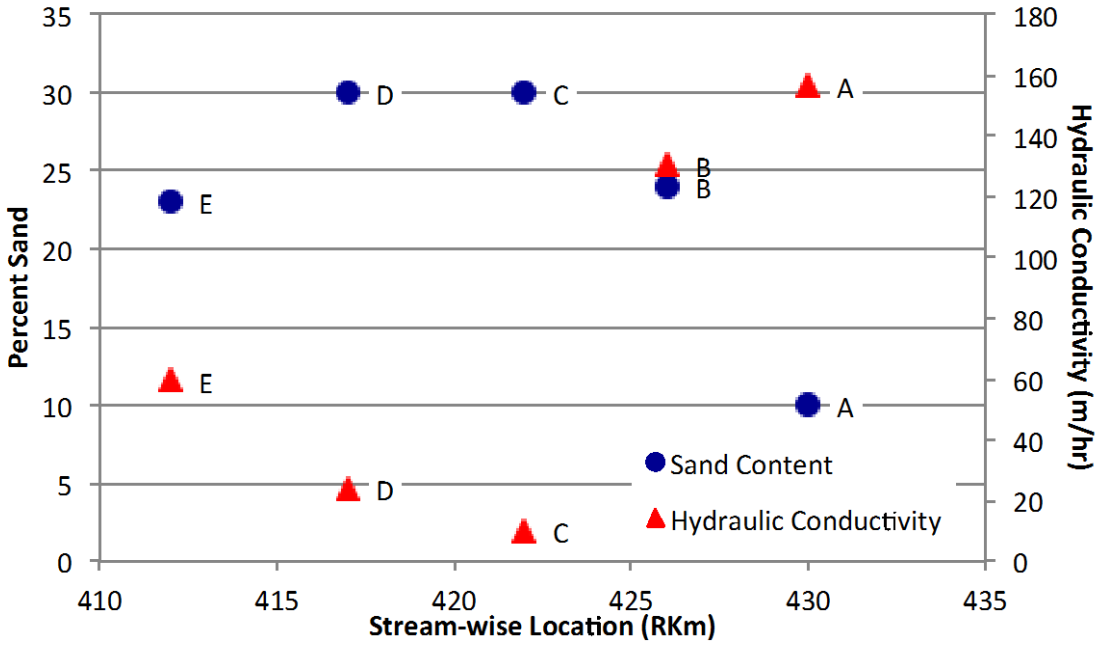

Figure 9. Percent sand content of the bed and the hydraulic conductivity as functions of stream-wise location. Percent sand content is from the truncated grain size distribution (Figure 4). The hydraulic conductivity shown is the mean of the measurements collected from the unsieved backfill after March 2012 (Figure 8).

These test results generally agree with the anticipated inverse relationship between hydraulic conductivity and sand content of the bed (Figure 9). The bed material at Sites C and D have the most sand and lowest conductivities, Site A has the least sand and highest conductivity, and Sites B and E have moderate amounts of sand and conductivities. Because Sites C and D have significantly lower conductivities it suggests that the unsieved backfill has similar relative differences in sand content between sites. The local amount of sand in the bed, thereby, appears to result in a distinct deviation from a simple trend in conductivity with distance downstream. Thus, the local sand content of the bed appears to control the difference in conductivity between the sites when using unsieved backfill. Moreover, these results indicate that the local sand content in the bed can result in lower the hydraulic conductivity within redds.

I use Figure 10 to compare the mean hydraulic conductivity measurements as a function of sand accumulation and to consider the effect of accumulation on differences between the sites and backfill types. In the plot on the left in Figure 10, a trend line fit to all the unsieved measurements with poor strength (R^2=0.01) and virtually no slope indicates that the conductivity of the unsieved backfill (solid symbols) do not show a consistent trend. This appears to suggest that the initial sand content of the unsieved backfill prevented an appreciable effect on the conductivity from accumulating sediment as measured in the sieved backfill. The plot on the right side of Figure 10 illustrates the measurements and trends using the hydraulic conductivity measurements from sieved backfill. When considering the sieved backfill, each site shows a decreasing trend with increasing accumulated sediment and the range of conductivities at the sites tend to overlap with the other sites thereby suggesting the common trend line (black line) can be used to approximate the relationship across the sites when using sieved backfill. The comparison using all the sieved backfill data indicates a strong inverse power function relationship by trend lines fit with OLS regression (R^2=0.65). Semi-log relationships were considered but the general trend produced from all the measurements is not as strong (R^2=0.51) (Appendix H, Figure H-1). The sieved backfill conductivities are generally similar to those of the unsieved backfill for equivalent amounts of accumulated sediment, although slightly less so for sites with greater sand content (i.e., Sites C and D). Overall, the data demonstrates that the conductivity strongly responds to sand accumulation and in a manner that appears consistent between sites and possibly between backfill types.

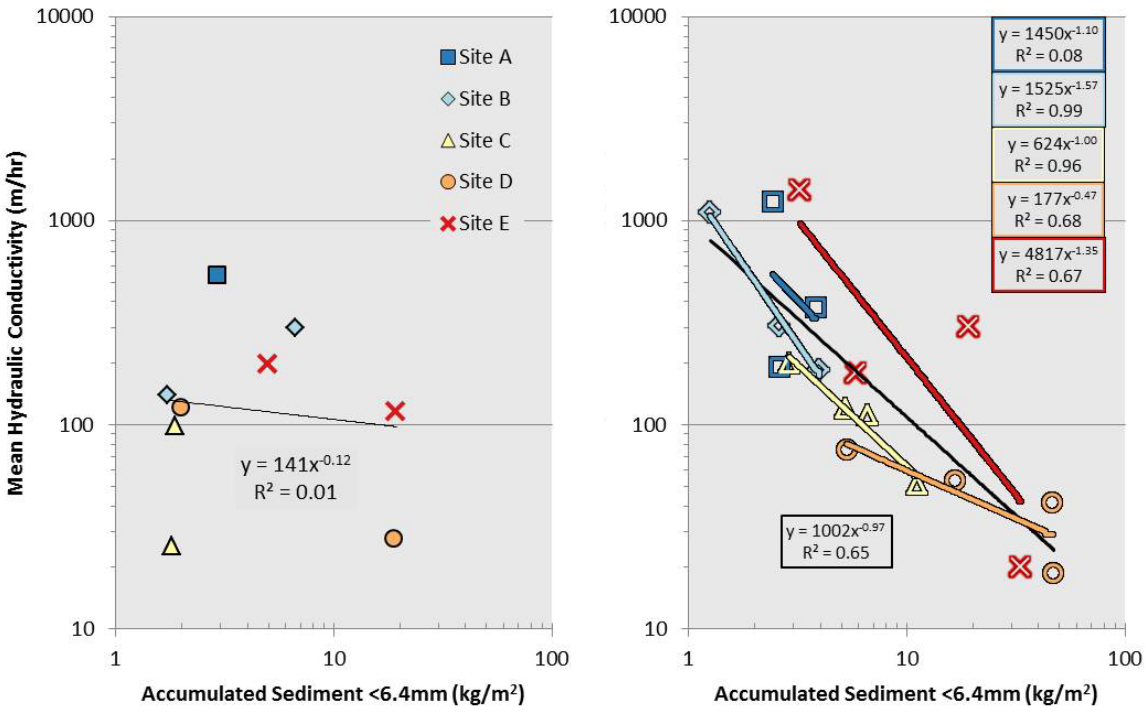

Figure 10. The mean hydraulic conductivity as a function of accumulated sediment finer than 6.4 mm. Data is shown for each site (distinguished by color) and backfill type. Left: The measurements from Experiment 1 that included unsieved piezometer backfill hydraulic conductivity measurements show that a general power function trend line fit by OLS regression (n=6) with virtually no predictive capability. Right: The measurements from the sieved backfill experiments are presented and OLS regression trend lines and equations are included for each site (n=3 to 4) and distinguished according to symbol colors, and a general trend line and equation for all the data (n=19) is indicated by the thin black line and font, respectively.

Over all, the generalized trend in Figure 10 (right) indicates that a relatively small amount of accumulation can cause a large reduction from the initial hydraulic conductivity. The generalized trend line indicates that for an order of magnitude increase in sand accumulation the hydraulic conductivity will decrease by an order of magnitude. As a result, with the first 10 kg/m^2 of accumulation (equivalent to 0.6 kg within a sediment bag) the hydraulic conductivity is indicated to decrease from 1,000 to 100 m/hr. Therefore, it is important to understand the processes that provide the accumulating sediment, such that the relationship between sediment accumulation and sediment delivered can be used to predict the effect on hydraulic conductivity.

3. Bed Load Transport

I use sediment transport measurements from a bed load sampler with a 7.6 cm by 7.6 cm square orifice to link the flow level and sediment supply to the changes in hydraulic conductivity and sand accumulation in the artificial redd backfill. Although the samples include grains up to 6.4 mm in diameter, the overwhelming majority of the sediment in transport is sand grains with diameters of 0.25 to 2 mm. As a result, I expect that with increasing discharge a larger fraction of the sampled sand grains were saltating along the bed within the lower 7.6 cm of flow while they were more likely to be rolling at lower flows.

The transport rate as a function of flow rate is variable between the sites and corresponds to the local, in channel sand supply (Figure 11). Although the sand within the bulk bed material generally increases with distance downstream, sand is also supplied from bank erosion, overbank sources, and the Cottonwood Creek and Little Dry Creek intermittent tributaries. Most of these sources are located between Sites B and C. The variability in the transport rate indicates differences in sediment delivery to the artificial redds and provides a potential explanation for the variability in sand accumulation and hydraulic conductivity between sites and experiments. In general, the two upstream-most sites have the lowest sediment transport and the downstream-most two sites have the greatest as a result of the longitudinal differences in the inchannel sand supplies. The transport rate at Site C is less than Sites A and B at flows less than 10 and 20 m^3/s, respectively, and is more at higher flows. The inconsistency in transport rate with distance downstream from the transport-rating curve of Site C is likely due to two factors: (i) the locally abundant sand supply provided from the Little Dry Creek diversion canal

(see description in Study Sites section and location in Figures 1 and 2) and an eroding bank that is composed sand (Figure 1); and (ii) the widest channel cross section with the lowest stream-wise slope (Table 1) that results in the discharge per unit width to be less than the other sites. As a result, the rate of increase in transport is lower at low discharges but increases more rapidly with increasing discharge due to the abundant sand supply.

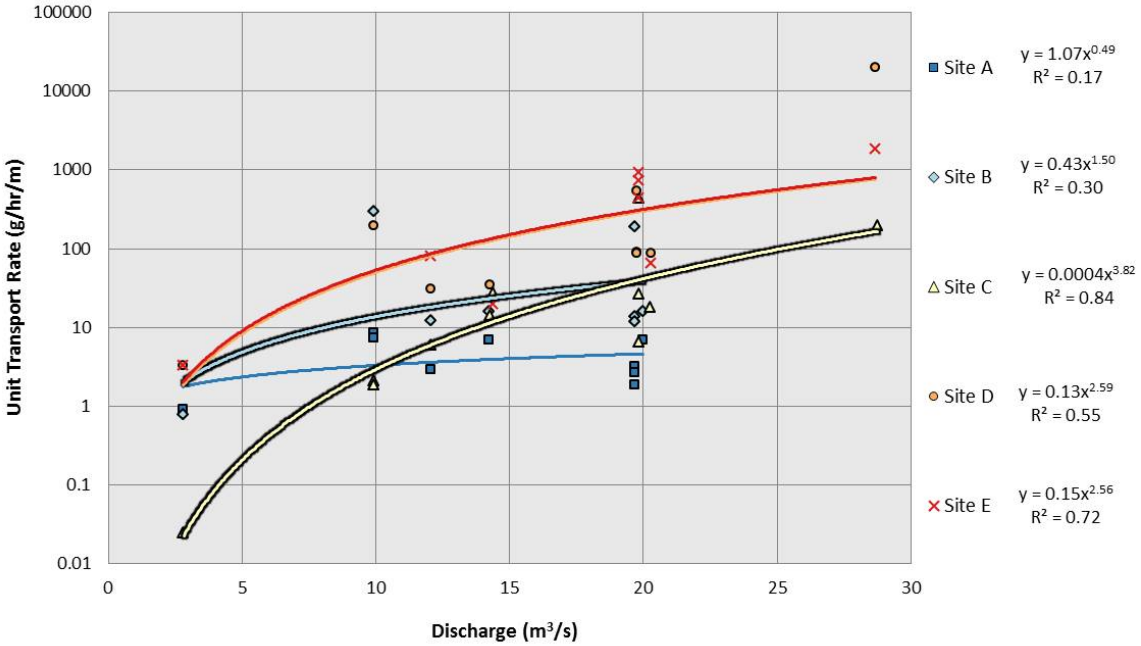

Figure 11. Bed load transport rate per unit width as a function of discharge for each site. Note that the fitted curves for Sites D and E are virtually equivalent thereby making it difficult to distinguish the curve of Site D. Transport rating curve power functions fit by OLS regression are included for each site.

Because sediment transport is a function of flow level, the amount of sediment accumulation is dependent on sediment delivered to the redds, and the total amount of sediment delivery depends on the local transport rate as a function of flow magnitude and duration, I compute the cumulative transport that occurs over the course of the experiments to provide a metric of the effect of flow and sediment supply at each site. I use the hydrographs (Figure 3) and the bed load transport rating curves (Figure 11) to compute the total amount of bed load transport per unit width at the sites for each

experiment in Figure 12. The resulting cumulative transport curves illustrate differences in the sediment delivered to the sites over the course of an experiment, such that Sites A and B generally have the least, Sites D and E have the most, and Site C is variable as it has among the lowest during the base flows and moderate during the higher discharge. The results also indicate that the small amount of accumulated sediment sampled in the first sediment bags is well explained by the cumulative transport results that show low amounts at those times. Although Experiment 2 has the shortest duration, the higher flows result in the greatest predicted cumulative transport, which the accumulation results tend to support (Figure 7). The least amount of transport occurs during Experiment 1, followed by Experiment 3 thereby confirming that the difference in sand accumulation between these experiments with base flow conditions is due to the minor differences in flow level that is sufficient to overcome the differences in duration of the experiments. Therefore, the differences in sand accumulation between experiments is generally well accounted for by the combined effects of flow level and duration.

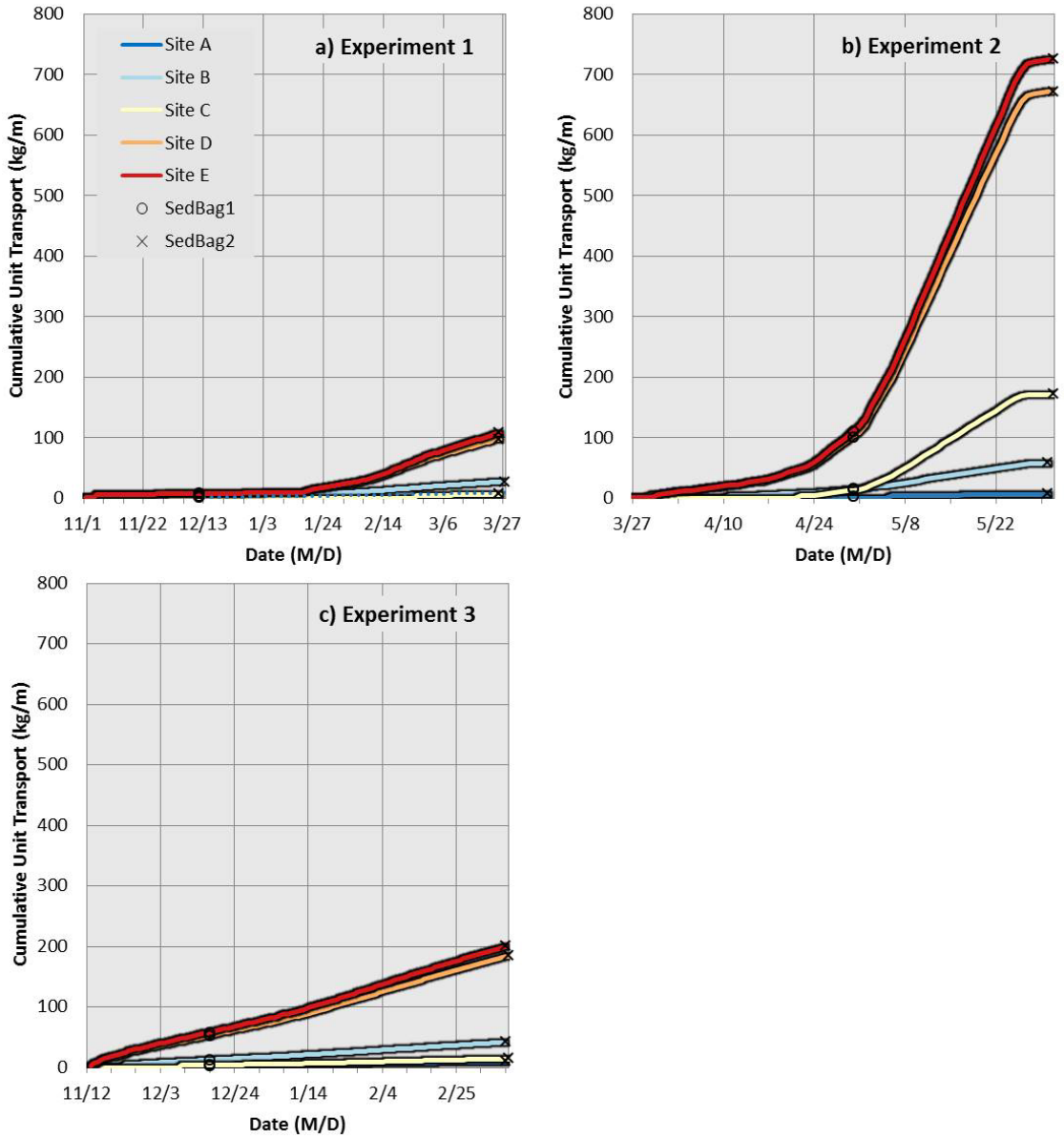

Figure 12. Cumulative unit bed load transport (lines) and sediment bag retrieval during each experiment (symbols). Each experiment begins upon installation of the sediment bags (SedBag) and piezometers. During Experiment 1 the second sediment bag (Sedbag2) was lost at Site A and the cumulative transport is indicated by a dotted blue line that is virtually equivalent with Site C.

To directly compare sediment delivery with its accumulation between sites, I fit power function trend lines with OLS regression to plots of the five to six sediment accumulation measurements at each site as functions of the predicted cumulative bed load transport (Figure 13, tabulated in Appendix I). The cumulative transport prediction associated with each sediment bag accumulation sample mass (Table 2) is indicated on

Figure 12 by symbols. Sites A and B only have data points for five sediment bag samples as mentioned previously. The fitted trend lines describe a direct and nonlinear relationship between sediment accumulation and cumulative transport. The rate of accumulation indicates that with greater cumulative transport accumulation occurs at a decreasing rate of transport. This effect results from the inability of the interstitial space to accommodate more sediment. Therefore, the trends suggest that the accumulation process is filling the accommodation space within the backfill thereby a greater proportion of the transport passes over the redds.

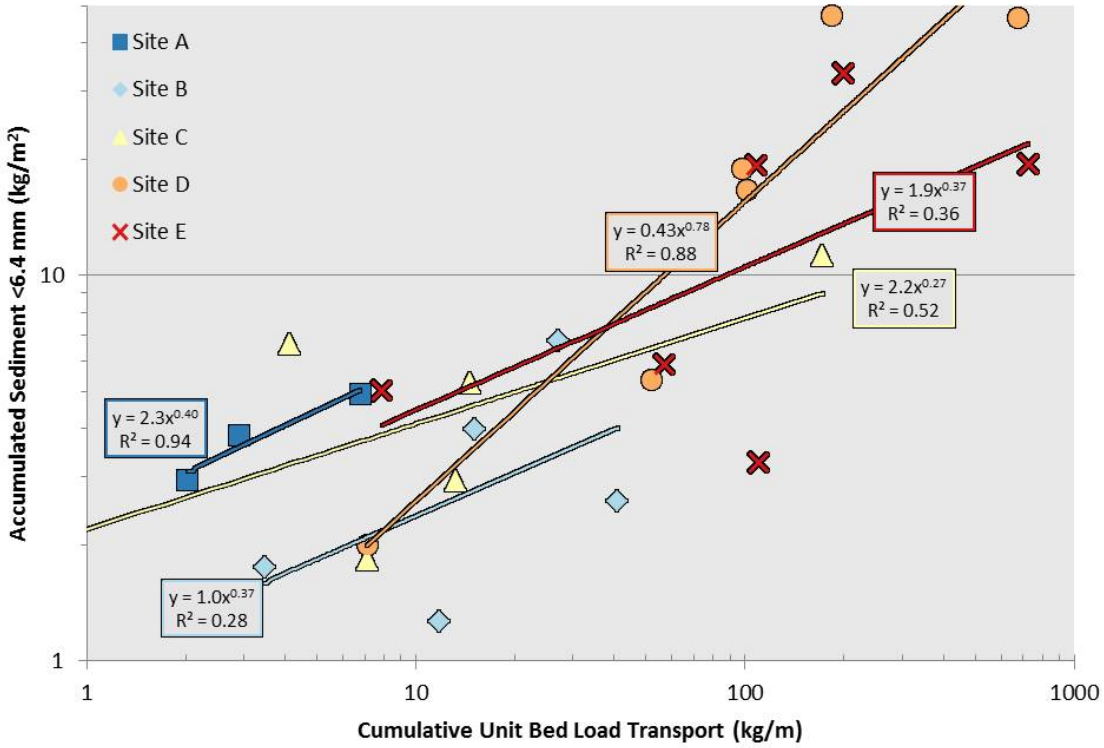

Figure 13. Accumulated sediment as a function of cumulative sediment transport. The mass of accumulated sediment finer than 6.4 mm per unit area is presented as a function of the cumulative unit bed load transport. Regression equations are provided for the trend lines of each site, which are distinguished by colors.

The accumulation measurements with cumulative transport trends are generally similar between sites, such that an explanation for their differences is not obvious. The data points generally appear to over lap thereby emphasizing the variability of the

measurements at a site. Most apparent are the similar slopes as indicated by the power function exponent that range from 0.27 to 0.40 at four sites while Site D has a value of 0.78. These results appear to indicate that the difference in the sieved backfill between at the study sites do not produce appreciable differences in the rate of accumulation with increasing cumulative transport. Therefore, along the reach it may be expected that the variability in sediment mixtures is large enough to produce similar rates of accumulation rates with increasing cumulative transport.

To compare the effect of cumulative bed load transport on the change in hydraulic conductivity, I use plots of the mean hydraulic conductivity as a function of cumulative sediment transport for each site. I separate the results into plots based on backfill type (Figure 14) (data in Appendix J) and compare the trends in hydraulic conductivity as a function of cumulative sediment transport for each site from power functions trend lines that are fit by OLS regression, which generally produce strong correlations (Table 3). Typically, the average hydraulic conductivity decreases with increasing cumulative transport, with six of the ten datasets producing statistically significant trends (p-values<0.02). Only the sieved backfill at Site A has an increasing trend, though not statistically significant (p-value=0.82).

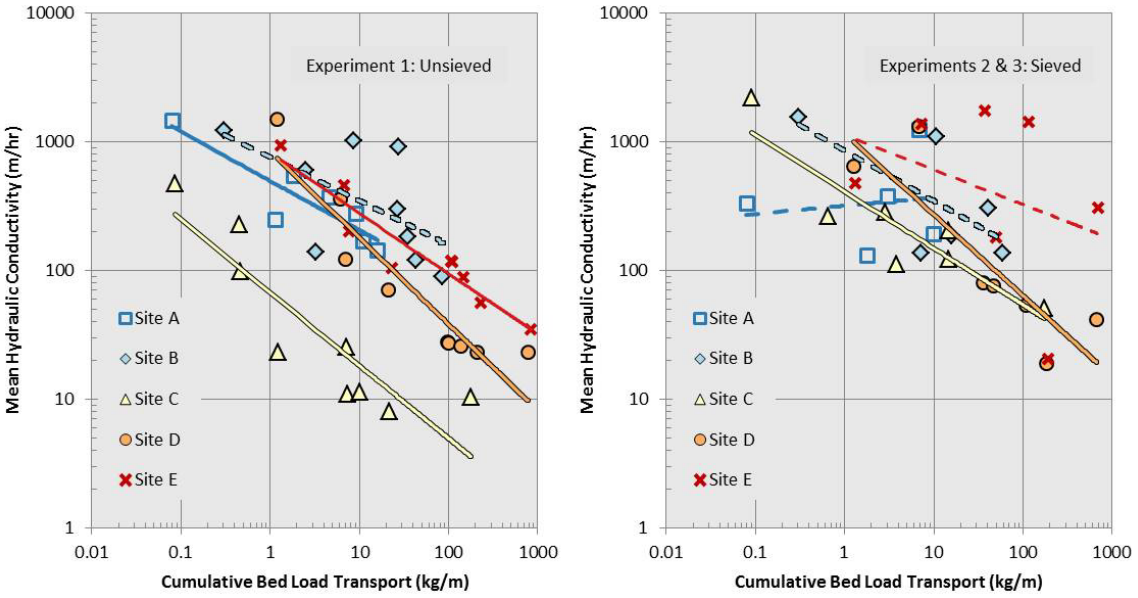

Figure 14. Average hydraulic conductivity on each monitoring event as a function of cumulative bed load transport. Data presented for the hydraulic conductivity with unsieved backfill (left) and with sieved backfill (right).

In most cases for a given site, the trends from sieved backfill have a greater magnitude than the unsieved backfill. This is evident by comparison of the intercepts of the regression functions in Table 3. The higher conductivity in the sieved backfill results from the greater porosity due to the absence of sand between the framework grains. Therefore, the sieved backfill produces higher hydraulic conductivity for a given amount of cumulative transport.

In the cases where the trends in hydraulic conductivity with cumulative transport are not significant, they appear to relate to previous observations of abnormally low initial hydraulic conductivity as noted at Site A during Experiment 2, unusual spikes in hydraulic conductivity occurring during the experiments at Site B, and abnormally high hydraulic conductivities throughout Experiment 2 at Site E. The absence of a decreasing trend in the hydraulic conductivity at Site A is likely the result of the low initial hydraulic conductivity, compounded by its having the narrowest range in cumulative transport (<10 kg/m). The anomalous spikes in hydraulic conductivity at Site B correspond to the

sediment bag retrieval events such that some of the subsequent conductivity measurements are greater after the retrievals. This may result from collapses in the layer of accumulated sediment during the retrieval efforts, although it is not certain why this was not observed elsewhere. I attribute the lack of a significant trend in hydraulic conductivity with transport at Site E to variability in the backfill packing and grain size composition. Here, the mean hydraulic conductivity during Experiment 2 is appreciably greater than the others and its sediment accumulation was less as compared to Experiment 3 (Figure 7) when cumulative transport indicates it should be greater (Figure 12). Considering that these apparent anomalous hydraulic conductivity measurements are nearly an order of magnitude different from the average trend in Figure 14, they are relatively easily to detect as outliers. Excluding these apparent anomalous data points, the remainder of the hydraulic conductivity measurements correlates well with cumulative transport.

Table 3 Parameters and statistics of the regression equations for the mean hydraulic conductivity as a function of cumulative unit bed load transport. The standard error (StEr) is provided for both coefficients. Probability (p) values >0.05 indicate that the relationship between mean hydraulic conductivity is not significantly dependent on the cumulative bed load transport. The regression equation is of the form: $\ln\langle K\rangle = m\ln\left(\sum q_{b,i}\, t\right) + \ln C$, where $\langle K\rangle$ is the mean hydraulic conductivity, in m/hr, measured on a given date, $q_{b,i}$ is the sediment transport rate that occurred over time t with subscript 'i' referring to the specific values for each increment of time since the start of the experiment, and *C* and *m* are the empirically fitted intercept and slope coefficients, respectively.

Site	Experiment	N	Intercept Coefficient, *C*	StEr	Slope Coefficient, *m*	StEr	R^2	p-value
A	1	7	6.20	0.167	-0.382	0.084	0.80	0.0062
A	2&3	4	5.76	0.470	0.064	0.256	0.02	0.8199
B	1	9	6.63	0.498	-0.340	0.171	0.36	0.0866
B	2&3	6	6.75	0.584	-0.393	0.204	0.48	0.1267
C	1	9	4.20	0.278	-0.566	0.110	0.79	0.0014
C	2&3	7	6.01	0.249	-0.439	0.093	0.82	0.0053
D	1	8	6.73	0.400	-0.671	0.096	0.87	0.0002
D	2&3	7	7.05	0.687	-0.629	0.164	0.75	0.0122
E	1	8	6.70	0.257	-0.469	0.061	0.90	0.0001
E	2&3	7	7.02	1.340	-0.269	0.314	0.13	0.4313

To determine if the trend in hydraulic conductivity with cumulative transport differs between sites, I use ANCOVA to test for significant differences in the slope and magnitude of the regression equations (Appendix J, Table J-1). Using the statistically significant trends, the range of slope coefficient values are from -0.67 to -0.38 (Table 3). Excluding Site A with sieved backfill, the ANOVA test results indicate that the slopes of the regression equations are not significantly different either when comparing (i) a site with sieved versus it with unsieved backfill (p-values>0.41) or (ii) paired sites with the same backfill type (p-values>0.06). This suggests that the rate of decrease in hydraulic conductivity as a function of cumulative transport is similar at all the sites regardless of differences in the backfill.

The magnitudes of the hydraulic conductivity versus cumulative transport trends, indicated by the regression equations intercept coefficients, for different backfill types at a site are only significantly different at Site C (p-value = $5x10^{-5}$) (Appendix J, Table J-2). The other sites did not show a significantly different magnitude between their backfill types (p-values > 0.06). Therefore, only Site C had significantly higher hydraulic conductivity when cleansed of grains smaller than 6.4 mm.

The magnitudes of the trend lines show greater variability between sites. The trends for the experiments with sieved backfill are not significantly different between sites (p-values > 0.05). However, the unsieved backfill from Site C has significantly lower conductivity than the unsieved backfill of the other sites (p-values < $2x10^{-5}$). Similarly, the unsieved backfill at Site D is significantly lower than the unsieved backfill at Sites B (p-value = 0.04) and E (p-value = 0.008). Because the magnitudes of the conductivity trends in sieved backfill are not significantly different between sites, these differences

between sites with unsieved backfill agree with the findings that the sand content in the unsieved backfill at Sites C and D that have the highest sand content in the bed material (Figure 4) are responsible for their lower hydraulic conductivities. However, although the amount of sand in the backfill inversely correlates with the magnitude of this trend, it does not result in a significantly different rate of change in conductivity with cumulative transport. Therefore, these results suggest that within the study reach the decreasing trends in hydraulic conductivity with cumulative transport can most often be approximated by a single function. This is likely due to the large amount of variability in sediment mixtures grain size distributions, sorting, and packing. Furthermore, in the two cases where a significantly different trend line is appropriate the difference is associated with them having more abundant sand in the backfill that causes a simple decrease in the overall magnitude of the trend. This may be explained by the effect of the sand in the initial backfill being distributed through the backfill column that causes a general decrease in the overall hydraulic conductivity of the backfill. Then as sediment accumulates as a concentrated layer near the bed surface it further reduces the conductivity by forming a seal at the boundary with the easiest path of resistance for water infiltrating the backfill. This concentrated seal near the surface appears to occur in both backfill types therefore it seems to be responsible for similar rate of change in hydraulic conductivity with cumulative transport as it is with accumulation and cumulative transport (Figure 13).

E. Discussion

The results demonstrate that over the course of an incubation period – about 60 days – the incubation habitat is adversely altered by fine sediment accumulation delivered by bed

load and saltating sediment transport that varies with location and flow level. The effect of these processes is to reduce the initial hydraulic conductivity of the redd by almost two orders of magnitude. To elucidate the impact that this has on salmon incubation habitat quality generally and their fry production specifically, I use a model that predicts percent egg survival to emergence (*S*) using hydraulic conductivity as the independent variable [*McBain and Trush,* 2001]. The model was developed from coupled measurements of redd hydraulic conductivity and survival of Chinook and Coho salmon eggs that are reported by *Tagart* [1976] and *McCuddin* [1977]. I use the conductivity measurements from unsieved backfill (presented in Figure 8, top), and apply the model:

$$S = 14.6 \ln(K) - 81.1 \quad (1)$$

where *K* is the hydraulic conductivity in cm/hr. The predictions indicate that although the initial conductivity is high and typically predicts greater than 75% survival, the change over the course of an incubation period would result in survival equal to or less than 50% at three of the sites (Figure 15). It follows that the processes that reduce the conductivity of the backfill at the time-scale of an incubation period (approx. 60 days) are important to salmon production.

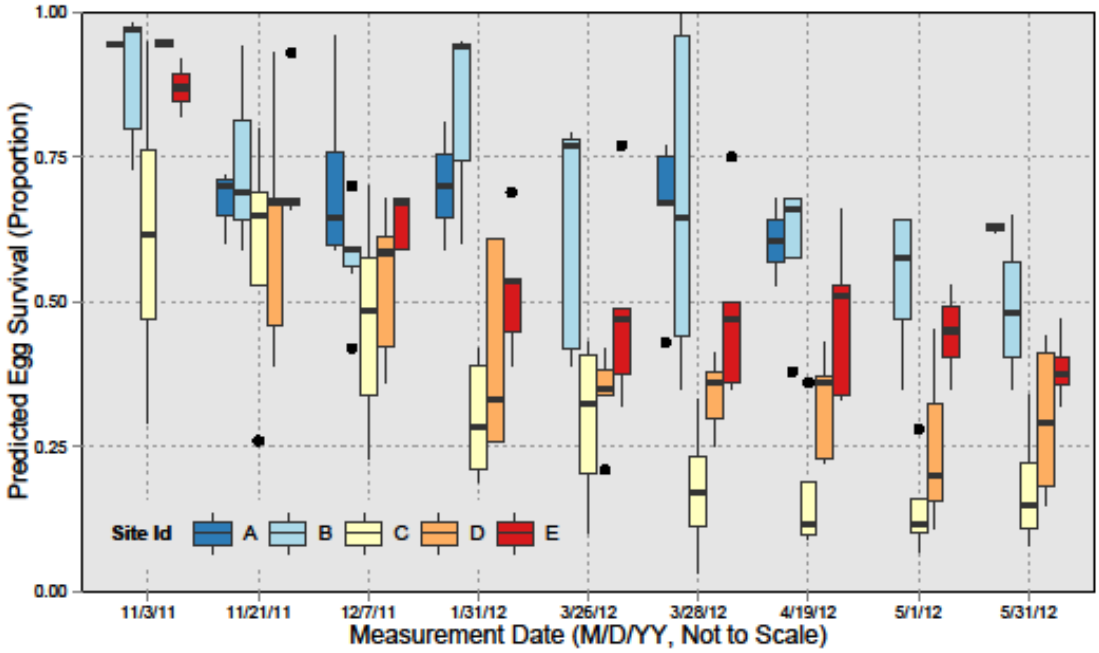

Figure 15. Predicted egg survival from hydraulic conductivity during Experiment 1. Predicted egg survival with time shows the median survival ranging from about 10% to just less than 100% and decreasing trends with time. By the end of the experiment the lowest median predicted survival was at Site C at 15%, followed by Site D at 30%, Site E at 35%, Site B at 50%, and Site A at 65%. See Figure 8 for descriptions of box plot features.

The model predictions indicate that the egg survival is strongly dependent on local factors. The decrease in conductivity of the backfill through time is a result of the accumulating sediment that depends on the local sediment transport rate. The differences in the conductivity between sites are also due to the initial grain size composition of the backfill. The initial sand content of the redd backfill affects the magnitude of the trend in hydraulic conductivity with cumulative bed load transport. This is apparent during Experiment 1 at Sites C and D, which have greater percentages of sand in the bulk bed sediment that I use for backfill (Figure 4) and the lowest conductivity (Figure 8, top). With the removal of grains smaller than 6.4 mm from the backfill the differences in the conductivity become insignificant thereby making the magnitude of conductivity as a function of cumulative transport similar between sites (Figure 14). Therefore, the egg survival predictions indicate that egg survival will depend on the amount of sediment that

accumulates during incubation and that along the study reach it will vary spatially as it depends on the abundance of sand in the backfill material.

The most accumulation of sediment is from the measurements at Site D during Experiments 2 and 3 and both are about 40 kg/m^2. However, at Site D there is also a 3.5 fold difference in the cumulative transport predictions between Experiment 2 and 3 that are approx. 700 kg/m and 200 kg/m, respectively. Because these are the largest amounts of accumulation measured during the experiments it suggests that during these experiments the backfill at Site D was virtually not able to accumulate additional sand. If the backfill can only accommodate 40 kg/m^2 of sediment accumulation, which amounts to a small thickness of about 24 mm spread evenly or about 72 mm of deposition within the void spaces between the gravels when assuming a porosity of 30%, it suggests only 25% of the vertical depth of the redd is filled. At the time that these sediment bag samples were collected the bed surface had sand filling the intergravel spaces (see photographs in Appendix F, Figure F-4). Therefore, it is assumed that the infiltrating sand penetrated to a limited depth of about 7 cm at which point the grains choked the throats between the framework grains and subsequently infiltrating grains filled the intergravel spaces above this depth, similar to that described by *Beschta and Jackson* [1979] from observations of sand infiltrating into flume beds. Therefore, this cap in the sand accumulation indicated by two measurements at Site D suggests that the infiltrating sand concentrates in a layer near the bed surface and did not distribute through the backfill column or penetrate to the bottom of the redd pit.

Because the amount of sediment accumulation depends on the amount delivered by bed load transport, the hydraulic conductivity of a redd is a function of the cumulative

sediment transport. Power functions describe decreasing trends in hydraulic conductivity with cumulative transport, typically with not significantly different magnitudes or rates of change, and strong correlations (R^2>0.7). However, the sediment accumulation measurements are less consistently accurately predicted by cumulative transport (R^2 of 0.28-0.94). From these results, I deduce that the accumulation measurements produce the majority of the observed variation from the prediction and that the average of the hydraulic conductivities at site produces more consistent results. I expect that the variation in accumulation is due to (i) the small sediment sample size that is more prone to inaccurately representing the average deposition over a redd and (ii) variability in the backfill over the sediment bags caused by differences in grain size distributions, sorting, and packing that affect interstitial spaces and pathways into which infiltrating sediment accumulate. Additionally, using sediment transport to predict changes in the hydraulic conductivity of a redd is physically reasonable as it is a mechanism that directly contributes to sediment accumulation and its variability is less when averaged over durations of weeks and months. Therefore, cumulative sediment transport offers a more reliable predictor of change in hydraulic conductivity than can be determined from sediment accumulation measurements.

When the redd backfill is sieved to reduce the difference in fine grain size composition between sites, the majority of the trends in hydraulic conductivity as a function of cumulative transport indicate that there is little difference between sites. In the few cases where the trends were significantly different from the predominant trend in hydraulic conductivity with increasing cumulative bed load transport, the complications were associated with a few anomalous hydraulic conductivity measurements at Sites A,

B, and E during Experiment 2, or the abundance of sand initially in the unsieved backfill (Site C and D during Experiment 1). Therefore, because of the apparent dependability of the relationship between the mean hydraulic conductivity and cumulative sediment transport it merits consideration as a habitat management tool.

The relationship between the hydraulic conductivity of a redd and sediment transport as a function of flow level implies that incubation habitat quality will be affected by flow level. From the results, I use the trend in hydraulic conductivity as a function of cumulative transport to demonstrate the relationship between flow level and egg survival. I use several different steady flows during typical incubation durations for Chinook salmon (~ 60 days) to illustrate the effect of flow level on cumulative sediment transport, hydraulic conductivity, and egg survival at Site C using the sieved backfill. First, I use the bed load rating curve (Figure 11) to compute the cumulative bed load transport for each flow level (Figure 16, left). The steady flows produce linearly increasing amounts of cumulative transport and whose slope directly corresponds with flow level. Second, I compute the mean hydraulic conductivity for each flow from the computed cumulative transport using the regression equation in Table 3 (Figure 16, middle). The predicted hydraulic conductivity decreases at a decreasing rate with time and the magnitude of the trends is inversely related to the flow level. Lastly, the percentage egg survival is predicted from the hydraulic conductivity using (1) (Figure 16, right). The trends in survival with time indicate that the change is initially very rapid and that the flow level is inversely related to survival. Therefore, the findings of this study demonstrate the effect of flow on hydraulic conductivity and a useful management tool for managing salmon spawning beds.

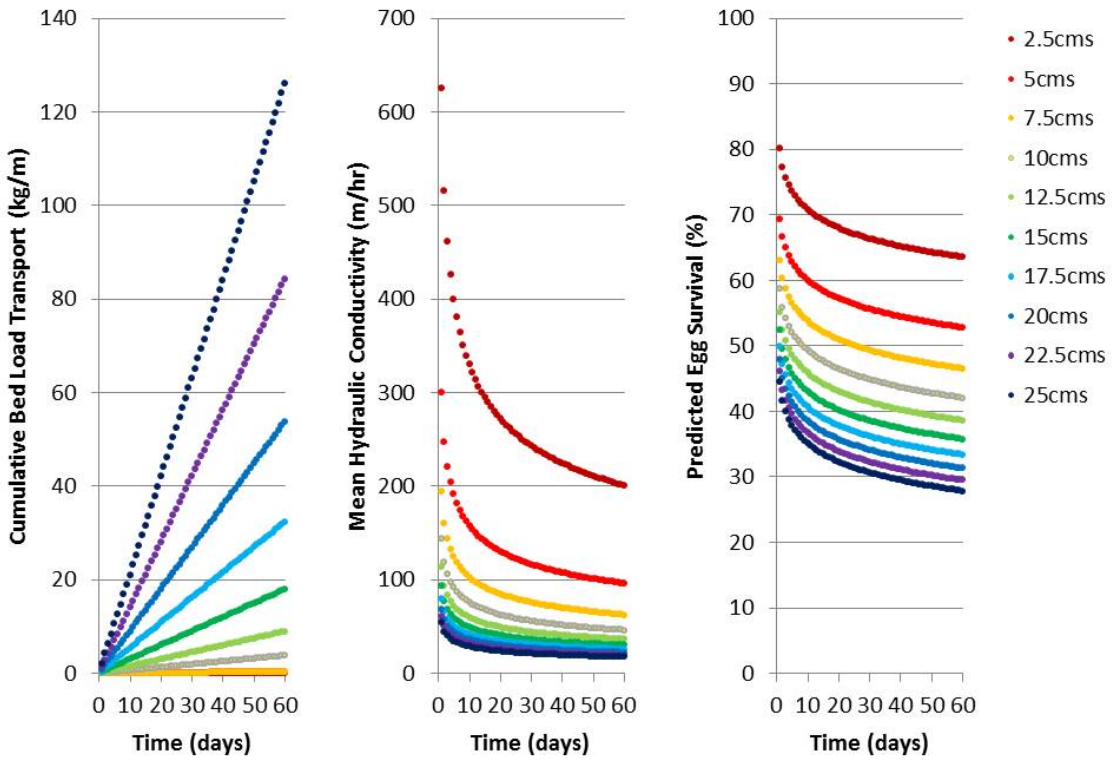

Figure 16. Effect of flow on cumulative bed load transport, hydraulic conductivity, and predicted salmonid egg survival at Site C. The effects of a variety of steady flow levels (colors) are shown over a 60 day period. The bed load transport-rating curve is used to compute the cumulative transport rate (left). The empirical relationship with cumulative transport is used to predict the mean conductivity (middle). The egg survival prediction model (1) is used to compute the egg survival (right). Depending on the flow level, the predicted egg survival after 60 days ranges from 64% to 28%. Although the 2.5 m^3/s to 7.5 m^3/s flows produce indistinguishable cumulative transport curves (left) they produce large differences in hydraulic conductivity (middle) and egg survival (right).

F. Conclusions

The hydraulic conductivity of the artificial redd backfill varies with space and time as it depends on the sediment grain size composition of the backfill of a redd and on the amount of accumulating sediment within the backfill. The range in the hydraulic conductivities did not vary noticeably between cleansed and uncleansed backfill or between flow treatments. However, the range does vary appreciably between sites and at a site with time from as high as 3,000 m/hr to as low as 200 m/hr. I find that the average hydraulic conductivity does express differences that are not expressed by the range of

values. The average hydraulic conductivity changes due to the effect of flow as it drives bed load transport and sediment accumulation. The average hydraulic conductivity varies significantly between backfill types (Figure 14) and between sites (Appendix G). The amount of sand in the backfill affects the magnitude of the conductivity but does not significantly affect the rate of change in conductivity as a function of cumulative sediment transport.

Hydraulic conductivity, sand accumulation, and cumulative bed load transport are all related. The hydraulic conductivity decreases at a log-log rate with increasing sand accumulation in the artificial redds and with increasing bed load transport over the artificial redds. Sediment accumulation increases at a log-log rate with the cumulative bed load transport. The relationship between hydraulic conductivity and cumulative bed load transport demonstrate physically meaningful results. This point is made from two observations. First, more sand initially in the backfill results in overall lower hydraulic conductivities and significantly so when comparing sites with 10% versus 30% sand in the local source material thereby indicating that the magnitude difference between the backfill types is due to the fine sediment distributed relatively evenly throughout the backfill. Second, the rate of change in the average hydraulic conductivity decreases at virtually equal rates with cumulative bed load transport thereby indicating that the changes with time are a result of infiltrating fines that concentrate in a layer at the surface of the redd and that have a similar effect on different backfill types. Therefore, cumulative sediment transport as a function of flow rate is found to satisfactorily explain changes in hydraulic conductivity.

The relationship between flow and hydraulic conductivity provides a useful tool for

characterizing the changes in salmon incubation habitat quality and production. I employed an empirically-based model (1) from coupled egg survival and hydraulic conductivity measurements by *Tagart* [1976] and *McCuddin* [1977], to demonstrate the utility of the reach-specific results for predicting salmon egg survival. The model is coupled with this study's empirically-determined trend in hydraulic conductivity as a function of cumulative bed load transport to demonstrate the relationship between flow, cumulative bed load transport, sediment accumulation, and egg survival.

G. References

Aceituno, M. E. (1990) Habitat preference criteria for Chinook salmon of the Stanislaus River, California, U.S. Department of Interior, Fish and Wildlife Service, Sacramento, California, 67pp.

Aceituno, M. E. (1993), The relationship between instream flow and physical habitat availability for Chinook salmon in the Stanislaus River, California, U.S. Department of Interior, Fish and Wildlife Service, Ecological Services, Sacramento, California, 93pp.

Barnard, K. and S. McBain (1994), Standpipe to determine permeability, dissolved oxygen, and vertical particles size distribution in salmonid spawning gravels, USDA Forest Service, *Fish Habitat Relationships Technical Bulletin 15*, April 1994.

Bennett, D. H., W. P. Connor, and C. A. Eaton (2003), Substrate composition and emergence success of Fall Chinook salmon in the Snake River, *Northwest Scientific Association, 77(2)*, 93-99.

Beschta, R. L., and W. L. Jackson (1979), The intrusion of fine sediments into a gravel bed, *Can. J. Fish. Aquat. Sci., 36*, 204-210.

Bjornn, T. C. (1969), Survival to emergence of trout and salmon fry in various gravel sand mixtures, in Forum on the relation between logging and salmon, American Institute of Fishery Research Biologists and Alaska Department of Fish and Game, Juneau Alaska, pp. 80-88.

Bunte, K., and S. R. Abt (2001), Sampling surface and subsurface particle-size distributions in wadable gravel- and cobble-bed streams for analyses in sediment transport, hydraulics, and streambed monitoring, U.S. Department of Agriculture, Forest Service, Rocky Mountain Research Station, *Gen. Tech. Rep. RMRS-GTR-74*, Fort Collins, CO, 428 p.

California Data Exchange Center (CDEC) (2015a), River stage, flow, electrical conductivity, and water temperature data from US Geological Survey gauge San Joaquin River below Friant (SJF), data retrieved on January 5, 2015, http://cdec.water.ca.gov/cgi-progs/queryF?s=SJF

California Data Exchange Center (CDEC) (2015b), River stage, flow, electrical conductivity, and water temperature data from U.S. Bureau of Reclamation gauge San Joaquin River at Hwy 41 (H41), data retrieved on January 5, 2015, http://cdec.water.ca.gov/cgi-progs/queryF?s=H41

Chapman, D. W. (1988), Critical review of variables used to define the effects of fines in redds of large salmonids, *Trans. Am. Fish. Soc.*, *117*, 1-21.

Crisp, D. T. (1993), The ability of U. K. salmonid alevins to emerge through a sand layer, *Journal of Fish Biology, 43*, 656-658.

Freeze, R. A., and J. A. Cherry (1979), *Groundwater*, Prentice-Hall, Englewood Cliffs, New Jersey, 604 pp.

Gard, M. (1997), Simulation of physical habitat for anadromous salmonids in the lower Trinity River, U.S. Department of Interior, Fish and Wildlife Service, Ecological Services, Sacramento, California. 30pp.

Greig, S. M., D. A. Sear, P. A. Carling, and L. Whitcombe (2005), Fine sediment accumulation in salmon spawning gravels and the survival; of incubating salmon progeny: Implications for spawning habitat management, *Science of the Total Environment, 344(1-3)*, 241-258.

Huntington, C., W. Nehlsen, and J. Bowers (1996), A survey of healthy native stocks of anadromous salmonids in the Pacific Northwest and Canada, *Fisheries, 21(3)*, 6-14.

Katz, J., P. B. Moyle, R. M. Quinones, J. Israel, and S. Purdy (2012), Impending extinction of salmon, steelhead, and trout (Salmonidae) in California, *Environmental Biology of Fishes*, DOI 10.1007/s10641-012-9974-8.

Kondolf, G. M., M. J. Sale, and M. G. Wolman (1993), Modification of fluvial gravel size by spawning salmonids, *Water Resour. Res., 29(7)*, 2265-2274.

Kondolf, G. M. and M. G. Wolman (1993), The sizes of spawning gravels, *Water Resour. Res., 29(7)*, 2275-2285.

Koski, K. V. (1966), The survival of Coho salmon (Oncorhynchus kisutch) from egg deposition to emergence in three Oregon coastal streams, M.S. thesis, 84 pp., Oreg. State Univ., Corvallis.

Lackey, R. T., D. H. Lach, and S. L. Duncan, editors (2006), Salmon 2100: the future of wild Pacific salmon, American Fisheries Society, Bethesda, Maryland.

Lichatowich, J. (1999), *Salmon without rivers: a history of the Pacific salmon crisis*, Island Press, Washington, D.C.

Lisle, T. E. (1989), Sediment transport and resulting deposition in spawning gravels, north coastal California, *Water Resour. Res.*, 25, 1303-1319.

Lisle, T. E. and J. Lewis (1992), Effects of sediment transport on survival of salmonid embryos in a natural stream: A simulation approach, *Can. J. Fish. Aquat. Sci., 49*, 2337-2344.

Lotspeich, F. B., and F. H. Everest (1981), A new method for reporting and interpreting textural composition of spawning gravel, U.S. Forest Service, Pacific Northwest Forest and Range Experiment Station, *Research Note PNW-369*, Portland, Oregon.

Malcolm, I. A., S. M. Greig, A. F. Youngson, and C. Souldby (2008), Hyporheic influences on salmon embryo survival and performance, pages 225-248 in D. A. Sear and P. D. DeVries, editors, Salmonid spawning habitat in rivers: physical controls, biological responses and approaches to remediation, *American Fisheries Society, Symposium 65*, Bethesda, Maryland.

McBain and Trush (2001), Spawning gravel composition and permeability within the Garcia River Watershed, California: Final Report, for Mendocino County Resource Conservation District, dated March 14, 2001.

McCuddin, M. E. (1977), Survival of salmon and trout embryos and fry in gravel-sand mixtures, Master's thesis, University of Idaho, Moscow.

McNeil, W. J., and W. H. Ahnell (1964), Success of pink salmon spawning relative to size of spawning bed materials, U.S. Fish and Wildlife Service, *Special Scientific Report – Fisheries 469*, Washington, D.C.

Montgomery, D. R. (2003), *King of fish: the thousand year run of salmon*, Westview Press, Oxford, UK, 304 pp.

Moyle, P. B., Purdy S. E., and J. A. Israel (2008), *Salmon, steelhead, and trout in California: status of an emblematic fauna*, California Trout, San Francisco, California, 316 pp.

Nehlsen, W., J. E. Williams, and J. A. Lichatowich (1991), Pacific salmon at the crossroads: stocks at risk from California, Oregon, Idaho, and Washington, *Fisheries, 16(2)*, 4-21.

Peterson, N. P., and T. P. Quinn (1996), Spatial and temporal variation in dissolved oxygen in natural egg pockets of chum salmon, in Kennedy Creek, Washington, *Journal of Fish Biology, 48*, 131-143.

Phillips, R. W., R. L. Lantz, E. W. Claire, and J. R. Moring (1975), Some effects of gravel mixtures on emergence of coho salmon and steelhead trout fry, *Trans. Am. Fish. Soc., 104*, 461-466.

Reiser, D. W. (1998), Sediment gravel bed rivers: ecological and biological considerations, pages 199-228 in P. C. Klingeman, R. L. Beschta, P. D. Komar, and J. B. Bradley editors, *Gravel-bed rivers in the environment*, Water Resources Publications, Highlands Ranch, Colorado.

San Joaquin River Restoration Program (SJRRP) (2014), Flow data: Final daily average, U.S. Bureau of Reclamation and California Department of Water Resources, retrieved on December 10, 2014, from: http://restoresjr.net/flows/Data/index.html

SJRRP (2016), Fall-run Chinook salmon spawning assessment during 2013 and 2014 within the San Joaquin River, California, *Annual Technical Report*, March 2016.

Shea, K., and M. Mangel (2001), Detection of population trends in threatened coho salmon (Oncorhynchus kisutch), *Can. J. Fish. Aquat. Sci.*, 58(2), 375-385.

Shumway, D. L., C. E. Warren, and P. Duodoroff (1964), Influence of oxygen concentration and water movement on the growth of steelhead trout and coho salmon embryos, *Trans. Am. Fish. Soc., 93*, 342-356.

Silver, S. J., C. E. Warren, and P. Duodoroff (1963), Dissolved oxygen requirements of developing steelhead trout and chinook salmon embryos at different velocities, *Trans. Am. Fish. Soc., 92(4)*, 327-343.

Sowden, T. K., and G. Power (1985), Prediction of rainbow trout embryo survival in relation to groundwater seepage and particle size of spawning substrates, *Trans. Am. Fish. Soc., 114*, 804-812.

Tagart, J. V. (1976), The survival from egg deposition to emergence of coho salmon in the Clearwater River, Jefferson County, Washington, Master's Thesis, University of Washington, Seattle.

Tappel, P. D., and T. C. Bjornn (1983), A new way of relating size of spawning gravel to salmonid embryo survival, *North American Journal of Fisheries Management, 3*, 123-135.

Terhune, L. B. D. (1958), The mark VI groundwater standpipe for measuring seepage through salmon spawning gravels, *Journal of the Fisheries Board of Canada, 15(5)*, 1027-1063.

Young, M. K., W. A. Hubert, and T. A. Wesche (1991), Selection of measures of substrate composition to estimate survival to emergence of salmonids and to detect changes in stream substrates, *North American Journal of Fisheries Management, 11*, 339-346.

World Wildlife Fund (2001), *The status of wild Atlantic salmon: a river by river assessment*, World Wildlife Fund, Washington, D.C.

Wilcock, P. R. (1996), Estimating local bed shear stress from velocity observations, *Water Resour. Res., 32(11),* 3361-3366.

Youngson, A. F., J. C. MacLean, and R. J. Fryer (2002), Declining trends in the abundance of early running two-sea-winter Atlantic salmon, Salmo salar, in Scottish rivers , *ICES Journal of Marine Science, 59,* 836-849.

Zimmerman, A. E., and M. Lapointe (2005), Intergranular flow velocity through salmonid redds: sensitivity to fines infiltration from low intensity sediment transport events, *River Research and Applications, 21,* 865-881.

Appendix A: Water Quality Monitoring

U.S. Fish and Wildlife Service (USFWS) and California Department of Water Resources (DWR) personnel measured water quality parameters such as temperature and DO in both the surface flow and hyporheic environment.

During the first month of Experiments 1 and 3 USFWS installed Hobo^{TM} temperature data loggers in pits at each site to record surface and hyporheic water temperature at 60 minute and 30 minute intervals, respectively. Surface and hyporheic water temperatures were continuously recorded at each site. During Experiment 1 one data logger recorded water temperatures in the water column while another recorded hyporheic temperatures within an egg tube pit. During Experiment 3 each site had one data logger recording surface water temperature, and five data loggers recording hyporheic water temperature in the pits. Additionally, at various times field surveys measured the water temperature from the surface flow and the piezometers (subsequent to purging) using an YSI Pro model temperature and DO probe.

DWR's California Data Exchange Center (CDEC) stream gage stations at San Joaquin River below Friant (SJF) [*CDEC*, 2015a] and San Joaquin River at Highway 41 (H41) [*CDEC*, 2015b] provide surface water temperatures at 15 minutes intervals. I used these datasets – when the Hobo data loggers were not deployed – to interpolate the water viscosity values for each site when calculating the hydraulic conductivity in the artificial redds. I also used the survey-measured hyporheic water temperatures to assess the error in the interpolated estimate of the water temperature.

DWR measured dissolved oxygen (DO) during piezometer monitoring surveys and USFWS continuously measured DO in the hyporheic zone. DWR measured DO in the

surface flow and the piezometers (subsequent to purging) with the YSI Pro model temperature and DO probe. USFWS deployed two data loggers at each site in separate pits in Experiment 3 to record DO at 5 minute intervals beneath 20 cm of backfill.

USFWS monitored electrical conductivity (EC) during Experiment 3 with continuously recording Hobo^{TM} data loggers. They placed two loggers in separate pits to record hyporheic conditions. In addition, I used the EC data recorded from the surface flow at the Friant (SJF) [*CDEC*, 2015a] and Highway 41 (H41) [*CDEC*, 2015b] stream gages.

Results

Below I present the monitoring results for water temperature, DO, and electrical conductivity (EC). I use the trends and changes in these monitored attributes of the surface and hyporheic flow to decipher the influence of groundwater and connectivity between the surface flow and the incubation environment.

a) Artificial Redd Water Temperature

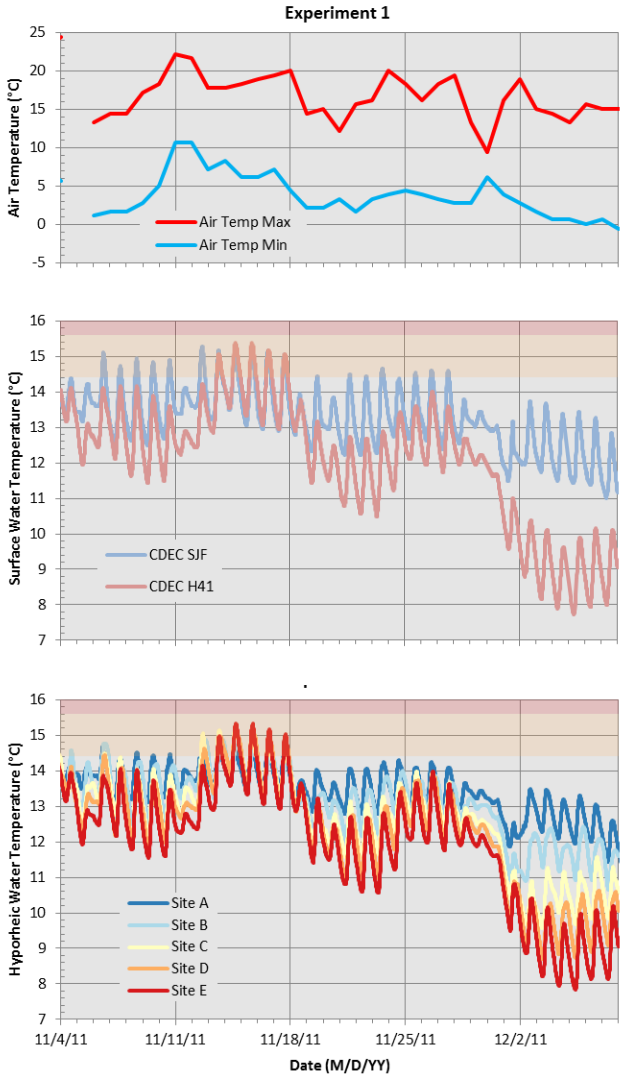

Figure A-1. Experiment 1 air and water temperature. Daily minimum and maximum air temperatures at Friant Dam (top) [*CDEC*, 2015c], surface water temperatures from stream gages at SJF and H41 (middle) [*CDEC*, 2015a,b], and hyporheic water temperatures from the artificial redd pits at each site (bottom). Water temperatures are primarily influenced by Friant release temperatures and the air temperature. The reduced diurnal signal between November 29 and December 1, 2011 appears to be a result of the smaller difference between daily minimum and maximum air temperatures. The water temperature data for each site is provided by U.S. Fish and Wildlife Service.

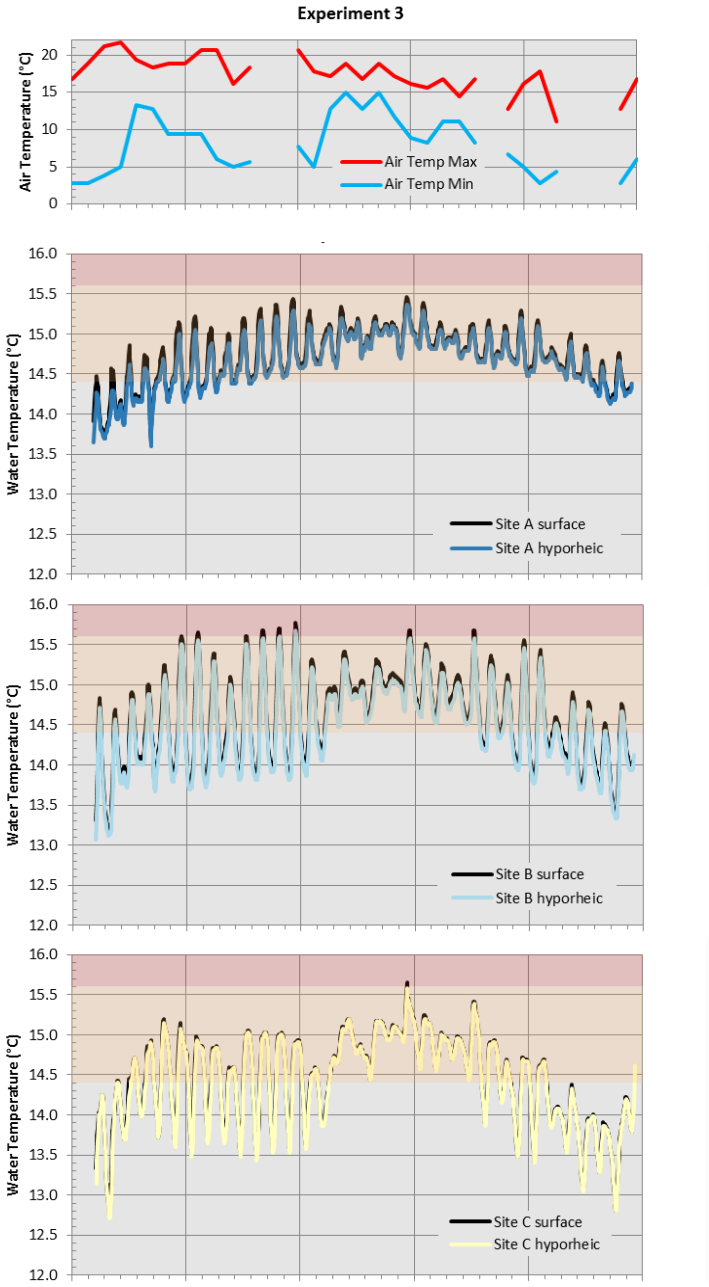
Experiment 3
Air Temperature (°C)
20
15
10
5
0
Air Temp Max
Air Temp Min
Water Temperature (°C)
16.0
15.5
15.0
14.5
14.0
13.5
13.0
12.5
12.0
Site A surface
Site A hyporheic
Site B surface
Site B hyporheic
Site C surface
Site C hyporheic

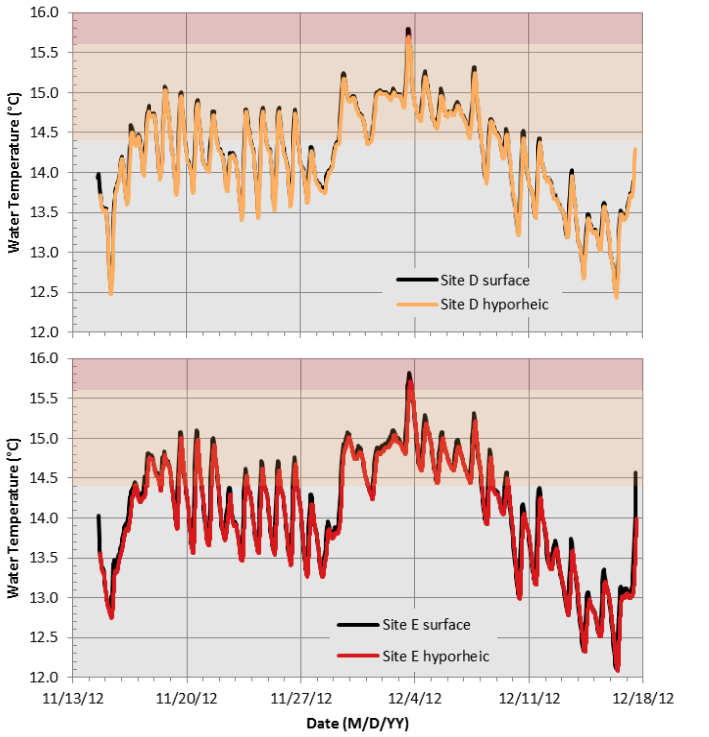

Figure A-2. Experiment 3 air and water temperatures. Daily minimum and maximum air temperatures (top) [*CDE*C, 2015c]. Hourly surface (black line) and hyporheic (colored line) water temperatures at each site show very good correspondence. Temperatures between the sites show a more complex pattern as daily minimum and reduced diurnal air temperature range have an increased affect with downstream distance. Water temperature data for each site is provided by U.S. Fish and Wildlife Service.

b) Dissolved Oxygen (DO)

During Experiment 1, DWR discretely measured the DO during piezometer monitoring surveys on November 3 and 21, and December 7, 2011. Measurements indicate DO concentrations were primarily a function of time and that there were significant differences over the course of the experiment (Figure A-3). In general, hyporheic DO was slightly less than that in the surface flow, but on November 21 the DO concentrations were as much as 3.5 mg/L less in the hyporheic and the difference increased with distance downstream by up to 42% (Site E). On this date the hyporheic DO measurement showed very little site specific differences, while the DO in the surface flow increased monotonically with downstream distance.

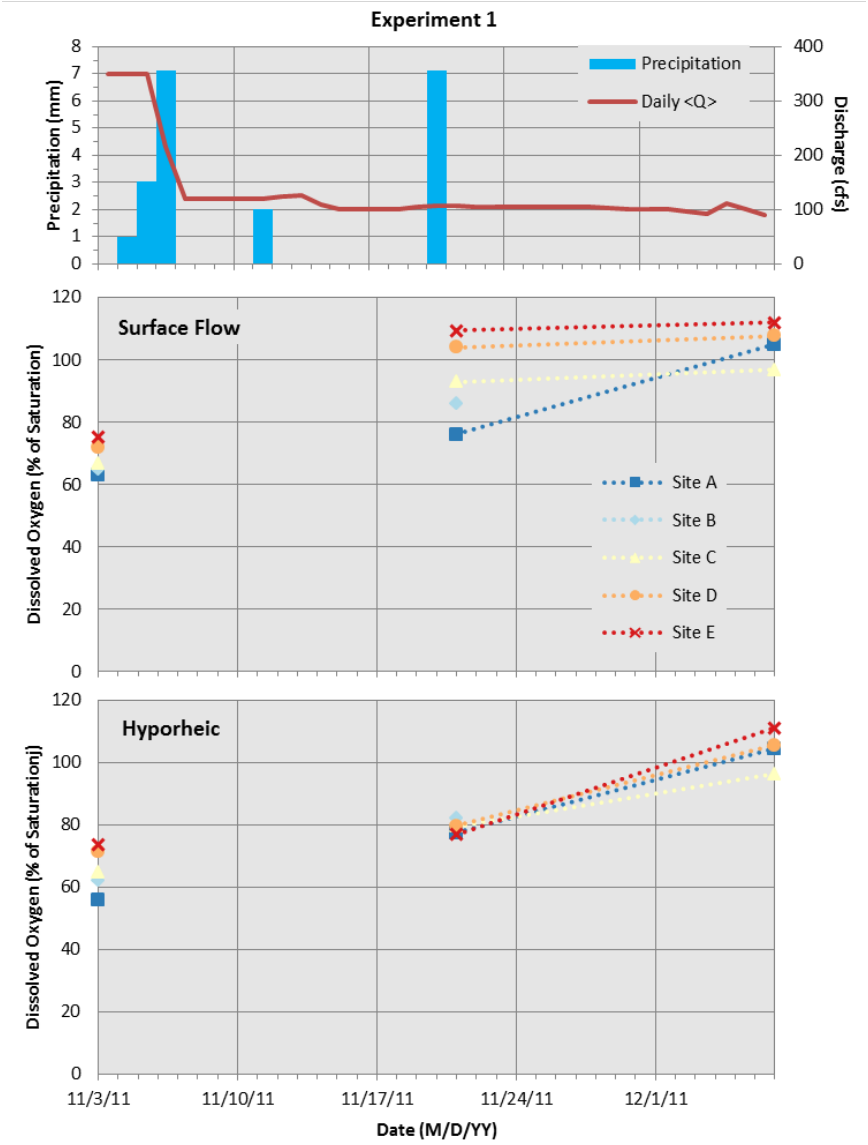

Figure A-3. Experiment 1 dissolved oxygen, precipitation, and discharge. Daily precipitation [*CDEC*, 2015c] and average discharge [*CDEC*, 2015a] (top) are illustrated with the surface (middle) and hyporheic (bottom) water percent DO saturation on November 3 and 21, and December 7, 2011. The DO gage was not calibrated on November 3; therefore those measurements are only useful relative to the measurements on that date. Otherwise, DO saturation appears to increase with time and is generally greater at sites further downstream. The November 20 precipitation coincides with the decrease in the hyporheic DO saturation while in the surface flow it increased. DO data for the sites is provided by U.S. Fish and Wildlife Service.

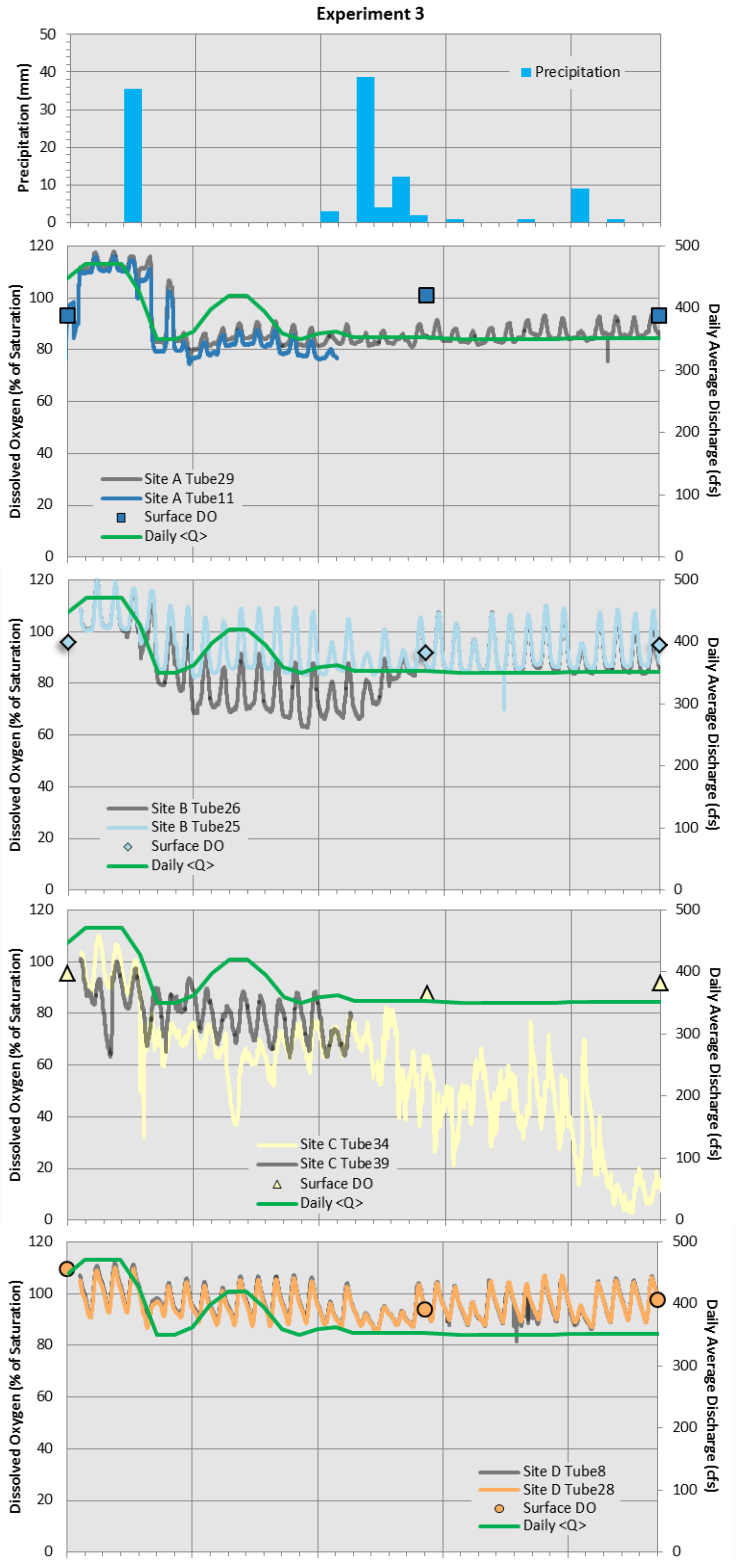
Experiment 3
Precipitation (mm)
Precipitation
Dissolved Oxygen (% of Saturation)
Daily Average Discharge (cfs)
Site A Tube29
Site A Tube11
Surface DO
Daily <Q>
Site B Tube26
Site B Tube25
Surface DO
Daily <Q>
Site C Tube34
Site C Tube39
Surface DO
Daily <Q>
Site D Tube8
Site D Tube28
Surface DO
Daily <Q>

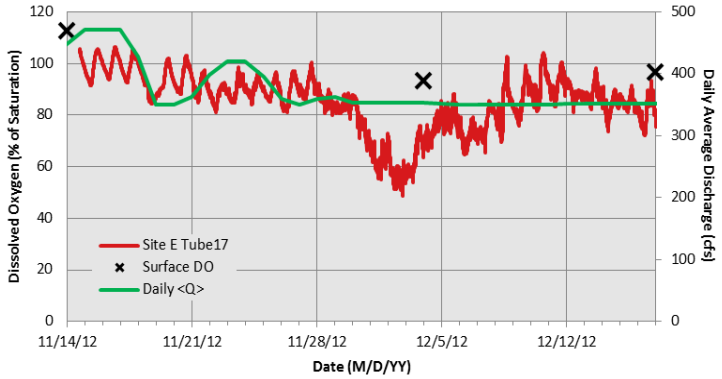

Figure A-4. Experiment 3 dissolved oxygen, precipitation, and discharge. DO in the hyporheic zone changes with time and site, while DO in the surface flow is relatively stable. Sites A and D hyporheic DO align with the surface flow. Sites C and E hyporheic DO depart from the surface flow. Their depressed levels are likely from groundwater upwelling. The lack of a clean diurnal signal is suspected to be a groundwater characteristic. Site B shows characteristics of both: (1) well defined diurnal signals and (2) both (i) depressed DO and (ii) alignment with the surface flow. Daily average discharge data is from CDEC [2015a]. Precipitation data is from *CDEC* [2015c]. DO data for each site is provided by U.S. Fish and Wildlife Service.

c) Electrical Conductivity (EC)

The EC of the water is indicative of the water quality and water source as it is a measure of the total dissolved solids.

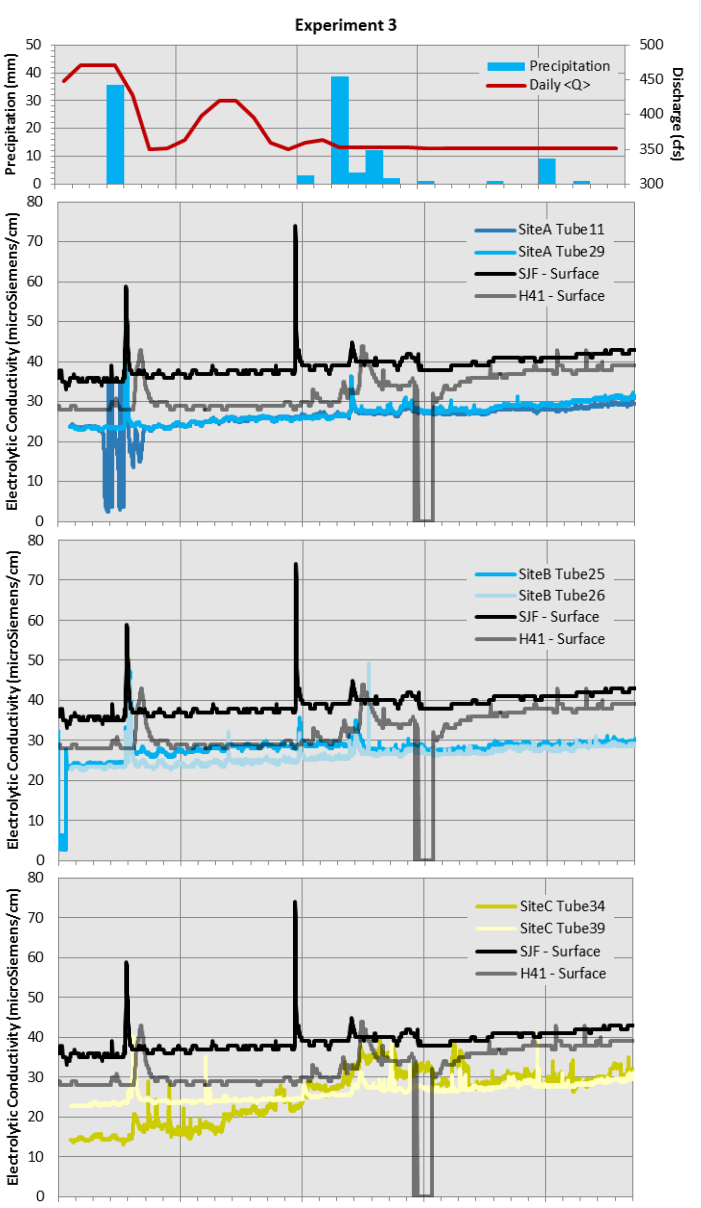
Experiment 3
Precipitation (mm)
Discharge (cfs)
Precipitation
Daily <Q>
Electrolytic Conductivity (microSiemens/cm)
SiteA Tube11
SiteA Tube29
SJF - Surface
H41 - Surface
SiteB Tube25
SiteB Tube26
SJF - Surface
H41 - Surface
SiteC Tube34
SiteC Tube39
SJF - Surface
H41 - Surface

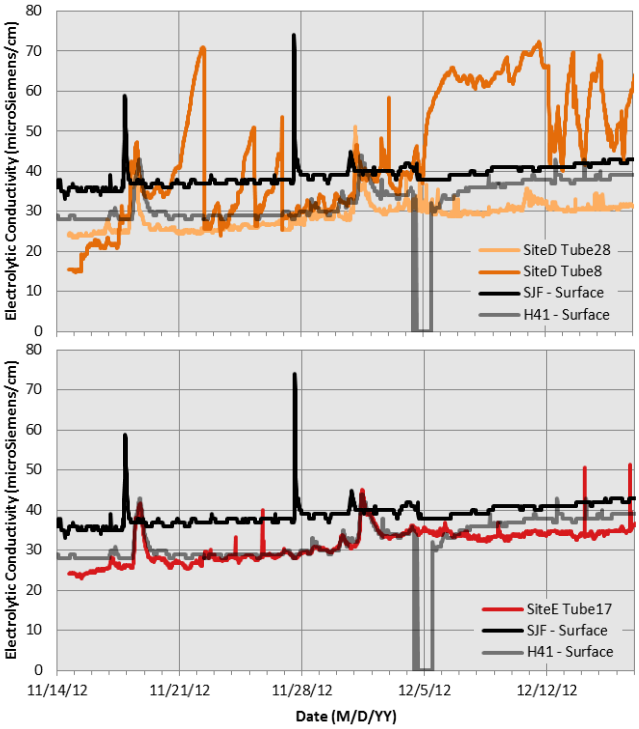

Figure A-5. Experiment 3 electric conductivity with precipitation and flow. The surface flow EC [*CDEC*, 2015a,b] can be used as a surface water tracer. An EC pulse detected at each site confirms surface flow connectivity with the artificial redds. Included is the corresponding daily average discharge and daily precipitation (top). There are two EC pulses that translate downstream and provide useful information for artificial redd and surface flow connectivity. These occur on November 18, 2012 and December 1, 2012. The November 18 pulse originates upstream of Site A. As it propagates downstream its concentration only slightly decreases and its peak is detected later at each successive site downstream. This demonstrates the high degree of connectivity between the surface flow within the artificial redd initially at all sites. The second EC pulse was also detected at all sites but increased in concentration toward Site D. This pulse is odd in that even though it propagates downstream being detected later in time with downstream distance, and additionally its concentration decreases from Site A to Site B to Site C, but it increases to a maximum at Site D and then decreases toward Site E. Site E in this case confirms the maximum at Site D in that the Site E EC concentration is also greater than the upstream most three sites. The precipitation events are suspected of being the primary contributor as they coincide with the most notable increases in EC levels. The EC data for the sites is provided by U.S. Fish and Wildlife Service.

Appendix B: Flow Velocity and Depth Measurements

I measured flow velocity and depth at each site immediately upstream of the artificial redds (see Figure 5). The duration of each velocity measurement was no less than 90 seconds so as to produce a time-averaged flow velocity. These measurements were made using a Sontek® RiverSurveyor® S5 raft mounted acoustic Doppler current profiler (ADCP). The ADCP measures velocities at discrete depths with intervals as narrow as 2 cm. These were then used to calculate the time- and depth-averaged velocity *U* (Table B-1). The ADCP also measures the flow depth *h* from its downward directed depth sounding beams. See methods in Chapter 2 for more details on flow velocity and depth measurements and calculations using ADCP measurements.

Table B-1. Flow velocity and depth measurements and calculated shear stress and slope. The shear stress (τ) was calculated from the time- and depth-averaged flow velocity (U) using the method presented by *Wilcock* [1996] and the method is described in Chapter 2. The water surface slope is calculated from the depth-slope product relationship with shear stress.

Q = 3 m^3/s				
Site	U (m/s)	h (m)	τ (Pa)	Slope
A	0.12	0.70	0.1	0.00002
B	0.34	0.37	0.8	0.0002
C	0.15	0.46	0.2	0.00005
D	0.43	0.34	1.7	0.0005
E	0.24	0.30	0.5	0.0002
Q = 10 m^3/s				
Site	U (m/s)	h (m)	τ (Pa)	Slope
A	0.61	0.79	3.1	0.0004
B	0.64	0.52	2.6	0.0005
C	0.37	0.61	1.1	0.0002
D	0.70	0.52	3.8	0.0008
E	0.55	0.43	2.3	0.0005
Q = 14 m^3/s				
Site	U (m/s)	h (m)	τ (Pa)	Slope
A	0.83	0.69	6.2	0.0009
B	0.91	0.56	5.1	0.0009
C	0.57	0.64	2.6	0.0004
D	1.00	0.59	7.3	0.0013
E	0.85	0.50	5.1	0.0010
Q = 19 m^3/s				
Site	U (m/s)	h (m)	τ (Pa)	Slope
A	0.95	0.76	7.7	0.0010
B	1.06	0.62	6.6	0.0011
C	0.64	0.72	3.2	0.0004
D	1.01	0.69	8.4	0.0012
E	1.02	0.58	6.9	0.0012
Q = 27 m^3/s				
Site	U (m/s)	h (m)	τ (Pa)	Slope
A	1.01	0.99	7.8	0.0008
B	NA	NA	NA	NA
C	0.81	0.80	4.8	0.0006
D	1.19	0.83	9.0	0.0011
E	1.11	0.58	8.3	0.0015

Appendix C: Sediment Bag Samples

The tables below present the mass retained in square sieves scaled in half-phi increments for each sediment bag sample.

Table C-1. Sieve measurements of the sediment bag samples from Experiment 1.

Sample ID:	Site A, RL	Site A, RR	Site B, RL	Site B, RR	Site C, RL	Site C, RR	Site D, RL	Site D, RR	Site E, RL	Site E, RR
Date Installed:	11/1/2011	11/1/2011	11/1/2011	11/1/2011	11/1/2011	11/1/2011	11/2/2011	11/2/2011	11/2/2011	11/2/2011
Date Sampled:	12/12/2011	Lost	12/12/2011	3/28/2012	12/12/2011	3/26/2012	12/12/2011	3/26/2012	12/12/2011	3/26/2012
Duration (days):	41	NA	41	148	41	146	40	145	40	145
Sieve (mm)	**Retained (g)**	**Retained (g)**	**Retained (g)**	**Retained (g)**	**Retained (g)**	**Retained (g)**	**Retained (g)**	**Retained (g)**	**Retained (g)**	**Retained (g)**
128	0		0	0	0	3900	0	0	0	0
88.9	2898.9		2600	0	1908.4	1889.6	3628.9	2900	0	0
63.5	5316.6		331.3	703.7	3659.3	2357.3	6233.5	5065.3	4423.7	5844.1
44.45	3063.5		557.8	1396.3	1286.5	319.8	845.9	3023.9	2963.7	2813.7
31.75	2012		1943.2	2482.9	0	495.5	1010.6	1613.5	3015.9	2062.3
22.225	1209.8		1608.4	1624.4	1562.2	476.2	615.9	1509.5	1639.7	1539.4
15.875	1343.6		850.8	889.2	656.3	311.9	561.7	429.7	1426.8	1224.8
11.1125	940.7		720	718.8	428.1	252	579.5	370.5	263.6	890.2
6.35	900		686.1	476.8	410.5	139.4	712.8	366.2	1064.1	1029.7
<6.35	155.9		92.6	357.6	100.3	97	106.4	1001.4	266	1026.4
5.6	65.4		56.8	53.7	42	5.5	48.1	41	117.8	100.2
4	29.9		10.7	38.6	10.5	1.8	13.6	19.4	66.8	90
2.8	10.8		4	50.2	3.7	0.7	4.7	29.8	27	104.1
2	3.1		1.4	42.2	2.2	0.4	1.7	60.2	7.1	95.3
1.4	2.4		1.9	47.8	2.9	0.4	2.8	105.9	3.8	128.2
1	1.3		1.4	35.8	3.4	0.5	2.7	119.3	1.9	136.1
0.71	1.6		1.5	31.8	4.2	0.7	3.2	190.1	1.7	159.3
0.5	1.4		1.3	22.7	4.6	10.5	3.5	217	2.5	109.9
0.355	5.4		1.2	10.8	3.2	4.4	3.9	113.8	3.7	50.8
0.25	4.1		1.7	6.8	3	4.4	5.1	50.1	5.5	25.9
0.18	3.3		1.9	3.6	2.4	6.8	3.6	16.9	5.7	9.8
0.125	3		1.4	2.1	2.1	8.3	2.7	8.2	4	4
0.09	3.2		1.4	1.7	2.2	8	2.4	6.3	3	2.3
0.063	3.9		1.5	1.7	12.8	11.9	2.5	6.7	3.3	2.6
<0.063	15.7		4.3	6.1	1.4	32	6.3	15	11.6	7
Total Mass (g)	17840	NA	9390	8648	10012	10238	14296	16278	15063	16430

Notes: RL = river left, RR = river right

Table C-2. Sieve measurements of the sediment bag samples from Experiment 2.

Sample ID:	Site A, RL	Site A, RR	Site B, RL	Site B, RR	Site C, RL	Site C, RR	Site D, RL	Site D, RR	Site E, RL	Site E, RR
Date Installed:	3/29/2012	3/29/2012	3/29/2012	3/29/2012	3/27/2012	3/27/2012	3/27/2012	3/27/2012	3/27/2012	3/27/2012
Date Sampled:	4/30/2012	5/30/2012	4/30/2012	5/30/2012	4/30/2012	5/31/2012	4/30/2012	5/31/2012	4/30/2012	5/31/2012
Duration (days):	32	62	32	62	34	65	34	65	34	65
Sieve (mm)	**Retained (g)**	**Retained (g)**	**Retained (g)**	**Retained (g)**	**Retained (g)**	**Retained (g)**	**Retained (g)**	**Retained (g)**	**Retained (g)**	**Retained (g)**
128	0	0	0	0	0	4000	0	0	0	0
88.9	2047	3000	12820.8	17553.7	3794.5	6399.4	4752.5	12000	0	0
63.5	2057.5	0	2027.4	0	6749	1557.1	4322.3	3061.6	1736.9	8969.8
44.45	2616.1	843.6	988	1901.3	1409.7	2029.3	197	3448.8	1815.2	7588.7
31.75	2088.1	473.5	2011.2	1099.6	1411.1	1368.4	484.2	1779.4	2164.6	3556.7
22.225	1733.5	377.7	1200.1	847.2	988.7	1462.2	697.2	891.1	1806.5	2192.5
15.875	1453.6	166.9	925.6	560.9	890.3	1199.2	359.1	512.4	1088.8	1063.3
11.1125	1016.2	133.6	531	397.3	654.6	780.2	224.6	322.5	628.1	571.1
6.35	1004.68	28	443.2	276.2	511.8	699.8	232.1	358	479.2	264.8
<6.35	204.3	129.2	210.9	2463.5	154.6	597.2	883.1	2476.3	173.3	1032.9
5.6	111.2	12.1	33.7	26.5	42.8	30.6	21.2	12.2	43.1	27.6
4	47.5	2.8	23.1	95.1	26	44.8	22.1	33.8	35.1	34.6
2.8	21.1	7.5	9.6	224	12	22.4	50	59.2	15.8	61.2
2	7	10.8	7.3	303.9	5.6	11.9	65.2	124.9	6.7	81.4
1.4	3.6	21.3	12.5	540.3	4.4	20.8	117.5	330.9	5.4	150.9
1	1.4	23.1	18.7	521.8	2.6	59.5	142.4	459.9	3.4	171.9
0.71	0.8	21	30.3	407.6	2.9	168	172.7	587.9	3.9	180.5
0.5	0.9	13	35.2	205.9	2.7	136	149.1	516.1	4.8	127.3
0.355	0.6	4.7	17.2	58.5	2.7	35.2	79.6	212.3	11.5	62.2
0.25	0.7	2.2	7.3	22.2	4.4	12.6	37.5	72.6	11.5	37.4
0.18	0.7	1.2	3.3	9.5	5.7	7.1	9.8	21.6	6.5	16.2
0.125	0.7	0.9	2.1	7.3	4.7	5.3	3.5	9.3	3.8	13.4
0.09	0.9	1.4	1.9	9.7	5.4	7.1	2.1	6.1	3.4	10
0.063	1	2.1	2.3	9.6	7.4	11.2	3.4	6.6	4.2	14.1
<0.063	4.5	4.5	6.1	17.3	24.7	23.9	5.8	15.1	13.7	44.7
Total Mass (g)	14219	5152	21158	25095	16564	20092	12151	24842	9892	25240

Notes: RL = river left, RR = river right

Table C-3. Sieve measurements of the sediment bag samples from Experiment 3.

Sample ID:	Site A, RL	Site A, RR	Site B, RL	Site B, RR	Site C, RL	Site C, RR	Site D, RL	Site D, RR	Site E, RL	Site E, RR
Date Installed:	11/13/2012	11/13/2012	11/13/2012	11/13/2012	11/13/2012	11/13/2012	11/13/2012	11/13/2012	11/13/2012	11/13/2012
Date Sampled:	12/17/2012	3/11/2013	12/17/2012	3/11/2013	12/17/2012	3/12/2013	12/17/2012	3/12/2013	12/17/2012	3/11/2013
Duration (days):	34	118	34	118	34	119	34	119	34	118
Sieve (mm)	**Retained (g)**	**Retained (g)**	**Retained (g)**	**Retained (g)**	**Retained (g)**	**Retained (g)**	**Retained (g)**	**Retained (g)**	**Retained (g)**	**Retained (g)**
128	0	0	0	7500	0	0	0	0	0	0
88.9	6000	4700	3050	3150	0	0	3300	7700	0	0
63.5	2000	4200	2650	1700	2700	4500	2600	3250	2700	3500
44.45	1900	1650	1250	0	1800	3600	2800	2800	5600	6050
31.75	1600	1200	850	1700	1900	1200	2150	600	3650	1700
22.225	1400	900	550	1250	1850	1000	900	500	1700	1400
15.875	1200	600	400	1400	1600	1200	700	200	750	1100
11.1125	1000	300	300	800	1400	850	400	100	500	600
6.35	900	250	200	500	800	700	200	100	300	300
<6.35	261	138	67	138	352	279	284	2502	312	1771
5.6	110.1	33.5	21.3	44.6	73	78.2	11.6	9.6	31.2	45.5
4	39.4	12	3.5	13.7	14	28.4	10	22.9	29.1	56.2
2.8	12.5	4.7	1.6	6.7	4.4	11	8.2	56.9	26.5	103.8
2	4.2	0.9	1.2	4.1	5.8	4.4	9.2	126.5	19.2	155.4
1.4	5	0.7	2.1	5.8	29.8	5.9	17.1	343.2	21.1	298.2
1	4	0.4	2.7	7.1	61.8	9.6	19.9	499.9	15.9	329.6
0.71	4.2	0.5	4.4	6.9	58	15.6	32.9	627.9	14.6	338.4
0.5	3.4	0.7	4	5.3	30.8	19.1	47.5	503.6	19.5	241
0.355	2.3	0.7	2.2	3.6	14.6	11.4	40.2	191.5	19.5	91.6
0.25	1.4	0.8	1.3	2.8	13.1	8.9	27	70.6	21.1	44.6
0.18	0.8	0.9	0.6	1.4	7.1	4.9	11.4	18.9	12.5	15.1
0.125	1.4	1	0.5	1	6.5	6.9	5.3	7.3	11.2	8.8
0.09	0.9	1.3	0.7	0.6	5.2	15.7	4.3	4.6	9.4	10.8
0.063	8	5.4	3.3	4.8	5.9	13.8	8.7	6.2	14.6	12.1
<0.063	61.4	72.5	16.1	27.9	20.2	43.8	30	9.5	45.5	17.8
Total Mass (g)	16259	13936	9316	18136	12400	13328	13333	17749	15511	16419

Notes: RL = river left, RR = river right

Grain Size Distributions for Grain Sizes Less than 6.4 mm

I separated the portion of the sediment bag samples with grain sizes less than 6.4 mm to determine the grain size distributions of the accumulated sediment. The total mass of sediment less than 6.4 mm and amount relative to the total sediment bag sample mass are presented in Figure B-1. When comparing the amounts of sediment accumulated at a site for an experiment most sample results show the anticipated increasing amount of sediment with the duration of sediment bag deployment (i.e., between sediment bag 1 and 2). There are discrepancies though. The largest discrepancy is from Site C during Experiment 3, which when comparing the distributions of the grain size gradations within the two samples (Figures B-2 and B-3) the first sample has a typical unimodal distribution, as observed in other samples with accumulated sediment, and the second sample suggests an absence of accumulation. This result appears to illustrate the difficulty of collecting representative samples from a heterogeneous gravel mixture that locally can accumulate variable amounts of sediment depending on the degree of grain size heterogeneity and presence or absence of large grains that can occlude fine sediment accumulation locally. Another discrepancy occurred at Site A during Experiments 2 and 3. Here, small amounts of fine sediment are from inadequate backfill cleansing. Otherwise, based on the total amount of sediment finer than 6.4 mm, the amount of sediment accumulated appears to provide reasonable results.

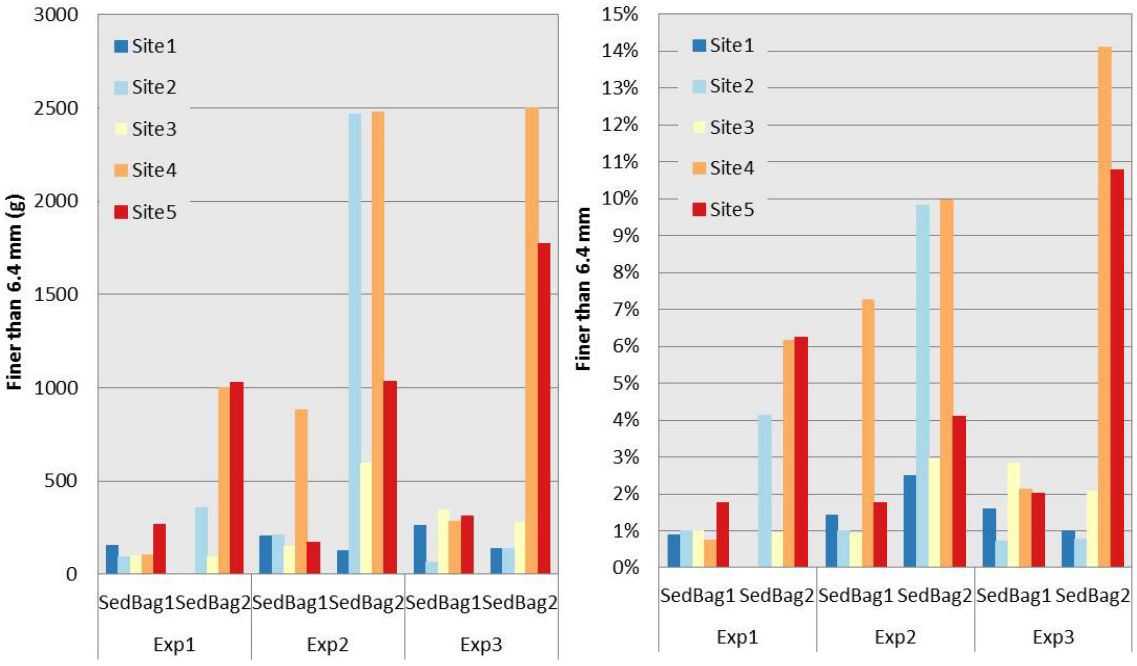

Figure C-1. Total sediment accumulation. The amount of accumulated sediment less than 6.4 mm by weight (left) and the amount relative to the total weight of the sediment within the sample (right) are provided for each sediment bag sample. Site A, and Site C to a lesser degree, shows consistently low accumulation. Site D consistently accumulated more than the other sites. Site E accumulated sediment sporadically, such that it had among the most accumulation in sediment bag 2 of Experiments 1 and 3 and moderate amounts at other times. During Experiment 2, the sediment bag 2 at Site B collected an unusually large amount of sediment that is believed to have been caused by a surface buoy that was attached to the sediment bag cable by others and that caused the cables to be violently shaken over the course of its deployment. As a result this sample is considered anomalous and not indicative of accumulation within a stable bed.

I provide the grain size distributions as probability distribution functions (Figure C-2) and cumulative distribution functions (Figure C-3). When ranked according to the magnitude of the modes of the probability distributions, in Figure C-2, the distributions indicate variability in the consistency with the ranks using hydraulic conductivity (Figure 8) and cumulative sediment transport (Figure 12). In one case, Sediment Bag 1 of Experiment 3, ranking the sites by the amount of accumulated sediment appears to correspond with the rankings by hydraulic conductivity and cumulative transport. However, similar comparisons using the other accumulated sediment samples were

inconsistent in both the absolute amount of accumulated sediment (Figure C-2) and the cumulative proportion of the sample (Figure C-3). These results indicate that the sediment bag technique did not produce dependable results for determining a sufficiently accurate effect on the hydraulic conductivity, which is confirmed by their measurements compared with the simultaneous measurements of hydraulic conductivity (Figure 10) and calculated sediment transport (Figure 13). This is further emphasized in Figure 13, which illustrates larger residual error of the individual measurements of the accumulated sediment trend with the cumulative sediment transport.

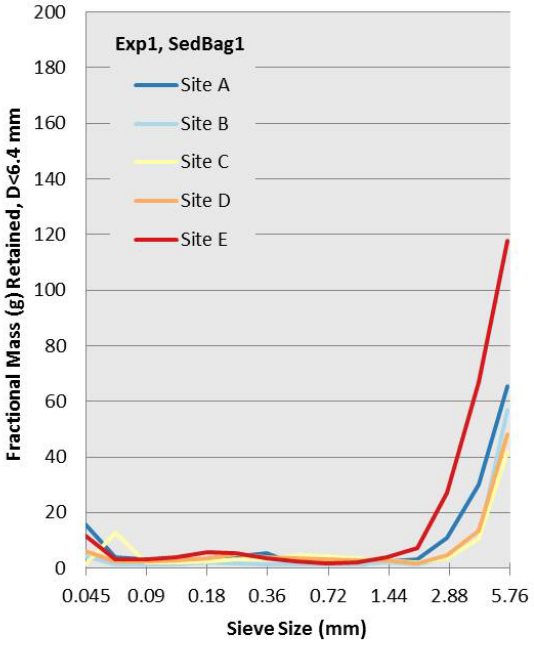
Exp1, SedBag1
Site A
Site B
Site C
Site D
Site E
Fractional Mass (g) Retained, D<6.4 mm
Sieve Size (mm)
0.045 0.09 0.18 0.36 0.72 1.44 2.88 5.76

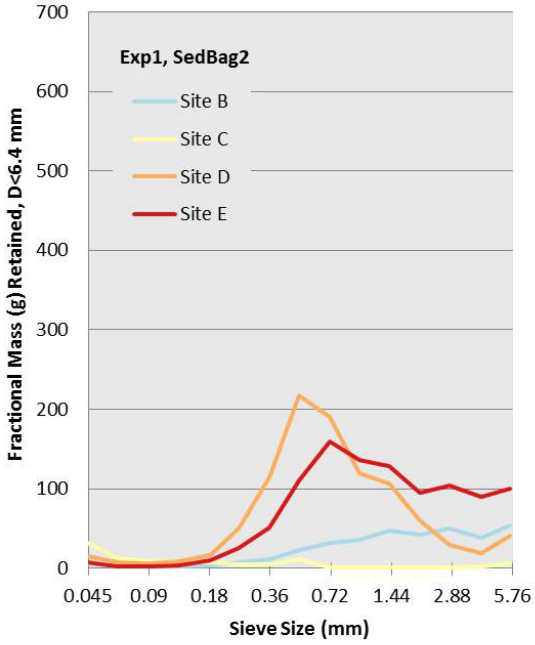
Exp1, SedBag2
Site B
Site C
Site D
Site E
Fractional Mass (g) Retained, D<6.4 mm
Sieve Size (mm)
0.045 0.09 0.18 0.36 0.72 1.44 2.88 5.76

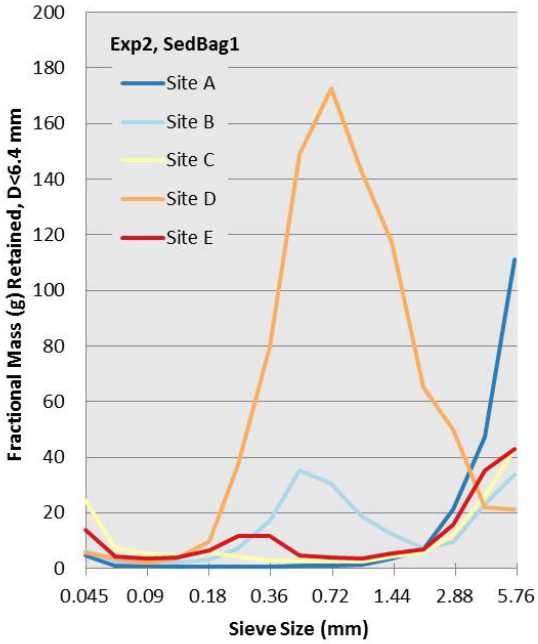
Exp2, SedBag1
Site A
Site B
Site C
Site D
Site E
Fractional Mass (g) Retained, D<6.4 mm
Sieve Size (mm)
0.045 0.09 0.18 0.36 0.72 1.44 2.88 5.76

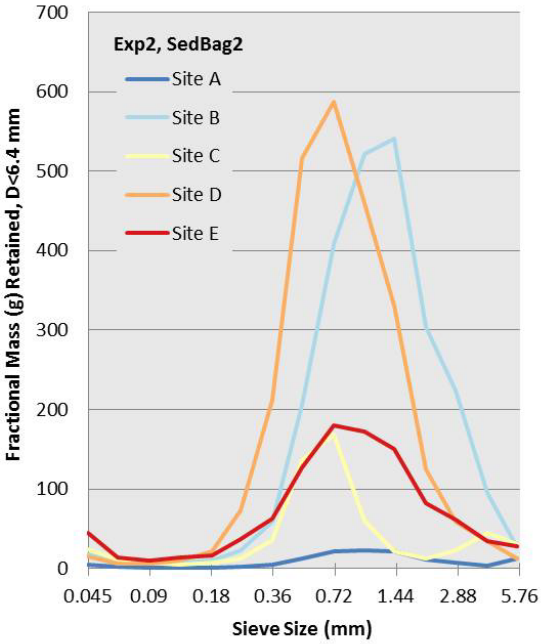
Exp2, SedBag2
Site A
Site B
Site C
Site D
Site E
Fractional Mass (g) Retained, D<6.4 mm
Sieve Size (mm)
0.045 0.09 0.18 0.36 0.72 1.44 2.88 5.76

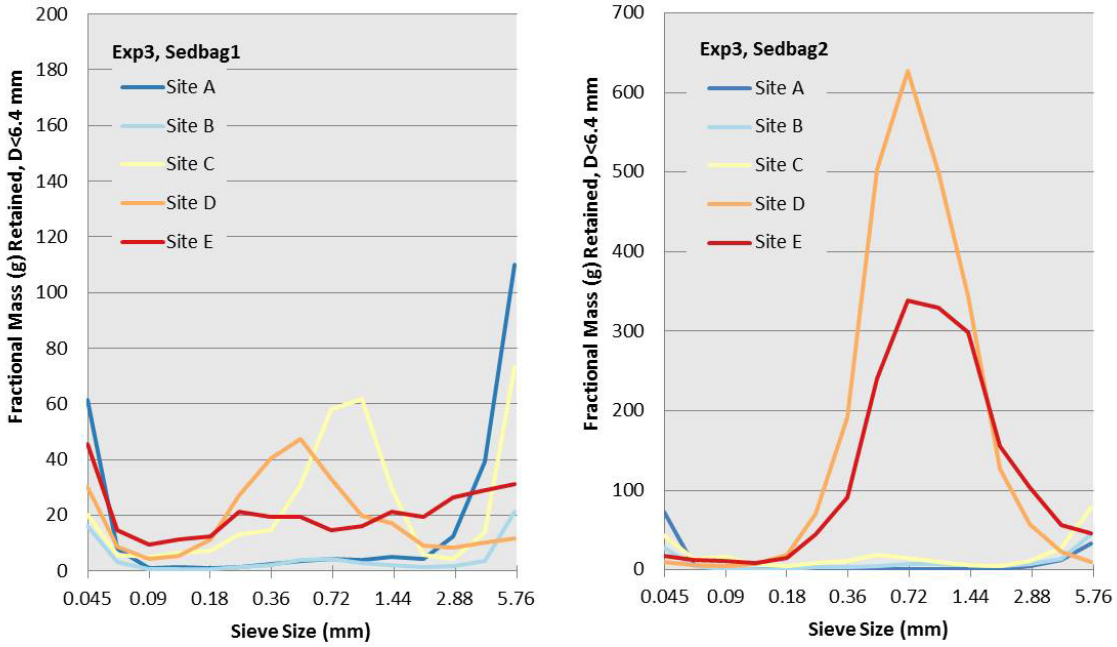

Figure C-2: Probability distributions of the sediment bag samples of accumulated grain sizes less than 6.4 mm. The unimodal distributions appear to indicate real measurements of sediment accumulation. Most of the modes of the distributions are at about 0.75 mm and indicate a similarity in the sediment accumulated between the sites. A large number of the samples show an increasing amount of grain sizes greater than about 2 mm that is probably due to residual grains that were not cleansed from the backfill during the sieving process (e.g., all samples in Experiment 1, Sediment Bag 1).

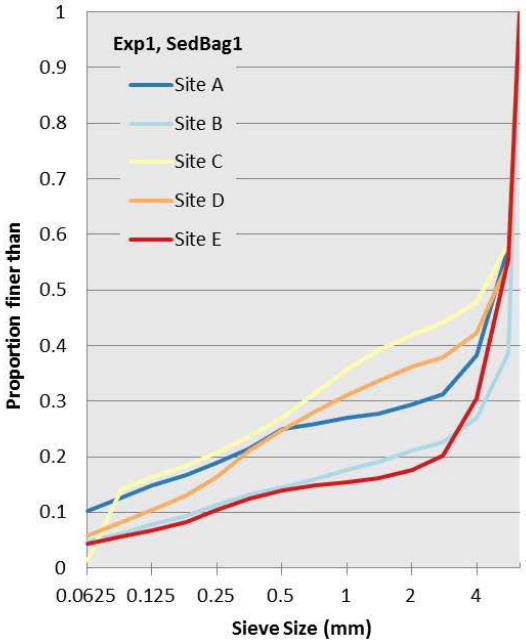
Exp1, SedBag1
Site A
Site B
Site C
Site D
Site E
Proportion finer than
Sieve Size (mm)
0.0625 0.125 0.25 0.5 1 2 4

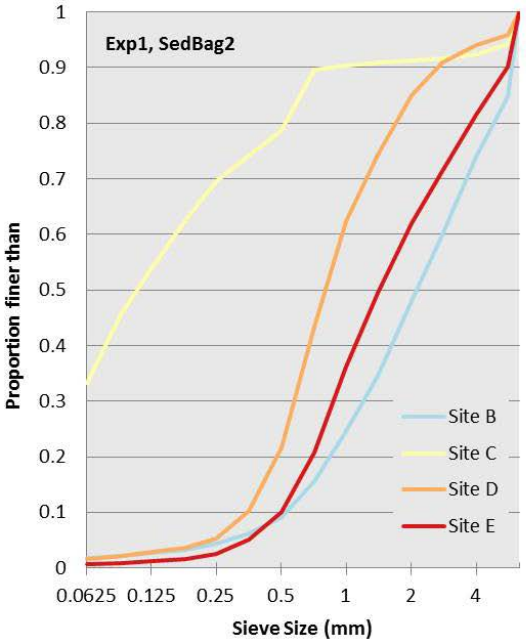
Exp1, SedBag2
Site B
Site C
Site D
Site E
Proportion finer than
Sieve Size (mm)
0.0625 0.125 0.25 0.5 1 2 4

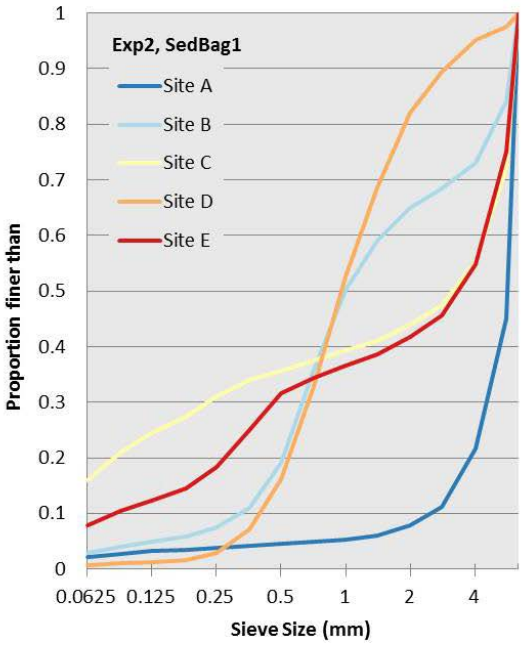
Exp2, SedBag1
Site A
Site B
Site C
Site D
Site E
Proportion finer than
Sieve Size (mm)
0.0625 0.125 0.25 0.5 1 2 4

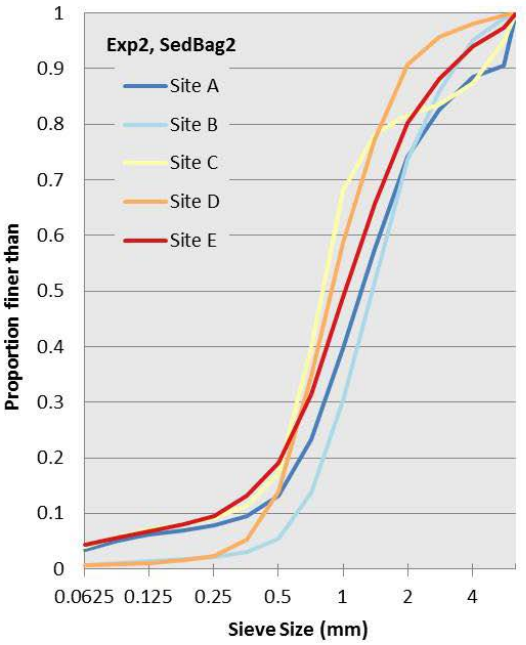
Exp2, SedBag2
Site A
Site B
Site C
Site D
Site E
Proportion finer than
Sieve Size (mm)
0.0625 0.125 0.25 0.5 1 2 4

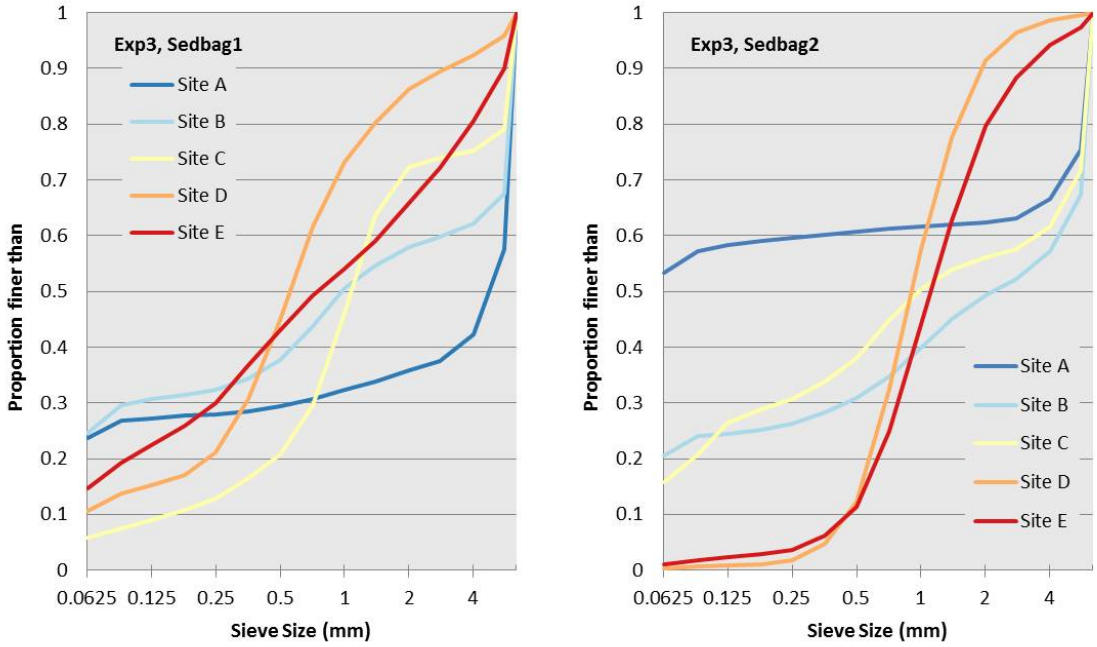

Figure C-3. Cumulative distributions of the accumulated grain sizes less than 6.4 mm from the sediment bag samples. The more sigmoidal shaped curves appear to be indicative of accumulation (e.g., all the samples for Experiment 2, sediment bag 2). Using only the strong sigmoidal curves the measurements indicate that the median grain sizes from accumulating grains is about 1 mm.

Appendix D: Hydraulic Conductivity Monitoring

Table D-1. Artificial Redd Experiment - Experiment #1, November 1 (Sites A, B, C) & 2 (Sites D and E), 2011 Artificial Redd Installed

Piezometer Measurements – Summary

Site	Piezometer	Date	dH	Volume	t	Inflow Rate	Max. Pump Rate	Turbidity	DO Hyporheic (Surface)	Temp. Hyporheic (Surface)	Median Temp.	Viscosity Factor	Hydraulic Conductivity
#			inches	mL	sec	mL/s	(±2 sec)		mg/L	degrees C	degrees C	Unitless	cm/hr
A	US RR	11/3/2011	0.06	2000	47	141.1	2L/~45sec	NA			13.8	1.11	155,771
A	DS RR	11/3/2011	<1	2000	50	>40.0	2L/~45sec	NA			13.8	1.11	>5,529
A	DS RR	11/21/2011	0.25	2000	47	79.3	2L/~45sec	clear		-12.7	13.1	1.09	28,111
A	DS RR	12/7/2011	0.5	2000	46	63.6	2L/47sec	clear			11.7	1.05	14,943
A	DS RR	1/31/2012	0.125	2000	45	107.3	2L/47sec	sl clear			9.2	0.98	60,441
A	DS RR	3/28/2012	0.25	2000	37	97.9	2L/37sec	sl turbid			9.7	1	46,706
A	DS RR Exp1	3/29/2012	0.5	2000	38	76.3	2L/38sec	sl turbid			9.5	0.99	22,928
A	DS RR Exp1	4/19/2012	1	2000	38	52.6	2L/37sec	cloudy			10	1.01	8,978
A	DS RR Exp1	5/30/2012	0.75	2000	38	67.8	2L/38sec	sl clear	9.64 (10.10)	11.3 (11.3)	11.1	1.03	17,403
A	US MID	11/3/2011	<1	2000	46	>43.5	2L/~45sec	NA			13.8	1.11	>6,531
A	US Mid	11/21/2011	<1	2000	45	>44.4	2L/~45sec	sl clear		-12.6	13.1	1.09	>6,704
A	US Mid	12/7/2011	0.06	2000	45	145.7	2L/~45sec	clear			11.7	1.05	162,167
A	US Mid	3/28/2012	0.25	2000	39	93.4	2L/37sec	sl clear			9.7	1	40,840
A	US Mid Exp1	3/29/2012	0.5	2000	38	76.3	2L/38sec	sl clear			9.5	0.99	22,928
A	US Mid Exp1	5/30/2012	0.75	2000	38	67.8	2L/38sec	sl clear	9.25 (10.04)	11.3 (11.3)	11.1	1.03	17,403
A	DS MID	11/3/2011	0.06	2000	48	139	2L/~45sec	NA			13.8	1.11	148,658
A	US RL	11/3/2011	<1	2000	52	>38.5	2L/~45sec	NA	5.63* (6.48*)	13.9 (13.6)	13.8	1.11	>5,131
A	US RL	11/21/2011	0.25	2000	44	84.1	2L/~43sec	sl clear	8.11 (8.05)	13.0 (12.3)	13.1	1.09	33,068
A	US RL	12/7/2011	0.25	2000	48	77.9	2L/~45sec	clear	11.32 (11.31)	11.8 (11.5)	11.7	1.05	25,734
A	US RL	1/31/2012	0.5	2000	47	62.3	2L/47sec	brown			9.2	0.98	13,229
A	US RL Exp1	3/29/2012	1	2000	52	38.5	2L/38sec	turbid			9.5	0.99	4,566
A	US RL Exp1	4/19/2012	0.5	2000	37	78.3	2L/37sec	cloudy			10	1.01	24,971

Table D-1. Artificial Redd Experiment - Experiment #1, November 1 (Sites A, B, C) & 2 (Sites D and E), 2011 Artificial Redd Installed

Piezometer Measurements – Summary

Site	Piezometer	Date	dH	Volume	t	Inflow Rate	Max. Pump Rate	Turbidity	DO Hyporheic (Surface)	Temp. Hyporheic (Surface)	Median Temp.	Viscosity Factor	Hydraulic Conductivity
#			inches	mL	sec	mL/s	(±2 sec)		mg/L	degrees C	degrees C	Unitless	cm/hr
A	US RL Exp1	5/30/2012	0.75	2000	39	66.1	2L/38sec	clear	9.30 (9.90)	11.1 (11.2)	11.1	1.03	16,245
A	DS RL	11/3/2011	<1	2000	60	>33.3	2L/~45sec	NA	5.84* (6.48*)	13.7 (13.6)	13.8	1.11	>3,979
A	DS RL	11/21/2011	0.5	2000	45	64.9	2L/~45sec	NA	8.04 (8.05)	12.9 (12.3)	13.1	1.09	16,375
A	DS RL	12/7/2011	0.5	2000	47	62.3	2L/~45sec	clear	11.12 (11.31)	11.6 (11.5)	11.7	1.05	14,175
B	DS RL	11/3/2011	0.06	2000	44	148.1	2L/~45sec	NA	6.60* (6.66*)	13.4 (13.3)	13.9	1.12	180,650
B	DS RL	12/12/2011	0.75	2000	46	55.9	2L/46sec	clear			10.4	1.02	10,486
B	DS RL	1/31/2012	0.06	2000	45	145.7	2L/45sec	sl brown			9.4	0.99	152,188
B	DS RL	3/26/2012	1	2000	61	32.8	2L/38sec	turbid			9.9	1	3,488
B	DS RL Exp1	3/29/2012	1	2000	73	27.4	2L/37sec	turbid			10.1	1.01	2,656
B	DS RL Exp1	4/19/2012	1	2000	63	31.7	2L/37sec	sl cloudy			10.8	1.03	3,387
B	DS RL Exp1	5/1/2012	1	2000	72	27.8	2L/37sec	sl clear			10.6	1.02	2,748
B	DS RL Exp1	5/30/2012	1	2000	75	26.7	2L/38sec	clear	8.89 (10.55)	13.3 (13.8)	12.3	1.07	2,713
B	US RL	11/3/2011	0.25	2000	44	84.1	2L/~45sec	NA	6.25* (6.66)	13.4 (13.3)	13.9	1.12	33,766
B	US RL	11/21/2011	<1	2000	47	>42.6	2L/~45sec	clear	8.53 (9.16)	12.0 (12.0)	12.8	1.08	>6,083
B	US RL	12/12/2011	1	2000	54	37	2L/49sec	clear			10.4	1.02	4,366
B	US RL	1/31/2012	0.5	2000	45	64.9	2L/45sec	sl clear			9.4	0.99	14,808
B	US RL	3/26/2012	1	2000	55	36.4	2L/38sec	sl cloudy			9.9	1	4,170
B	US RL Exp1	3/29/2012	1	2000	55	36.4	2L/37sec	clear			10.1	1.01	4,190
B	US RL Exp1	4/19/2012	NA	NA	NA	NA	NA	NA			10.8	1.03	NA
B	US MID	11/3/2011	0.06	2000	45	145.7	2L/~45sec	NA			13.9	1.12	171,837
B	US MID	11/21/2011	0.25	2000	47	79.3	2L/~45sec	clear		-11.8	12.8	1.08	27,894
B	US MID	12/12/2011	0.25	2000	46	80.8	2L/~45sec	sl clear			10.4	1.02	27,570

Table D-1. Artificial Redd Experiment - Experiment #1, November 1 (Sites A, B, C) & 2 (Sites D and E), 2011 Artificial Redd Installed

Piezometer Measurements – Summary

Site	Piezometer	Date	dH	Volume	t	Inflow Rate	Max. Pump Rate	Turbidity	DO Hyporheic (Surface)	Temp. Hyporheic (Surface)	Median Temp.	Viscosity Factor	Hydraulic Conductivity
#			inches	mL	sec	mL/s	(±2 sec)		mg/L	degrees C	degrees C	Unitless	cm/hr
B	US Mid	1/31/2012	0.06	2000	46	143.4	2L/45sec	sl clear			9.4	0.99	144,929
B	US Mid	3/26/2012	0.25	2000	36	100.2	2L/37sec	sl turbid			9.9	1	50,457
B	US Mid Exp1	3/29/2012	0.06	2000	37	168.1	2L/37sec	turbid			10.1	1.01	240,422
B	US Mid Exp1	4/19/2012	0.75	2000	37	69.7	2L/37sec	turbid			10.8	1.03	18,546
B	US Mid Exp1	5/1/2012	0.75	2000	37	69.7	2L/37sec	sl clear			10.6	1.02	18,465
B	US Mid Exp1	5/30/2012	1	2000	38	52.6	2L/38sec	sl clear	9.44 (10.45)	13.8 (14.4)	12.3	1.07	9,556
B	DS RR	11/3/2011	<1	2000	45	>44.4	2L/~45sec	NA			13.9	1.12	>6,846
B	DS RR	11/21/2011	<1	2000	49	>40.8	2L/~45sec	sl clear		-12.1	12.8	1.08	>5,598
B	DS RR	12/12/2011	0.5	2000	47	62.3	2L/~45sec	clear			10.4	1.02	13,687
B	DS RR	1/31/2012	0.06	2000	47	141.1	2L/45sec	sl cloudy			9.4	0.99	138,166
B	DS RR	3/26/2012	0.25	2000	38	95.6	2L/37sec	sl clear			9.9	1	43,934
B	DS RR Exp1	3/29/2012	1	2000	40	50	2L/37sec	turbid			10.1	1.01	7,998
B	DS RR Exp1	4/19/2012	NA	NA	NA	NA	NA	NA			10.8	1.03	NA
B	DS MID	11/3/2011	0.06	2000	45	145.7	2L/~45sec	NA			13.9	1.12	171,837
B	DS MID	11/21/2011	<1	2000	47	>42.6	2L/~45sec	sl clear		-12	12.8	1.08	>6,083
B	DS MID	12/12/2011	0.5	2000	47	62.3	2L/~45sec	cloudy			10.4	1.02	13,687
B	DS Mid	1/31/2012	0.25	2000	47	79.3	2L/45sec	brown			9.4	0.99	25,422
B	DS Mid	3/26/2012	<1	2000	37	>54.1	2L/37sec	v turbid			9.9	1	>9,536
B	DS Mid Exp1	3/29/2012	0.25	2000	37	97.9	2L/37sec	v turbid			10.1	1.01	47,259
B	DS Mid Exp1	4/19/2012	0.5	2000	37	78.3	2L/37sec	turbid			10.8	1.03	25,498
B	DS Mid Exp1	5/1/2012	0.75	2000	37	69.7	2L/37sec	cloudy			10.6	1.02	18,465
B	DS Mid Exp1	5/30/2012	0.66	2000	38	70.3	2L/38sec	cloudy-clear	9.09 (10.36)	13.0 (14.1)	12.3	1.07	19,816

Table D-1. Artificial Redd Experiment - Experiment #1, November 1 (Sites A, B, C) & 2 (Sites D and E), 2011 Artificial Redd Installed

Piezometer Measurements – Summary

Site	Piezometer	Date	dH	Volume	t	Inflow Rate	Max. Pump Rate	Turbidity	DO Hyporheic (Surface)	Temp. Hyporheic (Surface)	Median Temp.	Viscosity Factor	Hydraulic Conductivity
#			inches	mL	sec	mL/s	(±2 sec)		mg/L	degrees C	degrees C	Unitless	cm/hr
B	US RR	11/3/2011	0.125	2000	49	100.2	2L/~45sec	NA			13.9	1.12	56,101
B	US RR	11/21/2011	0.5	2000	49	59.8	2L/~45sec	clear		-11.8	12.8	1.08	13,197
B	US RR	12/12/2011	0.5	2000	47	62.3	2L/~45sec	clear			10.4	1.02	13,687
B	US RR	1/31/2012	0.06	2000	47	141.1	2L/48sec	sl clear			9.4	0.99	138,166
B	US RR	3/26/2012	0.25	2000	37	97.9	2L/37sec	clear			9.9	1	47,032
B	US RR Exp1	3/29/2012	0.06	2000	37	168.1	2L/37sec	sl clear			10.1	1.01	240,422
B	US RR Exp1	4/19/2012	0.5	2000	37	78.3	2L/37sec	v turbid			10.8	1.03	25,498
B	US RR Exp1	5/1/2012	1	2000	40	50	2L/37sec	clear			10.6	1.02	8,112
B	US RR Exp1	5/30/2012	1	2000	56	35.7	2L/38sec	clear	9.22 (10.44)	13.6 (14.3)	12.3	1.07	4,308
C	US RL	11/3/2011	0.25	2000	47	79.3	2L/~45sec	NA	6.82* (6.88*)	13.5 (13.4)	13.9	1.12	28,762
C	US RL	11/21/2011	0.33	2000	48	70.4	2L/~45sec	sl clear	8.23 (9.89)	12.0 (12.1)	12.4	1.07	19,918
C	US RL	12/7/2011	1	2000	89	22.5	2L/45sec	clear	10.80 (10.79)	10.5 (10.1)	10.4	1.02	2,050
C	US RL	1/31/2012	1	2000	131	15.3	2L/45sec	lt brown			9.7	1	1,279
C	US RL	2/7/2012	1	2000	148	13.5	2L/48sec	sl clear			9.4	0.99	1,115
C	US RL	3/26/2012	1	2000	311	6.4	2L/37sec	sl clear			10.6	1.02	515
C	US RR Exp1	3/28/2012	1	2000	473	4.2	2L/37sec	sl clear			11	1.03	313
C	US RL Exp1	4/19/2012	1	2000	330	6.1	2L/37sec	sl clear			11.8	1.06	497
C	US RL Exp1	5/1/2012	1	2000	300	6.7	2L/37sec	clear			11.6	1.05	551
C	US RL Exp1	5/31/2012	1	2000	301	6.6	2L/38sec	sl clear	5.90 (9.04)	13.0 (12.5) 730am	13.2	1.1	574
C	US MID	11/3/2011	0.06	2000	48	139	2L/~45sec	NA			13.9	1.12	149,186
C	US Mid	11/21/2011	0.25	2000	48	77.9	2L/~45sec	clear		-11.9	12.4	1.07	26,219
C	US Mid	12/7/2011	0.75	2000	47	54.7	2L/~45sec	sl clear			10.4	1.02	9,961

Table D-1. Artificial Redd Experiment - Experiment #1, November 1 (Sites A, B, C) & 2 (Sites D and E), 2011 Artificial Redd Installed

Piezometer Measurements – Summary

Site	Piezometer	Date	dH	Volume	t	Inflow Rate	Max. Pump Rate	Turbidity	DO Hyporheic (Surface)	Temp. Hyporheic (Surface)	Median Temp.	Viscosity Factor	Hydraulic Conductivity
#			inches	mL	sec	mL/s	(±2 sec)		mg/L	degrees C	degrees C	Unitless	cm/hr
C	US Mid	1/31/2012	1	2000	54	37	2L/45sec	brn			9.7	1	4,276
C	US Mid	2/7/2012	1	1300	29	44.8	2L/46sec	turbid brn			9.4	0.99	6,184
C	US Mid	3/26/2012	1	2000	52	38.5	2L/37sec	v turbid			10.6	1.02	4,706
C	US Mid Exp1	3/28/2012	1	2000	79	25.3	2L/37sec	v turbid			11	1.03	2,435
C	US Mid Exp1	4/19/2012	1	2000	70	28.6	2L/37sec	turbid			11.8	1.06	2,959
C	US Mid Exp1	5/1/2012	1	2000	108	18.5	2L/37sec	cloudy-turbid			11.6	1.05	1,676
C	US Mid Exp1	5/31/2012	1	2000	78	25.6	2L/38sec	clear	6.92 (9.24)	12.9 (12.3)	13.2	1.1	2,632
C	DS RL	11/3/2011	1	2000	105	19	2L/~45sec	NA	6.56* (6.88)	13.6 (13.4)	13.9	1.12	1,843
C	DS RL	11/21/2011	1	2000	118	16.9	2L/~45sec	clear	8.73 (9.89)	12.0 (12.1)	12.4	1.07	1,547
C	DS RL	12/7/2011	1	2000	138	14.5	2L/~45sec	clear	10.55 (10.79)	10.3 (10.1)	10.4	1.02	1,235
C	DS RL	1/31/2012	1	2000	169	11.8	2L/45sec	clear			9.7	1	973
C	DS RL	2/7/2012	1	2000	181	11	2L/40sec	clear			9.4	0.99	900
C	DS RL	3/26/2012	1	2000	198	10.1	2L/37sec	clear			10.6	1.02	844
C	DS RL Exp1	3/28/2012	1	2000	177	11.3	2L/37sec	clear			11	1.03	961
C	DS RL Exp1	4/19/2012	1	2000	270	7.4	2L/37sec	clear			11.8	1.06	624
C	DS RL Exp1	5/1/2012	1	2000	290	6.9	2L/37sec	clear			11.6	1.05	573
C	DS RL Exp1	5/31/2012	1	2000	213	9.4	2L/38sec	clear	6.44 (9.18)	13.1 (12.3) 730am	13.2	1.1	839
C	DS MID	11/3/2011	<1	2000	50	>40.0	2L/~45sec	NA			13.9	1.12	>5,549
C	DS Mid	11/21/2011	<1	2000	47	>42.6	2L/~45sec	sl clear		-12.1	12.4	1.07	>6,019
C	DS Mid	12/7/2011	0.5	2000	47	62.3	2L/~45sec	sl clear			10.4	1.02	13,698
C	DS Mid	1/31/2012	1	2000	180	11.1	2L/45sec	clear			9.7	1	910
C	DS Mid	2/7/2012	1	2000	198	10.1	2L/40sec	clear			9.4	0.99	818

Table D-1. Artificial Redd Experiment - Experiment #1, November 1 (Sites A, B, C) & 2 (Sites D and E), 2011 Artificial Redd Installed

Piezometer Measurements – Summary

Site	Piezometer	Date	dH	Volume	t	Inflow Rate	Max. Pump Rate	Turbidity	DO Hyporheic (Surface)	Temp. Hyporheic (Surface)	Median Temp.	Viscosity Factor	Hydraulic Conductivity
#			inches	mL	sec	mL/s	(±2 sec)		mg/L	degrees C	degrees C	Unitless	cm/hr
C	DS Mid	3/26/2012	1	2000	108	18.5	2L/37sec	sl clear			10.6	1.02	1,630
C	DS Mid Exp1	3/28/2012	1	2000	260	7.7	2L/37sec	sl clear			11	1.03	636
C	DS Mid Exp1	4/19/2012	1	2000	355	5.6	2L/37sec	clear			11.8	1.06	457
C	DS Mid Exp1	5/1/2012	1	2000	386	5.2	2L/37sec	clear			11.6	1.05	411
C	DS Mid Exp1	5/31/2012	1	2000	372	5.4	2L/38sec	clear	6.14 (9.20)	12.9 (12.3)	13.2	1.1	449
C	DS RR	11/3/2011	0.75	2000	51	50.4	2L/~45sec	NA			13.9	1.12	9,033
C	DS RR	11/21/2011	0.75	2000	49	52.5	2L/~45sec	clear		-12.1	12.4	1.07	9,511
C	DS RR	12/7/2011	1	2000	53	37.7	2L/~45sec	sl clear			10.4	1.02	4,522
C	DS RR	1/31/2012	1	2000	55	36.4	2L/45sec	sl clear			9.7	1	4,137
C	DS RR	3/26/2012	1	2000	54	37	2L/37sec	sl clear			10.6	1.02	4,389
C	DS RR Exp1	3/27/2012	NA	NA	NA	NA	NA	NA			10.6	1.02	NA
C	US RR	11/3/2011	<1	2000	49	>40.8	2L/~45sec	NA			13.9	1.12	>5,772
C	US RR	11/21/2011	0.125	2000	48	101.9	2L/~45sec	sl clear		-11.9	12.4	1.07	56,629
C	US RR	12/7/2011	0.25	2000	46	80.8	2L/~45sec	sl cloudy			10.4	1.02	27,592
C	US RR	1/31/2012	1	2000	79	25.3	2L/45sec	lt brn			9.7	1	2,347
C	US RR	3/26/2012	1	2000	66	30.3	2L/37sec	v turbid			10.6	1.02	3,129
C	US RR Exp1	3/27/2012	NA	NA	NA	NA	NA	NA			10.6	1.02	NA
D	DS RL	11/3/2011	0.06	2000	48	139	2L/~45sec	NA	7.20* (7.33*)	14.4 (13.9)	14	1.12	149,477
D	DS RL	11/21/2011	0.25	2000	50	75.1	2L/~51sec	sl clear	8.10 (11.04)	12.2 (12.2)	12	1.06	23,514
D	DS RL	12/7/2011	0.5	2000	48	61	2L/47sec	clear			9.7	1	12,767
D	DS RL	1/31/2012	NA	NA	NA	NA	NA	NA			9.9	1	NA
D	DS RL	3/26/2012	1	2000	68	29.4	2L/~37sec	clear			11.2	1.04	3,040

Table D-1. Artificial Redd Experiment - Experiment #1, November 1 (Sites A, B, C) & 2 (Sites D and E), 2011 Artificial Redd Installed

Piezometer Measurements – Summary

Site	Piezometer	Date	dH	Volume	t	Inflow Rate	Max. Pump Rate	Turbidity	DO Hyporheic (Surface)	Temp. Hyporheic (Surface)	Median Temp.	Viscosity Factor	Hydraulic Conductivity
#			inches	mL	sec	mL/s	(±2 sec)		mg/L	degrees C	degrees C	Unitless	cm/hr
D	DS RL Exp1	3/28/2012	1	2000	64	31.3	2L/37sec	v turbid			11.7	1.05	3,386
D	DS RL Exp1	4/19/2012	1	2000	68	29.4	2L/37sec	turbid			12.8	1.08	3,174
D	DS RL Exp1	5/1/2012	NA	NA	NA	NA	NA	NA			12.6	1.08	NA
D	DS RL Exp1	5/31/2012	1	2000	61	32.8	2L/38sec	clear	7.74 (9.95)	14.8 (15.1)	14.3	1.13	3,920
D	DS MID	11/3/2011	<1	2000	49	>40.8	2L/~45sec	NA			14	1.12	>5,783
D	DS Mid	11/21/2011	1	2000	62	32.3	2L/~51sec	clear		-12.1	12	1.06	3,593
D	DS Mid	12/7/2011	1	2000	70	28.6	2L/47sec	clear			9.7	1	2,795
D	DS Mid	1/31/2012	1	2000	114	17.5	2L/45sec	brn			9.9	1	1,504
D	DS Mid	3/26/2012	1	2000	165	12.1	2L/~37sec	sl clear			11.2	1.04	1,042
D	DS Mid Exp1	3/28/2012	1	2000	72	27.8	2L/37sec	turbid			11.7	1.05	2,829
D	DS Mid Exp1	4/19/2012	1	2000	162	12.3	2L/37sec	cloudy			12.8	1.08	1,110
D	DS Mid Exp1	5/1/2012	1	2000	179	11.2	2L/37sec	sl turbid			12.6	1.08	991
D	DS Mid Exp1	5/31/2012	1	2000	207	9.7	2L/38sec	sl clear	5.56 (10.36)	14.9 (15.3)	14.3	1.13	889
D	US RL	11/3/2011	0.06	2000	48	139	2L/~45sec	NA	7.31* (7.33*)	14.3 (13.9)	14	1.12	149,477
D	US RL	11/21/2011	0.06	2000	48	139	2L/~51sec	clear	8.83 (11.04)	12.7 (12.2)	12	1.06	141,698
D	US RL	12/7/2011	0.25	2000	56	68	2L/47sec	clear	11.76 (11.97)	10.2 (10.2)	9.7	1	16,908
D	US RL	1/31/2012	0.5	2000	45	64.9	2L/45sec	lt brown			9.9	1	15,030
D	US RL	3/26/2012	1	2000	79	25.3	2L/~37sec	turbid			11.2	1.04	2,449
D	US RL Exp1	3/28/2012	1	2000	58	34.5	2L/37sec	turbid			11.7	1.05	3,986
D	US RL Exp1	4/19/2012	1	2000	55	36.4	2L/37sec	v turbid			12.8	1.08	4,509
D	US RL Exp1	5/1/2012	1	2000	50	40	2L/37sec	turbid			12.6	1.08	5,351
D	US RL Exp1	5/31/2012	1	2000	51	39.2	2L/38sec	sl clear	8.00 (10.12)	14.6 (14.8)	14.3	1.13	5,390

Table D-1. Artificial Redd Experiment - Experiment #1, November 1 (Sites A, B, C) & 2 (Sites D and E), 2011 Artificial Redd Installed

Piezometer Measurements – Summary

Site	Piezometer	Date	dH	Volume	t	Inflow Rate	Max. Pump Rate	Turbidity	DO Hyporheic (Surface)	Temp. Hyporheic (Surface)	Median Temp.	Viscosity Factor	Hydraulic Conductivity
#			inches	mL	sec	mL/s	(±2 sec)		mg/L	degrees C	degrees C	Unitless	cm/hr
D	US MID	11/3/2011	0.06	2000	49	136.9	2L/~45sec	NA			14	1.12	142,795
D	US Mid	11/21/2011	1	2000	62	32.3	2L/~51sec	NA		-12	12	1.06	3,593
D	US Mid	12/7/2011	1	2000	65	30.8	2L/47sec	clear			9.7	1	3,130
D	US Mid	1/31/2012	1	2000	117	17.1	2L/45sec	sl clear			9.9	1	1,460
D	US Mid	3/26/2012	1	2000	77	26	2L/~37sec	sl clear			11.2	1.04	2,537
D	US Mid Exp1	3/28/2012	1	2000	94	21.3	2L/37sec	turbid			11.7	1.05	1,982
D	US Mid Exp1	4/19/2012	1	2000	72	27.8	2L/37sec	turbid			12.8	1.08	2,915
D	US Mid Exp1	5/31/2012	1	2000	104	19.2	2L/38sec	clear	8.08 (10.19)	14.9 (15.2)	14.3	1.13	1,880
D	DS RR	11/3/2011	0.06	2000	47	141.1	2L/~45sec	NA			14	1.12	156,630
D	DS RR	11/21/2011	0.25	2000	49	76.5	2L/~51sec	clear		-12.2	12	1.06	24,687
D	DS RR	12/7/2011	0.25	2000	48	77.9	2L/47sec	clear			9.7	1	24,394
D	DS RR	1/31/2012	0.5	2000	45	64.9	2L/45sec	clear			9.9	1	15,030
D	DS RR	3/26/2012	1	2000	55	36.4	2L/~37sec	clear			11.2	1.04	4,318
D	DS RR Exp1	3/27/2012	NA	NA	NA	NA	NA	NA	NA	NA	11.2	1.04	NA
D	US RR	11/3/2011	0.06	2000	49	136.9	2L/~45sec				14	1.12	142,795
D	US RR	11/21/2011	0.25	2000	49	76.5	2L/~51sec	clear		-12	12	1.06	24,687
D	US RR	12/7/2011	0.5	2000	47	62.3	2L/48sec	clear			9.7	1	13,438
D	US RR	1/31/2012	1	2000	78	25.6	2L/45sec	lt brn			9.9	1	2,405
D	US RR	3/26/2012	1	2000	53	37.7	2L/~37sec	turbid			11.2	1.04	4,620
D	US RR Exp1	3/28/2012	1	2000	129	15.5	2L/37sec	cloudy-sl clear			11.7	1.05	1,376
D	US RR Exp1	4/19/2012	1	2000	150	13.3	2L/37sec	sl clear			12.8	1.08	1,205
D	US RR Exp1	5/1/2012	1	2000	310	6.5	2L/37sec	clear			12.6	1.08	545

Table D-1. Artificial Redd Experiment - Experiment #1, November 1 (Sites A, B, C) & 2 (Sites D and E), 2011 Artificial Redd Installed

Piezometer Measurements – Summary

Site	Piezometer	Date	dH	Volume	t	Inflow Rate	Max. Pump Rate	Turbidity	DO Hyporheic (Surface)	Temp. Hyporheic (Surface)	Median Temp.	Viscosity Factor	Hydraulic Conductivity
#			inches	mL	sec	mL/s	(±2 sec)		mg/L	degrees C	degrees C	Unitless	cm/hr
D	US RR Exp1	5/31/2012	1	2000	259	7.7	2L/38sec	clear	7.70 (10.30)	15.3 (15.9)	14.3	1.13	697
E	DS RL	11/3/2011	0.06	2000	53	129.2	2L/~45sec	NA	7.40* (7.55*)	14.8 (14.7)	14.1	1.12	120,262
E	DS RL	11/21/2011	0.25	2000	50	75.1	2L/~45sec	clear	8.09 (11.52)	12.7 (12.6)	11.6	1.05	23,281
E	DS RL	12/7/2011	0.25	2000	49	76.5	2L/48sec	clear	12.33 (12.45)	10.3 (10.2)	9.1	0.98	22,774
E	DS RL	1/31/2012	1	2000	62	32.3	2L/45sec	sl clear			10.2	1.01	3,417
E	DS RL	3/26/2012	1	2000	88	22.7	2L/38sec	sl cloudy			11.8	1.06	2,159
E	DS RL Exp1	3/28/2012	1	2000	71	28.2	2L/37sec	v turbid			12.4	1.07	2,942
E	DS RL Exp1	4/20/2012	1	2000	83	24.1	2L/36sec	cloudy			14.2	1.13	2,485
E	DS RL Exp1	5/1/2012	1	2000	78	25.6	2L/37sec	sl turbid			13.5	1.1	2,649
E	DS RL Exp1	5/31/2012	1	2000	72	27.8	2L/38sec	sl clear	8.43 (10.16)	18.5 (18.9)	15.3	1.16	3,110
E	DS MID	11/3/2011	0.06	2000	70	105.4	2L/~45sec	NA			14.1	1.12	65,446
E	DS Mid	11/21/2011	0.25	2000	50	75.1	2L/~45sec	cloudy, brn		-12.6	11.6	1.05	23,281
E	DS Mid	11/21/2011	0.25	2000	48	77.9	2L/~45sec	cloudy, brn		-12.6	11.6	1.05	25,696
E	DS Mid	12/7/2011	0.25	2000	47	79.3	2L/48sec	sl clear; algae			9.1	0.98	25,201
E	DS Mid	12/7/2011	0.25	2000	47	79.3	2L/48sec	clear			9.1	0.98	25,201
E	DS Mid	1/31/2012	1	2000	55	36.4	2L/45sec	brown			10.2	1.01	4,196
E	DS Mid	3/26/2012	1	2000	74	27	2L/38sec	sl turbid			11.8	1.06	2,727
E	DS Mid	3/26/2012	1	2000	70	28.6	2L/38sec	sl cloudy			11.8	1.06	2,958
E	DS Mid Exp1	3/28/2012	1	2000	75	26.7	2L/37sec	turbid			12.4	1.07	2,719
E	DS Mid Exp1	4/20/2012	1	2000	85	23.5	2L/36sec	turbid			14.2	1.13	2,408
E	DS Mid Exp1	5/31/2012	1	2000	94	21.3	2L/38sec	turbid	7.90 (10.12)	18.1 (19.0)	15.3	1.16	2,179
E	DS RR	11/3/2011	NA	NA	NA	NA	NA	NA			14.1	1.12	NA

Table D-1. Artificial Redd Experiment - Experiment #1, November 1 (Sites A, B, C) & 2 (Sites D and E), 2011 Artificial Redd Installed

Piezometer Measurements – Summary

Site	Piezometer	Date	dH	Volume	t	Inflow Rate	Max. Pump Rate	Turbidity	DO Hyporheic (Surface)	Temp. Hyporheic (Surface)	Median Temp.	Viscosity Factor	Hydraulic Conductivity
#			inches	mL	sec	mL/s	(±2 sec)		mg/L	degrees C	degrees C	Unitless	cm/hr
E	DS RR	11/21/2011	0.25	2000	51	73.8	2L/~45sec	sl turbid		-12.6	11.6	1.05	22,202
E	DS RR	12/7/2011	0.5	2000	47	62.3	2L/48sec	clear			9.1	0.98	13,188
E	DS RR	1/31/2012	0.75	2000	47	54.7	2L/45sec	brown			10.2	1.01	9,888
E	DS RR	3/26/2012	1	2000	44	45.5	2L/38sec	sl clear			11.8	1.06	6,796
E	DS RR Exp1	3/28/2012	NA	NA	NA	NA	NA	NA			12.4	1.07	NA
E	US RR	11/3/2011	NA	NA	NA	NA	NA	NA			14.1	1.12	NA
E	US RR	11/21/2011	0.06	2000	49	136.9	2L/~45sec	sl turbid		-12.5	11.6	1.05	134,024
E	US RR	12/7/2011	0.5	2000	47	62.3	2L/47sec	sl clear			9.1	0.98	13,188
E	US RR	1/31/2012	0.875	2000	45	54.6	2L/45sec	brown			10.2	1.01	9,848
E	US RR	3/26/2012	1	2000	50	40	2L/38sec	sl clear			11.8	1.06	5,243
E	US RR Exp1	3/28/2012	1	2000	47	42.6	2L/37sec	sl turbid			12.4	1.07	6,021
E	US RR Exp1	4/20/2012	1	2000	42	47.6	2L/36sec	turbid			14.2	1.13	8,014
E	US RR Exp1	5/1/2012	1	2000	56	35.7	2L/37sec	sl cloudy			13.5	1.1	4,444
E	US RR Exp1	5/31/2012	1	2000	67	29.9	2L/38sec	clear	8.10 (10.15)	18.0 (18.8)	15.3	1.16	3,464
E	US MID	11/3/2011	NA	NA	NA	NA	NA	NA			14.1	1.12	NA
E	US Mid	11/21/2011	0.25	2000	49	76.5	2L/~45sec	sl turbid		-12.4	11.6	1.05	24,443
E	US Mid	12/7/2011	0.25	2000	47	79.3	2L/48sec	clear			9.1	0.98	25,201
E	US Mid	1/31/2012	0.25	2000	47	79.3	2L/45sec	cloudy			10.2	1.01	25,984
E	US Mid	3/26/2012	0.25	2000	38	95.6	2L/38sec	v turbid			11.8	1.06	46,236
E	US Mid Exp1	3/28/2012	0.33	2000	37	89.2	2L/37sec	v turbid			12.4	1.07	38,463
E	US Mid Exp1	4/20/2012	0.75	2000	36	71.6	2L/36sec	v turbid			14.2	1.13	21,903
E	US Mid Exp1	5/1/2012	1	2000	40	50	2L/37sec	turbid			13.5	1.1	8,760

Table D-1. Artificial Redd Experiment - Experiment #1, November 1 (Sites A, B, C) & 2 (Sites D and E), 2011 Artificial Redd Installed

Piezometer Measurements – Summary

Site	Piezometer	Date	dH	Volume	t	Inflow Rate	Max. Pump Rate	Turbidity	DO Hyporheic (Surface)	Temp. Hyporheic (Surface)	Median Temp.	Viscosity Factor	Hydraulic Conductivity
#			inches	mL	sec	mL/s	(±2 sec)		mg/L	degrees C	degrees C	Unitless	cm/hr
E	US Mid Exp1	5/31/2012	<1.0	2000	38	>52.6	2L/38sec	v turbid	8.77 (10.06)	18.6 (19.0)	15.3	1.16	>10,333
E	US RL	11/3/2011	NA	NA	NA	NA	NA	NA			14.1	1.12	NA
E	US RL	11/21/2011	NA	NA	NA	NA	2L/47sec			-12.5	11.6	1.05	NA
E	US RL	1/31/2012	1	2000	38	52.6	2L/38sec	turbid			10.2	1.01	9,012
E	US RL	3/26/2012	1	2000	43	46.5	2L/38sec	sl clear			11.8	1.06	7,139
E	US RL Exp1	3/28/2012	1	2000	43	46.5	2L/37sec	sl turbid			12.4	1.07	7,253
E	US RL Exp1	4/20/2012	1	2000	40	50	2L/36sec	cloudy			14.2	1.13	8,935
E	US RL Exp1	5/1/2012	1	2000	46	43.5	2L/37sec	cloudy			13.5	1.1	6,476
E	US RL Exp1	5/31/2012	1	2000	49	40.8	2L/38sec	sl clear	8.85 (9.90)	18.7 (19.2)	15.3	1.16	5,978

Table Notes:

1) dH = 0 indicates that the change in water surface was less than 1", but the actual change was not measured and, therefore, determining a hydraulic conductivity estimate can only be from the maximum pump rate. In most cases, the maximum pump rate estimated hydraulic conductivity is at least an order of magnitude less than the likely value, as indicated by many of the following measurements.

2) dH = 0.06 indicates there was no detectable decrease in water surface. In order to compute a representative hydraulic conductivity 0.06" was used.

3) Inflow rate was computed directly if dH = 1.0". For dH < 1.0" the inflow rate was computed using a relationship of inflow rate for measured dH and converted to an equivalent inflow rate if the dH were 1.0". See MSExcel worksheet "Piezo High K test" or Attachment A.

4) Hydraulic conductivity is calculated directly using the 3rd order polynomial regression function when dH = 1.0" and from the conversion process derived inflow rate when dH < 1.0". When dH < 1.0" but unquantified the minimum hydraulic conductivity possible (i.e., computed as though the dH = 1.0") is presented as indicated by the greater than symbol. In these cases, the actual hydraulic conductivity is very often likely to be much greater (e.g., by orders of magnitude).

Table D-2. Experiment #2, March 28 (Sites C, D, E) & 29 (Site A, B), 2012 Artificial Redds Installed

Piezometer Measurements – Summary

Site	Piezo.	Date	dH	Volume	t	Inflow Rate	Max. Pump Rate	Turbidity	DO Hyporheic (Surface)	Temperature Hyporheic (Surface)	Median Temp.	Viscosity Factor	Hydraulic Conductivity
#			inches	mL	sec	mL/s	(±2 sec)		mg/L	degrees C	degrees C	Unitless	cm/hr
A	RR	3/29/2012	0.5	2000	38	76.3	2L/38sec	clear			9.5	0.99	22,928
A	RR	4/19/2012	0.75	2000	37	69.7	2L/37sec	clear			10	1.01	18,163
A	RR	4/30/2012	0.25	2000	36	100.2	2L/36sec	clear			10.2	1.01	50,813
A	RR	5/30/2012	0.06	2000	38	164.9	2L/38sec	clear	9.56 (10.05)	11.4 (11.4)	11.1	1.03	232,555
A	RL	3/29/2012	0.25	2000	38	95.6	2L/38sec	clear			9.5	0.99	43,398
A	RL	4/19/2012	1	2000	40	50	2L/37sec	clear			10	1.01	7,980
A	RL	4/30/2012	0.5	2000	37	78.3	2L/37sec	clear			10.2	1.01	25,085
A	RL	5/30/2012	0.75	2000	37	69.7	2L/38sec	clear	9.64 (9.95)	11.2 (11.2)	11.1	1.03	18,692
B	RR	3/29/2012	0.06	2000	39	161.8	2L/37sec	clear			10.1	1.01	213,727
B	RR	4/19/2012	0.75	2000	36	71.6	2L/37sec	cloudy			10.8	1.03	19,974
B	RR	4/30/2012	0.75	2000	36	71.6	2L/36sec	turbid			10.8	1.03	19,982
B	RR	5/30/2012	0.66	2000	38	70.3	2L/38sec	sl clear	9.29 (10.51)	13.9 (14.2)	12.3	1.07	19,816
B	RL	3/29/2012	0.125	2000	38	123	2L/37sec	clear			10.1	1.01	93,035
B	RL	4/19/2012	1	2000	42	47.6	2L/37sec	turbid			10.8	1.03	7,309
B	RL	4/30/2012	0.75	2000	38	67.8	2L/38sec	sl turbid			10.8	1.03	17,275
B	RL	5/30/2012	1	2000	42	47.6	2L/38sec	sl clear	9.46 (10.49)	13.4 (14.0)	12.3	1.07	7,618
C	RL	3/28/2012	0.06	2000	39	161.8	2L/39sec	clear			11	1.03	218,913
C	RL	4/19/2012	0.5	2000	36	80.4	2L/37sec	cloudy			11.8	1.06	28,217
C	RL	4/27/2012	0.75	2000	36	71.6	2L/36sec	cloudy			11.1	1.04	20,149
C	RL	5/31/2012	1	2000	43	46.5	2L/38sec	sl cloudy	8.47 (9.15)	12.5 (12.3)	13.5	1.1	7,458
D	RL	3/28/2012	0.125	2000	37	125.6	2L/37sec	clear			11.7	1.05	103,629
D	RL	4/19/2012	1	2000	37	54.1	2L/37sec	cloudy			12.8	1.08	10,312

Table D-2. Experiment #2, March 28 (Sites C, D, E) & 29 (Site A, B), 2012 Artificial Redds Installed

Piezometer Measurements – Summary

Site	Piezo.	Date	dH	Volume	t	Inflow Rate	Max. Pump Rate	Turbidity	DO Hyporheic (Surface)	Temperature Hyporheic (Surface)	Median Temp.	Viscosity Factor	Hydraulic Conductivity
#			inches	mL	sec	mL/s	(±2 sec)		mg/L	degrees C	degrees C	Unitless	cm/hr
D	RL	4/30/2012	1	2000	42	47.6	2L/36sec	sl turbid			12.4	1.07	7,642
D	RL	5/31/2012	1	2000	51	39.2	2L/38sec	cloudy	8.25 (10.14)	14.8 (15.1)	14.3	1.13	5,390
D	RR	3/28/2012	0.5	2000	38	76.3	2L/37sec	clear			11.7	1.05	24,358
D	RR	4/19/2012	1	2000	48	41.7	2L/37sec	cloudy			12.8	1.08	5,837
D	RR	4/30/2012	1	2000	69	29	2L/36sec	turbid			12.4	1.07	3,074
D	RR	5/31/2012	1	2000	73	27.4	2L/38sec	sl turbid	7.67 (10.32)	14.8 (15.5)	14.3	1.13	2,970
E	RL	3/28/2012	0.25	2000	39	93.4	2L/37sec	sl clear			12.4	1.07	43,970
E	RL	4/20/2012	0.25	2000	36	100.2	2L/36sec	v turbid			14.2	1.13	56,637
E	RL	4/30/2012	1	2000	47	42.6	2L/36sec	v turbid			13.2	1.1	6,153
E	RL	5/31/2012	1	2000	39	51.3	2L/38sec	sl turbid	8.80 (10.10)	18.5 (18.7)	15.3	1.16	9,729
E	RR	3/28/2012	0.25	2000	37	97.9	2L/37sec	clear			12.4	1.07	50,286
E	RR	4/20/2012	0.06	2000	36	171.5	2L/36sec	sl cloudy			14.2	1.13	285,554
E	RR	4/30/2012	0.06	2000	36	171.5	2L/36sec	clear			13.2	1.1	277,958
E	RR	5/31/2012	0.25	2000	38	95.6	2L/38sec	clear	8.94 (10.10)	18.6 (18.9) 4:20pm	15.3	1.16	50,685

Table Notes:

1) dH = 0 indicates that the change in water surface was less than 1", but the actual change was not measured and, therefore, determining a hydraulic conductivity estimate can only be from the maximum pump rate. In most cases, the maximum pump rate estimated hydraulic conductivity is at least an order of magnitude less than the likely value, as indicated by many of the following measurements.

2) dH = 0.06 indicates there was no detectable decrease in water surface. In order to compute a representative hydraulic conductivity 0.06" was used.

3) Inflow rate was computed directly if dH = 1.0". For dH < 1.0" the inflow rate was computed using a relationship of inflow rate for measured dH and converted to an equivalent inflow rate if the dH were 1.0". See MSExcel worksheet "Piezo High K test" or Attachment A.

4) Hydraulic conductivity is calculated directly using the 3rd order polynomial regression function when dH = 1.0" and from the conversion process derived inflow rate when dH < 1.0". When dH < 1.0" but unquantified the minimum hydraulic conductivity possible (i.e., computed as though the dH = 1.0") is presented as indicated by the greater than symbol. In these cases, the actual hydraulic conductivity is very often likely to be much greater (e.g., by orders of magnitude).

Table D-3. Artificial Redd Experiment - Experiment #3, November 13, 2012 Artificial Redd Install. Piezometers in 5 egg pits and 2 sediment bag pits

Piezometer Measurements – Summary

Site	Piezometer	Date	dH	Volume	t	Inflow Rate	Max. Pump Rate	Turbidity	DO Hyporheic (Surface)	Temp. Hyporheic (Surface)	Median Temp.	Viscosity Factor	Hydraulic Conductivity
#			inches	mL	sec	mL/s	(±2 sec)		mg/L	degrees C	degrees C	Unitless	cm/hr
A	Egg tube 1	11/14/2012	<1.0	2000	38	>52.6	2L/~37sec	clear	7.00 (7.56)	14.0 (13.9)	13.5	1.1	>9,862
A	Egg tube 2	11/14/2012	<1.0	2000	38	>52.6	2L/~37sec	clear	7.03 (7.56)	13.8 (13.9)	13.5	1.1	>9,862
A	Egg tube 3	11/14/2012	NA	NA	NA	NA	NA	NA			13.5	1.1	NA
A	Egg tube 4	11/14/2012	<1.0	2000	37	>54.1	2L/~37sec	clear	7.16 (7.56)	13.8 (13.9)	13.5	1.1	>10,501
A	Egg tube 5	11/14/2012	NA	NA	NA	NA	NA	NA			13.5	1.1	NA
A	RL	11/14/2012	<1.0	2000	38	>52.6	2L/~37sec	clear	7.05 (7.56)	13.9 (13.9)	13.5	1.1	>9,862
A	RL	3/11/2013	0.625	2000	38	71.4	2L/~38sec	turbid brn			9.8	1	19,314
A	RR	11/14/2012	<1.0	2000	37	>54.1	2L/~37sec	clear	7.00 (7.56)	13.9 (13.9)	13.5	1.1	>10,501
A	RR	3/11/2013	0.625	2000	38	71.4	2L/~38sec	turbid brn			9.8	1	19,314
B	Egg tube 1	11/14/2012	<1.0	2000	38	>52.6	2L/~37sec	clear	7.93 (8.17)	13.3 (13.5)	13.4	1.1	>9,834
B	Egg tube 1	12/13/2012	0.06	2000	36	171.5	2L/~37sec	sl clear	8.16 (8.51)	14.0 (14.1)	14.2	1.12	284,916
B	Egg tube 2	11/14/2012	<1.0	2000	36	>55.6	2L/~37sec	clear	8.00 (8.17)	13.2 (13.5)	13.4	1.1	>11,180
B	Egg tube 2	12/13/2012	0.125	2000	38	123	2L/~37sec	clear	8.37 (8.51)	13.9 (14.1)	14.2	1.12	103,696
B	Egg tube 3	11/14/2012	<1.0	2000	40	>50.0	2L/~37sec	clear	8.00 (8.17)	13.3 (13.5)	13.4	1.1	>8,740
B	Egg tube 3	12/13/2012	0.06	2000	38	164.9	2L/~37sec	clear	8.43 (8.51)	13.9 (14.1)	14.2	1.12	252,458
B	Egg tube 4	11/14/2012	<1.0	2000	39	>51.3	2L/~37sec	clear	8.55 (9.00)	14.6 (14.7)	13.4	1.1	>9,260
B	Egg tube 4	12/13/2012	0.5	2000	38	76.3	2L/~37sec	clear	8.35 (8.51)	13.8 (14.1)	14.2	1.12	25,996
B	Egg tube 5	11/14/2012	<1.0	2000	39	>51.3	2L/~37sec	clear	8.64 (9.00)	14.3 (14.7)	13.4	1.1	>9,260
B	Egg tube 5	12/13/2012	0.375	2000	37	85.6	2L/~37sec	clear	8.41 (8.51)	13.8 (14.1)	14.2	1.12	35,826
B	RL	11/14/2012	<1.0	2000	39	>51.3	2L/~37sec	clear	8.80 (9.00)	14.5 (14.7)	13.4	1.1	>9,260
B	RL	12/13/2012	0.375	2000	38	83.5	2L/~37sec	sl clear	8.56 (8.51)	13.9 (14.1)	14.2	1.12	33,412
B	RL	3/11/2013	0.75	2000	38	67.8	2L/~38sec	cloudy			10.1	1.01	16,966

Table D-3. Artificial Redd Experiment - Experiment #3, November 13, 2012 Artificial Redd Install. Piezometers in 5 egg pits and 2 sediment bag pits

Piezometer Measurements – Summary

Site	Piezometer	Date	dH	Volume	t	Inflow Rate	Max. Pump Rate	Turbidity	DO Hyporheic (Surface)	Temp. Hyporheic (Surface)	Median Temp.	Viscosity Factor	Hydraulic Conductivity
#			inches	mL	sec	mL/s	(±2 sec)		mg/L	degrees C	degrees C	Unitless	cm/hr
B	RR	11/14/2012	<1.0	2000	39	>51.3	2L/~37sec	clear	8.78 (9.00)	14.4 (14.7)	13.4	1.1	>9,260
B	RR	12/13/2012	0.375	2000	38	83.5	2L/~37sec	clear	8.30 (8.51)	14.0 (14.1)	14.2	1.12	33,412
B	RR	3/11/2013	0.25	2000	38	95.6	2L/~38sec	sl clear			10.1	1.01	44,186
C	Egg tube 1	11/16/2012	0.25	2000	36	100.2	2L/~37sec	clear	8.14 (8.88)	14.3 (14.0)	14.1	1.12	56,410
C	Egg tube 1	12/13/2012	0.5	2000	38	76.3	2L/~37sec	turbid	9.03 (8.81)	14.1 (14.0)	13.8	1.11	25,742
C	Egg tube 2	11/16/2012	0.5	2000	36	80.4	2L/~37sec	clear	8.42 (8.88)	13.9 (14.0)	14.1	1.12	29,960
C	Egg tube 2	12/13/2012	1	2000	102	19.6	2L/~37sec	clear	6.95 (8.81)	13.9 (14.0)	13.8	1.11	1,898
C	Egg tube 3	11/16/2012	1	2000	53	37.7	2L/~37sec	clear	8.11 (8.88)	14.2 (14.0)	14.1	1.12	4,988
C	Egg tube 3	12/13/2012	1	2000	82	24.4	2L/~37sec	clear	8.14 (8.81)	13.8 (14.0)	13.8	1.11	2,495
C	Egg tube 4	11/16/2012	0.5	2000	36	80.4	2L/~37sec	clear	8.50 (8.88)	14.2 (14.0)	14.1	1.12	29,960
C	Egg tube 4	12/13/2012									13.8	1.11	NA
C	Egg tube 5	11/16/2012	1	2000	40	50	2L/~37sec	clear	8.45 (8.88)	14.1 (14.0)	14.1	1.12	8,899
C	Egg tube 5	12/13/2012	1	2000	89	22.5	2L/~37sec	clear	7.28 (8.81)	13.8 (14.0)	13.8	1.11	2,243
C	RL	11/16/2012	1	2000	98	20.4	2L/~37sec	clear	8.45 (8.88)	14.2 (14.0)	14.1	1.12	2,007
C	RL	12/13/2012	1	2000	126	15.9	2L/~37sec	clear	8.07 (8.81)	14.0 (14.0)	13.8	1.11	1,493
C	RL	3/12/2013	1	2000	292	6.8	2L/~38sec	clear			10.6	1.02	553
C	DS RL	12/13/2012	1	2000	290	6.9	2L/~37sec	clear	6.12 (8.81)	13.9 (14.0)	13.8	1.11	607
C	DS RL	3/12/2013	1	2000	320	6.3	2L/~38sec	clear			10.6	1.02	499
C	RR	11/16/2012	0.25	2000	37	97.9	2L/~37sec	clear	8.62 (8.88)	14.3 (14.0)	14.1	1.12	52,581
C	RR	12/13/2012	0.375	2000	38	83.5	2L/~37sec	sl clear	8.68 (8.81)	14.0 (14.0)	13.8	1.11	33,085
C	RR	3/12/2013	0.5	2000	38	76.3	2L/~38sec	turbid			10.6	1.02	23,662
D	Egg tube 1	11/15/2012	6	20	38	164.9	2L/~37sec	clear	8.12 (8.64)	12.5 (12.5)	13.4	1.1	247,726

Table D-3. Artificial Redd Experiment - Experiment #3, November 13, 2012 Artificial Redd Install. Piezometers in 5 egg pits and 2 sediment bag pits

Piezometer Measurements – Summary

Site	Piezometer	Date	dH	Volume	t	Inflow Rate	Max. Pump Rate	Turbidity	DO Hyporheic (Surface)	Temp. Hyporheic (Surface)	Median Temp.	Viscosity Factor	Hydraulic Conductivity
#			inches	mL	sec	mL/s	(±2 sec)		mg/L	degrees C	degrees C	Unitless	cm/hr
D	Egg tube 1	12/13/2012	1	2000	43	46.5	2L/~37sec	sl clear	8.53 (9.37)	13.9 (13.9)	13.4	1.1	7,453
D	Egg tube 2	11/15/2012	0.5	2000	39	74.5	2L/~37sec	clear	8.14 (8.64)	12.5 (12.5)	13.4	1.1	23,826
D	Egg tube 2	12/13/2012	1	2000	39	51.3	2L/~37sec	sl clear	8.98 (9.37)	13.9 (13.9)	13.4	1.1	9,265
D	Egg tube 3	11/15/2012	0.06	2000	38	164.9	2L/~37sec	clear	8.21 (8.64)	12.5 (12.5)	13.4	1.1	247,726
D	Egg tube 3	12/13/2012	0.75	2000	39	66.1	2L/~37sec	sl clear	8.85 (9.37)	13.9 (13.9)	13.4	1.1	17,299
D	Egg tube 4	11/15/2012	0.25	2000	36	100.2	2L/~37sec	clear	8.22 (8.64)	12.5 (12.5)	13.4	1.1	55,451
D	Egg tube 4	12/13/2012	1	2000	92	21.7	2L/~37sec	clear	8.11 (9.37)	13.7 (13.9)	13.4	1.1	2,131
D	Egg tube 5	11/15/2012	0.25	2000	38	95.6	2L/~37sec	clear	8.20 (8.64)	12.5 (12.5)	13.4	1.1	48,283
D	Egg tube 5	12/13/2012	1	2000	63	31.7	2L/~37sec	sl clear	8.50 (9.37)	13.8 (13.9)	13.4	1.1	3,635
D	RL	11/15/2012	0.5	2000	37	78.3	2L/~37sec	clear	8.32 (8.64)	12.5 (12.5)	13.4	1.1	27,375
D	RL	12/13/2012	1	2000	41	48.8	2L/~37sec	turbid	8.42 (9.37)	13.8 (13.9)	13.4	1.1	8,273
D	RL	3/12/2013	1	2000	81	24.7	2L/~38sec	sl clear			11.2	1.04	2,369
D	RR	11/15/2012	0.06	2000	37	168.1	2L/~37sec	clear	8.31 (8.64)	12.5 (12.5)	13.4	1.1	262,950
D	RR	12/13/2012	1	2000	53	37.7	2L/~37sec	turbid	8.72 (9.37)	13.8 (13.9)	13.4	1.1	4,902
D	RR	3/12/2013	1	2000	126	15.9	2L/~38sec	sl clear			11.2	1.04	1,395
E	Egg tube 1	11/15/2012	0.06	2000	38	164.9	2L/~37sec	clear	8.61 (8.93)	12.9 (13.0)	13.3	1.1	246,877
E	Egg tube 1	12/13/2012	0.875	2000	37	66.8	2L/~37sec	turbid	8.50 (9.37)	13.6 (13.6)	13.1	1.09	17,662
E	Egg tube 2	11/15/2012	0.25	2000	38	95.6	2L/~37sec	clear	8.41 (8.93)	12.9 (13.0)	13.3	1.1	48,117
E	Egg tube 2	12/13/2012	0.625	2000	37	73.3	2L/~37sec	turbid	8.95 (9.37)	13.5 (13.6)	13.1	1.09	22,645
E	Egg tube 3	11/15/2012	0.125	2000	38	123	2L/~37sec	clear	8.49 (8.93)	13.0 (13.0)	13.3	1.1	101,403
E	Egg tube 3	12/13/2012	0.625	2000	37	73.3	2L/~37sec	sl clear	9.86 (9.37)	13.1 (13.6)	13.1	1.09	22,645
E	Egg tube 4	11/15/2012	0.25	2000	39	93.4	2L/~37sec	clear	8.53 (8.93)	13.0 (13.0)	13.3	1.1	45,040

Table D-3. Artificial Redd Experiment - Experiment #3, November 13, 2012 Artificial Redd Install. Piezometers in 5 egg pits and 2 sediment bag pits

Piezometer Measurements – Summary

Site	Piezometer	Date	dH	Volume	t	Inflow Rate	Max. Pump Rate	Turbidity	DO Hyporheic (Surface)	Temp. Hyporheic (Surface)	Median Temp.	Viscosity Factor	Hydraulic Conductivity
#			inches	mL	sec	mL/s	(±2 sec)		mg/L	degrees C	degrees C	Unitless	cm/hr
E	Egg tube 4	12/13/2012	0.75	2000	38	67.8	2L/~37sec	clear	8.96 (9.37)	13.5 (13.6)	13.1	1.09	18,363
E	Egg tube 5	11/15/2012	0.06	2000	37	168.1	2L/~37sec	clear	8.62 (8.93)	13.0 (13.0)	13.3	1.1	262,048
E	Egg tube 5	12/13/2012	0.75	2000	37	69.7	2L/~37sec	sl clear	8.46 (9.37)	13.5 (13.6)	13.1	1.09	19,723
E	RL	11/15/2012	0.125	2000	37	125.6	2L/~37sec	clear	8.53 (8.93)	13.0 (13.0)	13.3	1.1	108,151
E	RL	12/13/2012	1	2000	45	44.4	2L/~37sec	turbid	9.06 (9.37)	13.5 (13.6)	13.1	1.09	6,704
E	RL	3/11/2013	1	2000	92	21.7	2L/~38sec	cloudy			11.4	1.04	2,020
E	RR	11/15/2012	NA	NA	NA	NA	NA	NA			13.3	1.1	NA
E	RR	12/13/2012	NA	NA	NA	NA	NA	NA			13.1	1.09	NA
E	RR	3/11/2013	NA	NA	NA	NA	NA	NA			11.4	1.04	NA
E	DS RR	3/11/2013	0.625	2000	38	71.4	2L/~38sec	cloudy			11.4	1.04	20,169

Table Notes:

1) dH = 0 indicates that the change in water surface was less than 1", but the actual change was not measured and, therefore, determining a hydraulic conductivity estimate can only be from the maximum pump rate. In most cases, the maximum pump rate estimated hydraulic conductivity is at least an order of magnitude less than the likely value, as indicated by many of the following measurements.

2) dH = 0.06 indicates there was no detectable decrease in water surface. In order to compute a representative hydraulic conductivity 0.06" was used.

3) Inflow rate was computed directly if dH = 1.0". For dH < 1.0" the inflow rate was computed using a relationship of inflow rate for measured dH and converted to an equivalent inflow rate if the dH were 1.0". See MSExcel worksheet "Piezo High K test" or Attachment A.

4) Hydraulic conductivity is calculated directly using the 3rd order polynomial regression function when dH = 1.0" and from the conversion process derived inflow rate when dH < 1.0". When dH < 1.0" but unquantified the minimum hydraulic conductivity possible (i.e., computed as though the dH = 1.0") is presented as indicated by the greater than symbol. In these cases, the actual hydraulic conductivity is very often likely to be much greater (e.g., by orders of magnitude).

Appendix E: Bed Load Samples

Table E-1. Bed load sample notes.

Site Id	Date Collected	Discharge (m^3/s)	Time Duration (min)	Lateral Position	Sample Weight (g)	Mass/time (g/hr)	Unit Transport Rate (g/hr/m)	Description of dried sample: texture, organics, suggestive info.
A	1/13/2012	2.8	60	Mid	0.07	0.07	0.92	Mostly vf sand, some organics, rusty colored
A	11/3/2011	9.9	30	RR	0.32	0.64	8.40	Vf sand, some organics, rusty colored
A	11/3/2011	9.9	30	RL	0.28	0.56	7.35	Vf sand, rust colored
A	11/13/2012	12.1	30	Mid	0.11	0.22	2.89	Med sand with some organics
A	4/19/2012	14.2	60	Mid	0.52	0.52	6.82	Vf sand, organics, light brown with some rust
A	10/18/2011	19.7	30	RR	0.12	0.24	3.15	Vf sand, some organics, light brown
A	10/18/2011	19.7	30	Mid	0.10	0.20	2.62	Vf sand, light brown
A	10/18/2011	19.7	30	RL	0.07	0.14	1.84	Vf sand, trace organics, light brown
A	4/26/2012	20.0	60	Mid	0.52	0.52	6.82	Vf sand, organics, light brown gray
B	1/13/2012	2.8	60	Mid	0.06	0.06	0.79	Vf sand, rusty colored
B	11/3/2011	9.9	30	RL	11.50*	23.00	301.84	Vf sand, organics, light brown
B	11/13/2012	12.1	30	Mid	0.46	0.92	12.07	Vf sand, organics, light rusty color
B	4/19/2012	14.2	150	Mid	3.04	1.22	15.96	F to med sand, organics, light brown
B	10/18/2011	19.7	30	RR	0.52	1.04	13.65	F sand, some organics
B	10/18/2011	19.7	30	Mid	0.45	0.90	11.81	Med sand, some organics
B	10/18/2011	19.7	30	RL	7.21*	14.42	189.24	F to vc sand, trace organics
B	4/26/2012	20.0	60	Mid	1.20	1.20	15.75	F sand, organics, light brown
C	1/13-14/2012	2.8	1280	Mid	0.04	0.00	0.02	Vf sand, light brown
C	11/3/2011	9.9	30	RR	0.08	0.16	2.10	Vf sand with organics, light brown
C	2/7/2012	9.9	270	Mid	0.63	0.14	1.84	Vf sand
C	11/13/2012	12.1	30	Mid	0.23	0.46	6.04	Vf sand, some organics, light brown
C	4/19/2012	14.3	60	Mid	1.09	1.09	14.30	Organics, vf sand, light brown (LDC = 0.14 m^3/s)
C	4/20/2012	14.4	60	Mid	2.11	2.11	27.69	Vf sand, some organics, light brown (LDC = 0.08 m^3/s)
C	10/19/2011	19.8	30	RR	1.01*	2.02	26.51	Med sand, some organics, light brown
C	10/19/2011	19.8	30	Mid	0.25	0.50	6.56	Organics and vf sand, light gray
C	10/19/2011	19.8	30	RL	16.92*	33.84	444.09	Med sand, trace vc, trace organics, light brown
C	4/27/2012	20.2	60	Mid	1.36	1.36	17.85	Vf sand, organics, light gray (LDC = 0.54 m^3/s)
C	5/3/2012	28.7	30	Mid	7.48*	14.96	196.33	F sand, some med sand, some organics, medium brown (LDC = 0.54 m^3/s)

Site Id	Date Collected	Discharge (m^3/s)	Time Duration (min)	Lateral Position	Sample Weight (g)	Mass/time (g/hr)	Unit Transport Rate (g/hr/m)	Description of dried sample: texture, organics, suggestive info.
D	1/13/2012	2.8	60	Mid	0.25	0.25	3.28	Vf sand, rusty colored
D	11/3/2011	9.9	30	RR	7.57*	15.14	198.69	Med sand, trace organics
D	11/13/2012	12.1	30	Mid	1.18	2.36	30.97	Organics, some f sand, light gray
D	4/19/2012	14.3	60	Mid	2.65	2.65	34.78	Organics and f sand, light gray
D	10/17/2011	19.8	20	RR	2.28	6.84	89.76	F to med sand, some organics, brown
D	10/17/2011	19.8	20	Mid	2.25*	6.75	88.58	Organics and f sand, trace vc sand
D	10/17/2011	19.8	20	RL	13.64*	40.92	537.01	Med to c sand, trace organics, 1x16mm gravel
D	4/26/2012	20.3	60	Mid	6.76	6.76	88.71	Organics, trace f to med sand, brown
D	5/4/2012	28.7	30	Mid	766.70*	1533.40	20123.36	C to vc sand, 1x16mm gravel
E	1/13/2012	2.8	60	Mid	0.25	0.25	3.28	Vf sand, rusty colored
E	11/13/2012	12.1	30	Mid	3.07	6.14	80.58	Vf to f sand, trace organics, light brown
E	4/20/2012	14.4	60	Mid	1.50	1.50	19.69	Vf sand, some organics, light gray brown
E	10/19/2011	19.8	30	RR	16.67*	33.34	437.53	Med sand, some f and c sand, trace organics, 1x8mm gravel
E	10/19/2011	19.8	30	Mid	34.76*	69.52	912.34	Med to vc sand, some f sand, 2x8mm gravel
E	10/19/2011	19.8	30	RL	28.18*	56.36	739.63	F to vc sand, 5x16mm gravel
E	4/26/2012	20.3	60	Mid	4.94	4.94	64.83	Organics, some f to c sand, light gray
E	5/4/2012	28.7	30	Mid	70.36*	140.72	1846.72	Vc sand, some med sand

Notes: * = sample sieved for grain size distribution; vf = very fine, f = fine, med = medium, c = coarse, vc =very coarse.

Table E-2. Bed load sample sieve results.

Location	Site D	Site E	Site C	Site D	Site D	Site B	Site C	Site C	Site E	Site E	Site E	Site B	Site D
Sample Date	5/4/2012	5/4/2012	5/3/2012	10/17/2011	10/17/2011	10/18/2011	10/19/2011	10/19/2011	10/19/2011	10/19/2011	10/19/2011	11/3/2011	11/3/2011
Duration	30 min	30 min	30 min	20 min	20 min	30 min	30 min	30 min	30 min	30 min	30 min	30 min	30 min
Q (m^3/s)	28.7	28.7	28.7	19.8	19.8	19.7	19.8	19.8	19.8	19.8	19.8	9.9	9.9
Sieve Date	6/15/2015	6/15/2015	6/16/2015	6/16/2015	6/16/2015	6/16/2015	6/17/2015	6/17/2015	6/16/2015	6/16/2015	6/16/2015	6/17/2015	6/17/2015
Sieve (mm)	**Retained (g)**	**Retained (g)**	**Retained (g)**	**Retained (g)**	**Retained (g)**	**Retained (g)**	**Retained (g)**	**Retained (g)**	**Retained (g)**	**Retained (g)**	**Retained (g)**	**Retained (g)**	**Retained (g)**
128	0.0	0.0	0.0	0.0	0.0	0.0	0.0	0.0	0.0	0.0	0.0	0.0	0.0
90	0.0	0.0	0.0	0.0	0.0	0.0	0.0	0.0	0.0	0.0	0.0	0.0	0.0
64	0.0	0.0	0.0	0.0	0.0	0.0	0.0	0.0	0.0	0.0	0.0	0.0	0.0
45	0.0	0.0	0.0	0.0	0.0	0.0	0.0	0.0	0.0	0.0	0.0	0.0	0.0
32	0.0	0.0	0.0	0.0	0.0	0.0	0.0	0.0	0.0	0.0	0.0	0.0	0.0
22.6	0.0	0.0	0.0	0.0	0.0	0.0	0.0	0.0	0.0	0.0	0.0	0.0	0.0
16	14.4	0.0	0.0	0.0	0.0	0.0	0.0	0.0	0.0	0.0	0.0	0.0	0.0
11.3	0.0	0.0	0.0	0.0	0.0	0.0	0.0	0.0	0.0	0.0	4.3	0.0	0.0
8.0	4.9	1.5	0.0	0.0	1.2	0.0	0.0	0.0	1.1	0.0	6.0	0.0	0.0
5.6	2.7	2.8	0.4	0.0	0.0	0.0	0.0	0.0	0.3	0.6	0.0	0.0	0.0
4.0	1.3	2.6	0.0	0.0	0.2	0.5	0.1	0.0	1.7	1.2	1.3	0.0	0.0
2.8	6.7	9.0	0.2	0.0	0.1	0.9	0.3	0.0	3.4	2.0	2.5	0.0	0.0
2.0	21.9	12.0	<0.1	0.0	0.8	1.0	0.5	0.0	5.1	1.9	2.1	0.0	0.0
1.4	79.0	16.1	<0.1	0.1	1.7	1.4	1.4	0.0	8.3	2.8	3.6	0.2	0.3
1.0	133.6	10.9	0.7	<0.1	2.2	1.1	2.4	0.1	6.7	2.5	2.7	<0.1	0.8
0.71	162.0	7.1	1.3	0.3	3.0	1.1	4.8	0.3	4.7	2.5	1.8	<0.1	1.8
0.50	116.9	3.7	1.7	0.7	2.6	0.7	5.0	0.3	2.0	1.6	1.3	0.1	2.5
0.355	37.0	1.7	0.7	0.5	1.0	0.3	1.5	0.1	0.8	0.6	0.8	<0.1	1.5
0.25	9.5	0.8	0.4	0.2	0.4	0.2	0.3	<0.1	0.5	0.2	0.6	<0.1	0.5
0.18	4.3	0.5	0.4	<0.1	0.1	<0.1	<0.1	<0.1	0.2	0.1	0.2	<0.1	0.1
0.125	3.4	0.5	0.3	<0.1	<0.1	<0.1	<0.1	<0.1	<0.1	<0.1	<0.1	0.1	<0.1
0.090	1.2	0.4	0.5	<0.1	<0.1	<0.1	<0.1	<0.1	<0.1	<0.1	<0.1	<0.1	<0.1
0.063	0.3	0.2	0.2	<0.1	<0.1	<0.1	<0.1	<0.1	<0.1	<0.1	<0.1	<0.1	<0.1
<0.063	0.4	0.2	0.3	<0.1	<0.1	<0.1	<0.1	<0.1	<0.1	<0.1	<0.1	0.3	<0.1
Mass prior	600.0	70.3	7.4	2.2	13.6	7.1	16.9	1.0	34.7	16.6	28.1	1.1	7.5
Mass after	599.5	70.0	7.1	1.8	13.3	7.2	16.3	0.8	34.8	16.0	27.2	0.7	7.5
% change	0%	0%	4%	18%	2%	-1%	4%	20%	0%	4%	3%	36%	0%

The variability in the rate of increase in sediment transport may be related to the abundance of fine sediment proximal to the sites. For instance, Site C has the finest grain size distribution in the bed load transported sediment (Figure E-1). The finer sediment is probably provided from the diversion canal (Figure 2) that episodically delivers silt and very fine sand to the site [field observations and unpublished data]. Furthermore, the ranking of finest to coarsest bed load corresponds with the bulk grain size distributions from the bed at each site (Figure 4). From the grain size distributions of the bed material and the sediment in transport the texture of the sediment is finest at Site C followed sequentially by Site D, Site B, and Site E. However, Site A is an outlier in this ranking as this upstream most site has the coarsest bed material and the finest sediment in transport. I did not sieve the sediment transport samples at Site A because they are exceedingly small. However, by visually inspecting these samples, I determined that they were composed overwhelmingly of very fine sand grains (Table E-1). Since the bed load sampler has a mesh size of 0.25 mm the samples underestimate the transport rate of the finest grains. Regardless, because of the paucity of silt and very fine sand on this reach of the San Joaquin River, if the very fine sand grains were more accurately sampled the difference in transport rates would not likely change the transport rate rankings between sites.

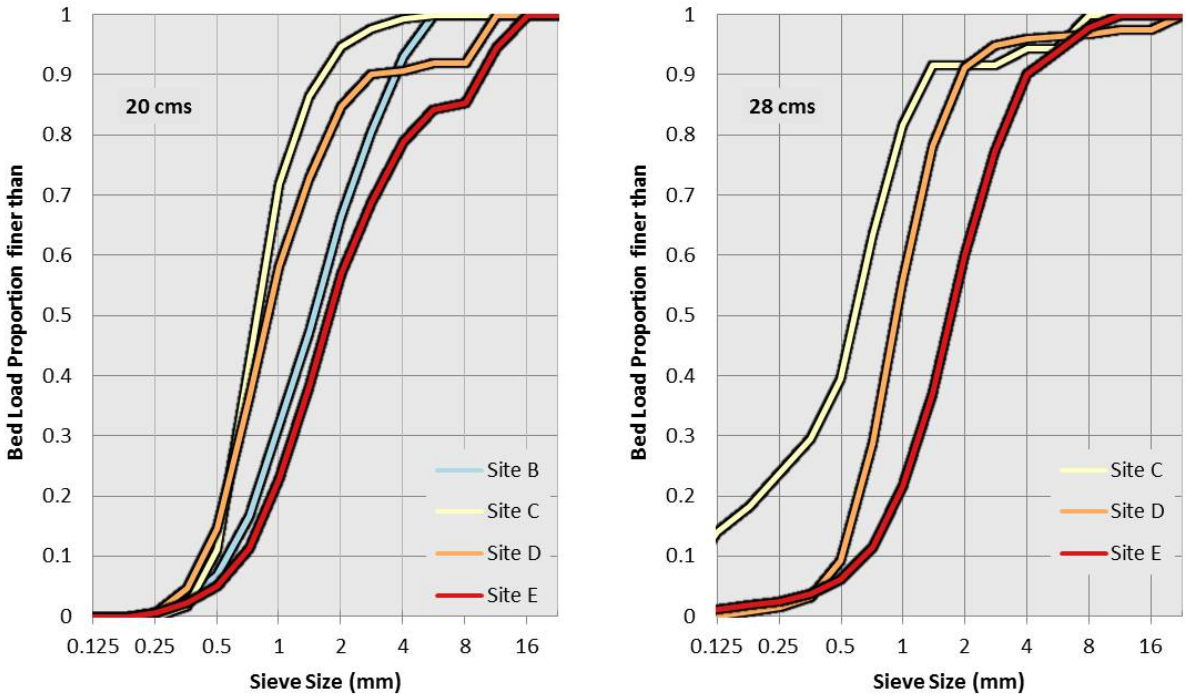

Figure E-1. Cumulative grain size distributions of bed load. (Left) Samples from 20 m^3/s and (right) 28 m^3/s. Samples that are included from the 20 m^3/s flow are greater than 7 g and those from the 28 m^3/s flow are from sites that were wade-able.

Appendix F: Artificial Redd Photographs

Figure F-1. Artificial redd at Site A on May 30, 2012. Coarse gravel and cobbles are present on the surface of this redd. No sand is visible on the artificial redd area. A piezometer cap is visible on the bottom of the photo and the sediment bag cable and floats are present above it. The piezometer cap is 5 cm in diameter.

Figure F-2. Artificial Redd at Site B on May 31, 2012. Coarse gravel and cobbles are present on the surface of this redd. Some sand is visible (above the cable floats and below the reference frame) beyond the artificial redd area. Over the cable the gravels are relatively free of sand. The reference frame is approximately 0.5 m square.

Figure F-3. Artificial Redd at Site C on May 31, 2012. A piezometer cap is shown in gravel with some signs of sand accumulation on the surface possibly indicating the backfill is approaching its capacity for accumulating sand. Piezometer cap is 5 cm in diameter.

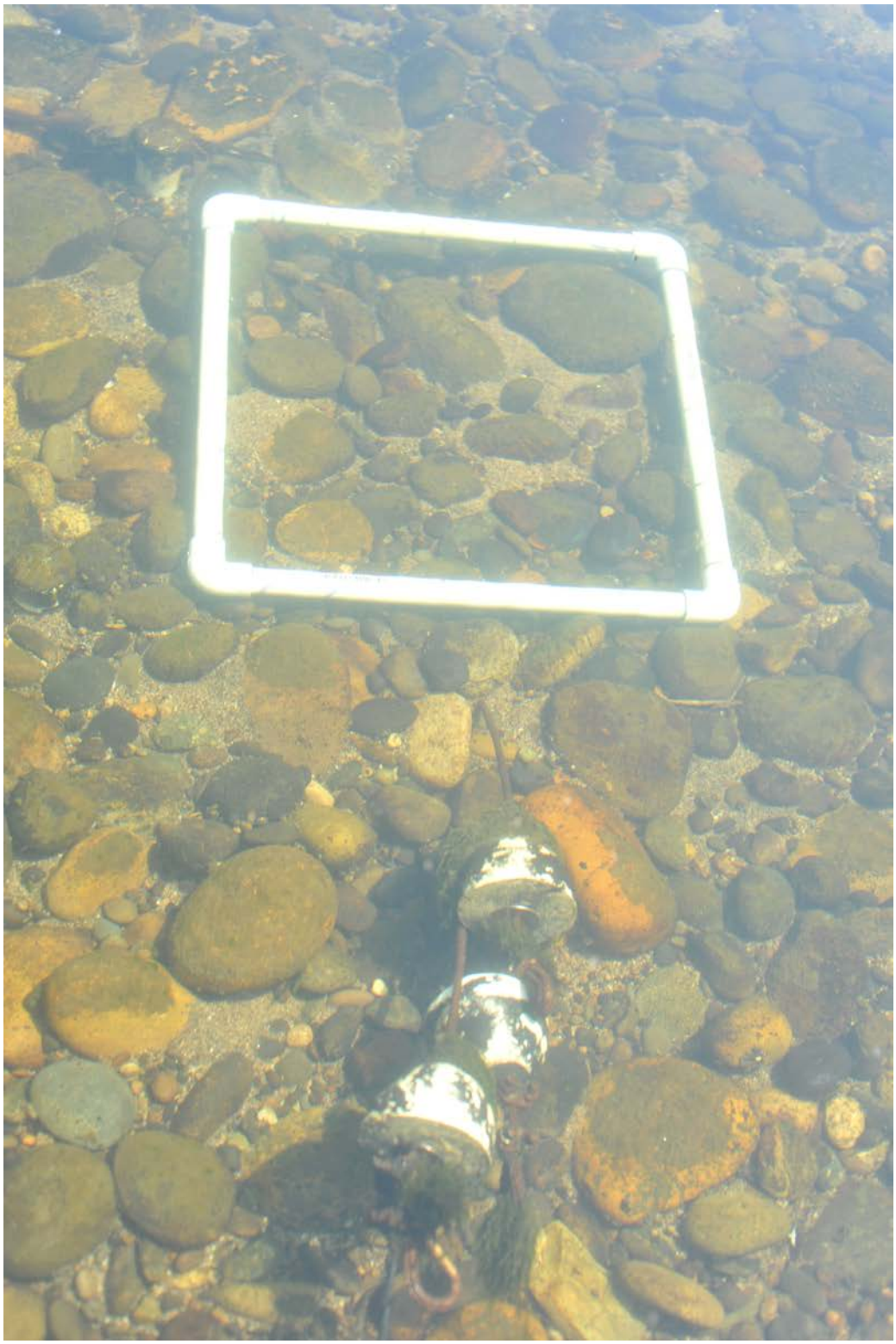

Figure F-4. Artificial Redd at Site D on May 31, 2012. Sand is visible on bed surface directly over the sediment bag thereby suggesting additional accumulation was no longer occurring within the backfill. The reference frame is approximately 0.5 m square. A piezometer cap is visible outside the upper left corner of the reference frame.

Figure F-5. Artificial Redd at Site E on May 31, 2012. A piezometer cap is visible outside the upper right corner of the reference frame. The reference frame is approximately 0.5 m square. A piezometer cap is visible outside the upper left corner of the reference frame.

Appendix G: Post-hoc Test for Significant Difference in Hydraulic Conductivity between Sites

During Experiment 1, the hydraulic conductivity stabilized after 146 days (end of March 2012). I use the measurement values after this point in time to estimate the mean hydraulic conductivity value for each site. This sample of individual measurements provides an estimate of variance about the mean value at which each site equilibrated. In some cases, the variability in the hydraulic conductivity overlaps with that of other sites. Here, I compare the 95% confidence interval in the mean hydraulic conductivity levels between all sites after March 2012 during Experiment 1. Paired sites whose confidence levels overlap have stabilized mean hydraulic conductivities that are not significantly different at the 0.95 confidence level.

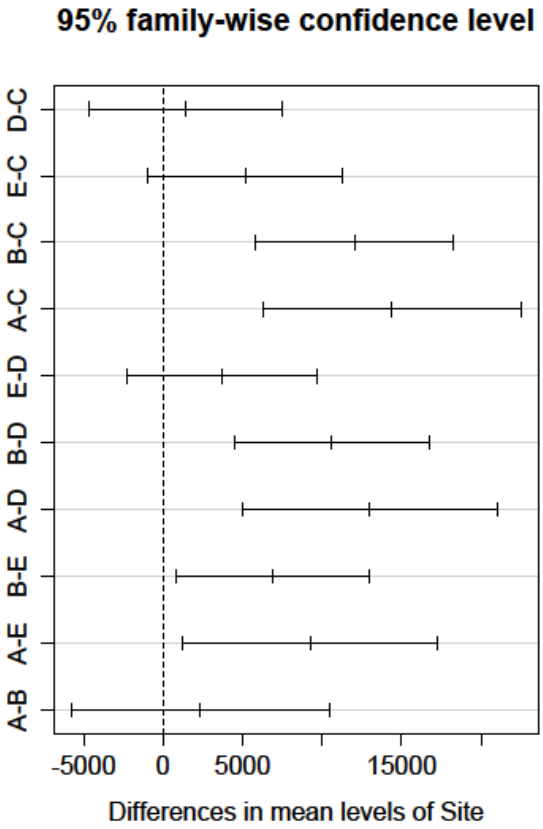

Figure G-1. Tukey HSD test for significant difference between sites in the mean hydraulic conductivity during Experiment 1 after stabilizing. The horizontal bars indicate the range of the differences between the mean hydraulic conductivity measurements for each paired comparison of sites. No significant difference in the range of values between sites is indicated where the range includes the vertical dashed line.

Appendix H: Hydraulic Conductivity as a Function of Accumulated Sediment

I consider semi-log and power functions for describing the trends in hydraulic conductivity with increasing accumulated sediment using the sieved backfill measurements from Experiments 2 and 3 (Figure H-1). The semi-log relationship produces trends that are more variable between sites (Figure H-1, left). The variation in these trends appears to result from the difference in accumulated sediment measured during the experiments. The sites with the least accumulated sediment (e.g., Sites A and B) have more steeply decreasing trends while those that accumulated more sediment (e.g., Sites D and E) have shallow decreasing trends. When considered together the semi-log trend, indicated by the fine black line, does not describe this change in slope. Power functions describe the trends from individual sites with generally similar coefficients of determination (R^2) (Figure H-1, right). However, the trend from all the measurements is better described by a power function than the semi-log relationship as indicated by the greater R^2. This generalized relationship indicates an order of magnitude decrease in conductivity with an order of magnitude increase in sand accumulation.

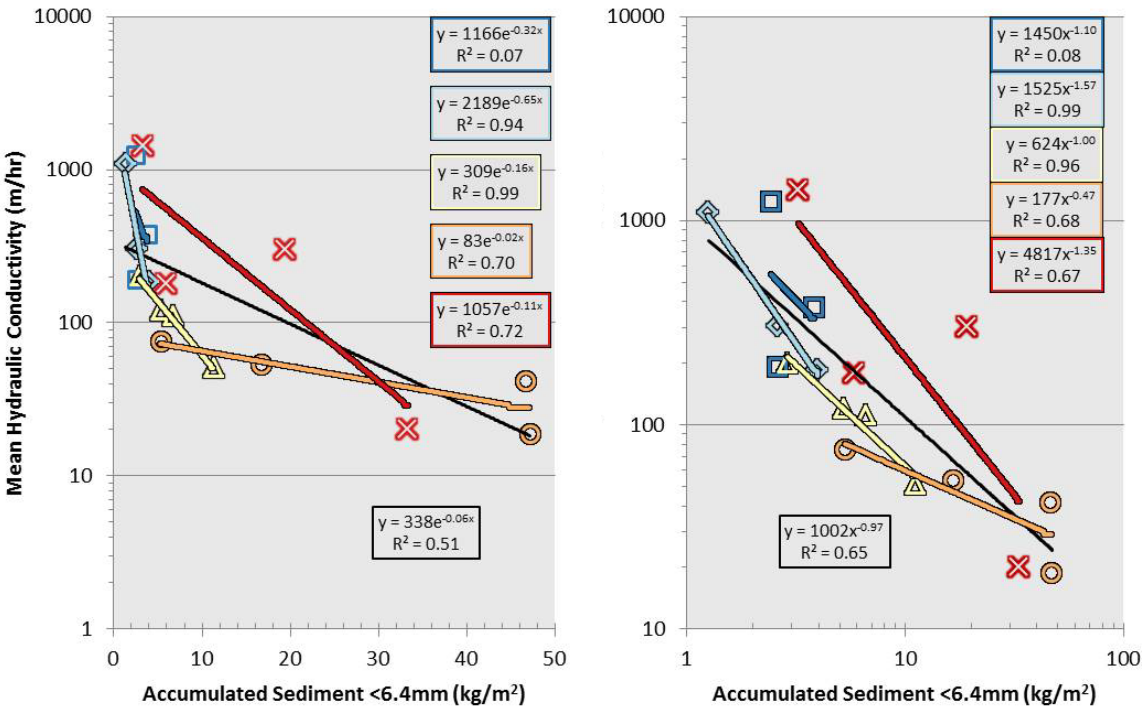

Figure H-1. Assessing the relationship between mean hydraulic conductivity and accumulated sediment.

Appendix I: Accumulated Grain Sizes <6.4 mm and Cumulative Transport

Table I-1. Comparison of the cumulative transport and accumulated sediment <6.4 mm in diameter. Accumulated sediment is shown as (i) the mass per unit area as defined by the circular rim of the sediment bag, and (ii) the accumulated sediment percent of the sample total mass in parentheses. The accumulated sediment mass is often nearly equivalent to the cumulative transport when sediment bags incurred small amounts cumulative sediment transport (e.g., cumulative transport less than about 4 kg/m). This suggests that the cleansed gravel backfill initially has a high trap efficiency and that after about 4 kg/m^2 of accumulation additional grains delivered to the redd are less likely to accumulate.

	Location	SedBag1 Accumulated <6.4mm kg/m^2 (%)	SedBag1 Cumulative Transport kg/m	SedBag2 Accumulated <6.4mm kg/m^2 (%)	SedBag2 Cumulative Transport kg/m
Experiment 1	Site A	1.7 (0.9)	1.6	NA (NA)	8.1
	Site B	1.0 (1.0)	3.5	3.8 (4.1)	27.2
	Site C	1.1 (1.0)	0.5	1.0 (0.9)	7.1
	Site D	1.1 (0.7)	6.2	10.8 (6.2)	83.5
	Site E	2.9 (1.8)	7.9	11.0 (6.2)	107.9
Experiment 2	Site A	2.2 (1.4)	2.9	1.4 (2.5)	7.5
	Site B	2.3 (1.0)	15.2	26.5 (9.8)	58.4
	Site C	1.7 (0.9)	13.2	6.4 (3.0)	171.8
	Site D	9.5 (7.3)	83.7	26.7 (10.0)	537.1
	Site E	1.9 (1.8)	110.5	11.1 (4.1)	725.9
Experiment 3	Site A	2.8 (1.6)	2.7	1.5 (1.0)	9.5
	Site B	0.7 (0.7)	11.8	1.5 (0.8)	41.1
	Site C	3.8 (2.8)	4.1	3.0 (2.1)	14.6
	Site D	3.1 (2.1)	43.9	26.9 (14.1)	155.1
	Site E	3.4 (2.0)	57.0	19.1 (10.8)	199.9

Appendix J: Hydraulic Conductivity versus Cumulative Transport

Table J-1. Results of ANCOVA tests for statistically significant difference between sites in the coefficients of the regression models of hydraulic conductivity as a function of cumulative transport (Figure 14). Two matrices are presented. (Top) Probability values are presented from the comparisons of regression models from Experiment 1 and (Bottom) from Experiments 2 and 3. A value indicates significantly different coefficients at a confidence level of 0.95 when it is less than 0.05. The upper right half (shaded blue) of the matrices provides the test results from the comparisons of slope coefficients and the lower left (shaded red) are those of the intercept coefficients. Diagonals (shaded gray) indicate the p-value of perfect correspondence in the coefficients when the regression results are compared to themselves.

Experiment 1 (Unsieved Backfill)		**Slope Coefficient**				
		Site A	**Site B**	**Site C**	**Site D**	**Site E**
Intercept Coefficient	**Site A**	1	0.844	0.286	0.060	0.416
	Site B	0.207	1	0.277	0.105	0.470
	Site C	8.67E-06	3.21E-06	1	0.492	0.473
	Site D	0.880	0.042	1.20E-05	1	0.098
	Site E	0.177	0.369	2.70E-07	7.77E-03	1

Experiments 2 & 3 (Sieved Backfill)		**Slope Coefficient**				
		Site A	**Site B**	**Site C**	**Site D**	**Site E**
Intercept Coefficient	**Site A**	1	0.200	0.061	0.045	0.490
	Site B	0.600	1	0.828	0.390	0.768
	Site C	0.717	0.054	1	0.326	0.595
	Site D	0.929	0.470	0.259	1	0.333
	Site E	0.541	0.431	0.062	0.081	1

Table J-2: Results from ANCOVA tests of statistically significant difference between backfill types at a site in the coefficients of the regression models of hydraulic conductivity as a function of cumulative transport (Figure J-1). The probability that the slope and intercept coefficients are not significantly different are given for the regression models from each site. A p-value less than 0.05 indicates that the coefficients are significantly different at a confidence level of 0.95.

Site	**slope coefficient**	**intercept coefficient**
A	0.088	0.856
B	0.847	0.993
C	0.416	4.8E-05
D	0.821	0.184
E	0.488	0.065

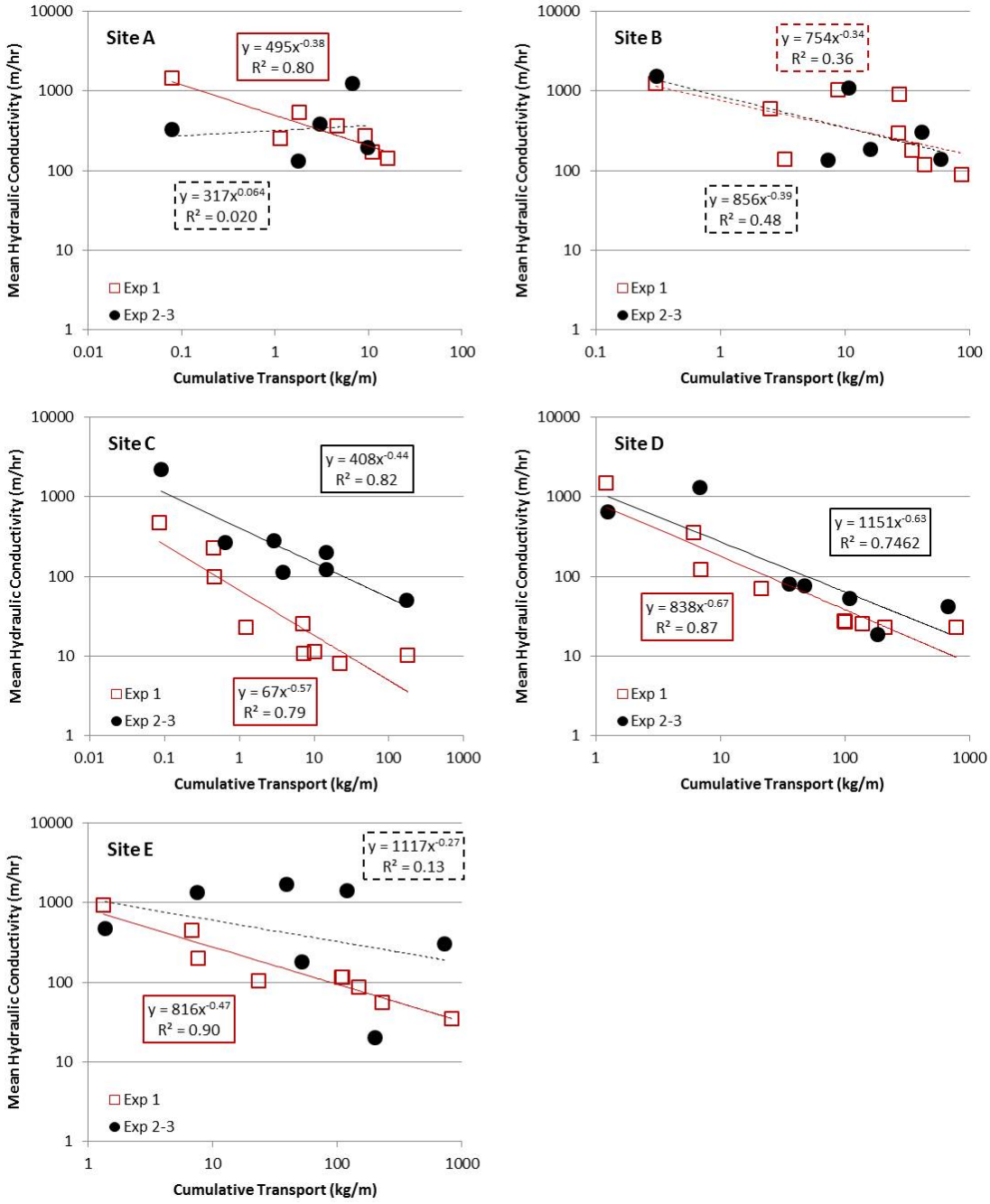

Figure J-1: Comparison of the average hydraulic conductivity as a function of cumulative bed load transport between backfill experiments at a site with and without cleansing. Data are presented at each site for Experiment 1 (red) that used unsieved backfill and for Experiments 2 and 3 (black) with backfill sieved to remove grains smaller than 6.4 mm. Dashed lines indicate regression trends that are not a significant function of cumulative transport (Table 3).